A NOVEL ALL WHEEL DRIVE TORQUE VECTORING CONTROL SYSTEM APPLIED TO FOUR WHEEL INDEPENDENT DRIVE ELECTRIC MOTOR VEHICLES UTILIZING SUPER TWISTING AND LINEAR QUADRATIC REGULATOR METHODS

A Thesis

presented to

the Faculty of California Polytechnic State University,

San Luis Obispo

In Partial Fulfillment

of the Requirements for the Degree Master of Science in Electrical Engineering

by

Kenneth D. Schmutz

December 2018

COMMITTEE MEMBERSHIP

TITLE:	A Novel All Wheel Drive Torque Vectoring Control System Applied to Four Wheel Independent Drive Electric Motor Vehicles Utilizing Super Twisting and Linear Quadratic Regulator Methods
AUTHOR:	Kenneth D. Schmutz
DATE SUBMITTED:	December 2018
COMMITTEE CHAIR:	Clay McKell, Ph.D. Lecturer in Electrical Engineering
COMMITTEE MEMBER:	Arthur MacCarley, Ph.D. Professor of Electrical Engineering
COMMITTEE MEMBER:	Helen Yu, Ph.D. Professor of Electrical Engineering

ABSTRACT

A Novel All Wheel Drive Torque Vectoring Control System Applied to Four Wheel Independent Drive Electric Motor Vehicles Utilizing Super Twisting and Linear Quadratic Regulator Methods

Kenneth D. Schmutz

This thesis contains the design and simulation test results for the implementation of a new all-wheel drive (AWD) torque vectoring (TV) control system. A separate algorithm using standard control methods is included in this study for a comparison. The proposed controller was designed to be applied to an AWD independent drive electric vehicle, however the main concepts can be re-purposed for other vehicle drive train configurations. The purpose of the control system is to assist the driver in achieving a desired vehicle trajectory whilst also maintaining stability and control of the vehicle. This is accomplished by measuring various real time parameters of the vehicle and using this information as feedback for the control system to act on. The focus of this thesis resides on the controller. Hence, this study assumes perfect observation of feedback parameters, therefore some uncertainties are not accounted for. Using feedback parameters, the control system will manage wheel slip whilst simultaneously generating a torque around the center of gravity of the vehicle by applying a torque differential between the left and right wheels.

The proposed TV algorithm is simulated in MATLAB/Simulink along with another separate TV algorithm for comparison. Both algorithms are comprised of two main parts: a slip ratio controller applied to each wheel individually and stability controller that manages yaw rate and side slip of the vehicle. The new algorithm leverages the super twisting algorithm for the slip ratio controller and uses a fusion of a linear quadratic regulator with the integral term of a super twisting algorithm to implement the yaw rate and side slip controller. The other algorithm used for comparison derives its implementation for the slip ratio controller and yaw rate and side slip controllers from simple and standard first order sliding mode control methods.

Both control algorithms were tested in three different main tests: anti-lock braking, sine dwell (SD) steering, and constant steering angle (CSA) tests. To increase the comprehensive nature of the study, the SD and CSA tests were simulated at 3 speeds (30,50, and 80 mph) and the steering angle parameter was varied from 2 to 24 degrees in increments of 2. The result of this study proves that the proposed controller is a feasible option for use in theory. Simulated results show advantages and disadvantages of the new controller with respect to the standard comparison controller. Both controllers are also shown to provide positive impacts on the vehicle response under most test conditions.

ACKNOWLEDGMENTS

The work in this thesis would not have been possible without the love and support from colleagues, family, and friends. I would like to thank my advisor Clay McKell for the generous amount of time and effort he put into my guidance and help.

To my parents Ken and Mary - Thank you for everything you have done for me. Words cannot express how grateful and lucky I am to be your son.

TABLE OF CONTENTS

LIST OF TABLES

LIST OF FIGURES

Chapter 1

Introduction

1.1 Electric Vehicles and Control Systems Background

The concept of electric vehicle technology is not new, as the first examples of this technology date back to the 1800s. This technology fell in popularity to the prominent internal combustion engine. However, due to major advancements in electronic technologies, the electric vehicle has made a resurgence in recent times. Newer technologies such as microcontrollers, FPGAs, and various sensors have enabled the ability to control these electric vehicles with precision. This precision control provided through electric motor controls can offer heightened level of vehicle stability management, efficiency, safety and performance.

Electric vehicles typically have 3 different layouts; front wheel drive, rear wheel drive, or all wheel drive. Each of these configurations has their own advantages pertaining to functionality, performance, efficiency, and cost. The all wheel drive layout is investigated in this study, as this offers the highest amount of control and performance. All wheel drive has different layouts in itself, where power is sent to the wheels through either a mechanical differential or an electronic (virtual) differential. This paper focuses on the setup where each wheel is driven independently by its own

motor, allowing for power allocation to be determined through a torque vectoring algorithm, which can be thought of as an implementation of a virtual differential.

1.2 Motivation and Goals

With the popularity of electronic controls and electric vehicles on the rise, many studies have focused on the several aspects of vehicle stability enhancement [18]. These topics include but are not limited to anti-lock braking control, active yaw control, and stability control systems. The main motivation for this thesis was to create a novel control system that addresses all of the topics mentioned above. An all wheel independent drive configuration as shown in Figure 1.1 offers the most flexibility and control performance, which is why this layout was chosen for this study.

The goal of this paper is to investigate and validate a novel torque vectoring controller that was created using Linear Quadratic Regulator (LQR) and Super Twisting Algorithm (STA) concepts. For validation, a second algorithm is analyzed which draws from standard sliding mode control concepts. These two separate algorithm strategies are analyzed in the following control situations: anti-lock braking control and active stability control. With the investigation results, insight will be provided into the performance of each algorithm as well as their advantages and disadvantages.

1.3 State-of-the-Art Stability Systems

Vehicle traction control systems (TCS), anti-lock braking systems (ABS) and electronic stability programs (ESP) first started appearing in the 1980s [28], and development of these systems continues in present day. These technologies provide aid to the driver and attempt to prevent the vehicle from losing control. An evasive maneuver is an example of a situation that can place the vehicle at its physical operating limits, where it becomes difficult or impossible for a driver to maintain control. With the aid of TCS, ABS, and ESP, a vehicle can prevent itself from becoming unstable whilst simultaneously helping the driver achieve their desired trajectory. ABS, TCS, and ESP systems have been studied extensively and proven to save lives. These sy-

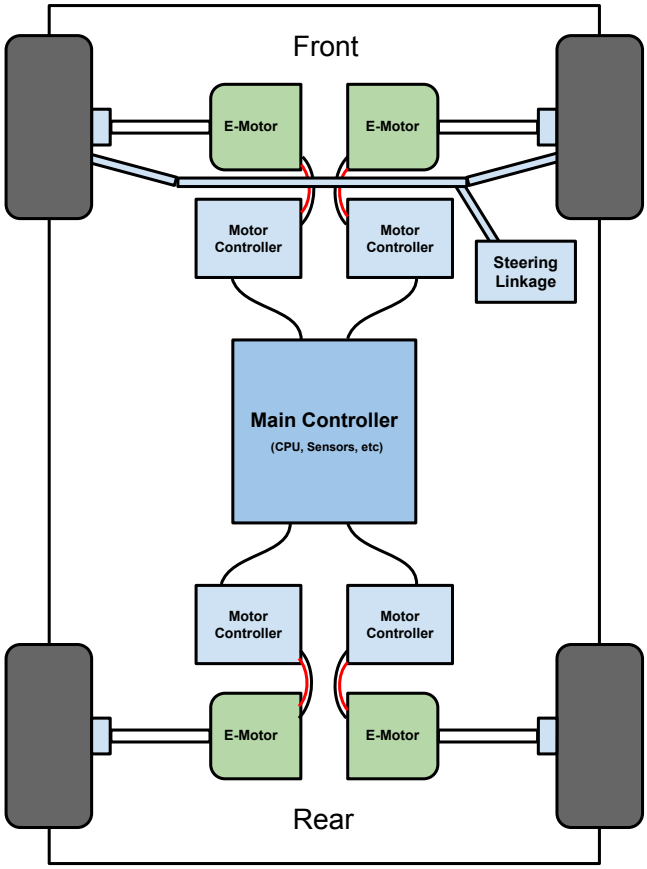

Figure 1.1: *Diagram of Electric Vehicle Configured for Independent AWD*

stems have become so important that the United States requires all light vehicles to be equipped with ABS, TCS, and ESP [29].

ABS, TCS and ESP require feedback to operate which comes from various sensors mounted to the vehicle. These sensors measure and provide state information to a main controller on the vehicle. The current vehicle state is then compared with a current desired state, and in the case of a significant difference the main controller will determine and actuate an appropriate intervention [15].

ABS prevents the wheels from locking up during braking and TCS prevents excessive wheel spin during acceleration. Both of these systems are lower level fundamental portions of an ESP, which relies on them. ESP is a higher level controller that mana-

ges transverse-dynamics by focusing on preventing a vehicle from over-steering and under-steering. It also attempts to keep the vehicle pointed the direction that the driver's steering input requests. There are several ways of accomplishing this including active steering (AS), torque vectoring (TV) and active damping (AD).

1.3.1 Active Steering Control

Active steering control offers three main configurations including active front steering (AFS) control, active rear steering (ARS) control, and four-wheel active steering (4WAS) control. AFS is typically used for stability control using feedback control methods. In contrast, ARS is typically used for enhancing vehicle maneuverability and can be implemented using feedback and feed forward methods. Robust strategies such as adaptive and sliding mode control are often used for active steering to account for vehicle uncertainties[2].

1.3.2 Active Damping Control

Active damping utilizes a variety of actuators including electro-hydraulic, electro-rheological and magnetorheological dampers which manage the vehicle suspension response. A typical trade off that is managed with these systems is between road holding and ride comfort. Sky-hook control is typically used for ride comfort while ground-hook control is used for road-holding [10]. Sky-hook control restricts the movement of sprung mass (vehicle chassis) to enhance ride comfort, whereas ground-hook control focuses on damping of unsprung mass (vehicle wheel) [39]. Further information on state-of-the-art suspension control can be found in Tseng's Article [40].

1.3.3 Torque Vectoring

To accomplish torque vectoring (TV) a vehicle requires the active ability to send different amounts of power to the wheels via a differential. This can be visualized in Figure 1.2 where the red and blue arrows represent braking and acceleration forces

applied by the vehicle wheels due to a torque vectoring system.

Figure 1.2: *Visualization of Torque Vectoring*

The two common kinds of differential actuator mechanisms used in TV control are either of mechanical or electrical nature. A mechanical differential utilizes clutch packs, which vary power to the wheels based upon their compression [7]. An electrical (virtual) differential uses separate electric motors to power wheels independently [8]. A main controller containing logic can then decide how much power to send to each wheel.

Torque vectoring control can be broken down into two major segments. These segments include the vehicle wheel slip ratio controllers, and the vehicle stability controller. Slip ratio controllers are a lower level controller with the purpose of ensuring that each wheel is producing the correct amount of force. This force applied to each wheel is determined by a higher level vehicle yaw/side-slip controller.

Information regarding the many slip ratio controller strategies can be derived

from studying anti-lock braking control systems. In an article from 2011 titled "An Antilock-Braking Systems (ABS) Control: A Technical Review" gives a slightly dated but comprehensive glimpse into the strategies used for slip ratio control [1]. Another article titled "A Review of Active Yaw Control System for Vehicle Handling and Stability Enhancement", explains high level details pertaining to structure and performance of several control algorithms proposed by many different authors to achieve vehicle stability enhancement [2]. Another article titled "Systematization of Integrated Motion Control of Ground Vehicles" describes the findings of several papers which attempt to integrate different control aspects into a single system controller [18]. All of these papers present several control options that include but are not restricted by forms of proportional integral control, sliding mode control, model predictive control, optimal control, fuzzy logic control, robust control, and adaptive control methods.

1.3.4 Thesis Relation to State-of-the-Art

This thesis focuses on the development of an ESP that includes ABS and TCS. The same control principles used for ABS are also used for TCS. Both ABS and TCS are the fundamental components of the overall ESP. The overlying ESP created in this thesis utilizes torque vectoring and determines the power sent to each wheel. A vehicle layout comprised of all-wheel independent electric motor drives is used in this thesis.

1.4 Related Technologies

With a resurgence of electric vehicle technology, several companies have taken the initiative to create their own technology to compete in the market place. Several examples can be seen today from well known automakers and start up companies.

Mercedes-Benz developed a prototype vehicle in electric all wheel independent drive configuration in 2011 called the SLS AMG Coupe Electric Drive. This vehicle is shown in Figures 1.3 and 1.4 and provides a great example of the technology that will be studied in this thesis.

Figure 1.3: *Mercedes-Benz E-CELL Body View [5]*

Another more recent example of the utilization of this technology can be found with the start-up company Zoox, which is developing an all-wheel drive and all wheel steering electric vehicle with the main purpose of acting as an autonomous taxi [36]. The vehicle is still in prototype stages, but shows that this technology is quite relevant at this time.

1.5 Report Outline

The technical portion of this thesis will begin with chapter 2. That chapter will review vehicle dynamics theory and present the equations used to implement a model in MATLAB Simulink. Chapter 3 will then discuss the parameters used to implement the model for simulation. Following this, chapter 4 will introduce the control algorithm strategy developed by the author of this paper, and describe the mathematical equations that represent it. The algorithm used for performance verification will then

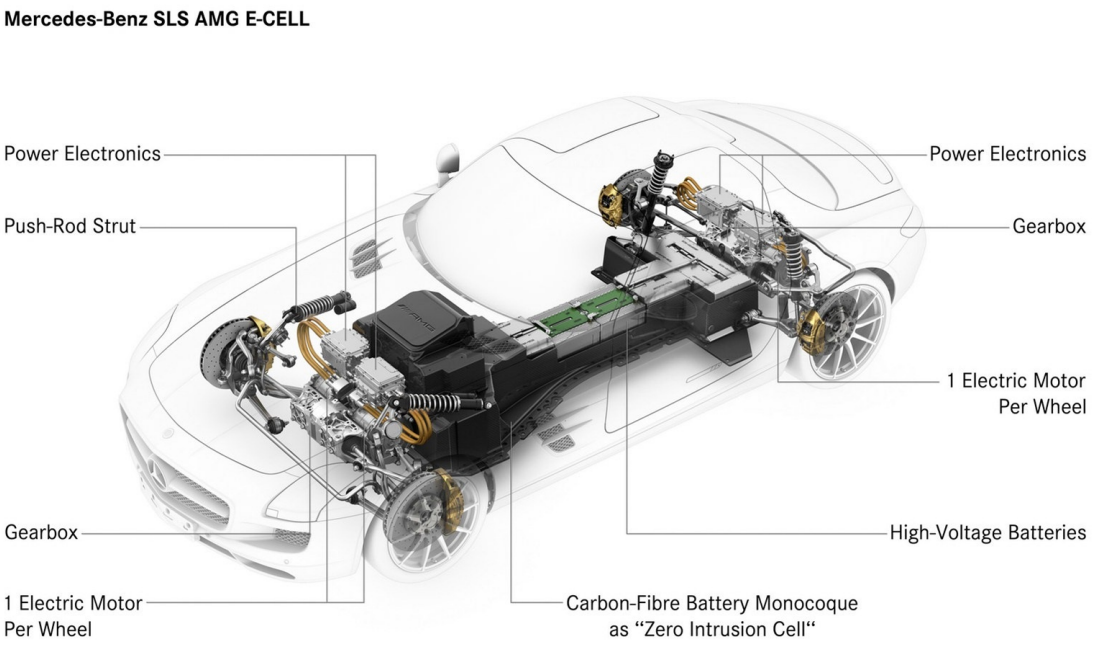

Figure 1.4: *Mercedes Benz ECELL Transparent View [6]*

be defined in chapter 5. With both of the control algorithms defined, chapter 6 will present test plans and results for both algorithms in different scenarios. Lastly, chapter 7 will provide a simple summary of the results and insights found. Limitations, improvements, and future work of this study will also be discussed.

Chapter 2

Vehicle Dynamics Theory and Modeling

2.1 Determination of Weight Transfer Characteristics

As a vehicle accelerates in any direction the chassis shifts its weight from a neutral stance. This creates an offset of weight distribution among each of the four tires. This weight change results in a change of the amount of force that each tire can produce. A torque vectoring control system will use this information in order to send the appropriate amount of torque to each wheel. Hence weight transfer is an important piece of the overall vehicle dynamics model. The following sections describe a derivation by Brian Beckman of a mathematical model for this phenomenon [3].

2.1.1 Weight Transfer Coordinate System

The development of a mathematical model to describe the vehicle characteristics is dependent on the definition of a coordinate system. Weight transfer characteristic equations are derived by first declaring a coordinate system and placing coordinates

within that system that represent the center locations of the wheels. Figure 2.1 shows a diagram of this coordinate system. The coordinate system consists of three independent vector directions: *X (longitudinal)*, *Y (Lateral)*, and *Z (Vertical)*. From this system, the locations of the center of each wheel are defined using symbolic constants. These constants are listed below in Table 2.2, and correspond to those pictured in Figure 2.1.

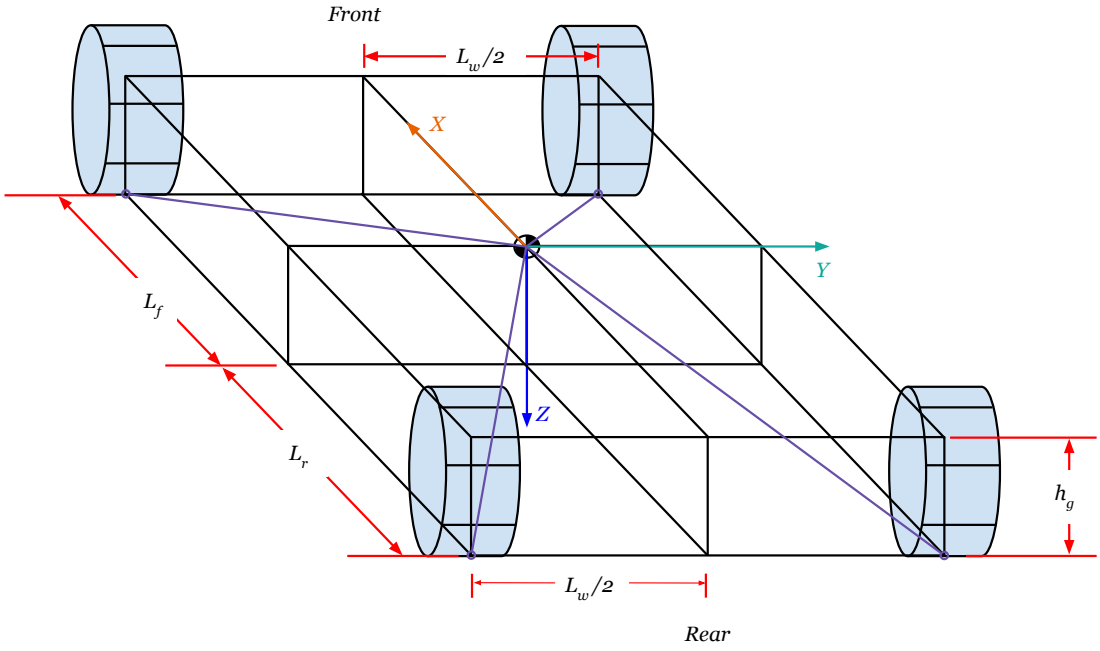

Figure 2.1: *Diagram of Coordinate System Used for Derivations of Weight Transfer*

2.1.2 Weight Transfer Force Derivations

From the above constant definitions, the locations of the tire contact patch are defined as a list of vectors:

$$TireLocs = \left[\{L_f, \frac{L_w}{2}, h_g\}, \{-L_r, \frac{L_w}{2}, h_g\}, \{-L_r, -\frac{L_w}{2}, h_g\}, \{L_f, -\frac{L_w}{2}, h_g\}\right] \quad (2.1)$$

Table 2.1: *Weight Transfer Coordinate Constants*

Constant	Units	Description
h_g	Meters [m]	Vertical distance of the Center of Gravity (CG) from the ground
L_f	Meters [m]	Longitudinal distance from the CG to the front axle geometry center
L_r	Meters [m]	Longitudinal distance from the CG to the rear axle geometry centers
L_w	Meters [m]	Lateral distance between wheels (Assuming that front and rear wheels are not staggered)

A list of 3-axis force vectors at each wheel are created. Numbers 1-4 are used to denote the locations of each tire. The "z" components of each vector are negated in order to simply produce a positive result.

Table 2.2: *Wheel Forces*

Variable	Units	Description
$f_{1x,y,z}$	Newtons [N]	Front Right Forces
$f_{2x,y,z}$	Newtons [N]	Rear Right Forces
$f_{3x,y,z}$	Newtons [N]	Rear Left Forces
$f_{4x,y,z}$	Newtons [N]	Front Left Forces

$$f\_tot\_x, y, z = \Big[\{f_{1x}, f_{1y}, -f_{1z}\}, \{f_{2x}, f_{2y}, -f_{2z}\}, \{f_{3x}, f_{3y}, -f_{3z}\}, \{f_{4x}, f_{4y}, -f_{4z}\}\Big] \tag{2.2}$$

By taking the vector cross product of the tire locations and the tire forces, the resul-

tant vector is the torque at each wheel.

$$\tau_{Tires} = TireLocs \otimes f\_tot\_x, y, z \tag{2.3}$$

τ_{Tires} is a set of four vectors that represent the torques at each tire about translated copies of the the x, y, and z axes, in a "right-hand sense". These vectors are then collapsed into a single vector that represents the total torques in the x, y, and z directions. This is accomplished by summing together the respective components of each vector into one. Meaning that each "x" component of each vector is combined to form a single "x" component of the new vector. This is repeated for the y and z axes. The resultant vector is shown below in the following equations:

$$\tau_x = -f_{1y}h_g - f_{2y}h_g - f_{3y}h_g - f_{4y}h_g - f_{1z}\frac{L_w}{2} + f_{4z}\frac{L_w}{2} - f_{2z}\frac{L_w}{2} + f_{3z}\frac{L_w}{2} \tag{2.4}$$

$$\tau_y = -L_r(f_{2z} + f_{3z}) + L_f(f_{1z} + f_{4z}) + (f_{1x} + f_{2x} + f_{3x} + f_{4x})h_g \tag{2.5}$$

$$\tau_z = -L_r(f_{2y} + f_{3y}) + L_f(f_{1y} + f_{4y}) + (-f_{1x} + f_{4x} - f_{2x} + f_{3x})\frac{L_w}{2} \tag{2.6}$$

τ_x, τ_y, and τ_z represent the torque in the X direction, Y direction, and Yaw about the center of gravity respectively. Assuming that the vehicle in question is a rigid body experiencing no lean or rollover in any direction, it can be assumed that the net torque about the x and y axes is zero. This also requires all four tires are in contact with the road surface.

We also assume that cross ratio weights on each tire is symmetric. This assumption is expressed by setting $f1z * f4z = f2z * f3z$. The final relationship is formed on the idea that the sum of the vertical loads at each wheel equals the total weight of the vehicle: $f1z + f2z + f3z + f4z = m * g$, where m is the mass of the vehicle and g is the acceleration due to gravity.

With these four equations set in place, Mathematica was used extensively in order to solve for the vertical forces on the front right, rear right, rear left and front left

wheels respectively [3]. F_X and F_Y represent the net forces in the center of gravity point in the x and y directions respectively.

$$f_{1z} = \frac{(-F_X h_g + L_r mg)(-F_Y h_g + mg\frac{L_w}{2})}{(L_f + L_r)mgL_w} \tag{2.7}$$

$$f_{2z} = \frac{(F_X h_g + L_f mg)(-F_Y h_g + mg\frac{L_w}{2})}{(L_f + L_r)mgL_w} \tag{2.8}$$

$$f_{3z} = \frac{(F_X h_g + L_r mg)(F_Y h_g + mg\frac{L_w}{2})}{(L_f + L_r)mgL_w} \tag{2.9}$$

$$f_{4z} = \frac{(-F_X h_g + L_f mg)(F_Y h_g + mg\frac{L_w}{2})}{(L_f + L_r)mgL_w} \tag{2.10}$$

2.2 Force Composition

The Force composition of the vehicle entails the calculation of the Longitudinal Force (F_X), Lateral Force (F_Y), and Torque (M_Z) in reference to the center of gravity of the vehicle. These calculations are made using nine inputs: longitudinal and lateral forces produced from each tire and user steering angle. Force Composition characteristic equations are derived from the diagram as shown in Figure 2.2.

The quantities within Figure 2.2 are described in Table 2.3. r is the yaw rate of the vehicle about the center of gravity point. This is simply a measure of how fast the vehicle is rotating. Body slip angle (β) computes the vehicle lateral motion and is defined as $arctan\left(\frac{V_Y}{V_X}\right)$. β is used as a measure of how straight the vehicle is traveling. Wheel slip angle (α_{ij}) is the difference between the steering angle (δ) and the angle at which the particular wheel is actually traveling. Understeer will typically produce larger wheel slip angles on the front wheels. In contrast, oversteer will typically produce larger wheel slip angles on the rear wheels, but can also increase the front wheel slip angles.

Table 2.3: *Description of Variables and Constants within the Vehicle Force Diagram*
**Note: The prefixes or subscripts containing variables i or j represent locations on the vehicle diagram. i=R or F (Rear or Front) and j=L or R (Left or Right) .*

Variable	Units	Description
α_{ij}	Degrees [°]	Slip angle of tire
β	Degrees [°]	Body slip angle
δ	Degrees [°]	Steering angle
ijF_X	Newtons [N]	Longitudinal force of each separate tire
ijF_Y	Newtons [N]	Lateral force of each separate tire
r	Degrees [°/s]	Yaw rate
V_X	meters/second [m/s]	Longitudinal Velocity of CG
V_Y	meters/second [m/s]	Lateral Velocity of CG

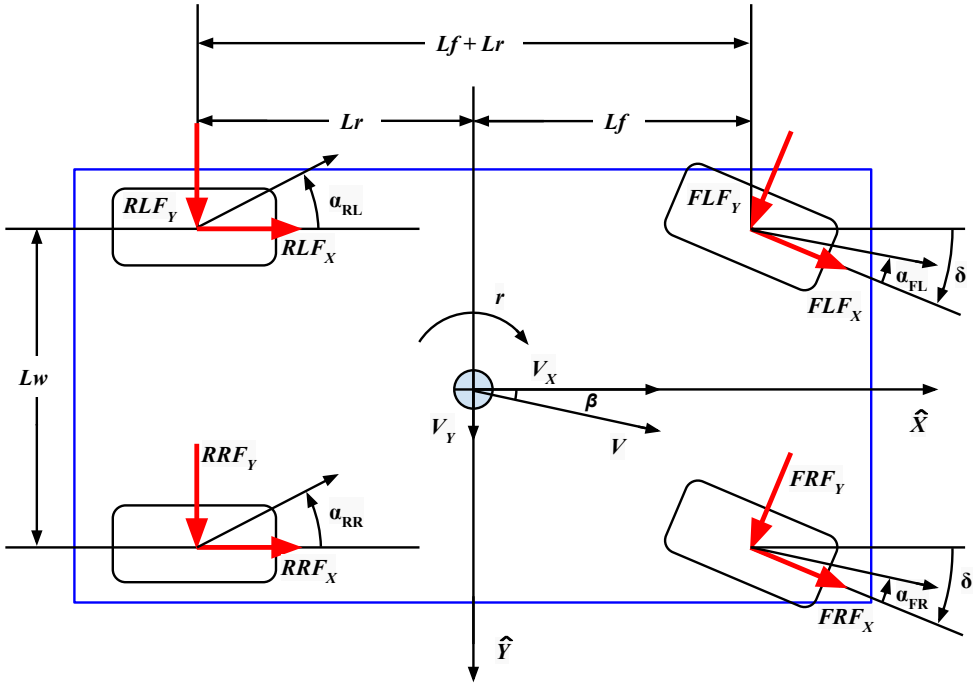

Figure 2.2: *Vehicle Force Diagram*

In order to derive the force composition equations, Newton's second law of motion was used for force as well as torque. The composition comprises of longitudinal force (F_X), lateral force (F_Y), and net yaw torque (M_Z) of the vehicle. Each wheel in Figure 2.2 is labeled with forces ijF_X and ijF_Y which are the longitudinal and lateral components of the overall individual tire forces respectively.

2.2.1 Longitudinal Force

The longitudinal force (F_X) is calculated as a summation of each tire force component which creates a resultant force parallel with the x-axis ($\hat{X}$). Figure 2.3 focuses on the front right wheel of Figure 2.2. It can be seen that the resultant force parallel with the x-axis (F_{X1}) is due to the orthogonal longitudinal and lateral forces of the

front right tire FRF_X and FRF_Y respectively.

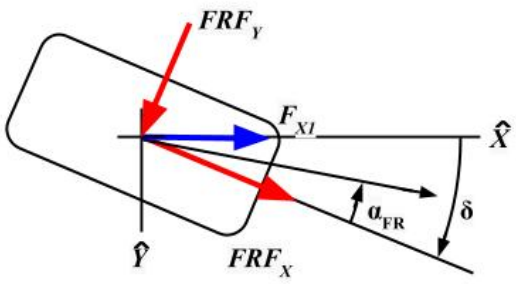

Figure 2.3: *Front Right Wheel Force Diagram for Longitudinal Force Derivation*

By using simple trigonometric relations, the resultant force parallel with the x-axis ($\hat{X}$) is $F_{X1} = \cos(\delta) * FRF_X - \sin(\delta) * FRF_Y$. The positive force results from FRF_X and the negative force is due to FRF_Y. The front left wheel is treated the same way as the front right wheel and the resultant force is $F_{X2} = \cos(\delta) * FLF_X - \sin(\delta) * FLF_Y$.

Moving to the rear of the vehicle, Figure 2.4 shows a diagram of the force components defined in Figure 2.2 for the rear right wheel.

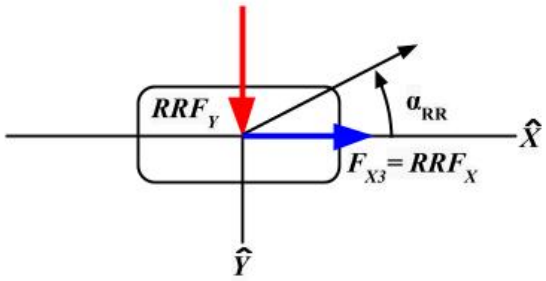

Figure 2.4: *Rear Right Wheel Force Diagram for Longitudinal Force Derivation*

The direction of the rear wheels within the model are assumed to be permanently set in parallel with the x-axis ($\hat{X}$). The rear wheels do not have a steering angle freedom, so the steering angle will always be 0 degrees. Due to this, the lateral force

RRF_Y does not cause a negative longitudinal force component of F_{X3} (longitudinal force parallel to the $\hat{X}$ axis of the rear right wheel). Therefore $F_{X3} = RRF_X$. The rear left wheel is treated the same way as the rear right wheel is treated, $F_{X4} = RLF_X$.

The net force in the longitudinal direction (F_X) is the sum of the longitudinal forces at each wheel:

$$F_X = (FRF_X + FLF_X)\cos(\delta) - (FRF_Y + FLF_Y)\sin(\delta) + RRF_X + RLF_X \quad (2.11)$$

2.2.2 Lateral Force

Moving on, the lateral force F_Y is calculated as a summation of each tire force component which creates a resultant force parallel with the y-axis ($\hat{Y}$). Observing Figure 2.5, it can be seen that the defined longitudinal and lateral forces of the front right wheel (FRF_X and FRF_Y) create a force that is parallel with the y-axis $\hat{Y}$. This is the force that effectively allows the car to turn.

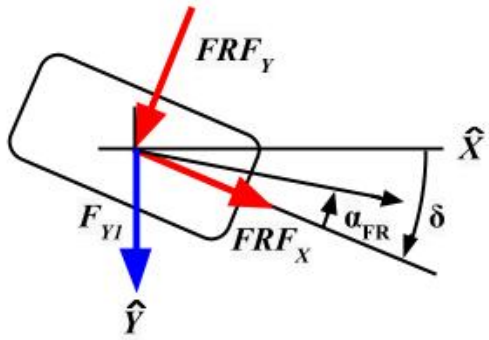

Figure 2.5: *Front Right Wheel Force Diagram for Lateral Force Derivation*

Both forces FRF_X and FRF_Y contribute positive portions of the total front right wheel lateral force, giving $F_{Y1} = \sin(\delta)FRF_Y + \cos(\delta)FRF_X$. The front left wheel is treated the same way as the front right wheel, $F_{Y2} = \sin(\delta)FLF_Y + \cos(\delta)FLF_X$. A positive force parallel to the y-axis $\hat{Y}$ represents a force that pushes right and a negative force represents left from the perspective of the driver.

The defined forces acting on the rear right wheel are shown in Figure 2.6. Since the longitudinal forces (RLF_X and RRF_X) of the rear wheels are always in parallel with the x-axis ($\hat{X}$), no force component parallel with the y-axis ($\hat{Y}$) is generated. This also implies that the full magnitude of the lateral force (RLF_Y) is seen in parallel with the y-axis ($\hat{Y}$). Therefore the rear lateral forces are $F_{Y3} = RRF_Y$, $F_{Y4} = RLF_Y$.

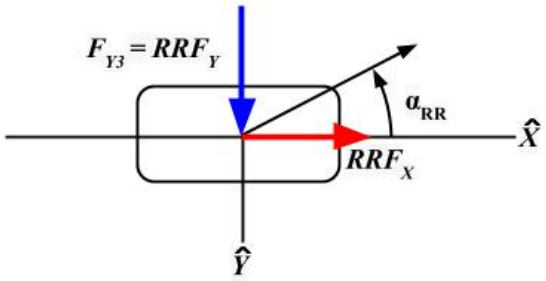

Figure 2.6: *Rear Right Wheel Force Diagram for Lateral Force Derivation*

The longitudinal force (F_Y) is calculated as a summation of each tire force component which creates a net force parallel with the y-axis ($\hat{Y}$):

$$F_Y = (FRF_X + FLF_X) * sin(\delta) + (FRF_Y + FLF_Y) * cos(\delta) + RRF_Y + RLF_Y \quad (2.12)$$

2.2.3 Torque

Lastly, the net yaw torque M_Z is calculated by summing the torques generated by each wheel. Starting with the front right wheel in figure 2.7, the torques generated about the vehicle center of gravity by the longitudinal and lateral forces (FRF_X and FRF_Y) are calculated.

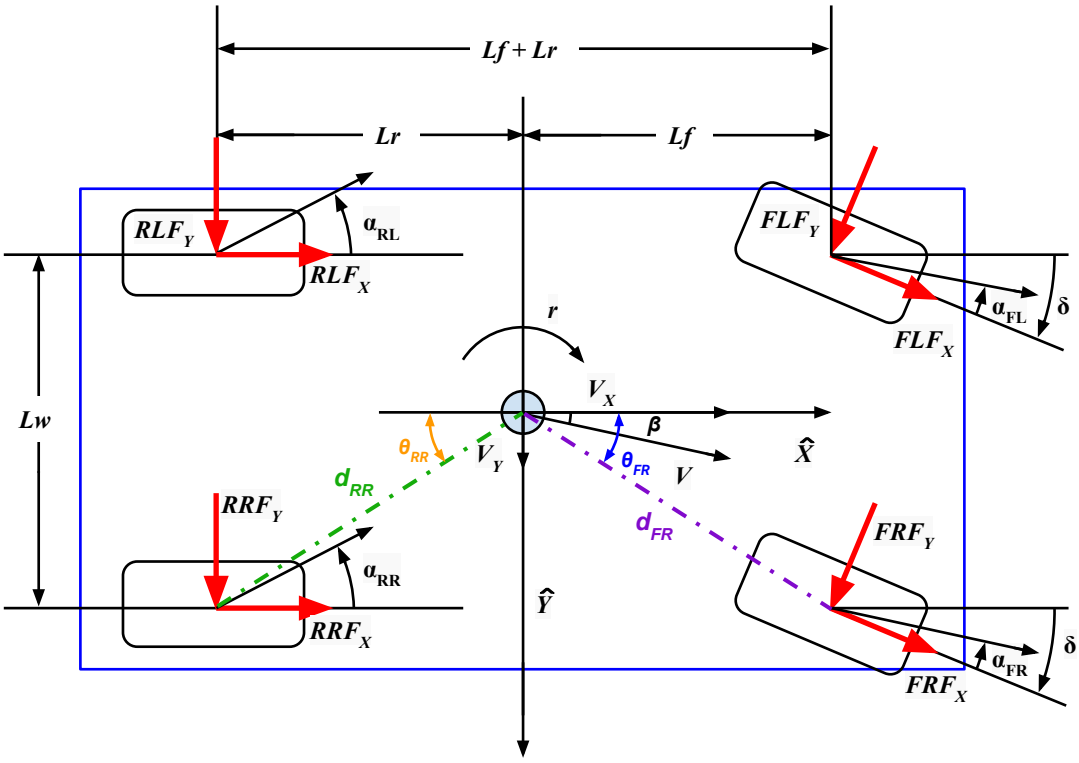

Figure 2.7: *Diagram Used for Vehicle Center of Gravity Torque Calculations*

θ_{ij} represents the angle of the tire contact patch with respect to the x-axis, and d_{ij} is the distance from the vehicle center of gravity point to the tire contact patch. Using these definitions, the torque generated by the front right longitudinal force (FRF_X) can be defined as $\tau_{FRF_X} = d_{FR} FRF_X \sin(\theta_{FR} - \delta)$. Likewise, the torque generated by the front right lateral force (FRF_Y) can be defined as $\tau_{FRF_Y} = d_{FR} FRF_Y \cos(\theta_{FR} - \delta)$. Given the dimensions of the vehicle, $\theta_{FR} = \arctan\left(\frac{L_w}{2L_f}\right)$ and $d_{FR} = \sqrt{{L_f}^2 + \left(\frac{L_w}{2}\right)^2}$. Summing τ_{FRF_X} and τ_{FRF_Y} produces the total torque generated about the vehicle center of gravity due to the front right wheel:

$$\tau_{FR} = d_{FR} FRF_X \sin(\theta_{FR} - \delta) + d_{FR} FRF_Y \cos(\theta_{FR} - \delta) \tag{2.13}$$

A similar process is followed for the front left wheel, hence:

$$\tau_{FL} = d_{FL}FLF_X \sin(\theta_{FL} + \delta) + d_{FL}FLF_Y \cos(-\theta_{FL} - \delta) \tag{2.14}$$

Moving to the rear of the vehicle, the rear wheel steering angles are fixed at zero. Therefore the rear wheels are treated differently than the front wheels when calculating their influence to the vehicle c.o.g. torque. Observing the rear right wheel in figure 2.7, the torque generated by the rear right longitudinal force (RRF_X) can be defined as $\tau_{RRF_X} = -d_{RR}RRF_X \sin(\theta_{FR})$. The torque generated by the rear right lateral force (RRF_X) can then be defined as $\tau_{RRF_Y} = -d_{RR}RRF_Y \cos(\theta_{RR})$. The summation of these two torques gives the total torque about the vehicle center of gravity due to the rear right wheel:

$$\tau_{RR} = -d_{RR}RRF_X \sin(\theta_{FR}) - d_{RR}RRF_Y \cos(\theta_{RR}) \tag{2.15}$$

A similar process is followed for the rear left wheel, hence:

$$\tau_{RL} = d_{RL}RLF_X \sin(\theta_{RL}) - d_{RL}RLF_Y \cos(\theta_{RL}) \tag{2.16}$$

To summarize, the torques about the vehicle center of gravity are placed in matrix format:

$$\begin{bmatrix} \tau_{FR} \\ \tau_{FL} \\ \tau_{RR} \\ \tau_{RL} \end{bmatrix} = \begin{bmatrix} d_{FR}FRF_X \sin(\theta_{FR} - \delta) + d_{FR}FRF_Y \cos(\theta_{FR} - \delta) \\ d_{FL}FLF_X \sin(\theta_{FL} + \delta) + d_{FL}FLF_Y \cos(-\theta_{FL} - \delta) \\ -d_{RR}RRF_X \sin(\theta_{FR}) - d_{RR}RRF_Y \cos(\theta_{RR}) \\ d_{RL}RLF_X \sin(\theta_{RL}) - d_{RL}RLF_Y \cos(\theta_{RL}) \end{bmatrix} \tag{2.17}$$

Now that a resultant torque has been calculated for each separate wheel, the total net torque about the center of gravity of the vehicle can be computed by adding all of the separate wheel torques together:

$$M_z = \tau_{FR} + \tau_{FL} + \tau_{RR} + \tau_{RL} \tag{2.18}$$

2.3 Wheel States

2.3.1 Wheel Speeds

Longitudinal wheel speeds V_{longij} are calculated in this section. Let us start by viewing figure 2.8.

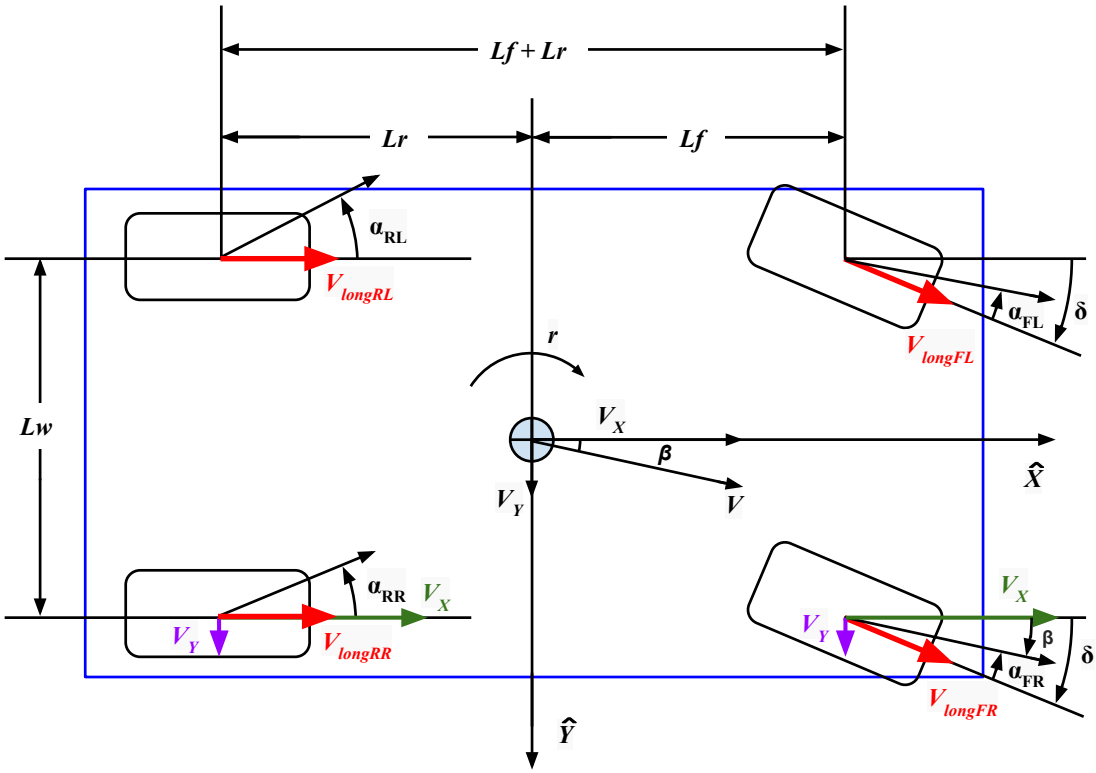

Figure 2.8: *Diagram of Coordinate System Used for Derivations of Longitudinal Wheel Velocities*

V_{longFR} is the longitudinal velocity at the hub of the front right wheel that will be solved for first. This velocity vector, as well as the respective longitudinal velocity vectors for all other wheels, are affected by vehicle longitudinal speed (V_X), vehicle lateral speed (V_Y), vehicle yaw rate (r), and steering angle (δ). By breaking the velocity vectors due the aforementioned parameters down into components, the total longitudinal velocity vectors for all wheels can be calculated. Calculating the effect of

V_X, we have $V_a = V_X \cos(\delta)$. Likewise, the effect of V_Y gives $V_b = V_Y \cos(\delta)$. Lastly, the effect of yaw rate r can be calculated as $V_c = -r\frac{L_w}{2}\cos(\delta) + rL_f \sin(\delta)$. Summing V_a, V_b, and V_c produces the total net longitudinal velocity of the front right wheel:

$$V_{longFR} = \left(V_X - r\frac{L_w}{2}\right)\cos(\delta) + (V_Y - rL_f)\sin(\delta) \tag{2.19}$$

The same methodology is used to solve for the front left wheel longitudinal velocity:

$$V_{longFL} = \left(V_X + r\frac{L_w}{2}\right)\cos(\delta) + (V_Y + rL_f)\sin(\delta) \tag{2.20}$$

The rear wheels of the vehicle are treated differently once again, as there is no steering angle to affect them. Focusing on the rear right wheel of figure 2.8, the effect of V_X on V_{longRR} is $V_d = V_X \cos(\delta)$. V_Y produces no effect since the steering angle is fixed at zero. Lastly, r generates $V_e = -r\frac{L_w}{2}\cos(\delta)$. Taking the sum of V_d and V_e creates the total net longitudinal velocity of the rear right wheel:

$$V_{longRR} = \left(V_X - r\frac{L_w}{2}\right)\cos(\delta) \tag{2.21}$$

Similar ideas are used to generate the rear left longitudinal velocity:

$$V_{longRL} = \left(V_X + r\frac{L_w}{2}\right)\cos(\delta) \tag{2.22}$$

To summarize this section, the longitudinal velocities of each wheel are placed in matrix format:

$$\begin{bmatrix} V_{longFR} \\ V_{longFL} \\ V_{longRR} \\ V_{longRL} \end{bmatrix} = \begin{bmatrix} \left(V_X - r\frac{L_w}{2}\right)\cos(\delta) + (V_Y - rL_f)\sin(\delta) \\ \left(V_X + r\frac{L_w}{2}\right)\cos(\delta) + (V_Y + rL_f)\sin(\delta) \\ \left(V_X - r\frac{L_w}{2}\right)\cos(\delta) \\ \left(V_X + r\frac{L_w}{2}\right)\cos(\delta) \end{bmatrix} \tag{2.23}$$

2.3.2 Wheel Slip Angles

The wheel slip angles (α_{ij}) measure the difference between the steering angle δ and the actual heading angle of each respective wheel. To solve for these, trigonometric relations are used to relate the velocity vectors to the slip angles. The slip angles are then found by breaking velocities of each wheel into subvectors.

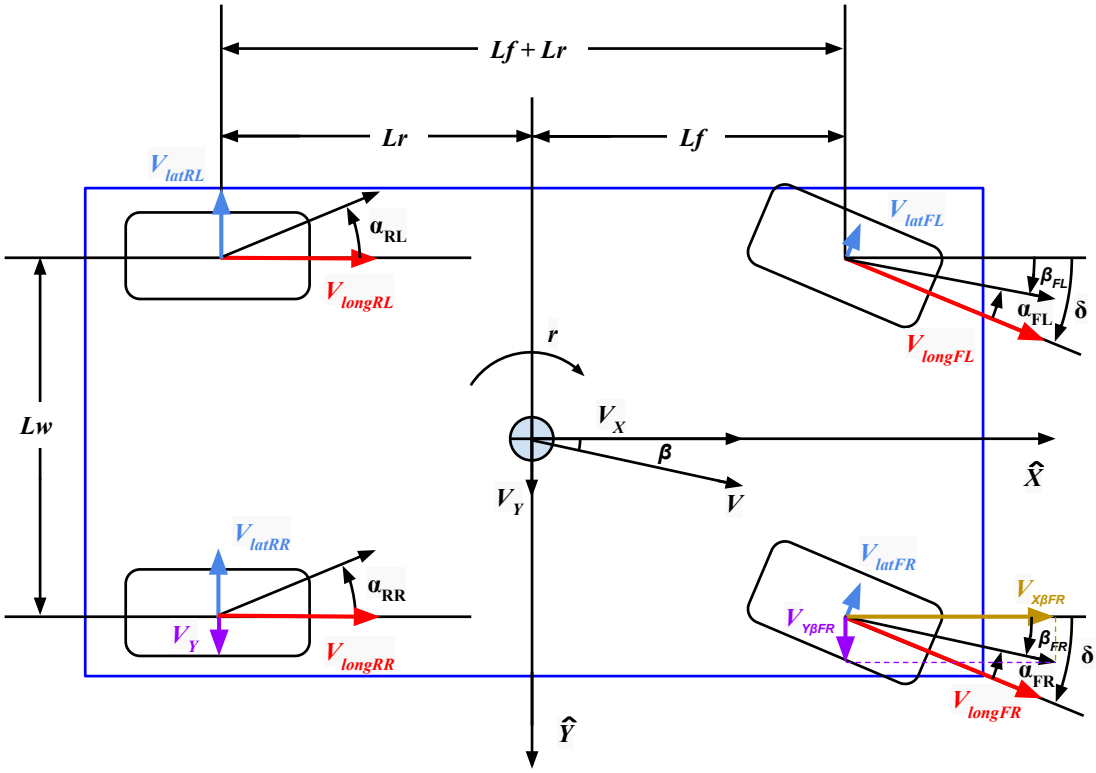

Figure 2.9: *Diagram Used for Wheel Slip Angle Calculations*

To begin, we focus on the front right wheel in figure 2.9, where $\alpha_{FR} = \delta - \beta_{FR}$. To solve for β_{FR}, the velocity vector of the actual heading of the front right wheel is broken down into components $V_{X\beta FR}$ and $V_{Y\beta FR}$. The front right slip angle can now be represented as $\alpha_{FR} = \delta - \arctan\left(\frac{V_{Y\beta FR}}{V_{X\beta FR}}\right)$. $V_{X\beta FR}$ and $V_{Y\beta FR}$ represent summed velocity vectors at the front right wheel due to V_X, V_Y and r. These summations give $V_{Y\beta FR} = V_Y + rL_f$ and $V_{X\beta FR} = V_X - r\frac{L_w}{2}$, hence the final form of the front right

slip angle is:

$$\alpha_{FR} = \delta - \arctan\left(\frac{V_Y + rL_f}{V_X - r\frac{L_w}{2}}\right) \tag{2.24}$$

Similar methodology is used for the front left wheel resulting in:

$$\alpha_{FL} = \delta - \arctan\left(\frac{V_Y + rL_f}{V_X + r\frac{L_w}{2}}\right) \tag{2.25}$$

At the rear right wheel of figure 2.9 we know the steering angle is zero, hence $\alpha_{RR} = -\beta_{FR}$. This also implies that, $V_{longRR} = V_{X\beta RR}$ and $V_{latRR} = V_{Y\beta RR}$. Therefore, the rear right slip angle can be defined as $\alpha_{RR} = \arctan\left(\frac{V_{latRR}}{V_{longRR}}\right)$. The influencing velocity vectors from V_X, V_Y and r are summed to generate expressions for V_{longRR} and V_{latRR}. Hence, the final formula for rear right slip angle is:

$$\alpha_{RR} = -\arctan\left(\frac{V_Y - rL_f}{V_X - r\frac{L_w}{2}}\right) \tag{2.26}$$

Derivations analogous to the rear right slip angle are used for the rear left:

$$\alpha_{RL} = -\arctan\left(\frac{V_Y - rL_f}{V_X + r\frac{L_w}{2}}\right) \tag{2.27}$$

For clarity, the slip angles of all wheels are condensed into matrix form:

$$\begin{bmatrix} \alpha_{FR} \\ \alpha_{FL} \\ \alpha_{RR} \\ \alpha_{RL} \end{bmatrix} = \begin{bmatrix} \delta - \arctan\left(\dfrac{V_Y + rL_f}{V_X - r\dfrac{L_w}{2}}\right) \\ \delta - \arctan\left(\dfrac{V_Y + rL_f}{V_X + r\dfrac{L_w}{2}}\right) \\ -\arctan\left(\dfrac{V_Y - rL_f}{V_X - r\dfrac{L_w}{2}}\right) \\ -\arctan\left(\dfrac{V_Y - rL_f}{V_X + r\dfrac{L_w}{2}}\right) \end{bmatrix} \tag{2.28}$$

2.4 3 DOF Vehicle Dynamics

To describe the forces that act upon the center of gravity point of the vehicle, the 3 Degree-of-Freedom equations are used. These equations provide the information to describe the longitudinal and lateral velocities of the center of gravity of the vehicle [21].

The basis of the Force equations revolve around Newton's second law. The longitudinal and lateral force equations comprise of inertial acceleration $\dot{V}_X$ and $\dot{V}_Y$ at the vehicle center of gravity, and the centripetal accelerations $\dot{V}_X r$ and $\dot{V}_Y r$. The torque about the center of gravity of the vehicle is simply expressed as a function of vehicle yaw rate r and moment of inertia J_Z. Assuming a rigid chassis where roll, pitch, and heave are omitted, the longitudinal force, lateral force, and torque at the vehicle center of gravity point are [20] :

$$F_X = m(\dot{V}_X - \dot{V}_Y r) \tag{2.29}$$

$$F_Y = m(\dot{V}_Y + \dot{V}_X r) \tag{2.30}$$

$$M_Z = J_Z * \dot{r} \tag{2.31}$$

2.5 Tire Model

The interaction between the road and the tires of the vehicle are incredibly important. The tire compound and structure govern a large portion of vehicle dynamics. Several different models have been created to describe the tire interaction with the road surface. The model chosen for this project was Hans Pacejka's Magic Tire Formula PAC2002 [32]. The output of this equation is a friction coefficient of the tire's adherence with the road under it.

2.5.1 Pure Longitudinal Slip

When the throttle of a vehicle is applied, a driving torque is applied to each wheel, causing the vehicle to move forward, as seen in figure 2.10. The adhesion or friction force between the wheel and the road surface is what allows for this to happen.

In the case where a large enough torque is present, the tire can break traction from the road surface. This slip can be defined by the rotational speed of the wheel (ω) exceeding the linear speed of the wheel (V_{Xij}). The wheel radius depends upon the vertical load present. Ru defines the radius under no load whereas Rl defines the radius under normal full load of the vehicle. In order to properly define this slip, a slip point S is defined as the center of rotation when the wheel is free rolling and has zero longitudinal slip. R_w defines the effective radius of the slip point S which is assumed to be an attached point to the wheel support or rim. Using the assumptions just previously mentioned, equation 2.32 is formed and defines the expression used to calculate slip (λ) under acceleration [35].

$$\lambda = \frac{\omega R_w - V_{Xij}}{\omega R_w} \tag{2.32}$$

It is important to note that the same equation does not work under braking cases.

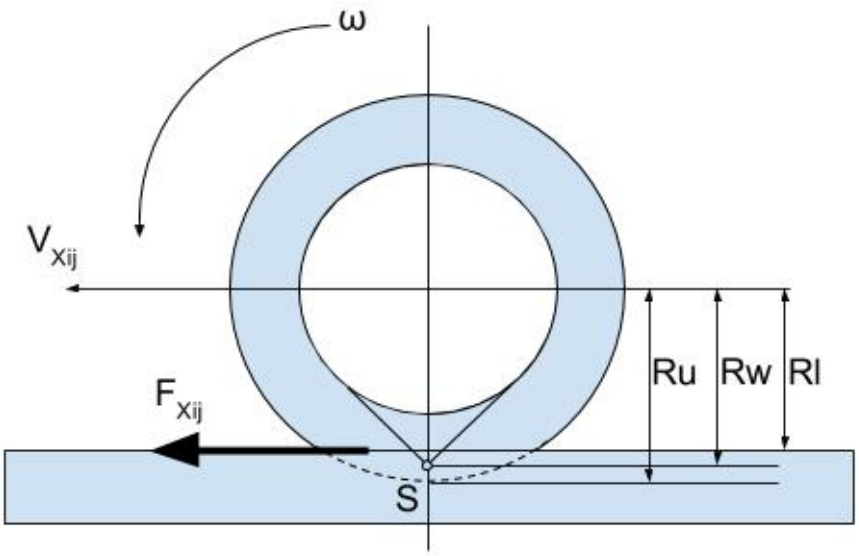

Figure 2.10: *Longitudinal Slip Diagram*

The reason for this can be understood when observing the equation under the extreme case where the wheel rotation has locked, and the vehicle is still moving forward. In this case, the wheel speed is zero, hence a divide by zero case is encountered. The expression for the the slip (λ) under deceleration is:

$$\lambda = \frac{\omega R_w - V_{Xij}}{V_{Xij}} \tag{2.33}$$

From these slip ratio equations, all values are bounded between -1 and 1, convenient for mathematical manipulation. A full wheel lock situation is represented by -1, and a full wheel spin situation is represented by 1. Directly in the middle, 0 represents a situation where the linear and angular wheel velocity are matched, hence the wheel has zero slip with respect to the road.

With a slip equation firmly defined, the longitudinal portion of Hans Pacejka's

Magic Tire Formula PAC2002 [32] can be introduced. The dynamic equation shown in 2.34 describes the longitudinal force generated by a wheel (F_{Xij}) with respect to slip (λ) originates from a semi-empirical basis.

$$F_{Xij} = D_X sin(C_X arctan(B_X\lambda - E_X(B_X\lambda - arctan(B_X\lambda)))) \tag{2.34}$$

$$B_X C_X D_X = C_\lambda \tag{2.35}$$

The variable D_X is called the peak factor, and sets the peak of the characteristic curve. The variable C_X is called the shape factor, and determines the part of the sine wave to be used. The variable B_X is the stiffness factor and this stretches the curve. The product of B_X,C_X, and D_X (C_λ) represents the longitudinal slip stiffness, which is the slope of the F_{Xij} curve. Lastly, the variable E_X is the curvature factor, and it is used to modify the curve characteristic around the peak of the curve.

The several parameters of Equation 2.34 are used to shape its curve and in turn change the handling characteristics of the tire. There are several different ways to choose the coefficients of this formula. The formulas chosen for this study to determine the coefficent values of Equation 2.34 are outlined in Equations 2.36 through 2.40.

$$D_X = \mu_{XP} F_Z \tag{2.36}$$

$$C_X = 2 - 2/\pi \arcsin\left(\frac{\mu_{XS}}{\mu_{XP}}\right) \tag{2.37}$$

$$B_X = \frac{K_{XN}}{C_X D_X} \tag{2.38}$$

$$sp = \frac{3}{B_X C_X} \tag{2.39}$$

$$E_X = \frac{B_X sp - \tan\left(\frac{\pi}{2C_X}\right)}{B_X sp - \arctan(B_X sp)} \tag{2.40}$$

μ_{XP} represents the peak friction coefficient, and μ_{XS} represents the friction coefficient value that Pacejka's curve asymptotically approaches. K_{XN} represents the normalized stiffness of Pacejka's curve.

2.5.2 Pure Lateral Slip

When a nonzero steering input is applied to a vehicle its direction will change. This is a resultant of the tires turning and creating a lateral force between the tire and the road surface. Similar to the Pacejka Formula for longitudinal force, the lateral force equation expresses a relationship between the wheel lateral force F_{Yij} and the slip angle α [32]. The slip angle is defined in Equation 2.41.

$$\alpha_{ij} = \arctan\left(\frac{V_{latij}}{|V_{longij}|}\right) \tag{2.41}$$

With the slip angle defined, Pacejka's Magic Formula is shown in the following semi-empirical equations:

$$F_{Yij} = D_Y sin(C_Y arctan(B_Y\alpha - E_Y(B_Y\alpha - arctan(B_Y\alpha)))) \tag{2.42}$$

$$B_Y C_Y D_Y = C_\alpha \tag{2.43}$$

Similar to the longitudinal equations, The variable D_Y is called the peak factor, and sets the peak of the characteristic curve. The variable C_Y is called the shape factor, and determines the part of the sine wave to be used. The variable B_Y is the stiffness factor and this stretches the curve. The product of B_Y,C_Y, and D_Y (C_α) represents the lateral slip stiffness, which is the slope of the F_{Yij} curve. Lastly, the variable E_Y is the curvature factor, and it is used to modify the curve characteristic around the peak of the curve.

The several parameters of Equation 2.42 are used to shape its curve and in turn change the handling characteristics of the tire. There are several different ways to choose the coefficients of this formula. The formulas chosen for this study to determine

the coefficient values of Equation 2.42 are outlined in Equations 2.44 through 2.47.

$$D_Y = \mu_{YP} F_Z \tag{2.44}$$

$$C_Y = 2 - 2/\pi \arcsin\left(\frac{\mu_{YS}}{\mu_{YP}}\right) \tag{2.45}$$

$$B_Y = \frac{K_{YN}}{C_Y D_Y} \tag{2.46}$$

$$ap = \frac{3}{B_Y C_Y} \tag{2.47}$$

$$E_Y = \frac{B_Y ap - \tan\left(\frac{\pi}{2C_Y}\right)}{B_Y ap - \arctan(B_Y ap)} \tag{2.48}$$

μ_{YP} represents the peak friction coefficient, and μ_{YS} represents the friction coefficient value that Pacejka's curve asymptotically approaches. K_{YN} represents the normalized stiffness of Pacejka's curve.

2.5.3 Combined Slip

In the case when the wheel longitudinal slip (λ) and wheel slip angle (α) are both non-zero, the longitudinal tire force (F_{Xij}) interacts the the lateral tire force (F_{Yij}). The total force generated by a single wheel ($\sqrt{{F_{Xij}}^2 + {F_{Yij}}^2}$) is limited by this interaction [32]. Equations 2.49 through 2.54 describe this effect [13]. Parameters r_{x1}, r_{x2}, r_{y1}, and r_{y2} are used as shaping factors for these curves and affect the values of scalars B_{xc}, B_{yc}, G_{xc}, and G_{yc}. F_{xc} and F_{yc} represent the new longitudinal and lateral forces respectively under the combined influences of slip ratio λ and wheel slip angle α.

$$B_{xc} = r_{x1} cos(atan(r_{x2}\lambda)) \tag{2.49}$$

$$G_{xc} = cos(atan(B_{xc}\alpha)) \tag{2.50}$$

$$F_{xc} = G_{xc}F_{Xij} \tag{2.51}$$

$$B_{yc} = r_{y1}cos(atan(r_{y2}\alpha)) \tag{2.52}$$

$$G_{yc} = cos(atan(B_{yc}\lambda)) \tag{2.53}$$

$$F_{yc} = G_{yc}F_{Yij} \tag{2.54}$$

2.6 Electric Motor Drive Model

The power train for this particular study involves four electric motors which are used to drive each wheel separately. Since the algorithms in this study are dependent on a torque input, a torque model is used to describe the output for each electric motor.

2.6.1 Electric Motor Torque Model

The dynamic response of modern motor drives is much faster than wheel dynamics [37]. Therefore an electric motor drive can simply be modeled using a second order response transfer function:

$$H_{mot}(s) = \frac{1}{1 + 2\zeta s + 2\zeta^2 s^2} \tag{2.55}$$

τ_d represents the commanded torque of the electric motor serving as an input to $H_{mot}(s)$. This torque is bounded by the max torque of the motor. ζ represents the time constant of the electric motor torque response. Finally the gear reduction

ratio GRR simply models a gearing system for power delivery and acts as a torque multiplier at the output of $H_{mot}(s)$.

Chapter 3

Vehicle Model Parameters

3.1 Test Vehicle

In MATLAB Simulink, a vehicle model was created to use as the plant during control algorithm testing. The equations that are used to build the vehicle model are described in Chapter 2. The vehicle plant model contains several variables which are used to describe various characteristics of the test vehicle. Sections 3.1.1 and 3.1.2 describe the vehicle characteristic values used for testing the algorithms of study in this thesis.

3.1.1 Chassis

The MATLAB vehicle chassis model has several dimensions and characteristic values which were chosen to realistically represent a real world vehicle. Table 3.1 shows the constants pertaining to the simulation chassis.

Table 3.1: *Vehicle Parameter Constants*

Constant	Units	Value
h_g	$[m]$	0.5
L_f	$[m]$	1.5
L_r	$[m]$	1.5
L_w	$[m]$	1.5
m	$[kg]$	1350
J_Z	$[kgm^2]$	1265.6
R_w	$[m]$	0.33
J_w	$[kgm^2]$	1.2

m is the mass of the vehicle and J_Z is the moment about the vehicle center of gravity point. R_w is the effective radius of the wheel and J_w is the moment of each separate wheel. All other constants in Table 3.1 have already been explained in Chapter 2.

3.1.2 Tires

Tires are crucial elements of a mathematical vehicle model. The equations in Section 2.5 describe the tire forces generated by interaction with the vehicle chassis and the road surface. The constants used within the aforementioned equations are explained in the detail within this section.

Pure Longitudinal Tire Characteristics

Within this study, Pacejka's Formula is used to describe longitudinal tire force with respect to longitudinal wheel slip as seen in Equation 2.34. This was outlined previously in Section 2.5.1. This formula has several parameters which are used to shape its curve and in turn change the handling characteristics of the tire. The values

used for the coefficients specified in Section 2.5.1 of Pacejka's longitudinal formula in dry road conditions are defined in Table 3.2. The coefficients were chosen to reflect the characteristics of a typical tire [33].

Table 3.2: *Pacejka's Longitudinal Formula Parameter Values for Dry Tarmac Conditions*

Constant	Value
μ_{XP}	0.99
μ_{XS}	0.27
K_{XN}	30
B_X	16.612
C_X	1.824
D_X	0.99
sp	0.099
E_X	0.775

By placing the values listed in Table 3.2 in Pacejka's Longitudinal Force Equation (2.34), a curve is generated. This curve displays the tire and road interaction on dry tarmac in Figure 3.1.

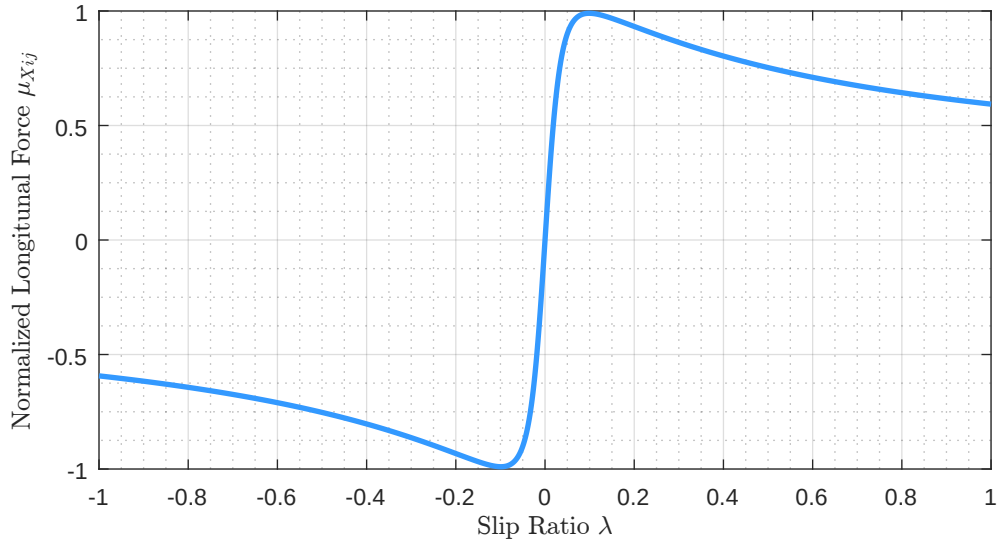

Figure 3.1: *Longitudinal Slip vs Longitudinal Friction Coefficient on Dry Tarmac*

Pure Lateral Tire Characteristics

Alongside Pacejka's Formula used to describe longitudinal tire force with respect to longitudinal wheel slip, another formula is used to describe the lateral tire force with respect to wheel slip angle. This was outlined previously in Section 2.5.2 and the end result is shown in Equation 2.42. This formula has several parameters which are used to shape its curve and in turn change the handling characteristics of the tire. The values used for the coefficients specified in Section 2.5.2 of Pacejka's lateral formula in dry road conditions are defined in table 3.3. The coefficients were chosen to reflect the characteristics of a typical tire [27].

Table 3.3: *Pacejka's Lateral Force Formula Parameter Values for Dry Tarmac Conditions*

Constant	Value
μ_{YP}	0.845
μ_{YS}	0.800
K_{YN}	27.051
B_Y	26.462
C_Y	1.209
D_Y	0.845
ap	0.099
E_Y	-0.855

By placing the values listed in Table 3.3 in Pacejka's Lateral Force Equation (2.42), a curve is generated. This curve displays the tire and road interaction on dry tarmac in Figure 3.2.

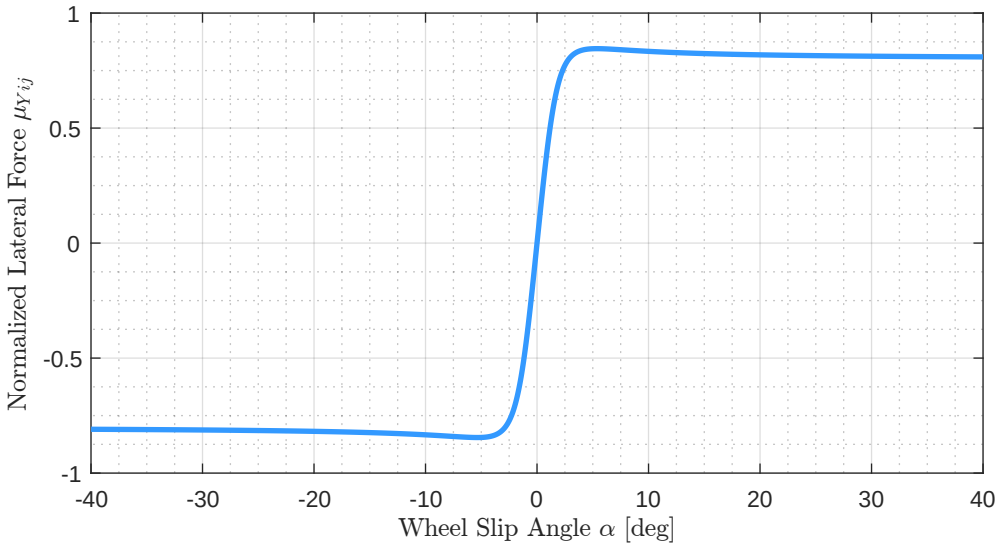

Figure 3.2: *Wheel Slip Angle vs Lateral Friction Coefficient on Dry Tarmac*

Combined Longitudinal and Lateral Tire Characteristics

As mentioned in Section 2.5.3, longitudinal slip λ and wheel slip angle α affect each other when their values are non-zero. An increase in either lateral or longitudinal force generated by the tire can cause a reduction in the other remaining force generated by the tire. Likewise, a reduction in either lateral or longitudinal force generated by the tire can cause an increase in the other remaining force generated by the tire. These tire characteristics are modeled in this study using Equations 2.49 through 2.54. Only four parameters can be used to shape the data curves which can be generated using the combined slip force equations and the values used in this study for these parameters are shown in Table 3.4. The coefficients were chosen to reflect the characteristics of a typical tire [32].

Table 3.4: *Pacejka's Combined Force Formula Parameter Values*

Constant	Value
r_{x1}	15
r_{x2}	15
r_{y1}	15
r_{y2}	15

By placing values from Table 3.4 into Equations 2.49 through 2.54, new surfaces are created that describe the longitudinal force (F_{xc}) and lateral force (F_{yc}) with respect to slip ratio and slip angle. Figure 3.3 displays the normalized longitudinal force with respect to longitudinal slip and wheel slip angle. Normalized lateral force is displayed with respect to longitudinal slip and wheel slip angle in Figure 3.4. The normalized forces can also be thought of as the friction coefficients of tire to road surface adhesion.

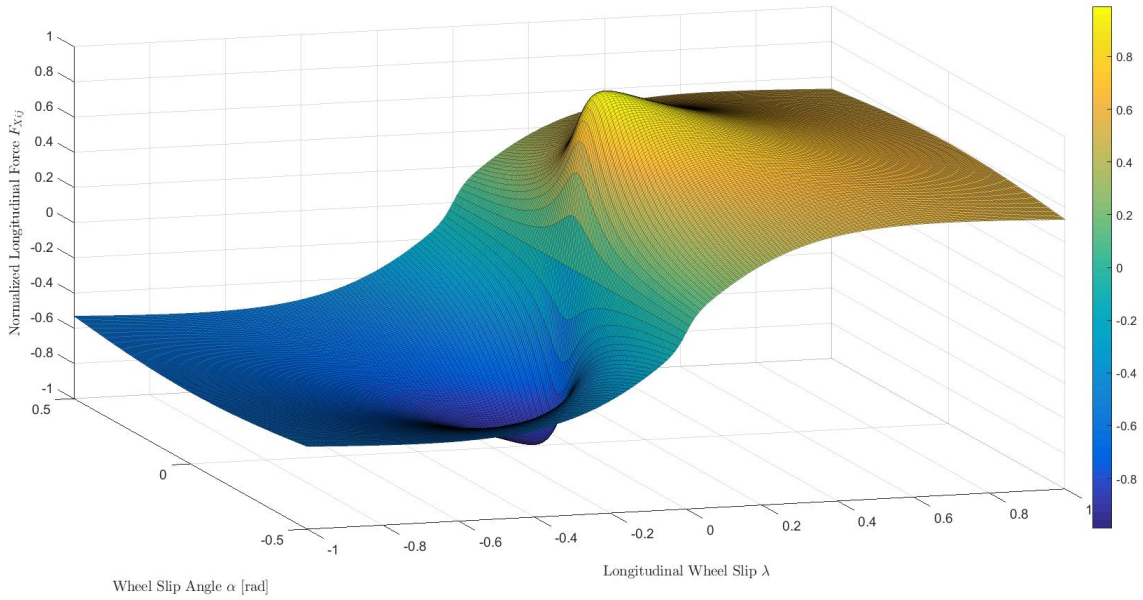

Figure 3.3: *Longitudinal Wheel Slip vs Wheel Slip Angle vs Normalized Longitudinal Force*

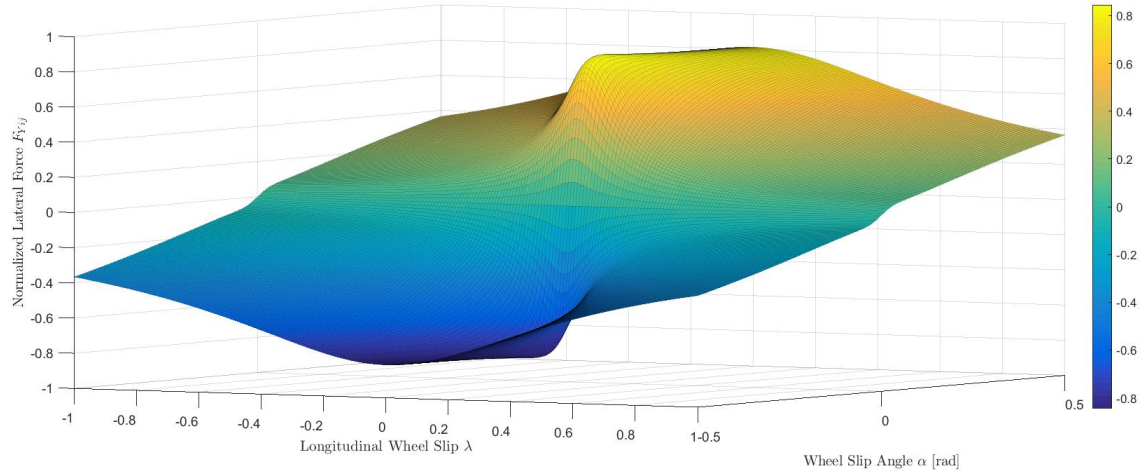

Figure 3.4: *Longitudinal Wheel Slip vs Wheel Slip Angle vs Normalized Lateral Force*

Figure 3.5 shows the the longitudinal force (F_{xc}) and lateral force (F_{yc}) at different slip angle values. Each horizontal arc on this graph represents the forces that can be generated at a specific wheel slip angle. The slip angle is swept from -6 (bright green) to 6 (dark blue) degrees in increments of 0.25 as each line progresses through the color gradient.

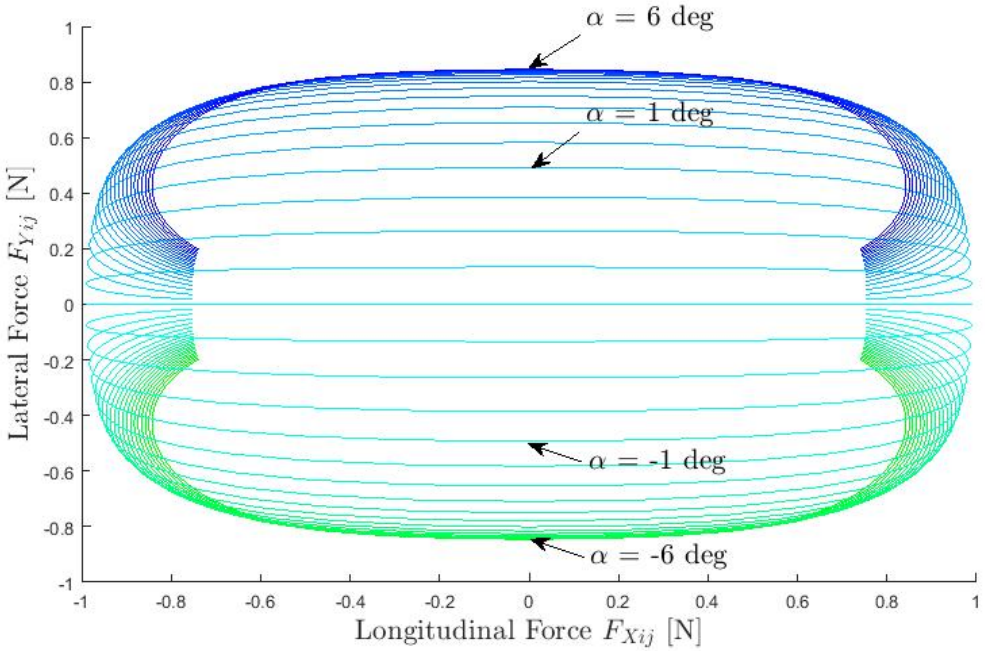

Figure 3.5: *Longitudinal Force vs Lateral Force at various Wheel Slip Angles*

The combined forces can also be visualized with respect to different longitudinal wheel slip values, shown in Figure 3.6. Each vertical arc on this graph represents the forces that can be generated by the tire at a specific longitudinal wheel slip. The slip ratio is swept from -0.15 (bright green) to 0.15 (dark blue) degrees in increments of 0.005 as each line progresses through the color gradient.

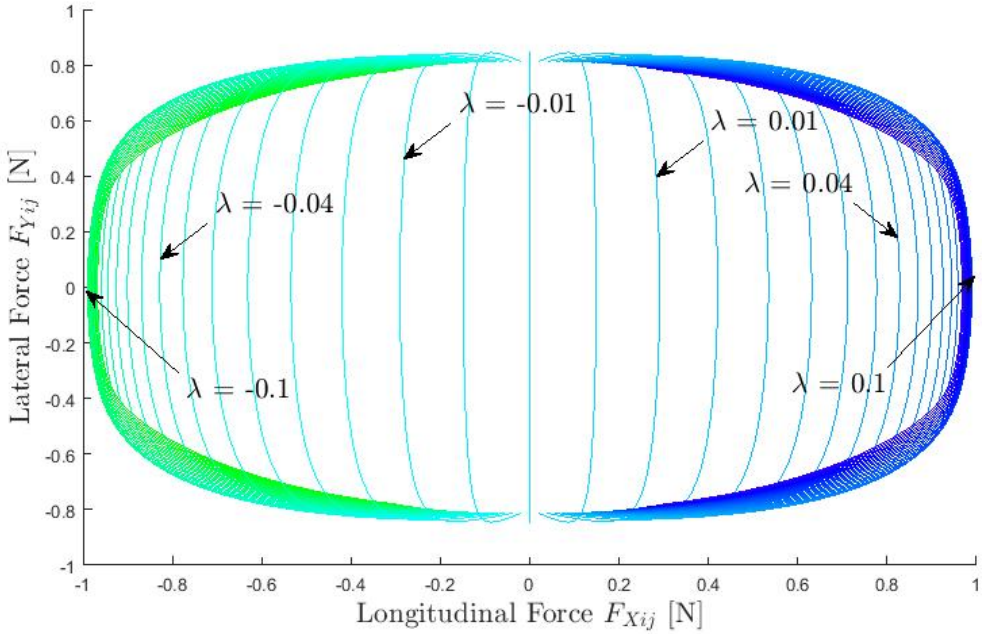

Figure 3.6: *Longitudinal Force vs Lateral Force at various Longitudinal Wheel Slips*

Figures 3.3 through 3.6 describe the tire characteristic models used on dry tarmac conditions for all tests in this thesis.

3.1.3 Electric Motor Drives

As seen in Section 2.6 the electric motor torque response is represented with Equation 2.55. τ_{AVAIL} represents the maximum torque value that the desired torque τ_d can reach. Table 3.5 shows the constants pertaining to the electric motor model. Current motor controllers can achieve torque responses within 3-15 ms [43] which provided a basis for the choice of the motor time constant. Depending on the size of the vehicle, fully electric independent drive torque vectoring vehicles can be equipped with motors with a peak torque rating in the range from 100-250Nm [16]. This motor can then be coupled with a gear reduction ratio to increase power, where values of roughly ten are possible [16].

Table 3.5: *Electric Motor Parameter Constants*

Constant	Units	Value
ζ	None	0.0014
τ_{AVAIL}	$[Nm]$	175
GRR	None	10

Using the values from Table 3.5, Figure 3.7 is generated which shows the step response for a desired torque step function used as the input.

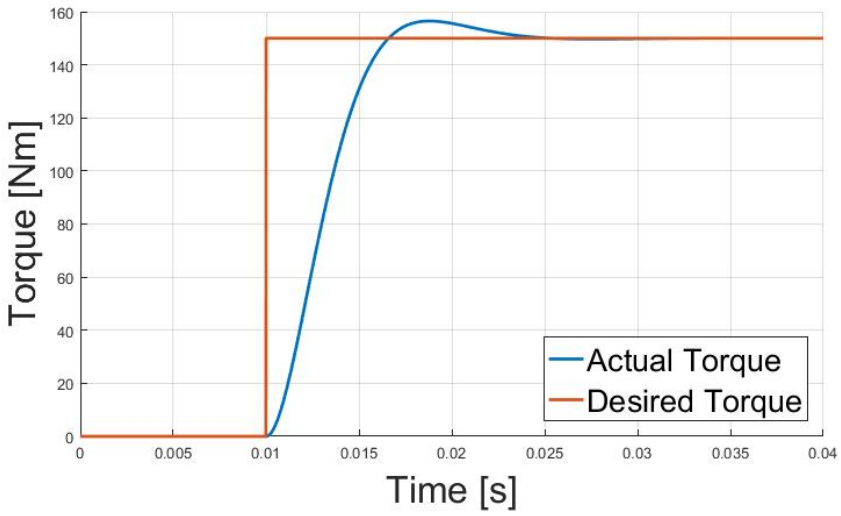

Figure 3.7: *Step Response Plot of Desired Torque Output vs Actual Torque Output with Respect to Time*

Chapter 4

Control Algorithm Strategy and Implementation

This chapter provides the details of the proposed algorithm which consists of two major components: the wheel slip ratio controller (one for each vehicle wheel) and the yaw rate controller. Both of these controllers work together to generate different torque values to apply to each separate wheel of the vehicle. The slip ratio controller is based off of a standard super twisting controller, while the yaw rate and side slip controller is created by the author as the fusion of a linear quadratic regulator and super twisting control concepts.

4.1 Super Twisting Algorithm Background

Sliding mode control (SMC) is a nonlinear control mechanism characterized by a discontinuous control action. This type of controller forces a sliding variable (σ) representing the deviation from a desired state to zero [26]. There are a few major advantages that sliding mode control has to offer. Arguably the most important benefit is that SMC can be insensitive to particular uncertainties including disturbances such as noise and system parameter variations and non-linearities [17]. The robust nature of this controller removes the necessity of a highly accurate system model. Another

advantage is that the sliding surface is set by the designer, providing extra flexibility for what can be accomplished. Despite the perks of sliding mode control, there are some drawbacks. First order SMC generates a discontinuous control effort, which leads to a chattering phenomenon. In cases where high precision is required, SMC may not be suitable because of this. Also, in certain circumstances the chattering effect may even cause damage to the actuators performing control. However, these drawbacks can be mitigated by a second order SMC. The super twisting algorithm (STA) is a second order sliding mode controller and is a continuous function [38]. This addresses the chattering issue whilst maintaining the robust nature of SMC. Several vehicle parameter uncertainties such as wheel radius, tire selection, temperature, road surface, etc., alter the dynamic response of the vehicle which makes SMC an attractive choice.

4.2 Linear Quadratic Regulator Background

The theory of optimal control solves for an optimal control law according to a specified figure of merit. The linear–quadratic regulator (LQR) is a form of optimal control that allows a designer to specify a cost function that determines what the LQR optimizes for [23]. The control law takes the form of a proportional feedback gain that operates with respect to state variables. To implement this control mechanism, a linearized model of the system plant must be created and placed into state space format: $\dot{x} = Ax + Bu$. A cost function $J(x,u) = \int_0^\infty (x^T Q x + u^T R u + 2x^T N u) dt$ is then formed by the designer which typically contains state parameters and controls along with weighting gains that determine the cost for each of these parameters. A major advantage associated with LQR is the fact that it can accommodate multivariable systems. Vehicle stability control systems often use more than one control objective [35]. Hence a compromise must be made that LQR can optimize for. Another advantage is that the cost function is set by the designer, which simplifies optimal design whilst providing some factors of design flexibility. It must be remembered that the LQR does not necessarily provide an optimal response, but rather an optimal response according to the designer's cost function. LQR also assumes perfect modeling through the linearized dynamics. Since the LQR is a proportional controller that

uses a linearized plant, it is susceptible to non-linearity characteristics of the subject under control, and may result in control error.

4.3 Proposed Algorithm Overview

Figure 4.1 shows a high level diagram of the proposed algorithm. The yellow blocks represent observed parameters that serve as inputs to the subsystems of the controller. The slip ratio controller modulates the amount of force that each wheel can produce, and consists of a super twisting algorithm. An output torque is generated based upon the difference between the desired and actual slip ratio (slip error) for each separate wheel. If the driver requests more power via the throttle position, the desired slip ratio will increase and the controller will apply more torque to each wheel. Vehicle stability is ensured via the yaw controller, which also alters the desired slip ratio for each wheel. The yaw controller consists of the summation of a linear quadratic regulator and the integral portion of a super twisting controller. Based upon the vehicle side slip and yaw errors, the desired slip ratios are altered to generate different torques at each wheel to achieve a desired yaw rate of the vehicle.

4.4 Slip Ratio Controller

The slip controller uses the same relationships in equations 2.33 and 2.32 to define the slip ratio during acceleration or deceleration. Observing Figure 4.2, Pacejka's longitudinal force curve is shown. The shaded green area represents the desired stable region of the curve, bounded by -0.1 $\leq \lambda \leq$ 0.1. Outside of this portion is the unstable regions where it is undesired to operate at [24]. This is because an increase in slip ratio causes a decrease in power generated by the wheel, which can lead to poor controller response.

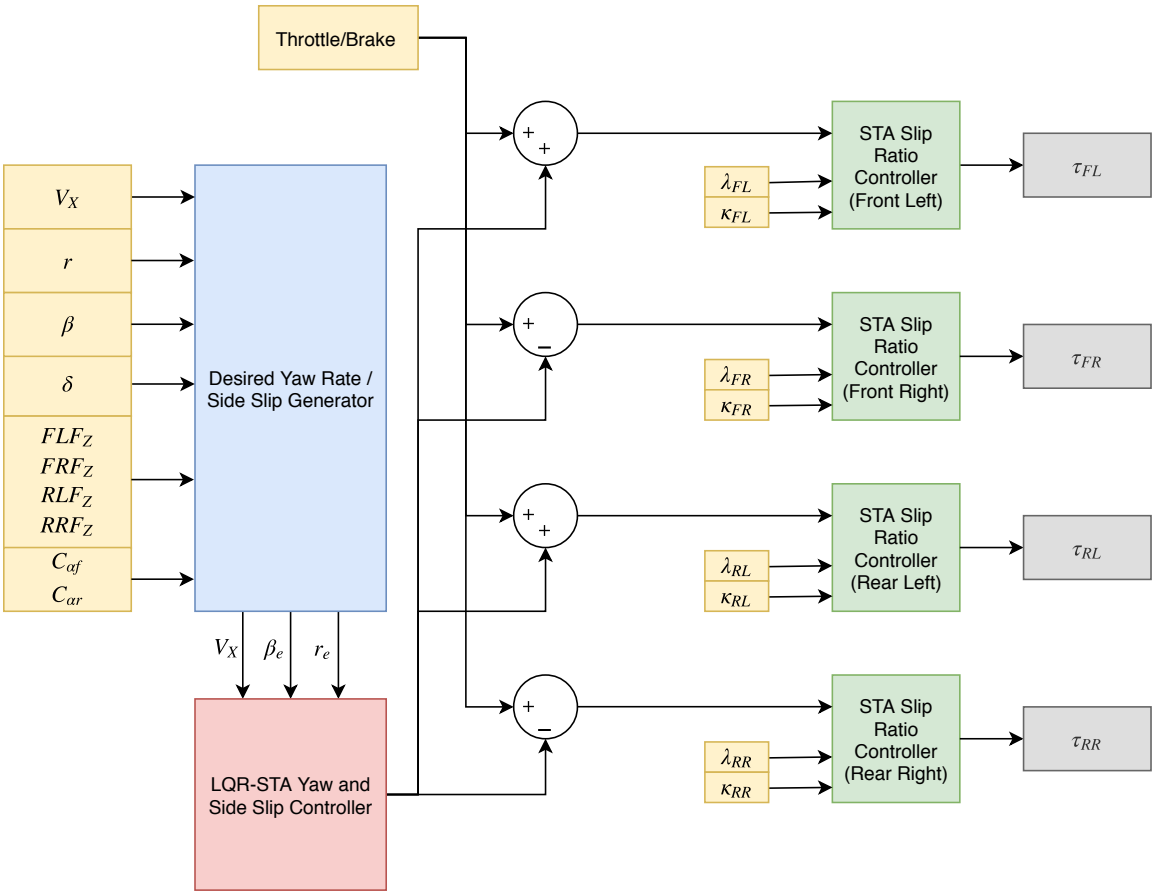

Figure 4.1: *High Level Block Diagram of LQR-STA Torque Vectoring Controller Architecture*

4.4.1 Super Twisting Slip Ratio Controller

Since the interaction between slip and tire force are non-linear, a super twisting controller is proposed for use. The super twisting control algorithm is a form of sliding mode control where the control effort is the sum of two terms: $u_\lambda = u_1(t) + u_2(t)$. Both constituent control terms are functions of a sliding surface, σ_λ:

$$\begin{aligned} \dot{u_1} &= -W_S \operatorname{sgn}(\sigma_\lambda) \\ u_2 &= -B_S \mid \sigma_\lambda \mid^\rho \operatorname{sgn}(\sigma_\lambda) \end{aligned} \tag{4.1}$$

Two positive scaling factors B_S and W_S can be used to tune the output of the controller which acts upon a sliding surface σ_λ. The sliding surface σ_λ is a plane

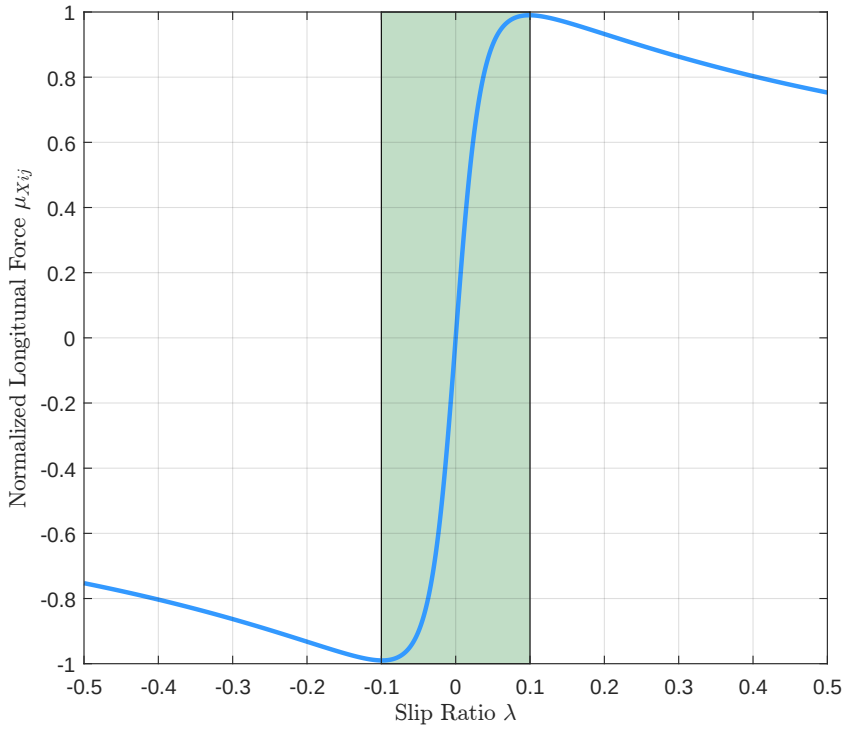

Figure 4.2: *Slip Ratio vs Friction Coefficient*

defined over the slip ratio error phase plane: $\sigma_\lambda = G_S\lambda_e + H_S\dot{\lambda}_e$.

G_S and H_S are positive scaling factors and λ_e is the slip error which is defined in equation 4.2. λ_d represents the desired slip ratio and λ is the actual slip ratio.

$$\lambda_e = \lambda_d - \lambda \tag{4.2}$$

For visual representation, the STA slip ratio controller is shown in block diagram format in figure 4.3.

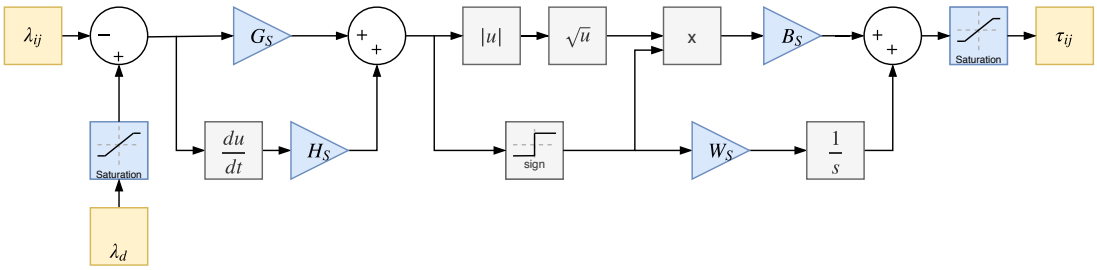

Figure 4.3: *Block Diagram of STA Slip Ratio Controller Architecture*

4.5 Yaw Rate and Side Slip Controller

Many stability enhancement controllers focus on yaw rate control, side slip control, or a combination of both. The proposed controller uses both yaw rate and side slip as parameters which the stability controller acts upon. A fusion of LQR and STA concepts are used for the yaw rate and side slip controller. Figure 4.4 shows a block diagram of the proposed yaw rate and side slip controller. The concepts shown in this figure will be explained in the rest of Chapter 4.

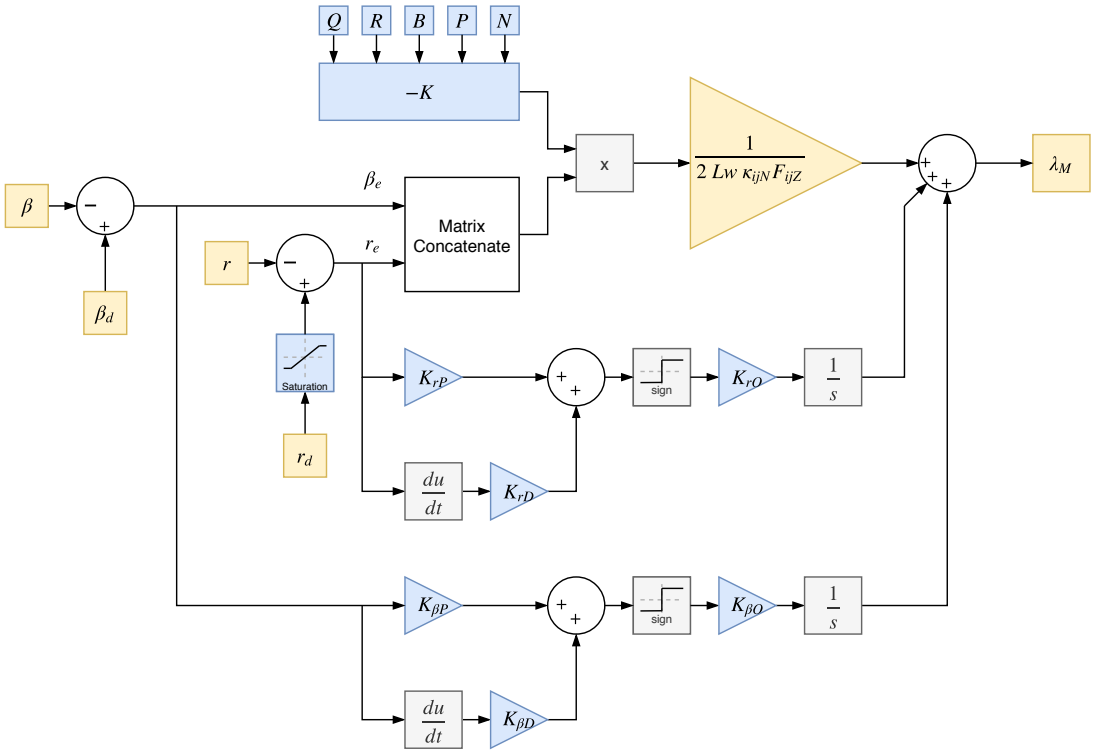

Figure 4.4: *Block Diagram of LQR-STA Yaw Rate and Side Slip Controller Architecture*

4.5.1 Yaw Rate and Side Slip Reference Generation

The desired yaw rate depends on the vehicle's current steering angle (δ), longitudinal velocity (V_X), and other physical characteristics of the vehicle's construction. To begin solving for the desired yaw rate, visit the concept of curvature k which is defined as $k = \frac{1}{R}$ and $k = \frac{d\theta}{ds}$ [34]. The first equation states that the curvature of a line is inversely related to its radius. For example, a straight line can be considered to have an infinite radius, meaning a curvature of zero. Moving to the second equation, the curvature of a given curve is expressed as a ratio of an angle between tangents to that curve $d\theta$ to the length of that segment ds between tangents. This can be explained by using a point with a tangent vector moving along a curve. Assuming a fixed distance between the points, $d\theta$ will increase along with k as the point is moved along

a curve toward a decreasing radius. Applying this concept to a vehicle in motion, we have $1/R = r/V_X$, which assumes a small vehicle slide-slip angle (β). Large values of β imply that the vehicle direction of travel is no longer tangential to it turn radius, hence the relation falls apart. R represents the vehicle turning radius. Re-arranging this equation provides a definition for the yaw rate: $r = V_X/R$. The steering angle required to negotiate a given curve is [41]:

$$\delta = \frac{L}{R} + \left(\frac{W_f}{C_{\alpha f}} - \frac{W_r}{C_{\alpha r}}\right)\frac{V_X^2}{gR} \tag{4.3}$$

Where L is the longitudinal wheel base of the vehicle: $L = L_f + L_r$ and g is the acceleration due to gravity. The inverse of Equation 4.3 is the turning radius that results from a given steering angle:

$$R = \left(L + \left(\frac{W_f}{C_{\alpha f}} - \frac{W_r}{C_{\alpha r}}\right)\frac{V_X^2}{g}\right)\frac{1}{\delta} \tag{4.4}$$

By substituting Equation 4.4 into $1/R = r/V_X$, the desired yaw rate can be expressed as a function of steering angle:

$$r_d = \frac{V_X}{L + \left(\frac{W_f}{C_{\alpha f}} - \frac{W_r}{C_{\alpha r}}\right)\frac{V_X^2}{g}}\delta \tag{4.5}$$

To achieve the desired yaw rate, a sliding mode control is implemented. Equation 4.6 defines the yaw error r_e, where r_d is the desired yaw rate, and r is the actual yaw rate of the vehicle.

$$r_e = r_d - r \tag{4.6}$$

4.5.2 Linear Quadratic Regulator Control Theory

The Linear Quadratic Regulator (LQR) control strategy is a form of optimal control and applies to linear systems. LQR is based upon the ability to create a linear model of the plant in state space format: $\dot{x} = Ax + Bu$, where x represents the state variable and u represents the control input.

The LQR state-feedback control law is a simple proportional controller, $u = -Kx$. However, the gain variable K is calculated to minimize the cost function

$$J(x,u) = \int_0^\infty (x^T Q x + u^T R u + 2x^T N u) dt. \tag{4.7}$$

The matrices Q, R, and N are used as weighting values that assign a cost to the variables x and u. The equation for the optimal gain K is [31]: $K = -R^{-1}(B^T P + N^T)$. P is solved for using the Algebraic Riccati Equation seen in equation 4.8, which is one of many ways to solve for coefficients that minimize the linear quadratic regulator equation.

$$A^T P + PA - (PB + N)R^{-1}(B^T P + N^T) + Q = 0 \tag{4.8}$$

4.5.3 Linearized Single Track Vehicle Model

LQR control requires the subject plant to be of linear nature, hence the vehicle model equations proposed in Chapter 2 must be modified or reconstructed to provide another model which the LQR control can use as a plant matrix. Figure 4.5 shows a diagram of the single track vehicle model for reference.

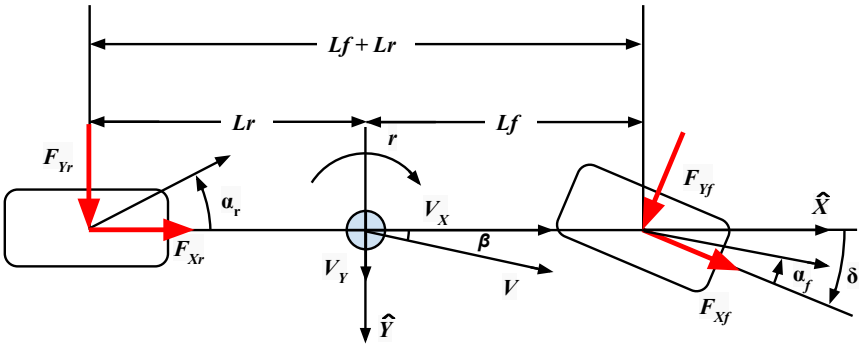

Figure 4.5: *Single Track Vehicle Model Diagram*

The linearization of the vehicle dynamics equations draws from the methods introduced by Jazar [19]. The conventions used in Figure 4.5 are slightly different and

warrant their own proof.

To begin, the force equations 2.11, 2.12, and 2.18 are simplified. Assuming a small steering angle δ, these force equations can be simplified to the following:

$$F_X \simeq F_{Xf} + F_{Xr} \tag{4.9}$$

$$F_Y \simeq F_{Yf} + F_{Yr} \tag{4.10}$$

$$M_Z \simeq L_f F_{Yf} + L_r F_{Yr} \tag{4.11}$$

where $F_{Xf} = FRF_X + FLF_X$, $F_{Xr} = RRF_X + RLF_X$, $F_{Yf} = FRF_Y + FLF_Y$, and $F_{Yr} = RRF_Y + RLF_Y$. F_{Xf} is the front longitudinal force, F_{Xr} is the rear longitudinal force, F_{Yf} is the front lateral force, and F_{Yr} is the rear lateral force. For estimations of the lateral forces of the single track model we use the front and rear cornering stiffness coefficients $C_{\alpha f}$ and $C_{\alpha r}$, to form a linear relationship between the lateral forces and the wheel slip angle in equations 4.12 and 4.13.

$$F_{Yf} = C_{\alpha f}\alpha_f \tag{4.12}$$

$$F_{Yr} = C_{\alpha r}\alpha_r \tag{4.13}$$

$C_{\alpha f}$ and $C_{\alpha r}$ condense the forces of the two track model so that $C_{\alpha f} = C_{\alpha fl} + C_{\alpha fr}$ and $C_{\alpha r} = C_{\alpha rl} + C_{\alpha rr}$. Substituting equations 4.12 and 4.13 into 4.10 and 4.11, the following new representations of F_Z and M_Z are formed:

$$F_Y = C_{\alpha f}\alpha_f + C_{\alpha r}\alpha_r \tag{4.14}$$

$$M_Z = L_f C_{\alpha f}\alpha_f - L_r C_{\alpha r}\alpha_r \tag{4.15}$$

The force equations for F_Y and M_Z are now dependent on the slip angles α_f and α_r. These slip angles represent the average of the individual front and rear slip angles

of the two track model (α_{FR}, α_{FL} and α_{RR}, α_{RL} respectively). Using this information, new slip angle equations are formed for the single track model:

$$\alpha_f = \delta - \beta_f \tag{4.16}$$

$$\alpha_r = \delta - \beta_r \tag{4.17}$$

β_f and β_r represent front and rear side slip angles of the single track model respectively. Their mathematical definition is as follows:

$$\beta_f = tan^{-1}\left(\frac{V_{yf}}{V_{xf}}\right) = tan^{-1}\left(\frac{V_y + L_f r}{V_x}\right) \tag{4.18}$$

$$\beta_r = tan^{-1}\left(\frac{V_{yr}}{V_{xr}}\right) = tan^{-1}\left(\frac{V_y - L_r r}{V_x}\right) \tag{4.19}$$

Assuming small slip angles for β_f,β_r, and β, $y = tan^{-1}(x)$ can be approximated as $y = x$. Therefore the slip angle equations for front and rear can be rewritten as:

$$\alpha_f = \delta - \beta - \frac{L_f r}{V_X} \tag{4.20}$$

$$\alpha_r = -\beta + \frac{L_r r}{V_X} \tag{4.21}$$

Note that the rear slip angle does not contain a steering angle term since the rear wheels are assumed fixed for this study. Now to realize the linearized equations for F_Y and M_Z, substitute equations 4.20 and 4.21 into equations 4.14 and 4.15, which results in the following:

$$F_Y = -(C_{\alpha f} + C_{\alpha r})\beta + \left(-\frac{C_{\alpha f} L_f}{V_X} + \frac{C_{\alpha r} L_r}{V_X}\right) r + C_{\alpha f}\delta \tag{4.22}$$

$$M_Z = -(L_f C_{\alpha f} - L_r C_{\alpha r})\beta + \left(-\frac{L_f^2 C_{\alpha f}}{V_X} - \frac{L_r^2 C_{\alpha r}}{V_X}\right) r + L_f C_{\alpha f}\delta \tag{4.23}$$

Further manipulation is still required for state space form of F_Y and M_Z. Substituting equations 4.22 and 4.23 into 2.29, 2.30, and 2.31, and solving for the first derivative of V_X, V_Y, and M_Z, a new set of differential equations is reached:

$$\dot{V}_X = \frac{F_X}{m} + rV_Y \tag{4.24}$$

$$\dot{V}_Y = \frac{1}{mV_X}(-L_fC_{\alpha f} + L_rC_{\alpha r} - V_X)r - \frac{1}{mV_X}(C_{\alpha f} + C_{\alpha r})V_Y + \frac{1}{m}C_{\alpha f}\delta \tag{4.25}$$

$$\dot{r} = \frac{1}{J_zV_X}(-L_f^2C_{\alpha f} - L_r^2C_{\alpha r} - V_X)r - \frac{1}{J_zV_X}(L_fC_{\alpha f} - L_rC_{\alpha r})V_Y + \frac{L_fC_{\alpha f}}{J_z}\delta \tag{4.26}$$

These formulas now form a dependency upon each other where r and V_Y of equation 4.24 are outputs of equations 4.25 and 4.26. This problem can be resolved by assuming V_X as a constant. This alters equation 4.24 to become $-\frac{F_X}{m} = rV_Y$, and creates its independence from the the others. V_X is assumed a constant because the tests involving state space linearized model do not vary throttle. However, some error is introduced due to the control algorithm's control effort slowing the vehicle. Despite this, the motors modeled in this study have a much smaller time constant than that of the vehicle velocity, providing another argument for treating V_X as a constant.

Using equations 4.25 and 4.26, a state space matrix for the single track model can be formed:

$$\begin{bmatrix} \dot{V}_Y \\ \dot{r} \end{bmatrix} = \begin{bmatrix} \frac{-(C_{\alpha f} + C_{\alpha r})}{mV_X} & \frac{-(L_rC_{\alpha r} - L_fC_{\alpha f})}{mV_X^2} - V_X \\ \frac{-(L_rC_{\alpha r} - L_fC_{\alpha f})}{V_XJ_z} & \frac{-(L_f^2C_{\alpha f} + L_r^2C_{\alpha r})}{V_XJ_z} \end{bmatrix} \begin{bmatrix} V_Y \\ r \end{bmatrix} + \begin{bmatrix} \frac{C_{\alpha f}}{mV_X} \\ \frac{L_fC_{\alpha f}}{J_z} \end{bmatrix} \delta \tag{4.27}$$

The first change to the state matrix will be to change the state V_Y to β. This can be accomplished through some simple mathematical relationships. By taking the derivative of β while assuming V_X as a constant, the result $\dot{\beta} = \frac{\dot{V}_Y}{V_X}$. One additional and last change is drawn from the assumption that β is small, which results in

$V_X = Vcos\beta \simeq V$, where V is the vehicle velocity magnitude. Substituting these relationships into equation 4.27, the final linearized single track vehicle state space model is formed:

$$\begin{bmatrix} \dot{\beta} \\ \dot{r} \end{bmatrix} = \begin{bmatrix} \frac{-(C_{\alpha f} + C_{\alpha r})}{mV_X} & \frac{-(L_r C_{\alpha r} - L_f C_{\alpha f})}{mV_X{}^2} - 1 \\ \frac{-(L_r C_{\alpha r} - L_f C_{\alpha f})}{V_X J_z} & \frac{-(L_f^2 C_{\alpha f} + L_r^2 C_{\alpha r})}{V_X J_z} \end{bmatrix} \begin{bmatrix} \beta \\ r \end{bmatrix} + \begin{bmatrix} \frac{C_{\alpha f}}{mV_X} \\ \frac{L_f C_{\alpha f}}{J_z} \end{bmatrix} \delta \tag{4.28}$$

4.5.4 Implementation of LQR Proportional Gain

To determine the optimal gain K for the LQR controller, the cost function in equation 4.7 is revisited. In its current state, the equation penalizes yaw rate and side slip. However, if the driver intervenes with a steering input, the desired yaw rate r_d will change and the controller will need to maintain stability of the vehicle simultaneously. Note that the desired side slip β_d is zero for this study. The definitions for state error x_e, and control error u_e are:

$$x_e = \begin{bmatrix} \beta - \beta_d \\ r - r_d \end{bmatrix} = \begin{bmatrix} \beta_e \\ r_e \end{bmatrix} \tag{4.29}$$

$$u_e = u - u_d \tag{4.30}$$

Since the control motors of the vehicle can respond much faster than the driver can produce steering input, the desired states x_d is treated as a constant and simplifies the control design. Treating x_d as a constant, the derivative of the reference state is zero. Therefore the cost function becomes:

$$J(x,u) = \int_0^\infty (x_e^T Q x_e + u_e^T R u_e + 2x_e^T N u_e) dt \tag{4.31}$$

This means the LQR controller will attempt to minimize the yaw error r_e, and the side-slip error β_e, which are the two key components of the stability control.

Recall the single track linearized vehicle dynamics model equations in state space form:

$$\dot{x} = Ax + Bu \tag{4.32}$$

$$x = \begin{bmatrix} \beta \\ r \end{bmatrix} \tag{4.33}$$

$$A = \begin{bmatrix} \dfrac{-(C_{\alpha f} + C_{\alpha r})}{mv} & \dfrac{-(L_r C_{\alpha r} - L_f C_{\alpha f})}{mv^2} - 1 \\ \dfrac{-(L_r C_{\alpha r} - L_f C_{\alpha f})}{J_z} & \dfrac{-(L_f^2 C_{\alpha f} + L_r^2 C_{\alpha r})}{v J_z} \end{bmatrix} \tag{4.34}$$

The remaining coefficients of equation 4.32 are B and u which pertain to the control input to the dynamic system. For this study, the control input is chosen as the torque around the center of gravity of the vehicle, M_z. The new control torque M_z can be added to the existing net torque of the system. Rewriting Newton's second law to apply to the system of study results in $M_z = J_z \dot{r}$. Solving for $\dot{r}$ gives $\dot{r} = \dfrac{M_z}{J_z}$, which shows no dependency on β. Therefore the state space model receives the addition of yaw control through the following equations for u and B.

$$u = M_z \tag{4.35}$$

$$B = \begin{bmatrix} 0 \\ \dfrac{1}{J_z} \end{bmatrix} \tag{4.36}$$

Revisiting the cost function in equation 4.31, the weighting matrices R and Q need to be defined. R corresponds to the cost associated with control actuation, and for this study it is chosen as a low value. This means that there is little to no penalty for control actuation. However, if desired, a larger or varying value could be chosen based on motor size or thermal conditions of the motor respectively. For this study, R is chosen as $R = [0.00001]$. Weighting matrix Q determines the cost associated

with yaw error r_e and the side-slip error β_e. Minimizing r_e means that the vehicle will behave as the driver instructs the vehicle to do, for better or worse. Minimizing β_e will help with stability by keeping the trajectory of the vehicle straight. A compromise between the two of these variables is necessary to find a control feedback that offers nimble vehicle response as well as a stable one. Q is defined as the following:

$$Q = \begin{bmatrix} Q_{11} & 0 \\ 0 & Q_{22} \end{bmatrix} \tag{4.37}$$

Q_{11} and Q_{22} are gain parameters that can be adjusted. As defined in equation 4.37, the matrix Q places a cost to yaw rate error and side slip error. Increasing Q_{11} or Q_{22} increases the cost associated with side slip error or yaw rate error respectively.

4.5.5 Implementation of Integral Portion of Stability Controller

Because the LQR controller involves a proportional control action, steady state error will exist. This error will also increase as the system reaches further into non-linear regions where the linearized single track model does not accurately describe the system under control. Another source of error will come from the linearized model of the force generated by each tire with respect to the slip ratio of the respective wheel. As the slip ratio increases, the linear model will deviate further from the true model given by Pacejka's magic formula. This error in turn will affect the accuracy of the yaw and side-slip controllers which rely on precise control of these forces. In an attempt to reduce the errors associated with non-linearities, it is proposed to alter the stability control law by adding two separate integrator terms in combination with the proportional gain term generated by the LQR controller. These integrator terms are borrowed from the traditional super-twisting controller, and are shown in equations 4.38 and 4.39.

$$\dot{u}_{\beta I} = K_{\beta O}\,\mathrm{sgn}(\sigma_\beta) \tag{4.38}$$

$$\dot{u}_{rI} = K_{rO}\,\mathrm{sgn}(\sigma_r) \tag{4.39}$$

σ_β and σ_r are the sliding surfaces for the side slip and yaw rate controllers respectively. They are defined in 4.40 and 4.41.

$$\sigma_\beta = (K_{\beta P}\beta_e + K_{\beta D}\dot{\beta}_e) \tag{4.40}$$

$$\sigma_r = (K_{rP}r_e + K_{rD}\dot{r}_e) \tag{4.41}$$

The effect and choices of adjustable gain terms $K_{\beta P}$, $K_{\beta D}$, $K_{\beta O}$, K_{rO}, K_{rP}, and K_{rD} can be found in Chapter 6

At low speeds, the side slip control effort causes increased RMS yaw rate and side slip errors. To prevent the side slip controller from causing these issues, it is turned off at low speeds. A simple switch function that is triggered when the vehicle longitudinal velocity falls below a threshold is created to mitigate this issue. This construction is shown in equation 4.42.

$$u_{\beta I} = \begin{cases} u_{\beta I}, & \text{if } V_X > 35mph \\ 0, & \text{if } V_X \leq 35mph \end{cases} \tag{4.42}$$

The final control effort is defined as the summation of both integrator terms and the LQR controller proportional gain, resulting in Equation 4.43.

$$u_T = -K \begin{bmatrix} \beta_e \\ r_e \end{bmatrix} + u_{\beta I} + u_{rI} \tag{4.43}$$

4.6 Motor Torque Controller

The LQR control M_z defined in section 4.5.4 determines the amount of torque to apply around the center of gravity of the vehicle. However, this value by itself does not describe what each individual wheel should do to achieve this net torque.

This section will provide a derivation for the forces that each wheel should produce to achieve the control torque M_z.

To begin, remember the fundamental torque relation $\tau = l \times F$, which can be rewritten in terms of the two track model as follows:

$$M_z = F_{LX}\frac{L_w}{2} - F_{RX}\frac{L_w}{2} \tag{4.44}$$

F_{LX} and F_{RX} represent the longitudinal forces generated by the left and right wheels respectively, and are described in the following equations:

$$F_{LX} = F_{FLX} + F_{RLX} \tag{4.45}$$

$$F_{RX} = F_{FRX} + F_{RRX} \tag{4.46}$$

Substituting equations 4.45 and 4.46 into equation 4.44, M_z becomes a function of the longitudinal forces generated by each wheel:

$$M_z = (F_{FLX} + F_{RLX})\frac{Lw}{2} - (F_{FRX} + F_{RRX})\frac{Lw}{2} \tag{4.47}$$

To distribute the control torque among the four wheels, the control is designed to nominally command 1/4 of the total control torque M_z from each wheel. Therefore the following equation can be constructed:

$$\frac{M_z}{4} = F_{ijX}\frac{Lw}{2} \tag{4.48}$$

The longitudinal force of any wheel F_{ijX} can be approximated as a linear relationship with respect to the slip ratio of the respective wheel by the longitudinal stiffness coefficient κ_{ij}. This is shown in the following equation:

$$F_{ijX} = \lambda_{ij}\kappa_{ij} \tag{4.49}$$

κ_{ij} is a function of vertical force on the respective wheel of interest, and is defined as $\kappa_{ij} = \kappa_{ijN}F_{ijz}$. κ_{ijN} is the normalized longitudinal stiffness and F_{ijz} is the vertical

force acting upon each wheel. Since F_{ijX} depends on F_{ijz}, a vertical force observer could be used to increase the accuracy of the force delivered by each wheel. For simplicity in this study, F_{ijz} is treated as a constant value of 1/4 of the vehicle's weight for each wheel and is described as $F_{ijz} = \frac{mg}{4}$. Making substitutions into equation 4.47, the following is formed:

$$\frac{M_z}{4} = \lambda_{ij}\ \kappa_{ijN}\ F_{ijz}\ \frac{Lw}{2} \tag{4.50}$$

Solving for λ_{ij}, we have:

$$\lambda_{ij} = \frac{\frac{M_z}{4}}{\kappa_{ijN}\ F_{ijz}\ \frac{Lw}{2}} \tag{4.51}$$

With this relationship, set $\lambda_{ij} = \lambda_M$ where λ_M is defined as the slip ratio effort demanded by the stability control system. This can be combined with the throttle controller slip ratio λ_t to generate an equation set that describes the final control slip ratios λ_{ijc}, where the subscript c simply stands for command:

$$\begin{bmatrix} \lambda_{flc} \\ \lambda_{frc} \\ \lambda_{rlc} \\ \lambda_{rrc} \end{bmatrix} = \begin{bmatrix} \lambda_t + \lambda_M \\ \lambda_t - \lambda_M \\ \lambda_t + \lambda_M \\ \lambda_t - \lambda_M \end{bmatrix} \tag{4.52}$$

Note that the accelerator position ranges from full throttle (maximum torque by slip ratio = 0.1) or fully open (zero torque by slip ratio = 0). These positions are derived from Pacejka's Longitudinal force curve shown in Figure 4.2 which was created using the values in Table 3.2. A slip ratio of zero produces no force, while a slip ratio of 0.1 produces maximum force.

Chapter 5

Comparison Algorithm Strategy and Implementation

To provide a baseline for the proposed algorithm to be compared with, a simple sliding mode (SM) controller was developed using concepts from other studies and text book information.

5.1 Comparison Algorithm Overview

Similar to the proposed algorithm, the comparison algorithm consists of 2 major parts: a slip ratio controller (for each wheel) and a yaw rate and side slip controller. For the purposes of comparing slip ratio controllers in the ABS test, the slip ratio controller is implemented using a sliding mode controller defined by Kim [22]. Kim's controller is not used in the sine dwell (SD) and constant steering angle (CSA) tests. The proposed super twisting algorithm is used instead for both the proposed and comparison algorithms. Because the comparison slip ratio controller is drastically outperformed by the proposed STA, the STA is used instead to provide a level playing ground for the yaw rate and side slip controllers to be judged on. This is summarized in Table 5.1.

Test	Slip Ratio Controller	Yaw Rate and Side Slip Controller
ABS	SMC	SMC
SD	STA	SMC
CSA	STA	SMC

Table 5.1: *Control Methods Used for the Comparison Algorithm Based on Different Tests*

The comparison algorithm's yaw rate and side slip controller is based upon concepts found in Rajamani's text [35] and simple first order sliding mode control techniques also found in Kim's paper [22].

5.1.1 Slip Ratio Controller

The slip controller uses the same relationships in equations 2.33 and 2.32 to define the slip ratio during acceleration or deceleration. Equation 5.1 forms a simple expression slip ratio error which is used within the sliding surface of the sliding mode controller.

$$\lambda_e = \begin{cases} \lambda_d - \lambda, & \text{if accelerating} \\ -(\lambda_d - \lambda), & \text{if braking} \end{cases} \tag{5.1}$$

Using Equation 5.1, the sliding surface is formed as:

$$\sigma_\lambda = G_c \lambda_e + \dot{\lambda}_e \tag{5.2}$$

G_c is simply a scaling gain used to adjust the effect of e_λ. Using the defined sliding surface, a simple sliding mode controller is applied:

$$u_c = \begin{cases} 1, & \text{if } \operatorname{sgn}(\sigma_\lambda) > 0 \\ 0, & \text{if } \operatorname{sgn}(\sigma_\lambda) < 0 \end{cases} \tag{5.3}$$

The normalized control effort u_c is then multiplied by a maximum torque τ_{max} and fed through a single pole low pass filter with time constant τ_{sr} which produces the output torque τ_{out}.

$$\tau_{out} = u_c \, \tau_{max} \left(\frac{1}{1 + s\tau_{sr}} \right) \tag{5.4}$$

This control scheme is used for each of the four wheels of the vehicle. A block diagram representation of the slip ratio controller is shown in Figure 5.1.

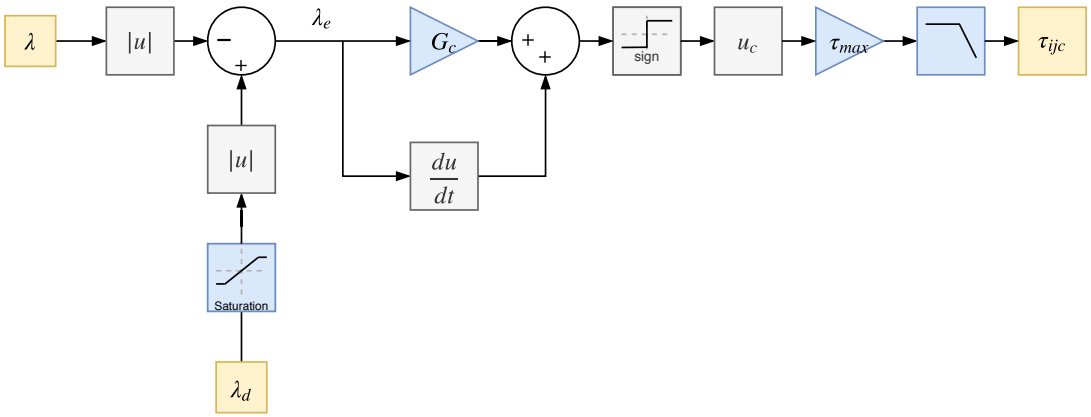

Figure 5.1: *Block Diagram of SMC Slip Ratio Controller Architecture*

5.1.2 Yaw Rate and Side Slip Controller

Using the simple expressions for yaw error ($r_e = r_d - r$) and side slip error ($\beta_e = \beta_d - \beta$), a sliding surface can be used as defined by Rajamani [35]:

$$\sigma_{r\beta} = G_r r_e + \dot{r}_e + G_b \beta_e + \dot{\beta}_e \tag{5.5}$$

G_d and G_b are scaling factors for yaw rate and side slip errors and decide the amount of influence the controller should provide for both errors. With the sliding

surface $\sigma_{r\beta}$ defined, a simple sliding mode controller is applied:

$$u_{r\beta} = \begin{cases} 1, & \text{if } \operatorname{sgn}(\sigma_{r\beta}) > 0 \\ -1, & \text{if } \operatorname{sgn}(\sigma_{r\beta}) < 0 \end{cases} \tag{5.6}$$

The normalized side slip and yaw rate control effort $u_{r\beta}$ is now multiplied by a gain G_k and fed into a single pole low pass filter with a time constant $\tau_{r\beta}$. This results in the amount of torque change ($\Delta\tau$) that alters the driver torque command.

$$\Delta\tau = u_{r\beta}\, G_k \left(\frac{1}{1 + s\tau_{r\beta}} \right) \tag{5.7}$$

A block diagram representation of the SM side slip and yaw rate controller is shown in figure 5.2.

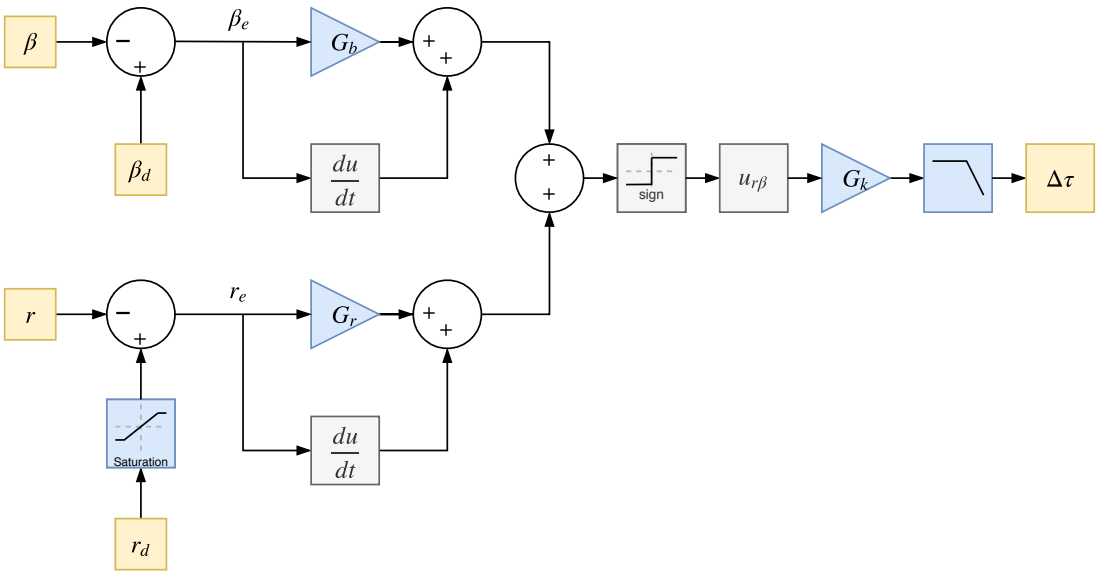

Figure 5.2: *Block Diagram of SM Yaw Rate and Side Slip Controller Architecture*

5.1.3 Motor Torque Controller

The motor torque controller uses a simple relationship that is a summation of the driver's throttle input (τ_{dem}) and the torque generated by the yaw rate and side slip controller ($\Delta\tau$). This relationship for each wheel is shown in the following equation:

$$\begin{bmatrix} \tau_{flc} \\ \tau_{frc} \\ \tau_{rlc} \\ \tau_{rrc} \end{bmatrix} = \begin{bmatrix} \tau_{dem} + \Delta\tau \\ \tau_{dem} - \Delta\tau \\ \tau_{dem} + \Delta\tau \\ \tau_{dem} - \Delta\tau \end{bmatrix} \tag{5.8}$$

τ_{flc}, τ_{frc}, τ_{rlc}, and τ_{rrc} are the final torques commanded by the front left, front right, rear left, and rear right wheels respectively. To convert from torque values to slip ratio values, a similar process can be used as seen in section 4.6.

Chapter 6

Algorithm Performance Testing and Assessment

There are several ways to evaluate the performance of an algorithm designed for vehicle dynamics control. Three test cases were chosen which represent important functionality of the vehicle control system and also offer merits which can be objectively compared and judged. These test cases include an anti-lock braking, sine dwell, and constant steering angle tests.

6.1 Anti-Lock Braking Control Tests

This section will show the advantages found through simulations of using a super twisting algorithm over a simple sliding mode controller which has been derived from Kim's paper [22]. Tuned gain parameters of the slip ratio STA and SM controllers are also reported. The anti-lock braking system test is used as a way to determine the control algorithm effectiveness of braking a vehicle from an initial velocity to a complete stop. It also provides proper insight into how well the controller can track a desired slip ratio. The test is ran by setting the initial longitudinal velocity of the vehicle to 26.8m/s (60 miles per hour) and applying full brake immediately until the vehicle comes to complete stop. The initial lateral velocity of the vehicle is set to zero

Gain Parameter	B_s	W_s	ρ	G_s	H_s
Value	60	1000	0.5	4	0.1

Table 6.1: *Tuned Slip Ratio STAC Gain Parameter Values for ABS Test*

Gain Parameter	G_c	τ_{sr}	τ_{max}
Value	5000	0.04	175

Table 6.2: *Tuned Slip Ratio SMC Gain Parameter Values for ABS Test*

along with the initial yaw rate.

6.1.1 Slip Ratio Test Gain Parameters and Tuning

Tuning the gain parameters of the STAC was performed by hand. Through this process, several observations are worth noting. In general, a larger G than Q led to a more stable control effort. With larger Q values, the controller struggled to minimize the sliding surface as oscillations became increasingly worse. Gains B and ρ adjust the control response similar to the proportional gain of a PI controller. Lastly, W adjusts the control response in the same way that the integral gain of a PI controller would. W must be tuned very carefully to eliminate offset error whilst avoiding excessive oscillations from control effort. Table 6.1 provides the gains used for the STAC for the ABS test.

Gain parameters for the comparison SM slip ratio controller were tuned by hand to optimize its ABS test performance. Only three parameters (G_c, τ_{max}, and τ_{sr} were available for tuning the SMC. G_c adjusts the weighting of λ_e in the sliding surface σ_λ and keeping its value larger lead to better slip ratio tracking. Smaller values (< 500) allow $\dot{\lambda}_e$ to dominate the sliding surface, leading larger slip ratio errors. Increasing the time constant τ_{sr} smooths the control output at the expense of slowing the control response. Finally, τ_{max} determines the amplitude of the switching generated by the sliding surface. Table 6.2 shows the gains used for the SMC during the ABS test.

6.1.2 Results

Observing Figure 6.1, the slip ratio response of the ABS test for both SMC and STA controllers is displayed for each wheel. The tire model used in this study has an optimal friction coefficient while at the slip ratio of -0.1 while braking, hence a throttle input of full brake corresponds to this slip ratio. The SMC response shows oscillations which are larger for the rear wheels than the front. This is a symptom of weight transfer to the front of the vehicle which decreases the power necessary to create excess slip at the rear wheels. The initial response of the SMC is faster than that of the STA, hence the SMC will decelerate faster than the STA for a brief period of time. However, the STA excels at tracking the desired slip ratio and provides drastically reduced oscillations in control effort. Both controllers experience a growth in oscillations as the vehicle comes closer to a full stop. This is partly due to the way that the slip ratio is defined, which can be seen in Equation 2.33. As the longitudinal velocity of the vehicle decreases, the angular velocity of the wheel must be controlled with increasing precision to maintain the desired slip ratio. In real world applications, measurement accuracy of the angular and longitudinal velocity decreases as the vehicle speed approaches zero which presents another set of problems which are not covered in this paper.

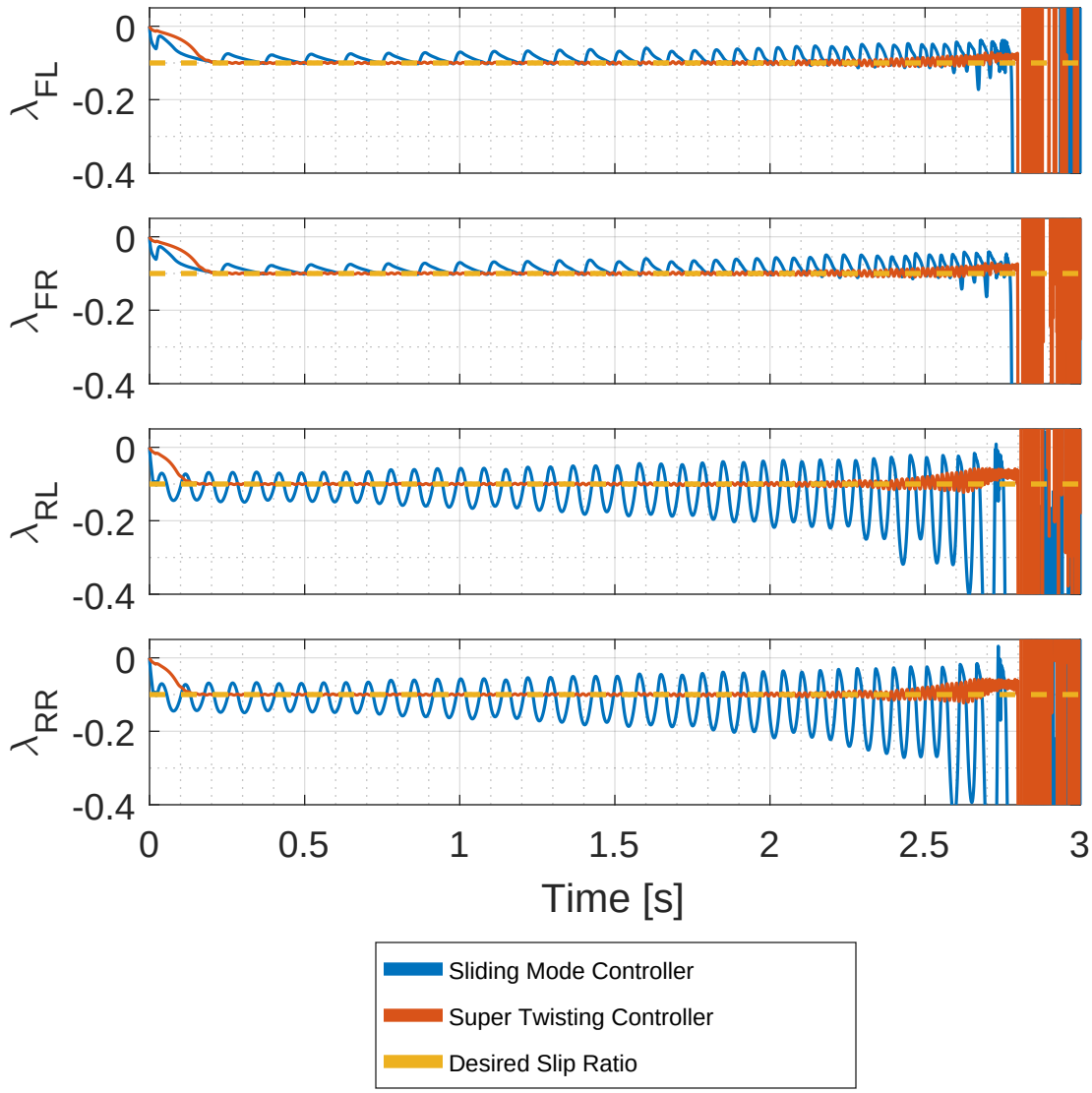

Figure 6.1: *Slip Ratio Responses of ABS Test for Sliding Mode and Super Twisting Controllers*

A visualization tool that is often used to observe the effectiveness of sliding mode controllers is the phase portrait. The axes are composed of the sliding surface σ_λ and its derivative $\dot{\sigma}_\lambda$. Gain parameters within the sliding surfaces were normalized for proper comparisons in the phase portraits. Figure 6.2 displays the comparison of phase portrait plots for the SMC and STA during the ABS test. To avoid plot

clutter, the data is only displayed between the simulation times of 0.3 and 1 second. Note that this omits the reaching phase (times 0 to 0.3) of the control effort, as this is not the focus of the plot. Both the SMC and STAC produce a control effort that attempts to minimize σ_λ and $\dot{\sigma}_\lambda$. The phase portraits show clearly that the STAC holds much closer to the origin than the SMC. It can also be observed that the phase portrait loops expand as the vehicle slows. This is another way of showing that control accuracy degrades with a decrease in vehicle speed.

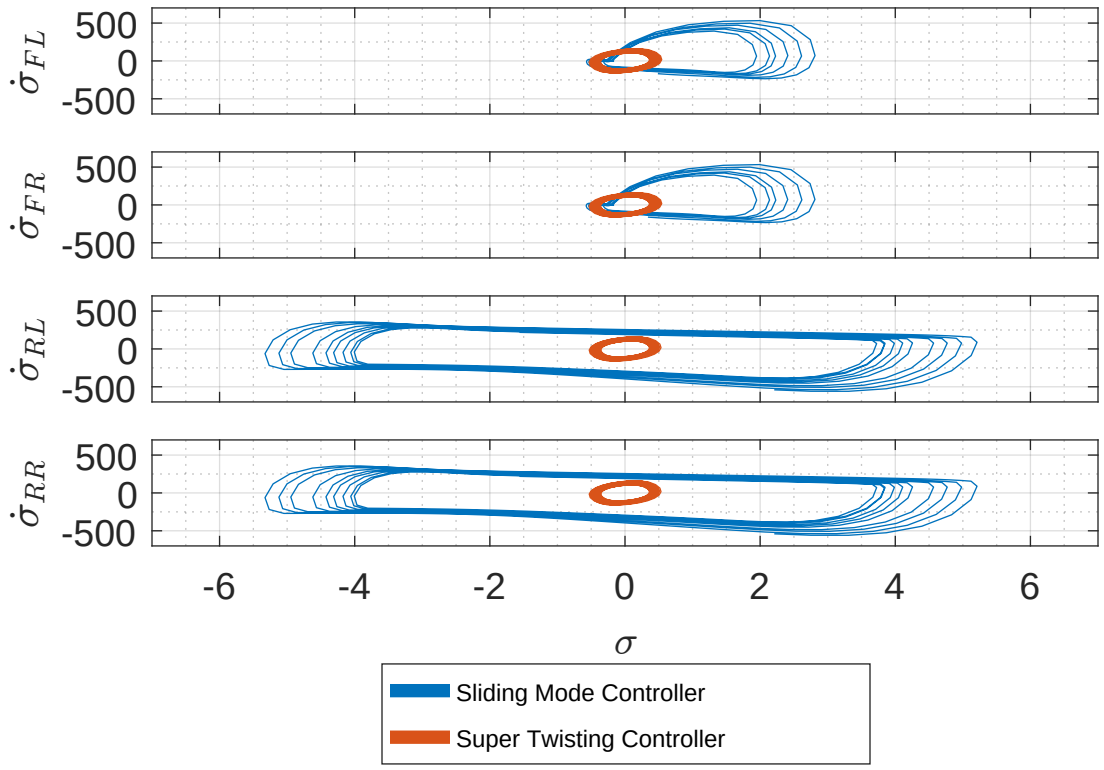

Figure 6.2: *Slip Ratio Controller Phase Portrait for each wheel of ABS Test for Sliding Mode and Super Twisting Controllers Captured from 0.3s to 1s of Simulation Time*

As mentioned previously, the initial response of the STAC was on the slower side and resulted in a slightly increased 60-0 stopping time. This issue can be addressed by increasing the gain parameter W. This can be dangerous, as an increased W can lead to instability. To prevent this, the gain W can be switched to a higher value only when certain conditions are met. For a simple proof of concept test, W was set

to change to a value of 6000 only if $\mid e\lambda_e \mid > 0.05$ and a change in throttle command was detected. The results are shown in Figure 6.3. It can be noted that the front and rear wheels stabilize to the desired slip ratio about 0.1 and 0.05 seconds faster respectively when using the Altered Super Twisting Algorithm (ASTA) versus the normal STA. The rest of the control effort is left almost completely unchanged. This method is not used during the following CSA or sine dwell tests.

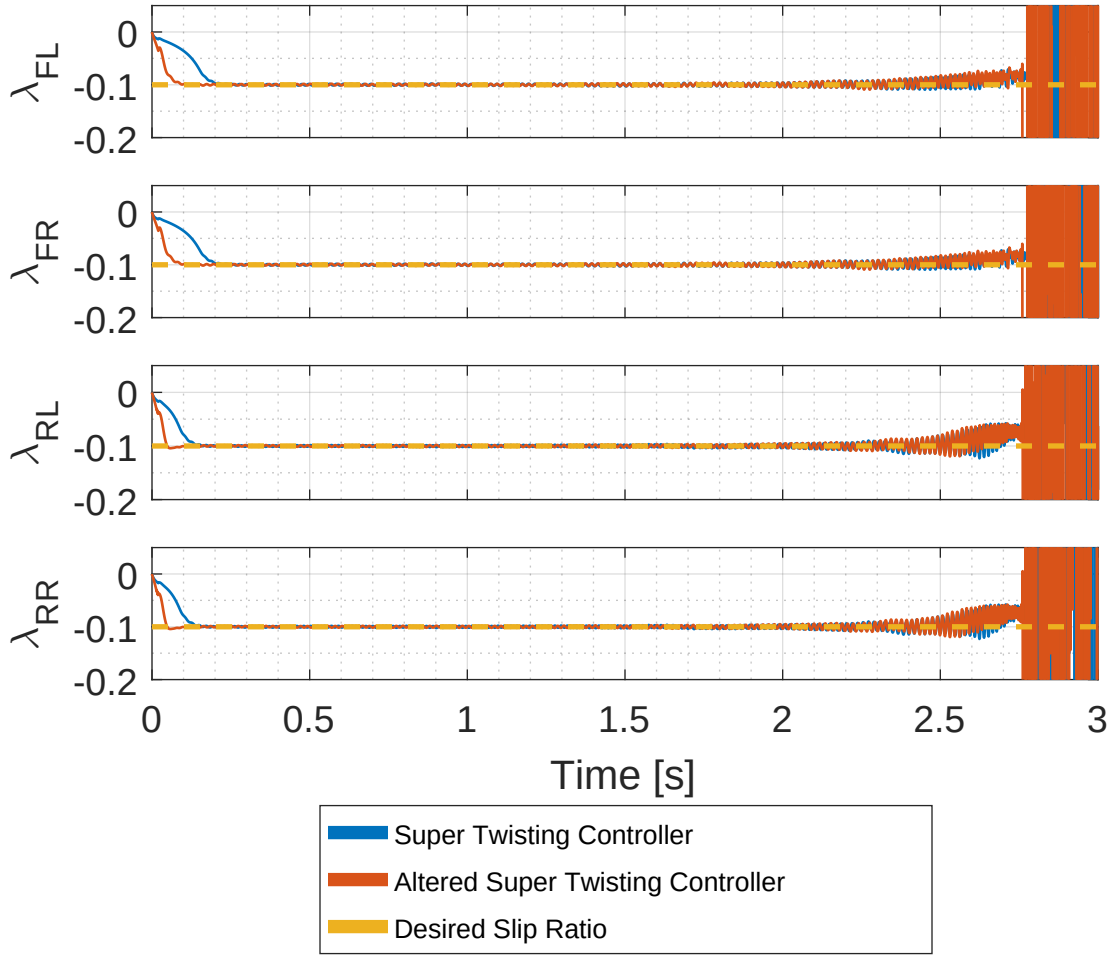

Figure 6.3: *Slip Ratio Responses of ABS Test for Super Twisting and Altered Super Twisting Controllers*

For simple comparison, Table 6.3 shows the 60-0 times for both the SMC and the STAC. The STA and altered STA hold lower RMS slip ratio errors which is reflected in the lower 60-0 stopping times.

	60-0 Stopping Time [s]
SMC	2.963
STA	2.813
ASTA	2.774

Table 6.3: *60-0 Stopping Times for SMC and STAC*

The slip ratio controller gains were slightly modified for the upcoming discussed tests (SD and CSA). The ABS test was used as a method to tune the slip ratio controller gain values to a vicinity that is optimal for other tests.

6.2 Yaw and Side Slip LQR-STAC Gain Parameters and Tuning

The constant steering angle test introduces yaw control action, which involves new gain parameters. As before, the tuning of all gain parameters was done by hand. The tuning objective was chosen to obtain less rms error for vehicle side slip and yaw whilst maintaining an acceptable vehicle trajectory. For the CSA and SD tests, the slip ratio controller parameters were re-tuned to provide a better response. The revised gain parameters would sacrifice some ABS test performance for a greatly improved performance for the SD and CSA tests. All gain parameters used for the SD and CSA tests can be found in tables 6.4, 6.5, and 6.6.

When adjusting $K_{\beta P}$ and K_{rP} of the LQR-STAC it was important to keep their values larger than their derivative counterparts ($K_{\beta D}$ and K_{rD}). This helped prevent excessive oscillations and unstable control effort. Adjusting $K_{\beta O}$ and K_{rO} determined how quickly the integrator could respond. Too small of a value for these gains gave the vehicle a sluggish response that maintained stability at lower speeds but failed to maintain a proper trajectory at higher speeds. Too large of a gain provided control efforts which were too strong and of oscillatory nature, leading to poor results at all speeds. R was set to a low value, meaning that little to no cost was associated with control effort. This value could be increased if the designer was more concerned about

Gain Parameter	B_s	W_s	ρ	G_s	H_s
Value	60	820	0.5	0.13	0.002

Table 6.4: *Tuned Slip Ratio STAC Gain Parameter Values for ABS Test*

Gain Parameter	$K_{\beta P}$	$K_{\beta D}$	$K_{\beta O}$	K_{rP}	K_{rD}	K_{rO}	Q_{11}	Q_{22}	R
Value	3	0.2	6.8	0.15	0.03	5.5	0.1	10	0.00001

Table 6.5: *Tuned Gain Parameter Values of Proposed LQR-STAC for SD and CSA Tests*

efficiency and wanted to lower stability control effort. Lastly, the effect of altering Q was not as dramatic as many of the other gains, however still noticeable. Adjusting Q_{22} higher than Q_{11} led the vehicle to have a more nimble control response which in general led to better handling characteristics.

For the SM yaw rate and side slip comparison controller, three gains (G_b, G_r, G_k) and a time constant ($\tau_{r\beta}$) were tuned by hand. Balancing the values of G_b and G_r was very important, as these values determine the priority of the controller. Increasing G_b places higher value on side slip control whereas increasing G_r prioritizes yaw control. Higher values of G_b with respect to G_r led to a more stable control response and provided the best results. It was also important to keep G_b and G_r at values $\gg 1$. This ensures that the derivative errors $\dot{\beta}_e$ and $\dot{r}_e$ do not dominate the control effort, as this lead to oscillations. G_k is set to determine the amplitude of the switching output generated by the sliding surface $\sigma_{r\beta}$. Lastly, increasing the time constant $\tau_{r\beta}$ smooths the control output at the expense of slowing the control response. $\tau_{r\beta}$ was set relatively low to prioritize control accuracy over chatter reduction.

Gain Parameter	G_b	G_r	G_k	$\tau_{r\beta}$
Value	10	5	0.2	0.008

Table 6.6: *Tuned Gain Parameter Values of SM Comparison Controller for SD and CSA Tests*

6.3 Sine Dwell Stability Control Test

The sine dwell test was established in FMVSS No. 126 as a standard by the National Highway Traffic Safety Administration (NHTSA) and describes a procedure to adjudicate the performance of electronic stability control systems [30]. This test determines the controller's ability to maintain stability at higher speeds in the presence of a steering input that resembles a 0.7Hz sine wave with a 500ms dwell inserted into the waveform. The vehicle must begin the sine dwell test with an initial longitudinal velocity $V_X = 50$[mph], and the amplitude of the steering hand wheel must reach at least 180 degrees. Normally, the test specifies a peak input steering wheel angle, however for this study the steering system is not modeled. Instead, the steering angle of the front wheels is used, and the hand wheel steering angle is back calculated using a simple steering ratio. The general waveform for the front wheel steering is shown in Figure 6.4 with respect to time.

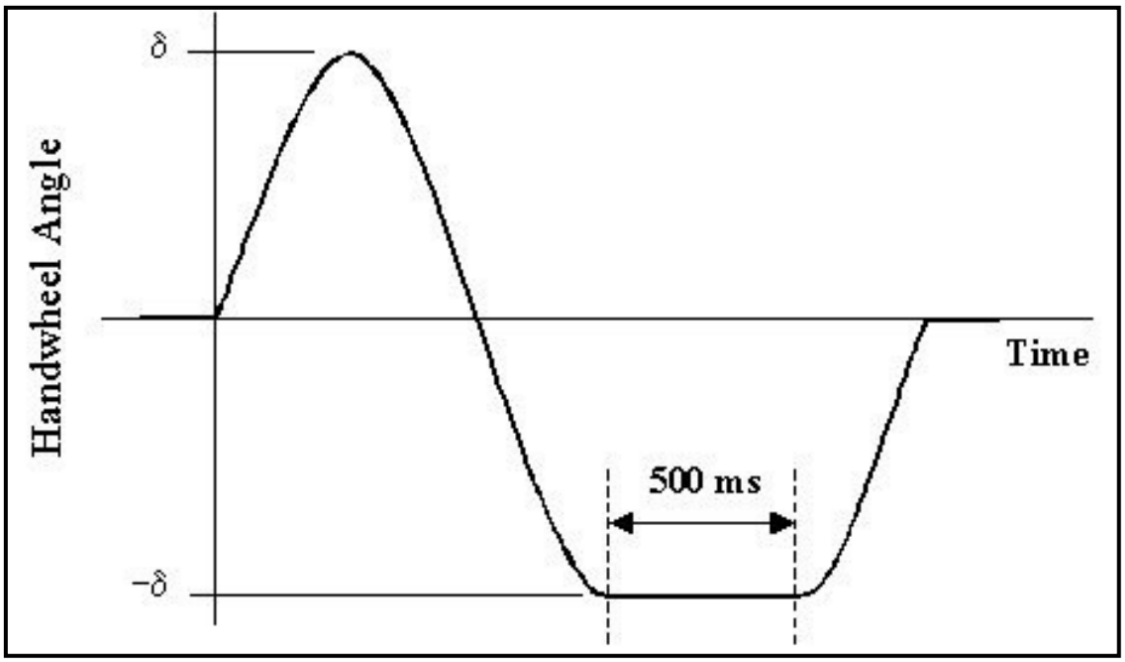

Figure 6.4: *Sine Dwell Steering Input Profile [11]*

FMVSS No. 126 defines lateral stability and responsiveness as the two categories

of evaluation criteria for the sine dwell test. The lateral stability category has the following criteria:

LS1. One second after completion of the steering input for the 0.7 Hz Sine with Dwell maneuver, the yaw rate of the vehicle has to be less than or equal to 35 percent of the first local peak yaw rate produced by the steering reversal.

LS2. 1.75 seconds after completion of the steering input, the yaw rate of the vehicle has to be less than or equal to 20 percent of the first local peak yaw rate produced by the steering reversal.

These criteria are used as predictors that determine the likelihood of the vehicle entering an uncontrolled spin. Visualization of these criteria are shown in Figure 6.5.

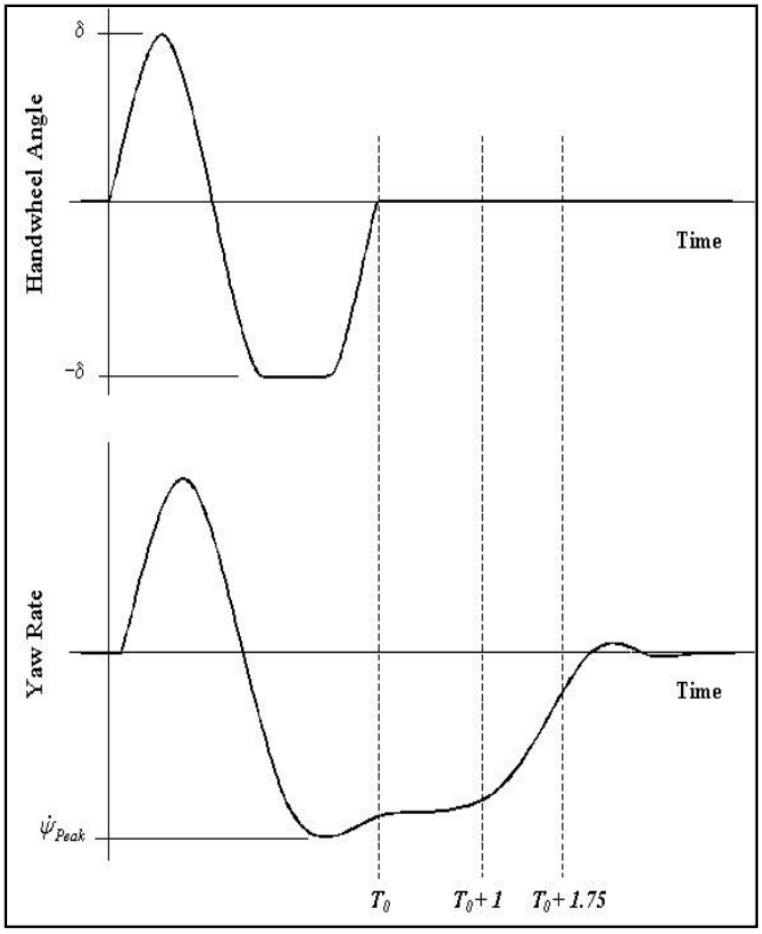

Figure 6.5: *Steering Wheel Position and Yaw Rate Information Used to Assess Lateral Stability (LS1 measured at $T_0 + 1$;LS2 measured at $T_0 + 1.75$) [11]*

R1. An ESC equipped vehicle must have a lateral displacement of at least 1.83 meters (6 feet) at 1.07 seconds after the initiation of steering for vehicles with a GVWR of 3,500 kg (7,716 lb) or less, and 1.22 meters (5 feet) for vehicles with a GVWR greater than 3,500 kg (7,716 lb).

This criterion ensures that the control system does not overly hinder the agility of the vehicle. For this study, the vehicle is modeled with a weight of less than 3,500 kg, so a lateral displacement of at least 6 feet is the target. Visualization of this criterion is shown in Figure 6.6.

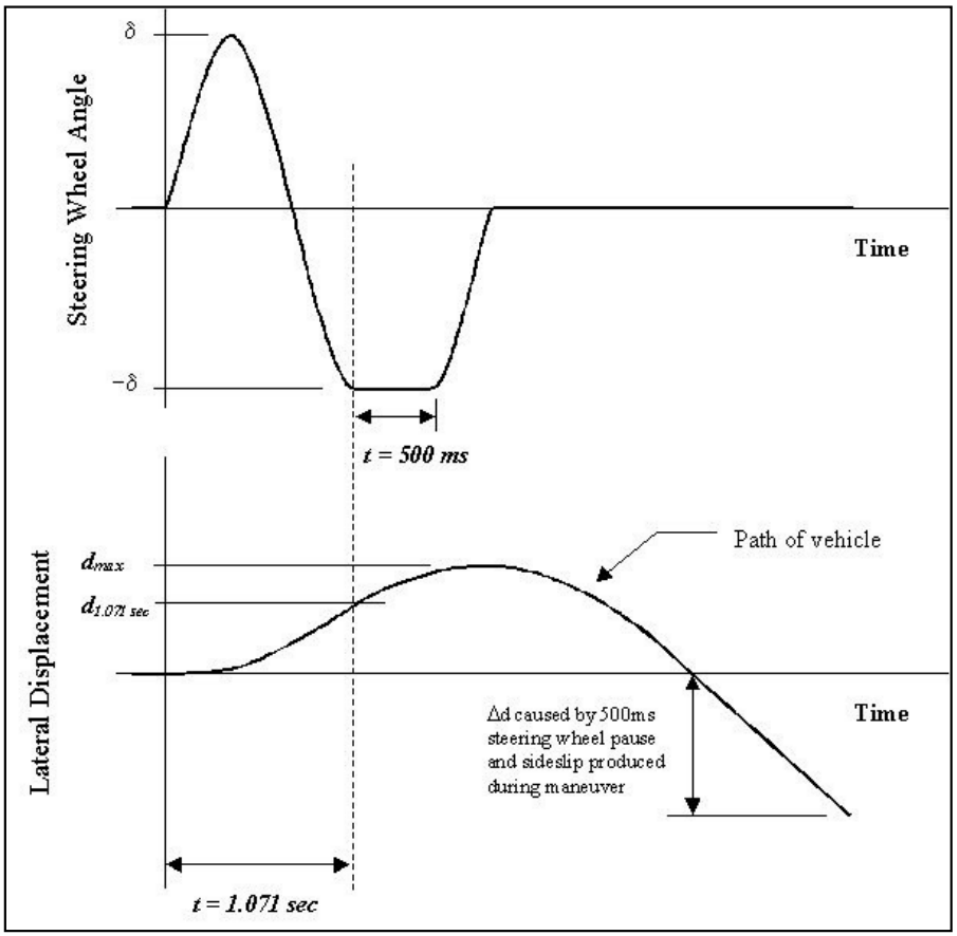

Figure 6.6: *Steering Wheel Angle and Lateral Displacement Trajectory for Sine Dwell Test (R1 measured at* $t = 1.07$ *seconds) [11]*

The sine dwell test maneuver is applied at three different speeds, 30, 50 and 80 mph. This will offer a perspective into how well the vehicle control system maintains control at medium and high speeds.

6.3.1 SD Test Results

In this section, a review of the collection of data is given to provide insight into the sine dwell test. Vehicle telemetry and trajectories plots as well as some respective tables of performance metrics can be found in the appendix. The performance metrics

are used to evaluate the vehicle controller performance while the telemetry information is used to verify that the vehicle performed as expected while under controller influence. The LQR-STA controller attempts to minimize both vehicle yaw and side slip, which are the primary metrics of focus, as well as the FMVSS 126 criteria.

SD FMVSS 126 Test Criterion Discussion

Observing the telemetry and yaw figures located in the appendix, it can be determined whether the vehicle meets the yaw test criterion when under the influence of both stability control systems. The vehicle trajectory figures in the appendix can be used to visualize the path of the vehicle and the corresponding tables can be used to determine if the vehicle passes the responsiveness criterion. Tables A.8, A.9, A.18, and A.19 show the yaw rate at t=1 and t=1.75 seconds after steering input completion for all test cases. However, FMVSS 126 specifies a vehicle speed of 50 mph, so this speed case will be of primary focus. It is also the only speed where the yaw criterion have a standard to meet, as this is not defined for the other speeds.

At 50 mph, both the LQR-STA and SM controllers pass the FMVSS 126 criterion for all tested peak steering angles of 2-24 degrees. The yaw rate settled to acceptable levels t=1 and t=1.75 seconds after steering input completion, and at t=1.07 both controllers allowed for the vehicle center of gravity to maneuver at least 6 ft laterally. To translate the maximum front tire steering angle of 24 degrees to steering wheel angle, a simple calculation can be performed. Assuming a typical steering ratio of 15 [42], the steering wheel input to achieve 24 degrees of tire steering angle at the front wheels is 360 degrees, or one full rotation of the steering wheel.

Observing the responsiveness criterion in Tables A.10 and A.20 both algorithms fail at 2 degrees peak steering amplitude, but pass at all other steering angles (4-24). The failure at 2 degrees is simply due to vehicle physics and is not the controller's fault. Remember that FMVSS requires a hand wheel steering angle of at least 180 degrees, which translates to 12 degrees steering angle at the front wheels. This means that both algorithms provide adequate responsiveness and do not excessively hinder the driver's steering actions according to the FMVSS 126 test.

30, 50, and 80 mph SD Test Telemetry Discussion

This section will discuss the information regarding vehicle telemetry (V_X, V_Y, r) for the SD test, which can be found in Figures A.1 through A.6, and A.20 through A.25, and tables found in sections A.5 and A.6.

Tests ran at 30 mph produced a final V_X that was roughly the same as the starting V_X for both the LQR-STA and SMC controllers. An interesting flaw to point out of the LQR-STA controller is that V_X increased during the 30 mph tests, even though no throttle was applied as seen in Figure A.1. This was caused by the switching of the slip ratio controllers. Even though the switching control command was balanced around zero, the actual control output averaged to a positive biased output which added a slightly positive throttle command to the wheels which in turn slightly increased the vehicle's longitudinal speed (V_X). This only occurred during 30 mph tests when the steering angles were 2,4, and 6 degrees. At steering angles above 12 degrees, V_Y and r tended to have larger peaks for the LQR-STA controller as seen in Figures A.20 and A.21.

Revisiting the 50 mph testing cases, it can be seen that the SMC controller tends to hold vehicle momentum, as the final V_X values are typically higher than that of the LQR-STA controller (Figures A.3 and A.4). However, at a steering angle of 18 degrees and larger, the speeds are within 1.2 mph of each other for the LQR-STA and SM controllers (Figures A.22 and A.23). Peak values for V_Y and r tend to be higher for the LQR-STA controller, however this is not always the case. Larger differences are found at the lower steering angles of 2-12 degrees (Figures A.3 and A.4).

80 mph testing provided varied results for the final V_X values. Neither controller exhibited a consistent higher/lower velocity at the end of the test. Also at almost all tests at 80 mph and any steering angle, the peak V_Y and r values for the SMC controller were higher than that of the LQR-STA controller (Example in Figure A.24). A note that can be made about the LQR-STA controller is that the higher vehicle speeds led to more oscillations in control effort (Example in Figure A.6). These oscillations would typically attenuate to relatively small levels, but still continued to the end of the test. This can be seen in the 80 mph testing at steering angles of 2-18 degrees (Figures A.5, A.6, and A.24) for the LQR-STA controller.

30, 50, and 80 mph SD Test Trajectories Discussion

This section interprets the data regarding vehicle trajectories for all SD tests can be found in Figures A.7 through A.12, Figures A.26 through A.31 and Tables A.10 and A.20.

30 mph testing showed that both controllers' influence on the vehicle is very alike at lower speeds (Figures A.7, A.8, A.26, and A.27). The SM controller exhibited larger lateral position displacements than the LQR-STA controller at steering angles of 16 or larger (Figures A.26 and A.27). Both controllers maintain stability throughout all test conditions at 30 mph.

At 50 mph, very noticeable differences between controllers are apparent in the vehicle trajectories beginning at a steering angle of 6 degrees. Larger steering angles produce even more variation. At a steering angle of 6 degrees, the SM controller encounters an anomaly, where the vehicle trajectory never crosses into the left hand plane (Figure A.9). An interesting anomaly found with the LQR-STA controller occurs at steering angles of 10 and 12, where the vehicle experiences positive yaw after the steering input is finished (Figure A.10). This is evidence of the yaw controller response providing a slightly under-damped control. The SM controller offers a more responsive control, as the t=1.07 lateral position was larger for all test cases at 50 mph (Example in Figure A.28). Lastly, it is important to note that both controllers kept the vehicle stable for all 50 mph cases.

80 mph testing proved to be a challenge for the SM controller at higher steering angles. At 4 degrees steering angle, the SM controller cannot bring the vehicle out of the right hand plane (Figure A.11). Also for the SM controller, 6 and 8 degrees of steering angle produces heavy yaw and side slip but the vehicle maintains control (Figures A.11 and A.12). Finally, at a steering angle of 10 degrees and greater, the SM controller enters a spin out condition. The LQR-STA controller maintains control through its shallower trajectory through steering angles of up to 18 degrees (Figure A.30). At 20 degrees and larger steering angles, the LQR-STA controller sends the vehicle either into an oscillatory or spin out state (Figure A.31).

30, 50, and 80 mph SD Test Yaw and Side Slip Errors Discussion

By observing the yaw and side slip errors and their corresponding desired rate with respect to time in Figures A.13 to A.16 and Figures A.32 to A.35, it provides a chance to attain a deeper understanding into the control mechanisms for both algorithms. Figures A.17 through A.19 and Figures A.74 through A.76 show a comparison of the LQR-STA and SM controller rms errors for yaw rate and side slip. Tables A.4 through A.7 and Tables A.14 through A.17 also provide maximum and minimum values for yaw and side slip in every case of the SD test.

For 30 mph testing at steering angles 2-12, the LQR-STA mostly provided better results than the SM controller in terms of rms error for yaw rate and side slip (Figure A.17). Exceptions were found at 10 and 12 degrees. Note that the LQR-STA controller is designed such that the side slip controller is not activated at lower speeds. This means the yaw controller is working by itself at the 30 mph tests. In contrast, at steering angles of 14-24 the SM controller provides better performance in terms of rms yaw and side slip errors (Figure A.36). Peak levels of r and β tend to run higher for the LQR-STA controller.

As the vehicle speed is brought to 50 mph, rms yaw error is increased, while the rms β error is decreased for most cases (Figures A.18 and A.37). Peak r values tend to be higher for the LQR-STA controller while peak β values tend to be lower. The 50 mph case shows that the LQR-STA controller sacrifices yaw control accuracy for general stability.

80 mph testing highlights the stability capabilities of the LQR-STA controller. Test cases with steering angles from 6-18 show that the LQR controller provides rms yaw errors that rival or are better than the SM controller whilst providing drastically better side slip performance (Figures A.19 and A.38). steering angles 2 and 4 show significantly larger rms yaw error for the LQR-STA controller (Figure A.19), and this could be a result of the side slip controller performing unnecessary action. Peak values of r and β tend to be higher for the SM controller during 80 mph testing, as the SM controller struggled to maintain control of the vehicle.

An important take away from the yaw rate graphs is that the LQR-STA controller generates a distinctively different response than the SM controller. The yaw rate

on the LQR-STA controller tends to alternate between zero and the target yaw rate (Example in Figure A.13), which is a result of the yaw rate and side slip controllers fighting for priority. In a way, this can be thought of as pulse width and amplitude modulation of the yaw rate. An important detail that generalizes the side slip responses is that the LQR-STA controller keeps the duration of increased side slip shorter than that of the SM controller (For example, compare Figure A.15 to Figure A.16).

6.4 Constant Steering Angle Control Test

The constant steering angle control system test is used as a way to determine the control algorithm stability effectiveness during a constant steering angle turn. The test is ran by starting the vehicle with an initial longitudinal velocity with zero throttle input and applying a ramp function to the steering angle input which eventually saturates. To provide a more comprehensive result, the test was ran at different starting velocities (30, 50 and 80mph), and for each starting velocity, the test was ran at 12 different steering saturation angles (2, 4, 6 ,8, 10, 12, 14, 16, 18, 20, 22, and 24 degrees). The steering angle ramp has a slope of 12 degrees per second for all tests. The initial lateral velocity of the vehicle is set to zero along with the initial yaw rate.

6.4.1 CSA Test Results

This section provides a similar analysis as seen in the SD Test Results section. Vehicle telemetry, trajectory, performance metrics, as well as yaw and side slip errors will be examined at all test cases in this section. Note that the arrows located on the trajectory plots represent the vehicle position and direction the vehicle points at 1 second intervals. The plots and tables for these data sets can also be found in the Appendix to avoid excessive clutter in this section.

30, 50, and 80 mph CSA Test Telemetry Discussion

This section will discuss the information regarding vehicle telemetry (V_X, V_Y, r) for the CSA test, which can be found in Figures A.39 through A.44, and A.58 through A.63, and tables found in sections A.7 and A.8.

At 30 mph testing, remember that the LQR-STA controller provides influence only through its yaw rate integral term (beta integral control action is suppressed by design). At low steering angles (2,4,6,8), the final V_X is slightly larger for the LQR-STA controller (Figures A.39 and A.40). This is the same issue seen in the SD testing which only occurs at low speeds and smaller steering angles. Further improvement of this algorithm should address this issue, but this is out of the scope of this paper. At steering angles of 10 degrees and larger, the final V_X of the SM controller is larger (Example in Figure A.58. V_Y and r are very similar at low steering angles (2,4,6), which is most likely a result of the vehicle requiring minimal control at low speeds and steering angles (Figure A.39). Beginning with 8 and larger, peak V_Y values are larger for the LQR-STA controller (Example in Figure A.40). This makes sense, as the side slip controller has no effect at small speeds. No major differences of r values between controllers are seen until steering angles of 12 and above. For these cases the SM controller generates larger yaw rates over most of the test time (Example in Figure A.58). An interesting note can be made about the LQR-STA controller at a SA of 24 degrees where chattering can be observed towards the end of the test data (Figure A.59). By this time the vehicle is traveling so slowly that yaw control is unnecessary. An improved version of this controller could essentially eliminate control actions at such small velocities to prevent chattering.

50 mph testing shows once again that lower steering angles of 2,4, and 6 do not tend to produce a trend for V_X, V_Y, and r values. However, now that the vehicle is traveling fast enough to activate the side slip controller, yaw rate switching for the LQR-STA controller can be seen on the r graphs. Some switching is also apparent on the V_Y graphs for the LQR-STA controller. Continuing to steering angles of 8 and larger, the LQR-STA controller yaw rate switches between a smaller value (0-10 degrees) to a larger value (20-50 degrees) until the vehicle slows to speeds $\leq$ 35 mph. This is a resultant of the side slip and yaw control integrator elements fighting for

control until the side slip controller is switched off. The switching also allows for the lateral velocity of the the vehicle using the LQR-STA controller to remain quite low until lower speeds. Once the side slip controller switches off, the V_Y values increase momentarily and settle. In general the SM controller produces higher initial peak values of V_Y and r. Also, the LQR-STA controller slowed the vehicle faster than the SM controller in almost all cases. Figure A.42 provides examples for everything discussed in this paragraph aside from the first sentence.

Testing at 80 mph was very similar to that of the 50 mph tests. Once again, the LQR-STA controller slowed the vehicle faster than the SM controller in almost all test cases. The main differences found here were that both controllers produced similar initial peak r values, and that the SM controller produces significantly higher peak V_Y values that taper slowly back to zero with the slowing of the vehicle. Figure A.44 provides examples for these concepts.

30, 50, and 80 mph CSA Test Trajectories Discussion

This section interprets the data regarding vehicle trajectories for all CSA tests can be found in Figures A.45 through A.50, and Figures A.64 through A.69.

30 mph testing trajectories were nearly identical for steering angles 2-8 (Example in Figure A.45). For steering angles 10 and larger, the LQR-STA controller has a slower turn in response, meaning that its trajectory follows an initially wider path (Example in Figure A.64). After settling into the turn, the LQR-STA controller also holds a slightly smaller curvature to it path, which means that the radius of its turn is larger than that of the SM controller.

Bringing the test speed to 50 mph showed some interesting changes from the 30 mph data. At low steering angles (2 and 4), the LQR-STA controller acted similar to the 30 mph data in the sense that the initial turn in of its trajectory was smaller than that of the SM controller (Figure A.47). However, the curvature of the trajectories matches much closer as the vehicle settled into its turn. At steering angle of 8, the LQR-STA controller starts to distinguish itself from the SM controller by providing a faster turn in response, which also creates a larger initial curvature to the trajectory (Example in Figure A.48). This turn in response creates a trajectory gap between

the two controllers and only gets wider as the steering angle is increased (Effect seen in A.67).

By design, the LQR-STA side slip controller turns on control effort at higher speeds. 80 mph testing showcases the effect of this design construction. For all 80 mph tests, the LQR-STA controller provides a slower turn in response than the SM controller (Example in Figure A.50). This is a sacrifice that the LQR-STA controller makes to keep the vehicle side-slip drastically lower than the SM controller during the earlier trajectory path. Starting with an steering angle of 8, the SM controller essentially holds the vehicle in a controlled drift through for the first 7 seconds of simulation time (Figure A.50). SM controller trajectory data show that during this time the arrows point further inward compared to the vehicle trajectory. This same behavior follows for all tested steering angles larger than 8 for the SM controller (Figures A.50, A.68, and A.69).

30, 50, and 80 mph CSA Test Yaw and Side Slip Errors Discussion

Yaw and side slip errors are discussed in this section for the CSA test. The yaw and side slip errors and their corresponding desired rate with respect to time are given in Figures A.51 to A.54 and Figures A.70 to A.73. Figures A.55 through A.57 show a comparison of the LQR-STA and SM controller rms errors for yaw rate and side slip. Tables A.24 through A.27 and Tables A.31 through A.34 also provide maximum and minimum values for yaw and side slip in every case of the SD test.

At 30 mph, the rms side slip and yaw errors are both lower for the LQR-STA controller for steering angles of 2-8 degrees (Figure A.55). At steering angles of 12 degrees and higher, the LQR-STA controller excels diminishing yaw error drastically more than the SM controller (Figures A.55 and A.74). In contrast, at steering angles of 10 and larger, the rms side slip error is larger for the LQR-STA controller, however the difference in error is not as drastic as seen for rms yaw errors. These details once again highlight that the LQR-STA controller ignores side slip control at lower speeds to prioritize yaw rate control.

50 mph testing further reinforced that the LQR-STA controller can have some slightly negative effects at lower steering angles (2 and 4 degrees). This steering angle

and vehicle speed combination generated slight control oscillations on the output which in turn caused drastically larger rms yaw errors (Figure A.56). RMS Side slip errors stayed lower for the LQR-STA controller for steering angles 2 through 10 degrees (Figure A.56). At steering angles 12 and larger, the SM controller resulted in smaller side slip errors, however this conclusion is somewhat misleading (Figure A.56 and A.75). As mentioned several times before, the LQR-STA controller turns slide-slip control off when the vehicle slows past (35 mph). Hence, if the rms side slip errors are taken only during the duration of time that the vehicle spent faster then 33 mph, it can be seen that the LQR-STA controller outperforms the SM controller. With this is consideration, the LQR-STA controller has lower rms side slip and yaw errors whist attempting to control the vehicle at steering angles of 12 and higher.

With slight exception to an steering angle of 2 degrees, 80 mph testing showed that the rms yaw errors were very similar for both controllers (Figures A.57 and A.76). Since the vehicle spent more time at higher velocities, the LQR-STA controller was able to engage the side slip control alongside yaw control which produced a lower rms side slip error for all tested steering angles. Higher speed testing showed that the LQR-STA controller can maintain drastically lower side-slip values whilst maintaining a decent level of yaw rate control simultaneously.

Chapter 7

Conclusion

7.1 Algorithm Comparison and Insight Summary

In this thesis, a new torque vectoring strategy was proposed which could be applied to AWD vehicles, and was tested with a simulated AWD independent drive electric vehicle model. The control system consists of two main parts, a wheel slip ratio controller and a stability controller. A separate slip ratio controller is used for each wheel that monitors and maintains the current slip ratio to a desired amount to each wheel of the vehicle to modulate force generated by each wheel. The desired amount of torque that is sent to each wheel is modified by either the throttle/brake input and the stability controller. The stability controller monitors the yaw rate and side slip of the vehicle and determines the amount of torque around the center of gravity of the vehicle necessary to minimize yaw and side slip error. This torque is then translated into forces that are applied to each wheel of the vehicle. The proposed torque vectoring strategy leverages super twisting control methods for the slip ratio controllers. For the stability (yaw rate and side slip) controller, a Linear Quadratic Regulator was fused with the integrator term from a super twisting controller. This created a control strategy similar to a PI contol, where the LQR portion acts as a proportional control term, STA integrator terms act like the integral term. To provide a base line comparison, a separate algorithm was implemented using a simple first

order sliding controls and implemented using a well known definitions for the sliding surfaces [35].

Three test cases were used to examine the performance of both the proposed and simple controllers, including anti-lock braking, sine dwell, and constant steering angle tests. The purpose of the ABS test was to provide insight into the performance of the slip ratio controller, whereas the sine dwell and constant steering angle tests were used to examine the performance of the stability controllers. For the sine dwell and constant steering angle tests, the proposed STAC replaced the SMC slip ratio controller in the comparison algorithm to provide a level playing ground for the stability control evaluation. To provide a more comprehensive result for the SD and CSA tests, trials were ran and recorded at multiple speeds and steering angles. Both tests were run at 30, 50, and 80 mph while varying the steering input angle parameter from 2-24 degrees in 2 degree increments. For the SD test, the SA parameter represents the amplitude of the steering action, and for the CSA test the parameter represents the final steering angle that the steering input saturates at. Speeds were chosen to represent low, medium, and high speed cases. The steering angles were chosen to show a large range of steering inputs that range from 30 to 360 degrees rotation at the steering wheel.

ABS testing resulted in a strong display of evidence that the slip ratio STAC outperforms the SMC. The STAC tracks the desired slip ratio far better than the SMC and does not exhibit the sensitivity to weight transfer that the SMC suffers from. A slight downside to the STAC is that its initial response time is a bit sluggish compared to that of the SMC. A simple fix of manually increasing the integral gain parameter showed that this could be improved upon, but was not used in further testing due to its ad-hoc nature.

Given that the slip ratio STAC proved far more effective than the SMC, the STAC was implemented in both the proposed and simple controllers for stability testing. The reason for this was to provide a level playing ground that the separate yaw controllers could act upon. Therefore, the SD and CSA tests could offer a more accurate comparison of the stability control systems.

SD testing simulated an emergency maneuver situation. The most important

result of the SD test was that both algorithms passed the FMVSS 126 stability and responsiveness criterion. This means that both algorithms have a high probability of stability in evasive maneuver situations. 30 mph testing showed some slight anomalies at smaller steering angles for the LQR-STA controller. Both controllers acted quite similar throughout the extent of 30 mph SD testing. 30 mph tests were also ran on a vehicle model with no controller, and these tests showed that the LQR-STA and SM controller efforts had minimal reduction in yaw and side slip error as well as minimal vehicle agility increase in some cases. These benefits were mainly seen at higher SAs. This could imply that control effort at these low speeds/SAs is potentially unnecessary or undesired. 50 mph testing showed that both controllers performed important stability control action when compared to the vehicle response using no controller. The LQR-STA controller generally provided a better side slip control, translating into a less maneuverable but more stable response than the SM controller. These trends found in 50 mph testing were continued through 80 mph testing at higher extremes. At 80 mph the LQR-STA controller once again sacrificed responsiveness for vehicle stability, which became very important at higher speeds at which the LQR-STA controller kept the vehicle from spinning out where the SM controller failed to do so.

CSA testing simulated a situation where a driver enters a turn by increasing the SA until hitting a saturation limit and holding at that SA. Once again, the benefits of the LQR-STA controller were mainly realized at higher speeds (50 and 80 mph). 30 mph testing showed that The LQR-STA and controllers offer a bit more responsiveness through a quicker turn in. This is accomplished by sacrificing some side slip control but these lower speeds the vehicle is more stable intrinsically and side slip control isn't as necessary. 50 mph testing showed that both control systems drastically aid in preventing vehicle under steer. The LQR-STA controller offers better yaw rate and side slip control, as well as a faster turn in response at these speeds. At 80 mph testing, the LQR-STA controller sacrifices initial turn in response to prevent the vehicle from excessive yaw. This means the LQR-STA controller vehicle did not initially cover as much lateral distance as the SM controller but maintained a more stable state. Remember that by design the LQR-STA controller turns on side slip control effort with speeds larger than 35 mph. These effects are also the most apparent at SAs of

6 to 8 degrees and larger.

Overall, this paper shows that the proposed torque vectoring scheme is, in theory, a viable solution for providing stability control to AWD electric vehicles. For slip ratio control, the proposed STA controller provides a drastically improved desired slip ratio tracking response, which make it a solid choice to use instead of a first order sliding mode controller. ABS testing puts the desired slip ratio at the peak of the force curve making it a very difficult situation to maintain desired slip ratio. This is why it was used for comparison testing. Moving on, both the proposed and comparison algorithms for yaw and side slip control offer advantages and disadvantages that one must consider. A major advantage that the LQR-STA controller offers is mid speed stability and responsiveness, as well has high speed stability. The LQR-STA controller is very difficult to tune, as there are many gain parameters that need to be adjusted for proper response. Through tuning, it was also found that the LQR-STA controller seemed fragile, in the sense that some gain parameters had a narrow value range that created a desired response. The SM controller was more robust in this sense.

7.2 Limitations and Notes

In this study, limitations and miscellaneous details are noted that the reader should be aware of. Firstly, the gain parameters chosen in this paper were tuned by hand to the best of the writer's abilities. For the slip ratio controller, the gains were tuned to minimize slip ratio error. For the yaw rate and side slip controllers, gains were tuned with the mindset that yaw rate errors, side slip errors, and vehicle trajectories were the most important criteria to judge the performance of each algorithm. An important note to make is that the MATLAB simulations in this study collected data at 1 kHz. This presented some challenges due to the large amount of time it could take to simulate longer simulation times at 1kHz.

7.3 Future Works

This study proposed a novel torque vectoring control system and proved feasibility in ideal situations. These ideal situations make assumptions. An example would be knowing Pacejka's Longitudinal Force curves for the tires. Studying the use of the proposed algorithm concurrently with observers to estimate vehicle uncertainties would provide a useful study to help validate how pragmatic this controller idea is. Another source of future work would be proving the stability of the proposed controller, which fell outside the scope of this paper.

Bibliography

[1] A. Aly, E.-S. Zeidan, A. Hamed, and F. A. Salem. An antilock-braking systems (abs) control: A technical review. (10.4236/ica.2011.23023), 2011.

[2] M. K. Aripin, S. Yahaya, K. Danapalasingam, K. Peng, N. Hamzah, and M. F. Ismail. A review of active yaw control system for vehicle handling and stability enhancement. (437515), 2014.

[3] Beckman, Brian. The physics of racing. http://phors.locost7.info/files/Beckman˙-˙The˙Physics˙of˙Racing.pdf, 2008. [Online; accessed 1-Dec-2018].

[4] M. Bian, L. Chen, Y. Luo, and K. Li. A dynamic model for tire/road friction estimation under combined longitudinal/lateral slip situation, 04 2014.

[5] Brock, Matthias. Sls amg e-cell: the high-voltage gullwing. http://media.daimler.com/marsMediaSite/en/instance/ko/SLS-AMG-E-CELL-the-high-voltage-gullwing.xhtml?oid=9914569, 2010. [Online; accessed 4-Feb-2018].

[6] Brock, Matthias. The drive system of the mercedes-benz sls amg e-cell: Advanced technology made visible. http://media.daimler.com/marsMediaSite/en/instance/ko/The-drive-system-of-the-Mercedes-Benz-SLS-AMG-E-CELL-Advanced-technology-made-visible.xhtml?oid=9917787, 2012. [Online; accessed 2-Feb-2018].

[7] Y.-F. Chen, I.-M. Chen, J. Chang, and T. Liu. Design and analysis of a new torque vectoring system with a ravigneaux gearset for vehicle applications. 2017.

[8] L. De Novellis, A. Sorniotti, P. Gruber, L. Shead, V. Ivanov, and K. Höpping. Torque vectoring for electric vehicles with individually controlled motors: State-of-the-art and future developments. *26th Electric Vehicle Symposium 2012, EVS 2012*, 2, 06 2012.

[9] M. Dousti, S. Baslamisli, E. Teoman Onder, and S. Solmaz. Design of a multiple-model switching controller for abs braking dynamics. 37:6, 09 2014.

[10] C. P.-V. C. S. O. S. S. S. L. Dugard. Survey on some automotive semi-active suspension control methods: a comparative study on a single-corner model. In *Preprints of the 18th IFAC World Congress Milano (Italy) August 28 - September 2, 2011*, Sep. 2011.

[11] G. Forkenbrock, P. Boyd, and NHTSA. Light vehicle esc performance test development. (Paper Number 07-0456), 2007.

[12] C. Geng, L. Mostefai, M. Denai, and Y. Hori. Direct yaw-moment control of an in-wheel-motored electric vehicle based on body slip angle fuzzy observer. *IEEE Transactions on Industrial Electronics*, 56(5):1411–1419, May 2009.

[13] V. Geus. Model predictive controller design for an autonomous corner module. Master of science thesis, Delft University of Technology, 2010.

[14] B. Giorgio, F. Antonella, L. Arie, and U. Elio. On second order sliding mode controllers. 247, 1999.

[15] R. GmbH. *Automotive Handbook*. Wiley, 2011.

[16] T. Goggia, A. Sorniotti, L. D. Novellis, A. Ferrara, P. Gruber, J. Theunissen, D. Steenbeke, B. Knauder, and J. Zehetner. Integral sliding mode for the torque-vectoring control of fully electric vehicles: Theoretical design and experimental assessment. *IEEE Transactions on Vehicular Technology*, 64(5):1701–1715, May 2015.

[17] G. P. Incremona, E. Regolin, A. Mosca, and A. Ferrara. Sliding mode control algorithms for wheel slip control of road vehicles. In *2017 American Control Conference (ACC)*, pages 4297–4302, May 2017.

[18] V. Ivanov and D. Savitski. Systematization of integrated motion control of ground vehicles. *IEEE Access*, 3:2080–2099, 2015.

[19] R. Jazar. *Vehicle Dynamics: Theory and Application*. Springer, 2008.

[20] M. Jonasson. *Exploiting individual wheel actuators to enhance vehicle dynamics and safety in electric vehicles*. PhD thesis, KTH Royal Institute of Technology, 2009.

[21] U. Kiencke and L. Nielsen. *Automotive Control Systems: For Engine, Driveline, and Vehicle. Second Edition*. Springer, 2005.

[22] J. Kim, C. Park, S. Hwang, Y. Hori, and H. Kim. Control algorithm for an independent motor-drive vehicle. 59(7), 2010.

[23] D. Kirk. *Optimal Control Theory: An Introduction*. Dover Publications, 2004.

[24] M. Kissai, B. Monsuez, A. Tapus, and D. Martinez. A new linear tire model with varying parameters. In *2017 2nd IEEE International Conference on Intelligent Transportation Engineering (ICITE)*, pages 108–115, Sep. 2017.

[25] M. Klomp. *Longitudinal Force Distribution and Road Vehicle Handling*. PhD thesis, Chalmers University of Technology, 2010.

[26] A. Levant and L. V. Levantovsky. Sliding order and sliding accuracy in sliding mode control. *International Journal of Control - INT J CONTR*, 58:1247–1263, 12 1993.

[27] W. Milliken. *Race Car Vehicle Dynamics*, chapter 2, page 26. SAE International, 1995.

[28] I. E. Mousavinejad, Y. Zhu, and L. Vlacic. Control strategies for improving ground vehicle stability: State-of-the-art review. In *2015 10th Asian Control Conference (ASCC)*, pages 1–8, May 2015.

[29] National Highway Traffic Safety Administration. Federal motor vehicle safety standards electronic stability control systems controls and displays. https://www.nhtsa.gov/sites/nhtsa.dot.gov/files/fmvss/ESC˙FR˙03˙2007.pdf, 2007. [Online; accessed 15-Dec-2018].

[30] National Highway Traffic Safety Administration. Fmvss no. 126 electronic stability control systems. https://www.nhtsa.gov/sites/nhtsa.dot.gov/files/fmvss/ESC˙FRIA˙2007. [Online; accessed 19-Sept-2018].

[31] K. Ogata. *Modern Control Engineering (5th Edition)*. Prentice Hall, 2010.

[32] H. Pacejka. *Tire and Vehicle Dynamics, 3rd Edition*. Butterworth-Heinemann, 2012.

[33] J. Pauwelussen, W. Dalhuijsen, and M. Merts. Tyre dynamics, tyre as a vehicle component part 1.: Tyre handling performance. Technical report, HAN University, 2007. pg. 10.

[34] A. Pressley. *Elementary Differential Geometry*. Springer undergraduate mathematics series. Springer, 2001.

[35] R. Rajamani. *Vehicle Dynamics and Control*. Springer, 2006.

[36] Said, Carolyn. Secretive robot-car maker zoox opens up. https://www.sfchronicle.com/business/article/Secretive-robot-car-maker-Zoox-opens-up-13221844.php, 2018. [Online; accessed 9-Sept-2018].

[37] F. Tahami, R. Kazemi, S. Farhanghi, and B. Samadi. Fuzzy based stability enhancement system for a four-motor-wheel electric vehicle. 02(01-1588), 2002.

[38] Y. S. F. P. M. Taleb. Lyapunov design of adaptive super-twisting controller applied to a pneumatic actuator. In *Proceedings of the 18th World Congress The International Federation of Automatic Control Milano (Italy) August 28 - September 2, 2011*, volume 44, pages 3051–3056, Sep. 2011.

[39] A. Tiwari, M. Lathkar, P. D. Shendge, and S. B. Phadke. Skyhook control for active suspension system of heavy duty vehicles using inertial delay control. In *2016 IEEE 1st International Conference on Power Electronics, Intelligent Control and Energy Systems (ICPEICES)*, pages 1–6, July 2016.

[40] H. E. Tseng and D. Hrovat. State of the art survey: active and semi-active suspension control. *Vehicle System Dynamics*, 53(7):1034–1062, 2015.

[41] J. Wong. *Theory of Ground Vehicles*. John Wiley & Sons, 2008.

[42] T. Yoshino and H. Nozaki. Variable gear ratio control using vehicle body slip angle. *Engineering*, 06:439–448, 01 2014.

[43] F. Yu, M. Cheng, K. Tong, and F. Li. Control and performance evaluation of multiphase fspm motor in low-speed region for hybrid electric vehicles. *Energies*, 2015.

Appendix A

Plots, Figures, and Tables

A.1 SD Test Figures for Steering Angles 2-12 Degrees

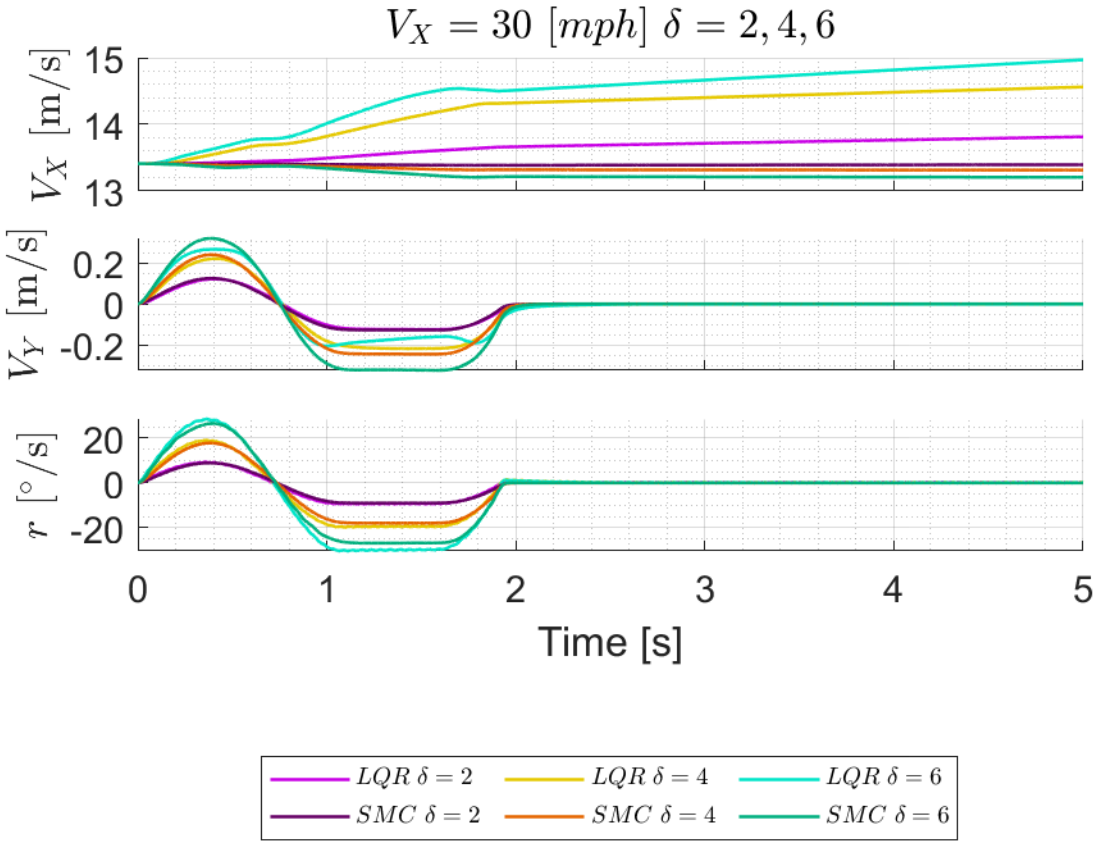

Figure A.1: *SD Test Comparison for LQR-STA and SMC Telemetry at* $V_X = 30$ *and* $\delta = 2, 4, 6$

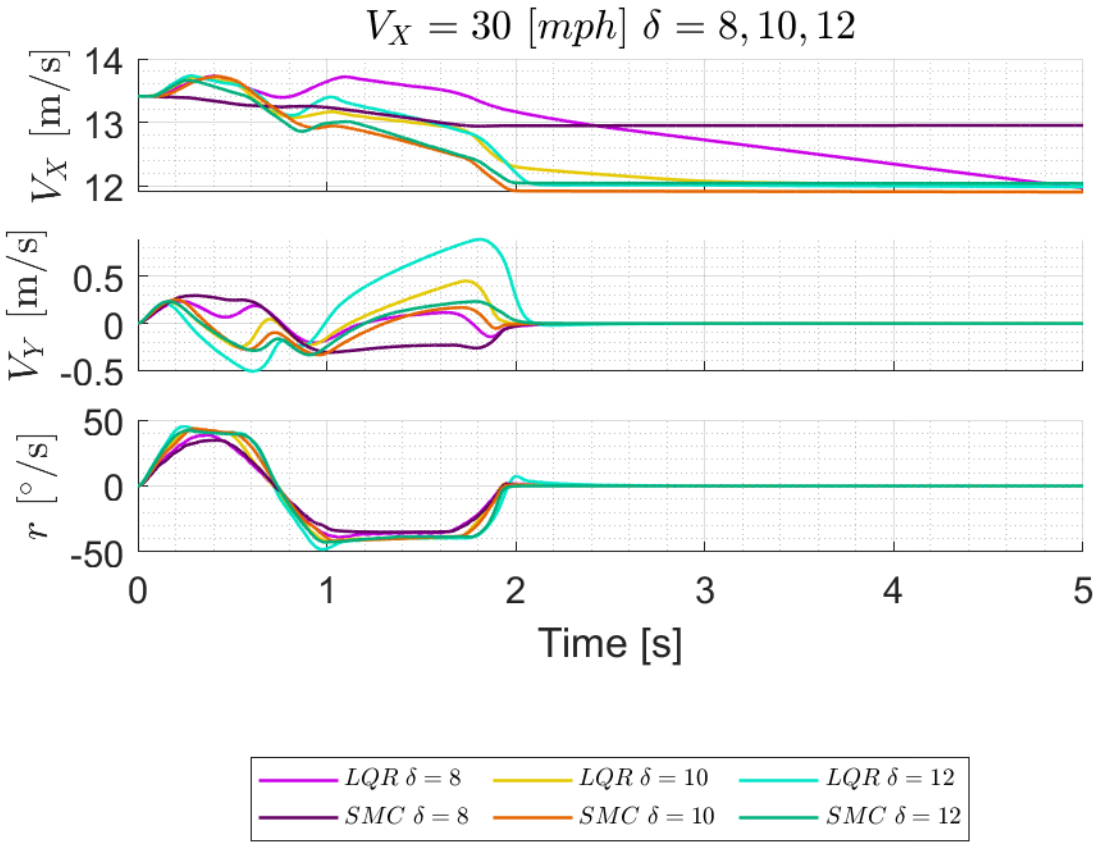

Figure A.2: *SD Test Comparison for LQR-STA and SMC Telemetry at* $V_X = 30$ *and* $\delta = 8, 10, 12$

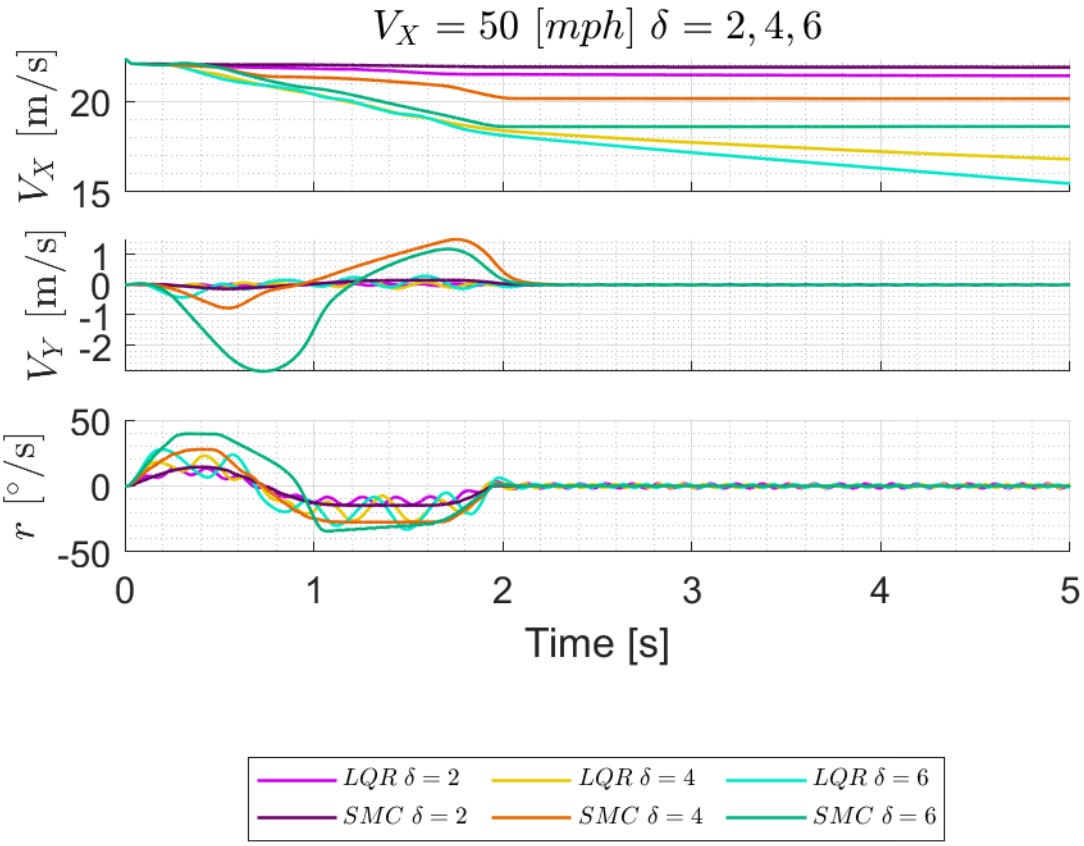

Figure A.3: *SD Test Comparison for LQR-STA and SMC Telemetry at* $V_X = 50$ *and* $\delta = 2, 4, 6$

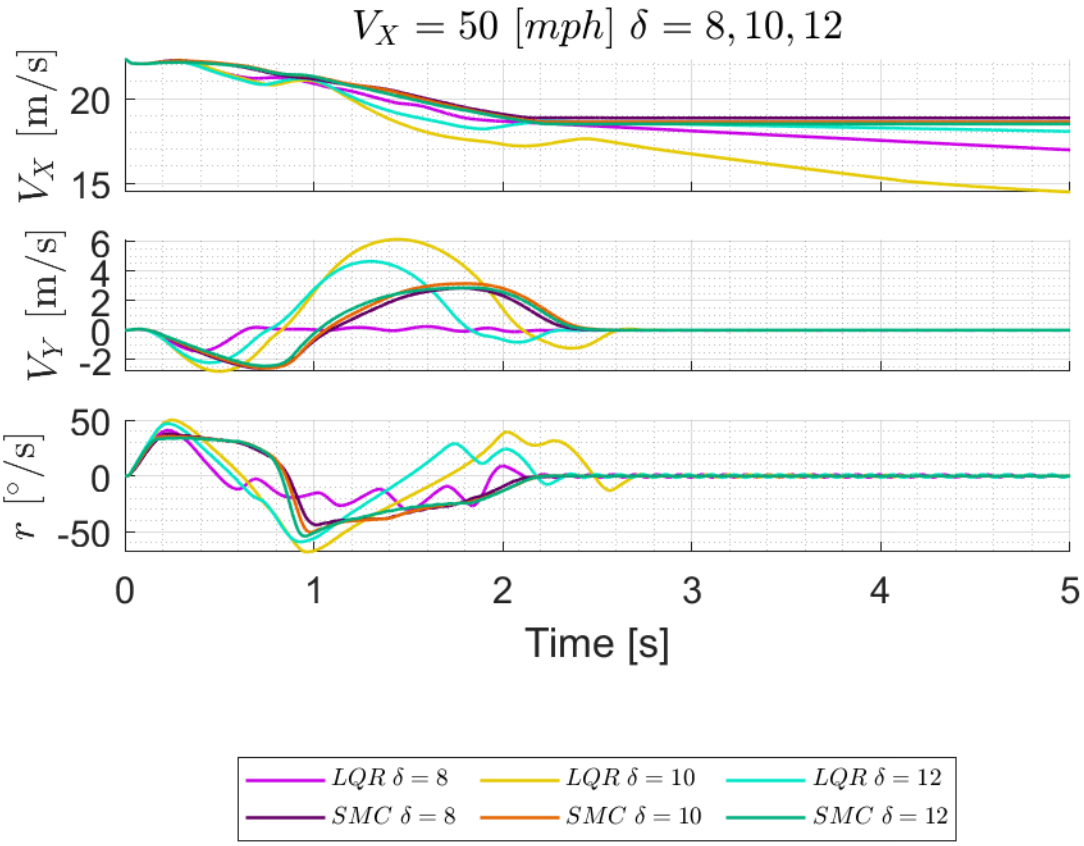

Figure A.4: *SD Test Comparison for LQR-STA and SMC Telemetry at* $V_X = 50$ *and* $\delta = 8, 10, 12$

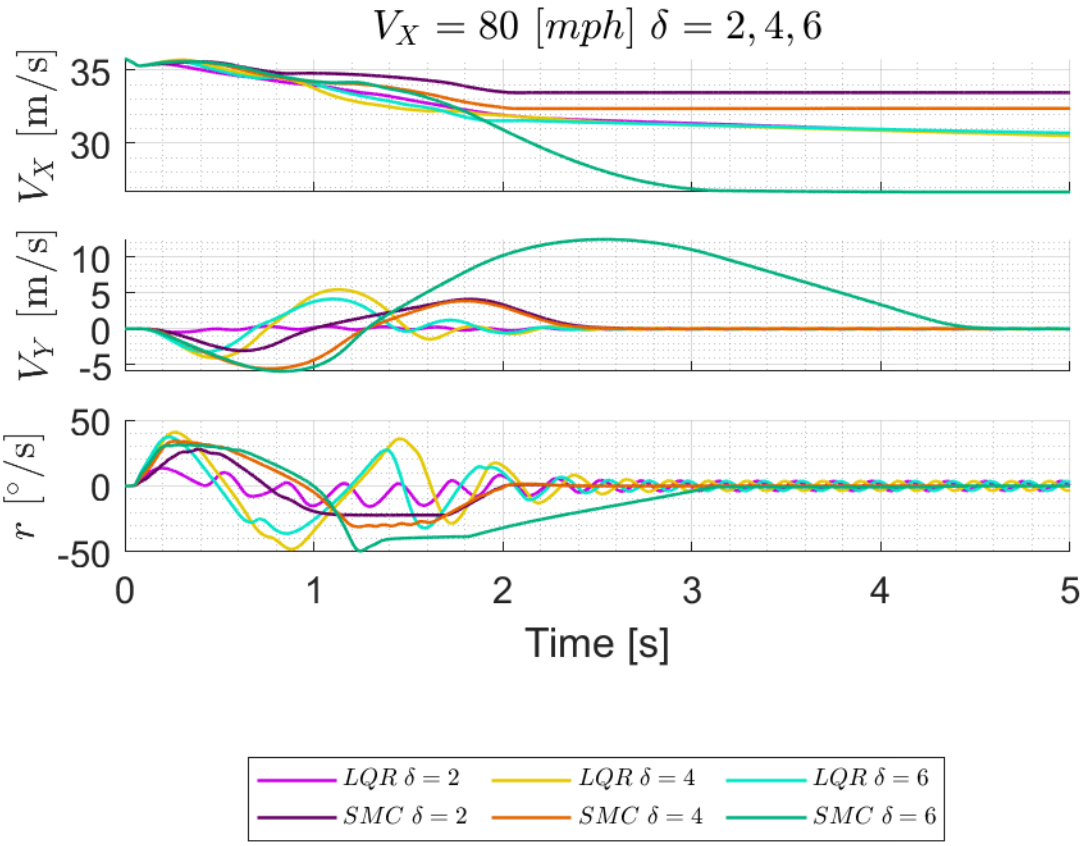

Figure A.5: *SD Test Comparison for LQR-STA and SMC Telemetry at* $V_X = 80$ *and* $\delta = 2, 4, 6$

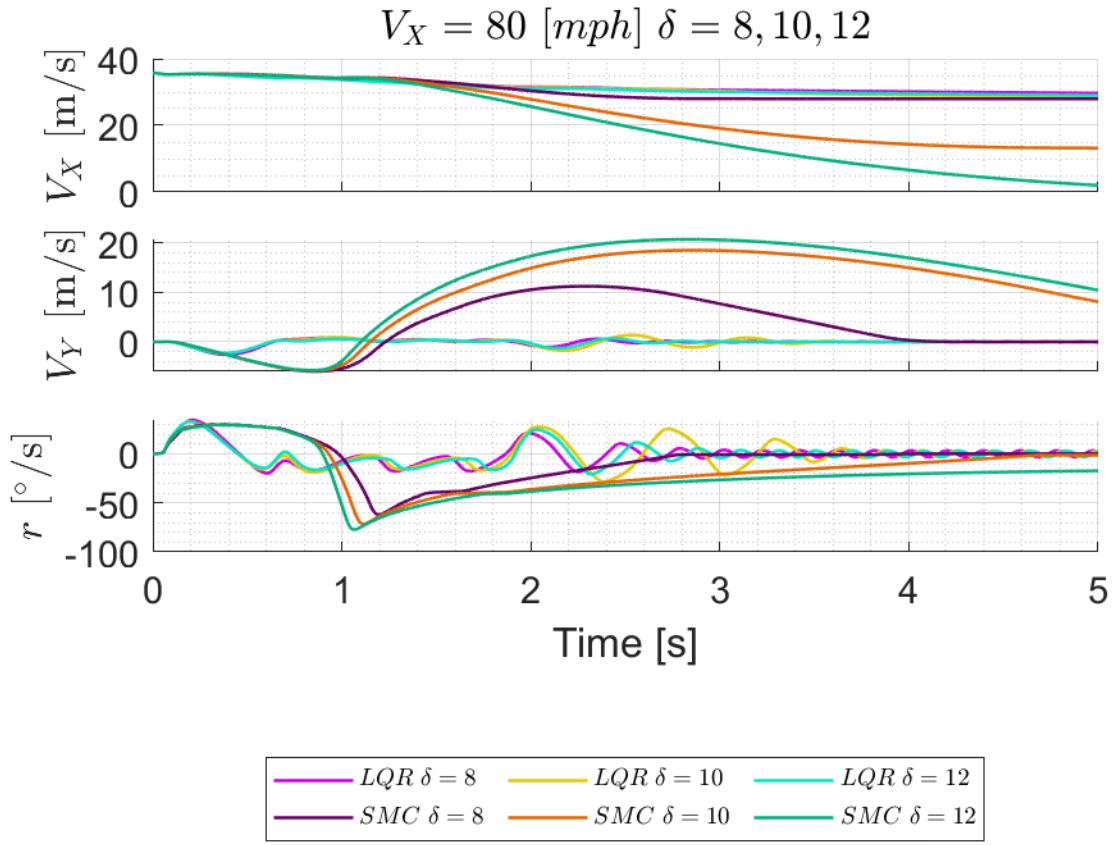

Figure A.6: *SD Test Comparison for LQR-STA and SMC Telemetry at* $V_X = 80$ *and* $\delta = 8, 10, 12$

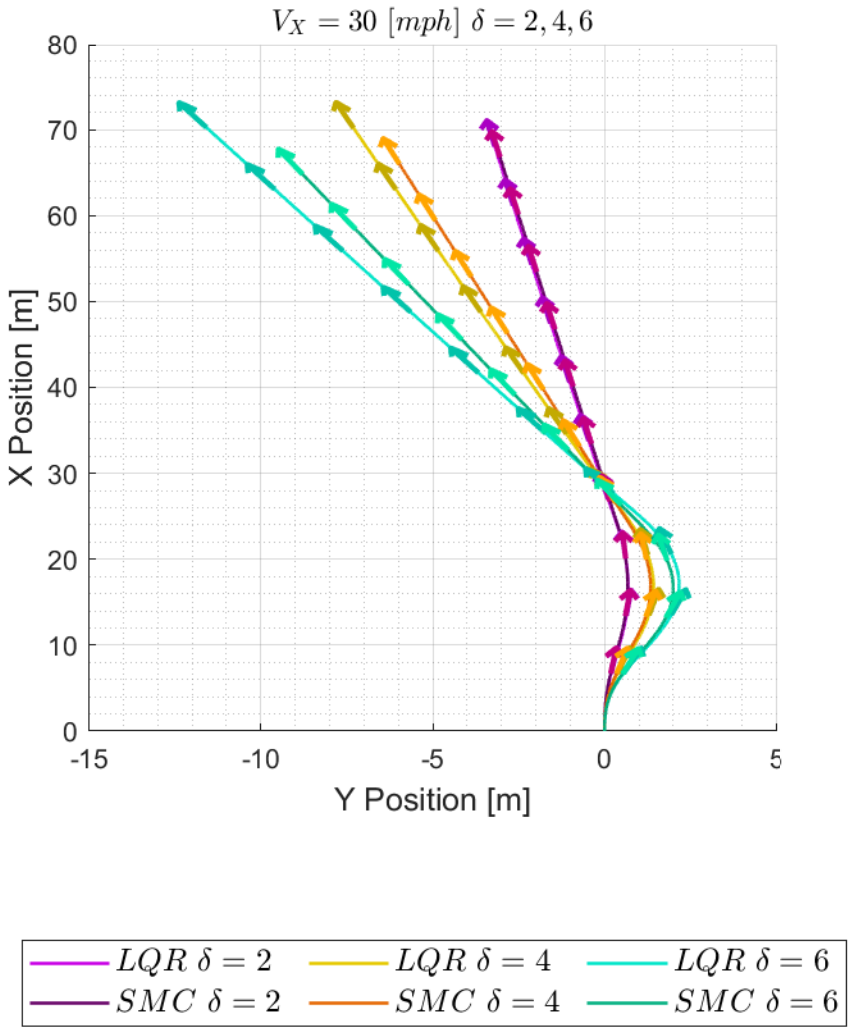

Figure A.7: *SD Test Comparison for LQR-STA and SMC Vehicle Trajectories at* $V_X = 30$ *and* $\delta = 2, 4, 6$

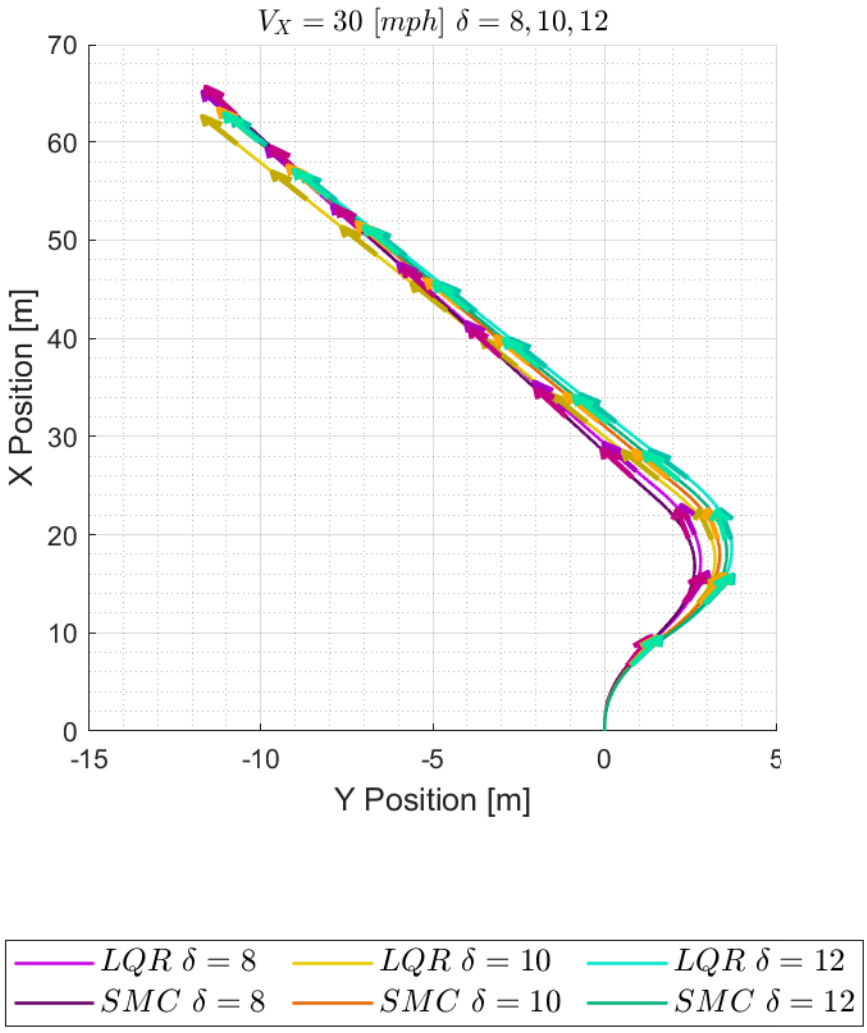

Figure A.8: *SD Test Comparison for LQR-STA and SMC Vehicle Trajectories at* $V_X = 30$ *and* $\delta = 8, 10, 12$

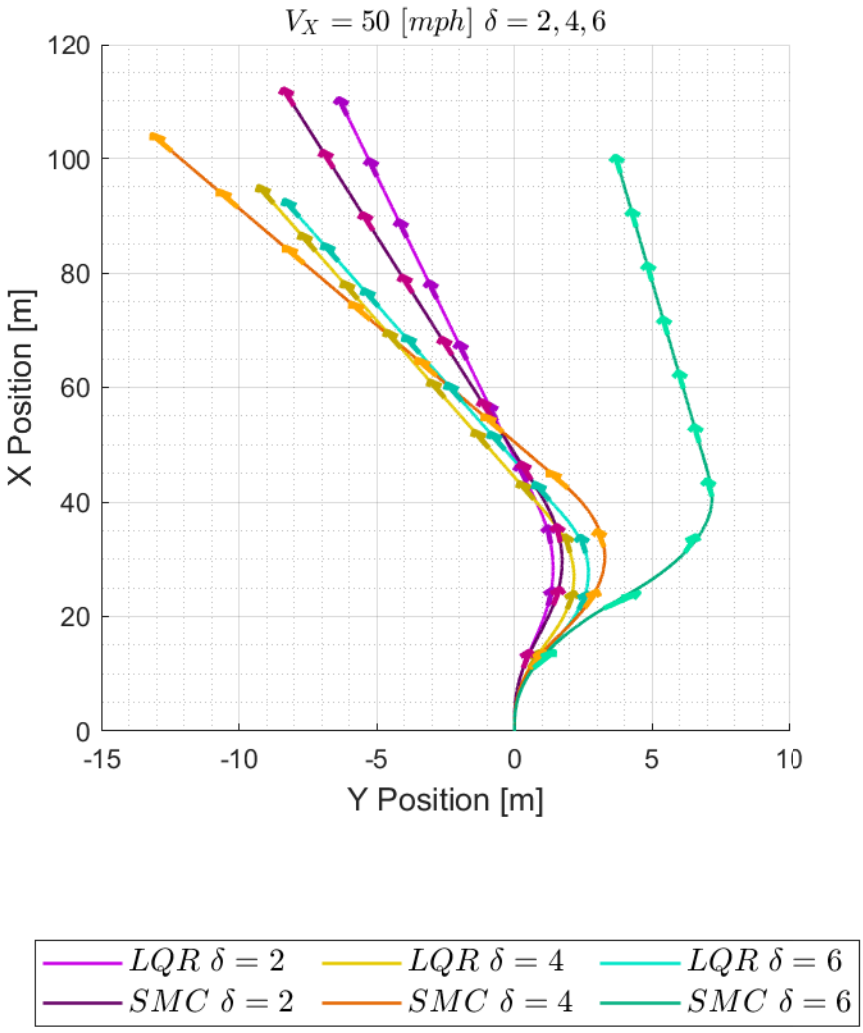

Figure A.9: *SD Test Comparison for LQR-STA and SMC Vehicle Trajectories at* $V_X = 50$ *and* $\delta = 2, 4, 6$

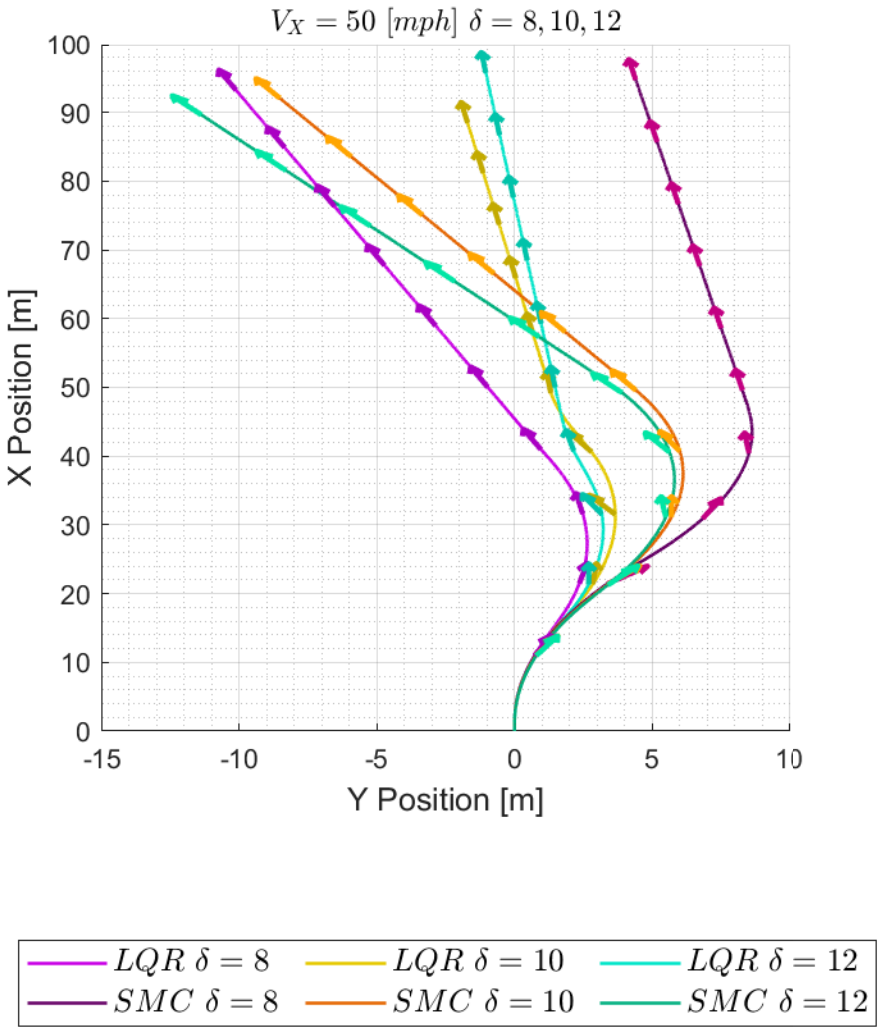

Figure A.10: *SD Test Comparison for LQR-STA and SMC Vehicle Trajectories at* $V_X = 50$ *and* $\delta = 8, 10, 12$

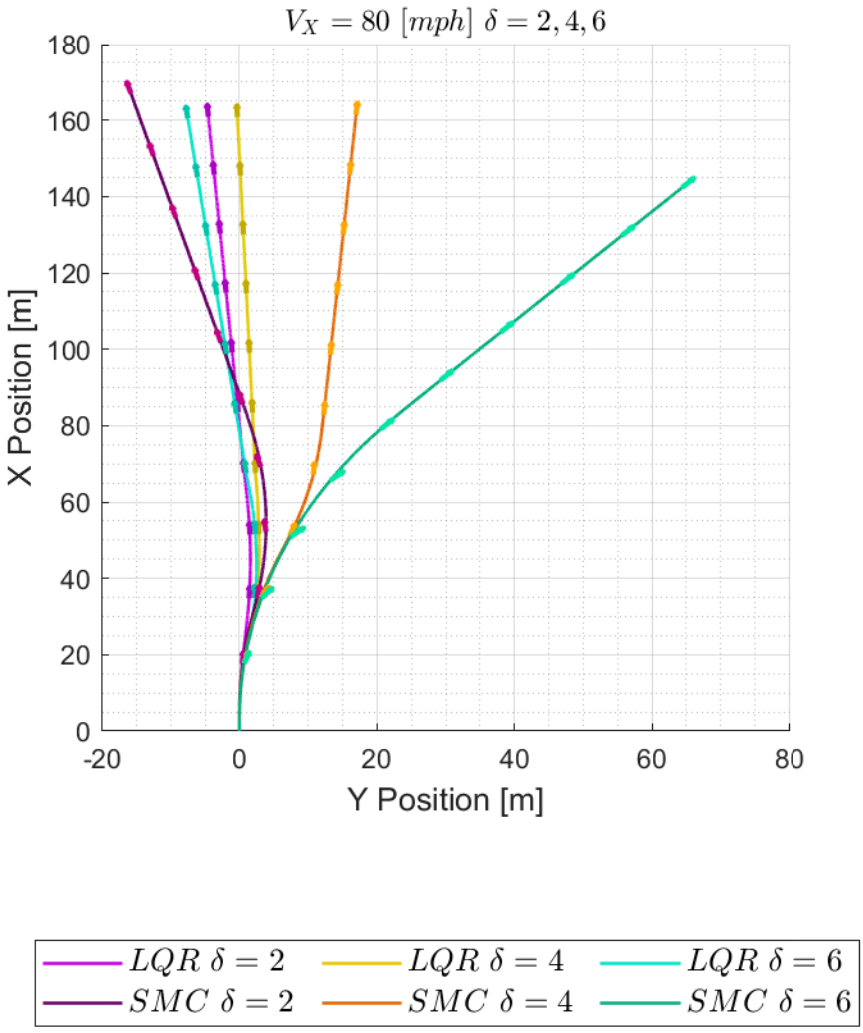

Figure A.11: *SD Test Comparison for LQR-STA and SMC Vehicle Trajectories at* $V_X = 80$ *and* $\delta = 2, 4, 6$

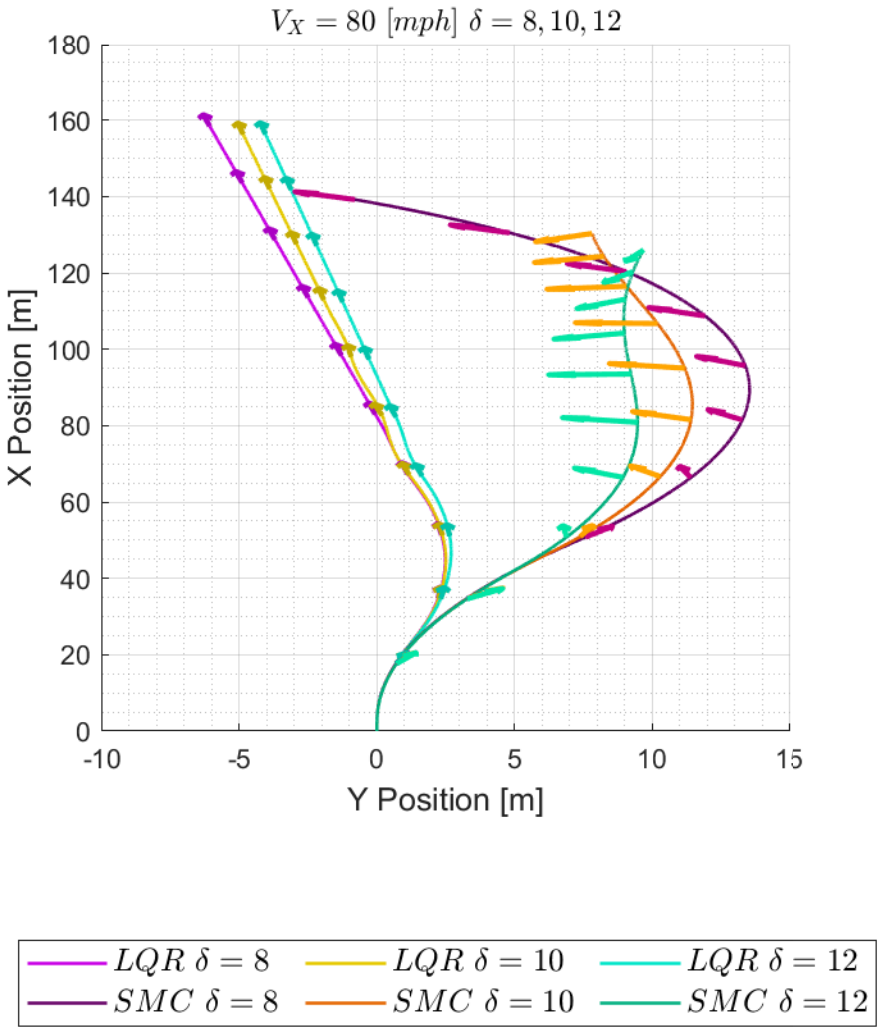

Figure A.12: *SD Test Comparison for LQR-STA and SMC Vehicle Trajectories at* $V_X = 80$ *and* $\delta = 8, 10, 12$

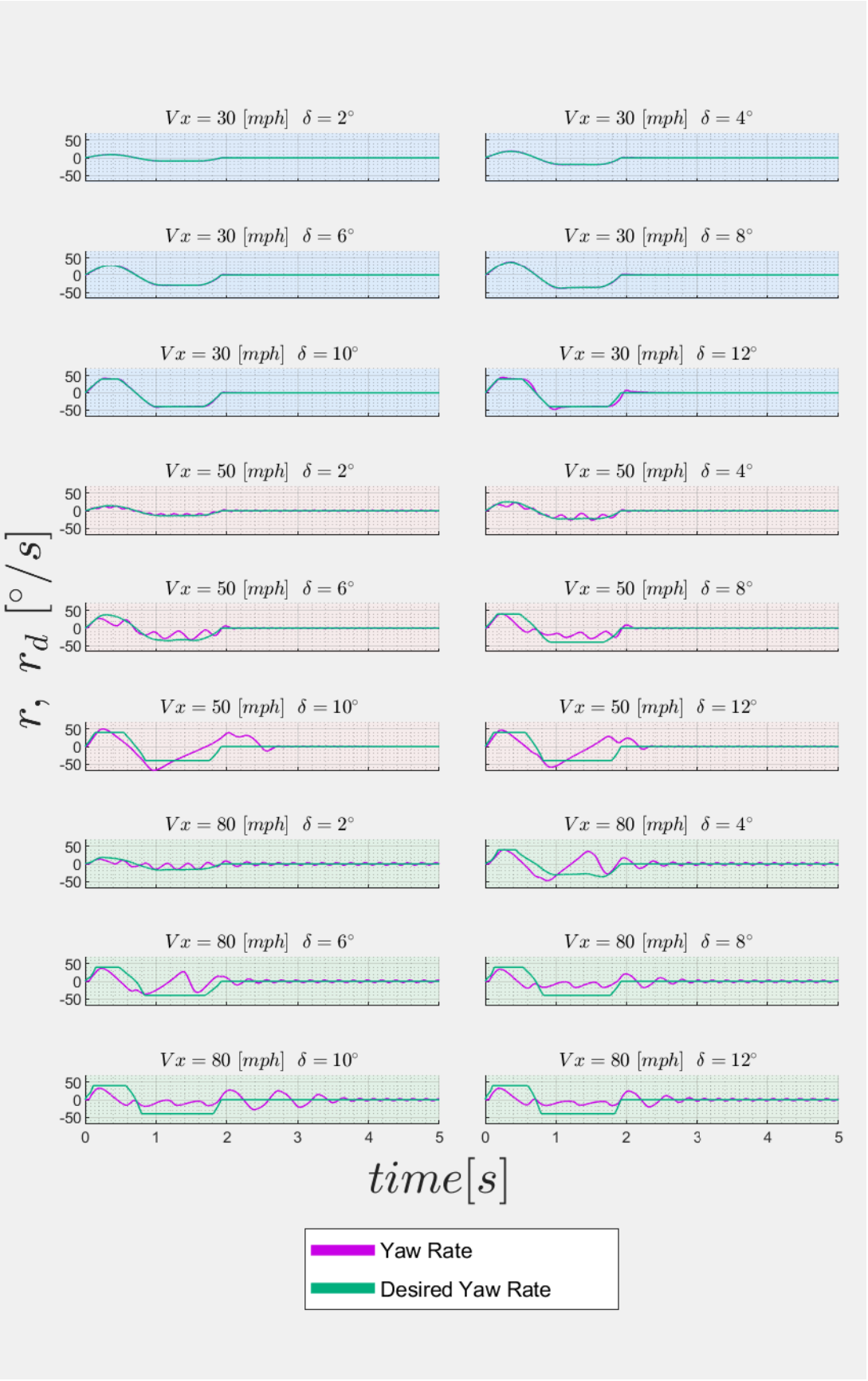

Figure A.13: *SD Test Yaw Errors for LQR-STA* ($\delta = 2 - 12$)

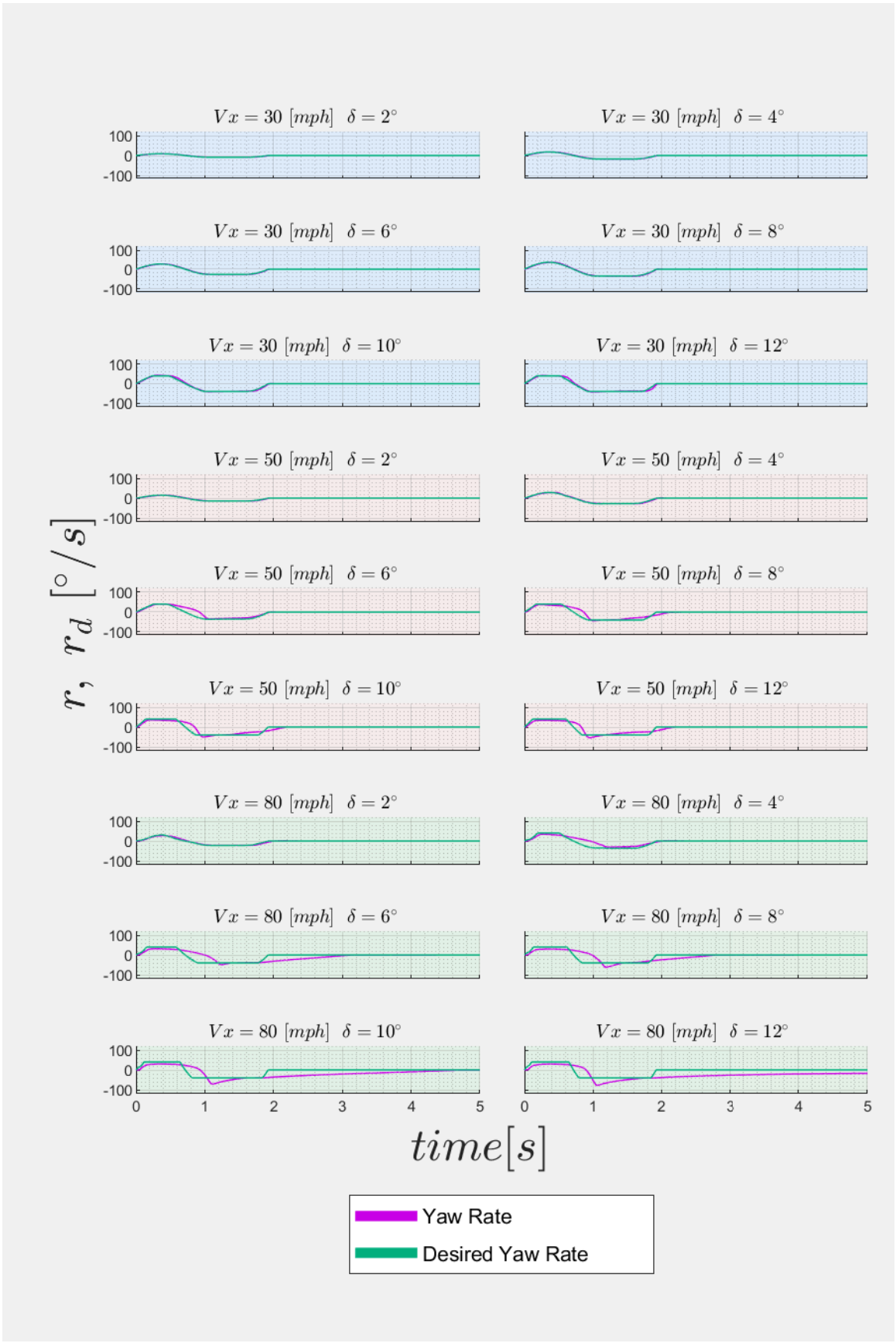

Figure A.14: *SD Test Yaw Errors for SMC ($\delta = 2 - 12$)*

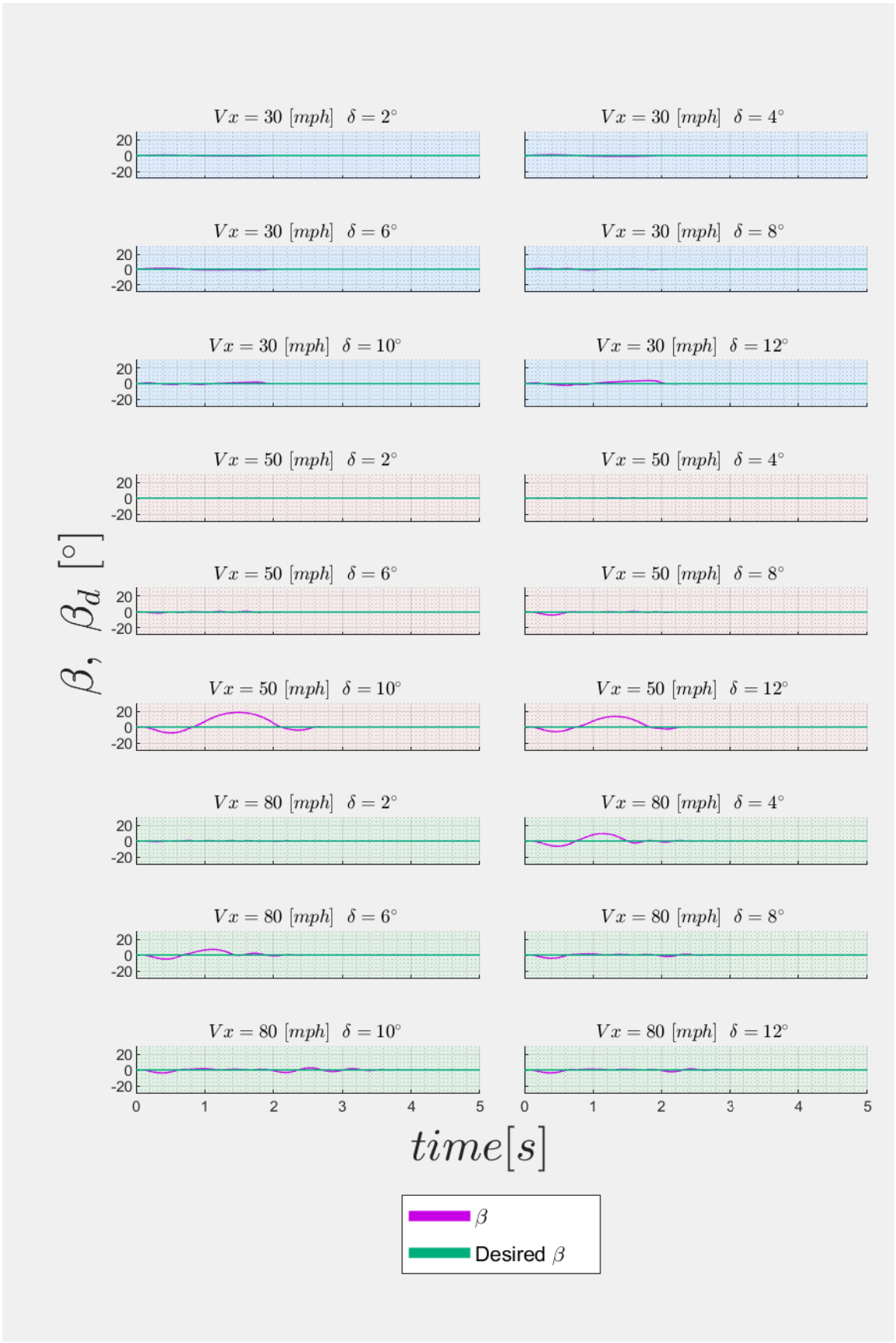

Figure A.15: *SD Test Side Slip Errors for LQR-STA* ($\delta = 2 - 12$)

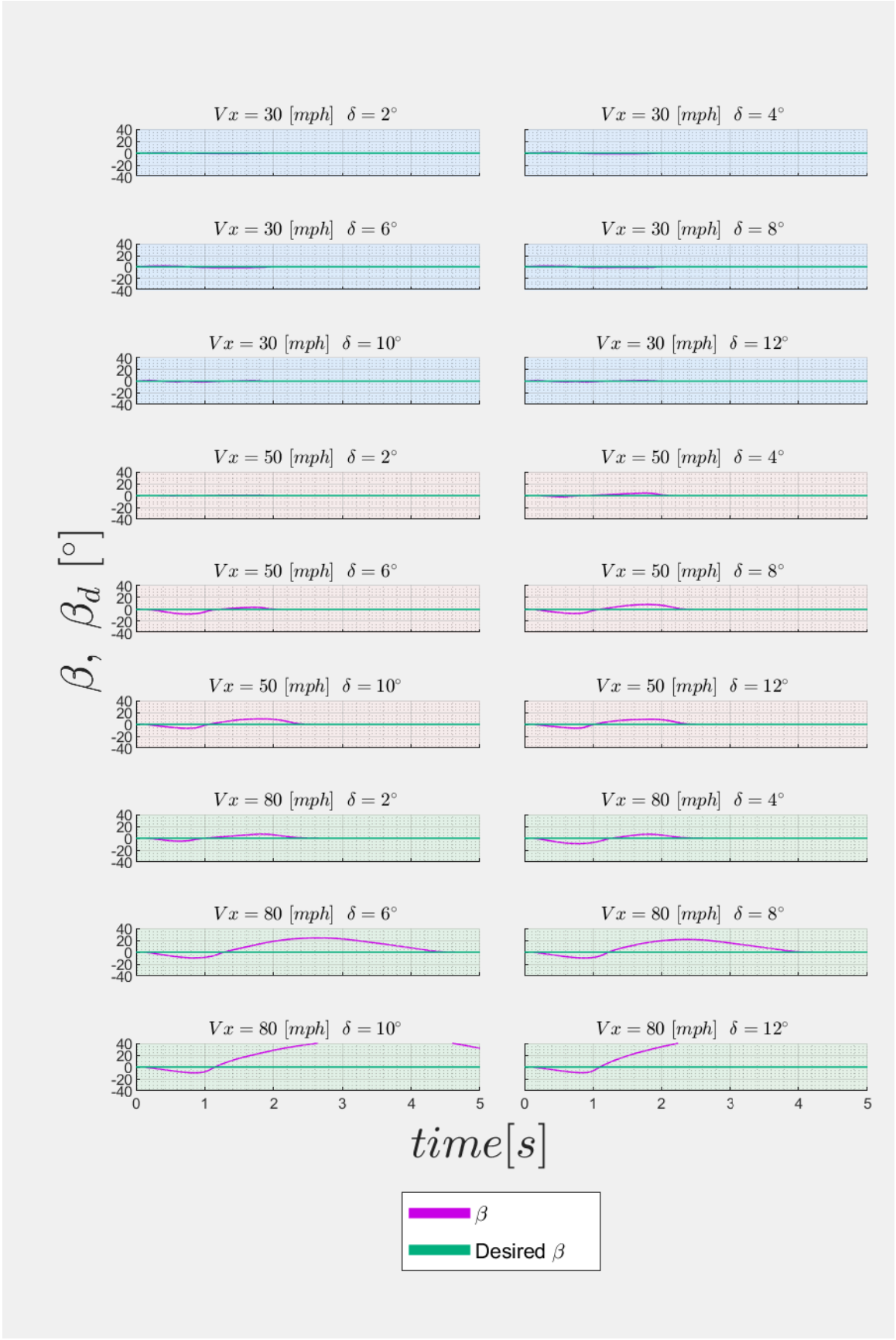

Figure A.16: *SD Test Side Slip Errors for SMC ($\delta = 2 - 12$)*

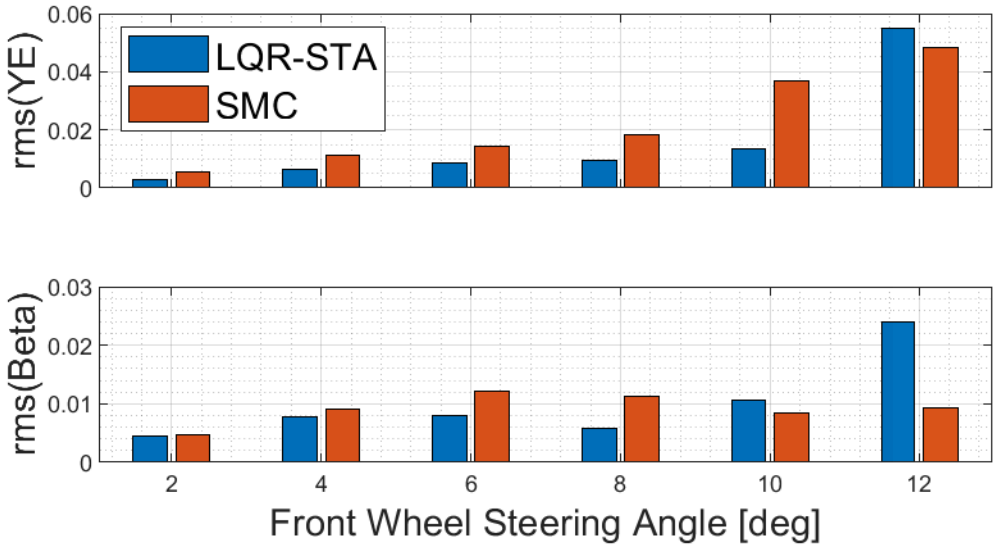

Figure A.17: *SD Test RMS Yaw and Side Slip Errors Comparison Between LQR-STA and SMC at* $V_X = 30$ *and* $\delta = 2 - 12$

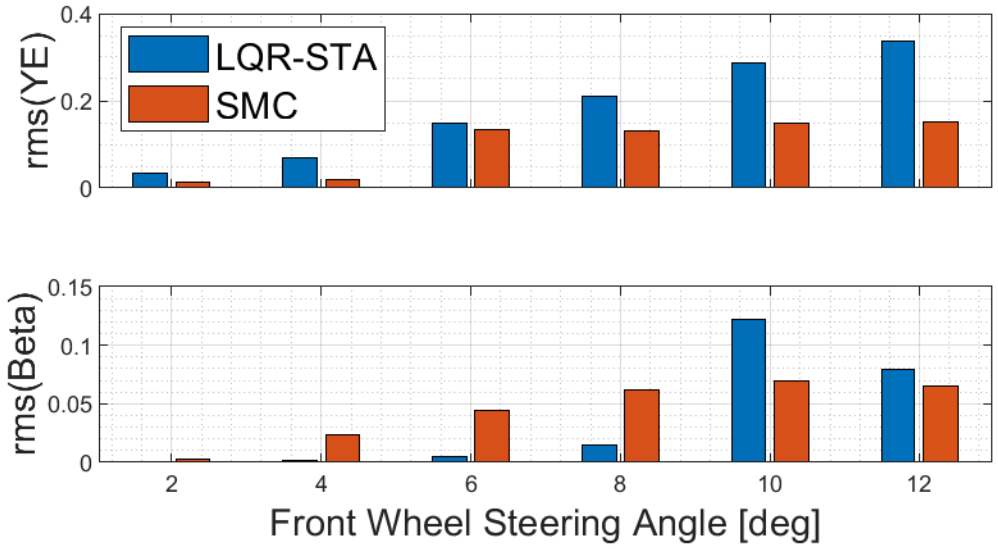

Figure A.18: *SD Test RMS Yaw and Side Slip Errors Comparison Between LQR-STA and SMC at* $V_X = 50$ *and* $\delta = 2 - 12$

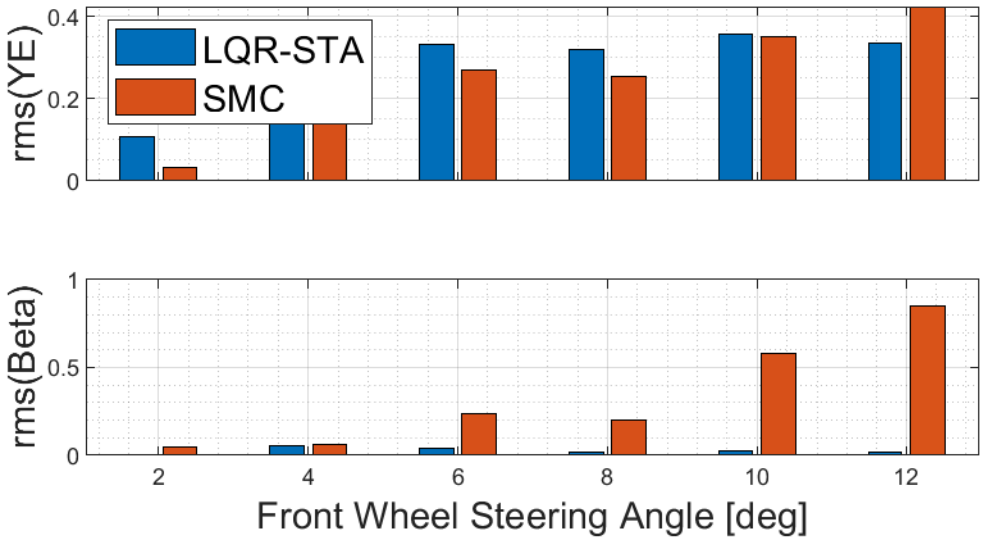

Figure A.19: *SD Test RMS Yaw and Side Slip Errors Comparison Between LQR-STA and SMC at* $V_X = 80$ *and* $\delta = 2 - 12$

A.2 SD Test Figures for Steering Angles 14-24 Degrees

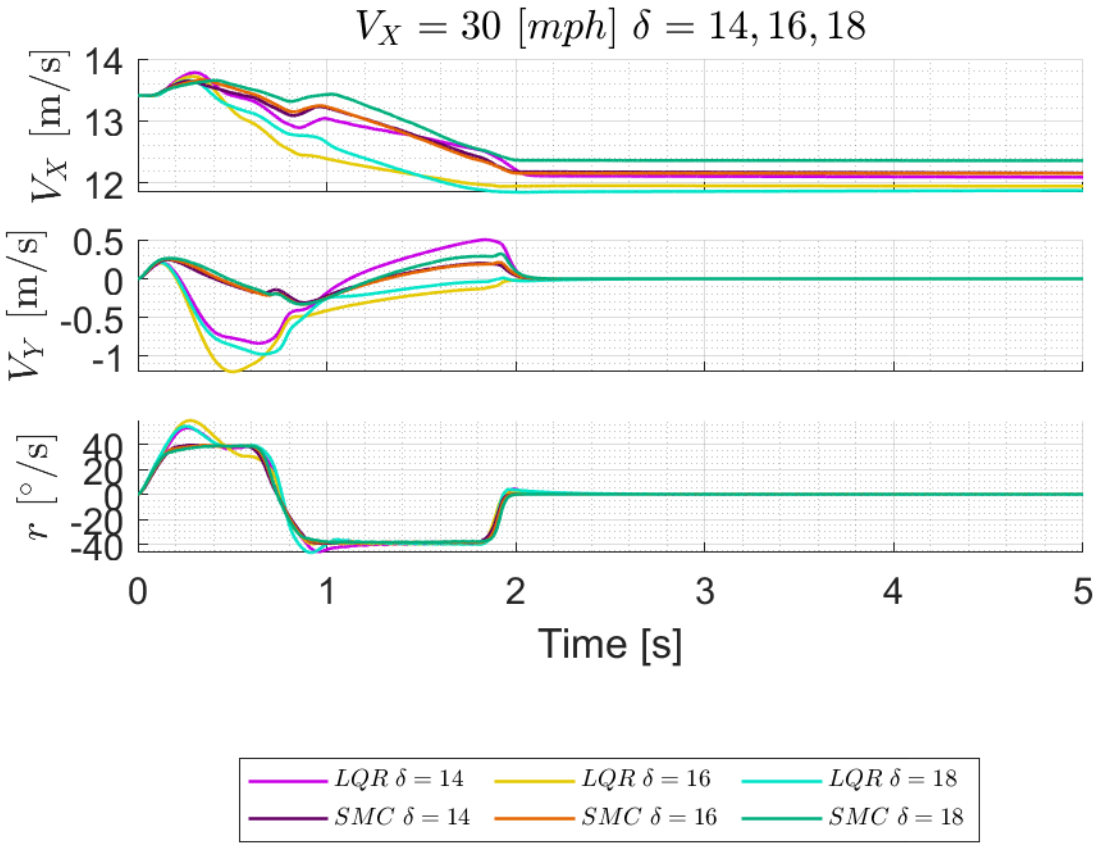

Figure A.20: *SD Test Comparison for LQR-STA and SMC Telemetry at* $V_X = 30$ *and* $\delta = 14, 16, 18$

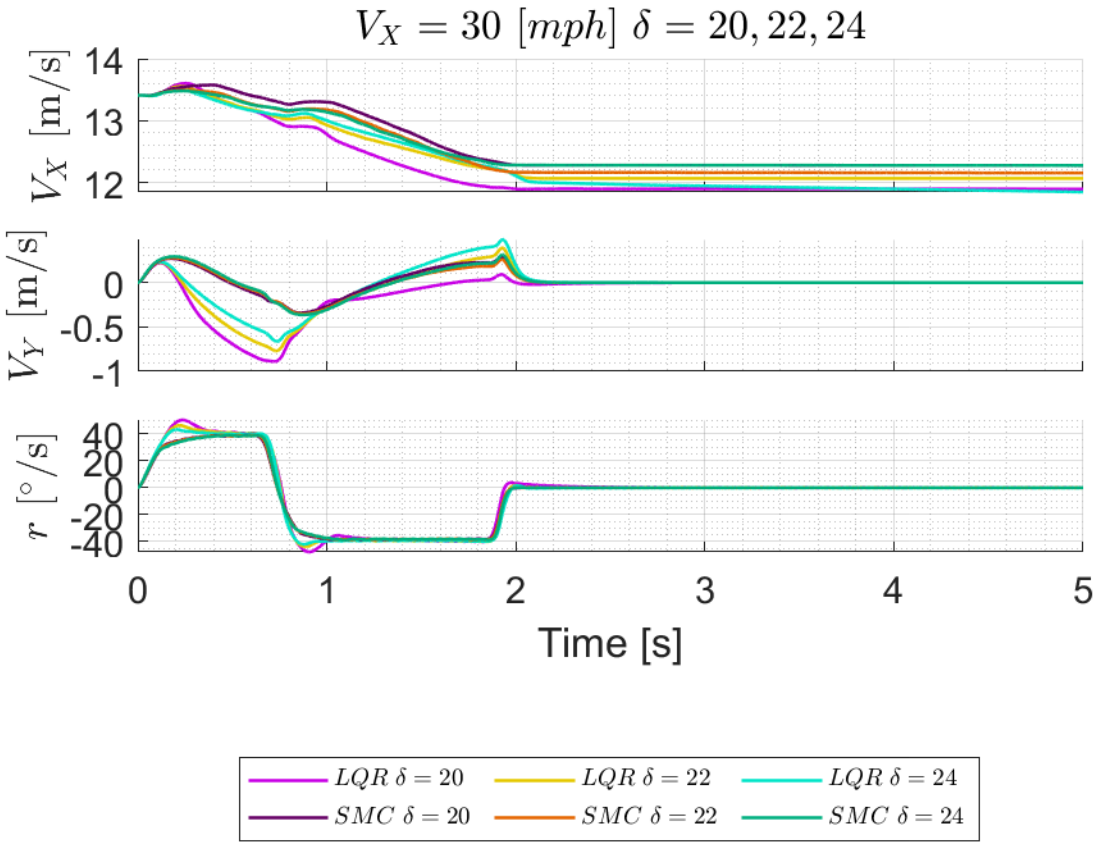

Figure A.21: *SD Test Comparison for LQR-STA and SMC Telemetry at* $V_X = 30$ *and* $\delta = 20, 22, 24$

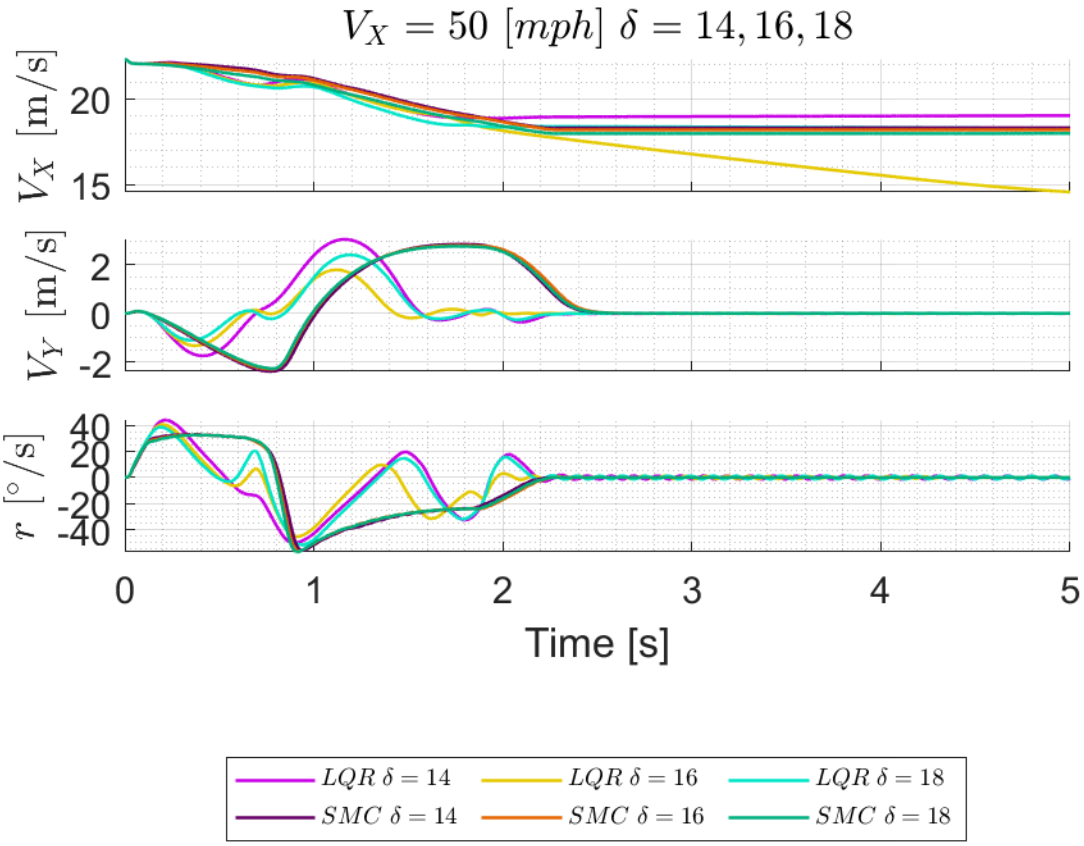

Figure A.22: *SD Test Comparison for LQR-STA and SMC Telemetry at* $V_X = 50$ *and* $\delta = 14, 16, 18$

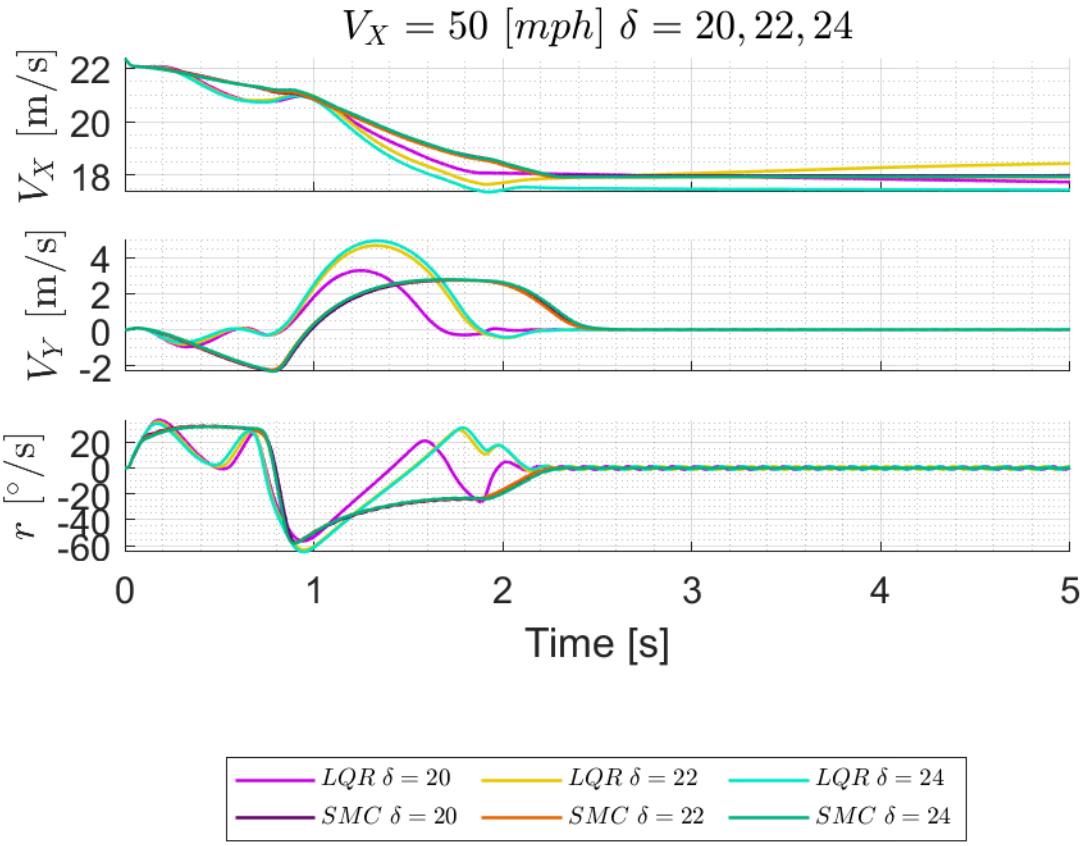

Figure A.23: *SD Test Comparison for LQR-STA and SMC Telemetry at* $V_X = 50$ *and* $\delta = 20, 22, 24$

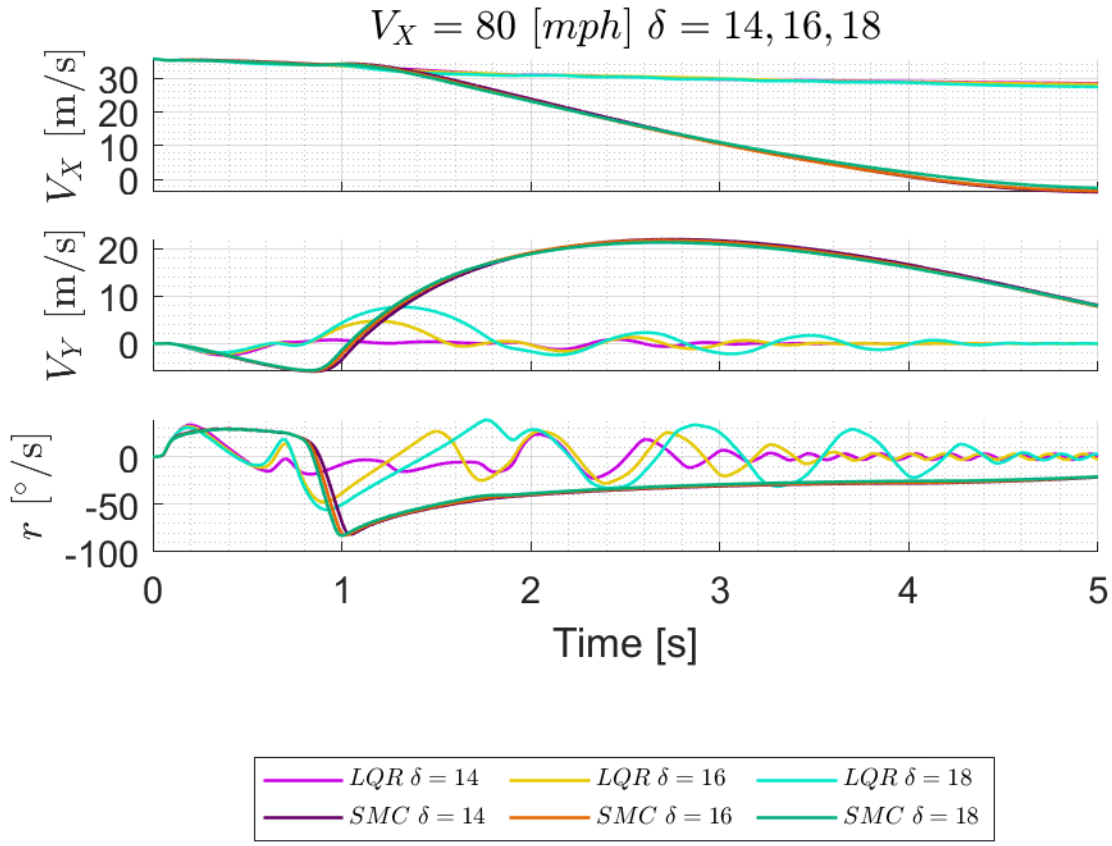

Figure A.24: *SD Test Comparison for LQR-STA and SMC Telemetry at* $V_X = 80$ *and* $\delta = 14, 16, 18$

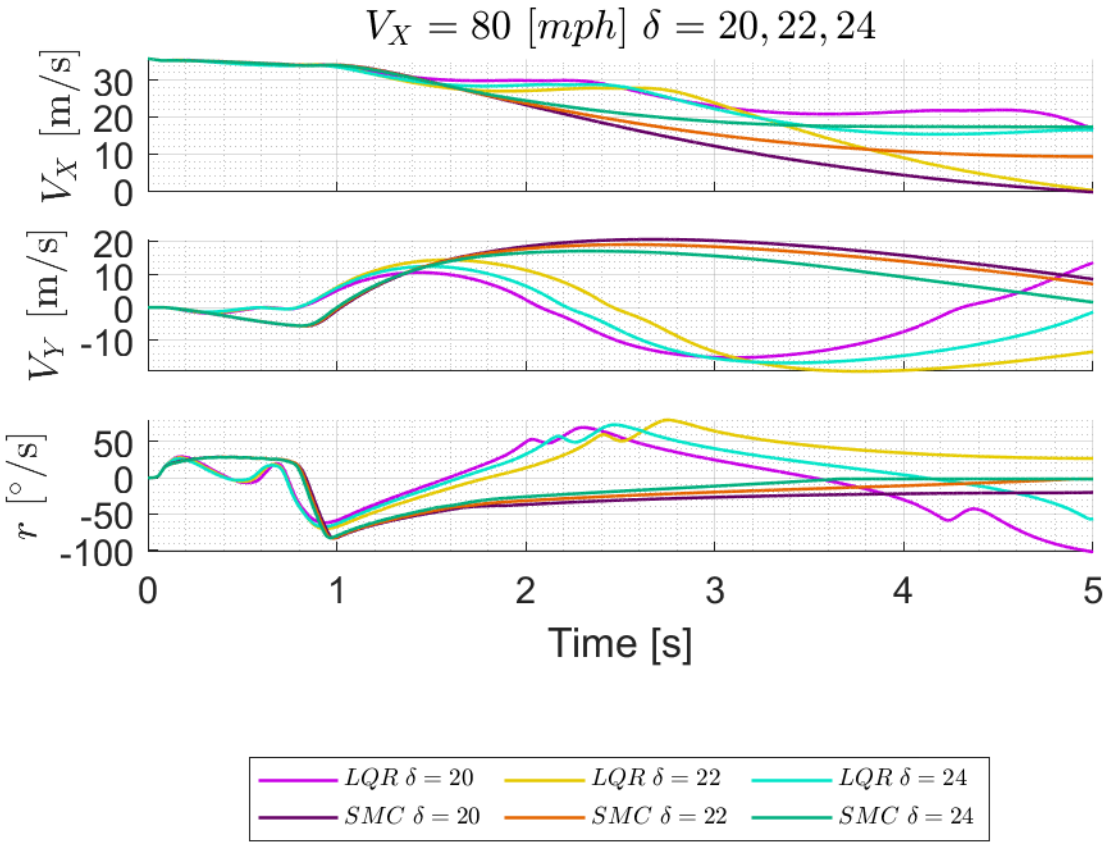

Figure A.25: *SD Test Comparison for LQR-STA and SMC Telemetry at* $V_X = 80$ *and* $\delta = 20, 22, 24$

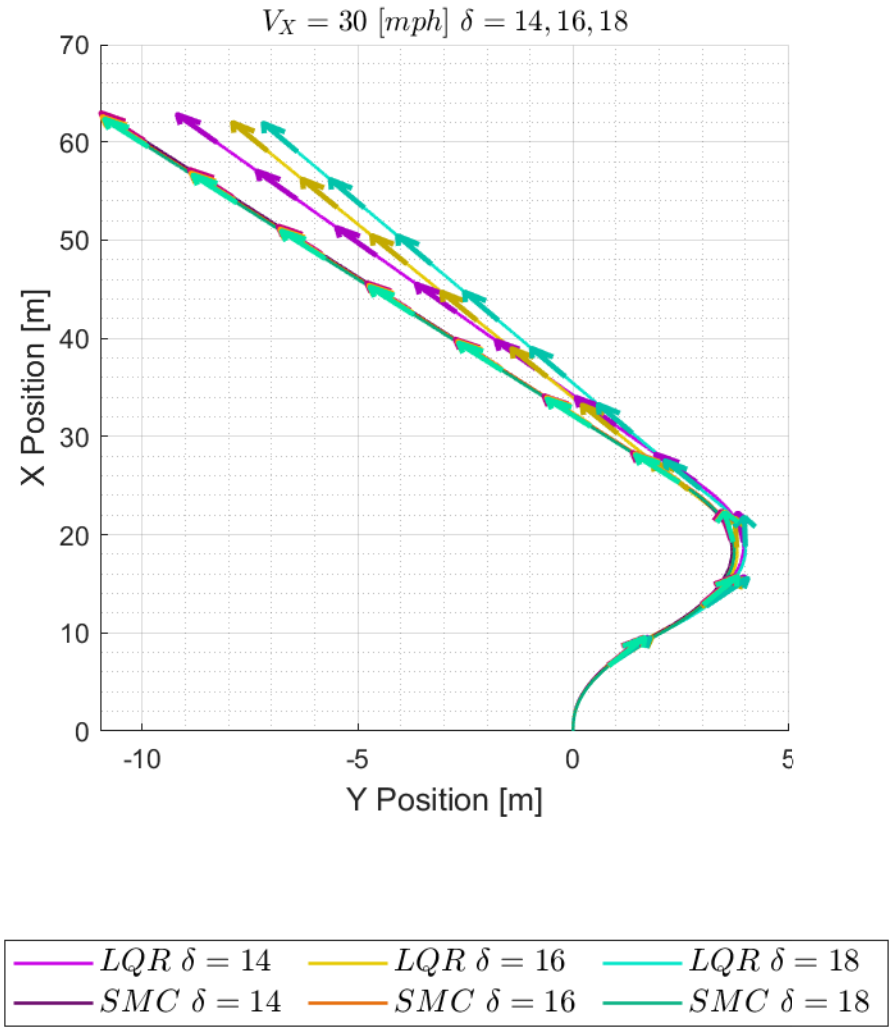

Figure A.26: *SD Test Comparison for LQR-STA and SMC Vehicle Trajectories at* $V_X = 30$ *and* $\delta = 14, 16, 18$

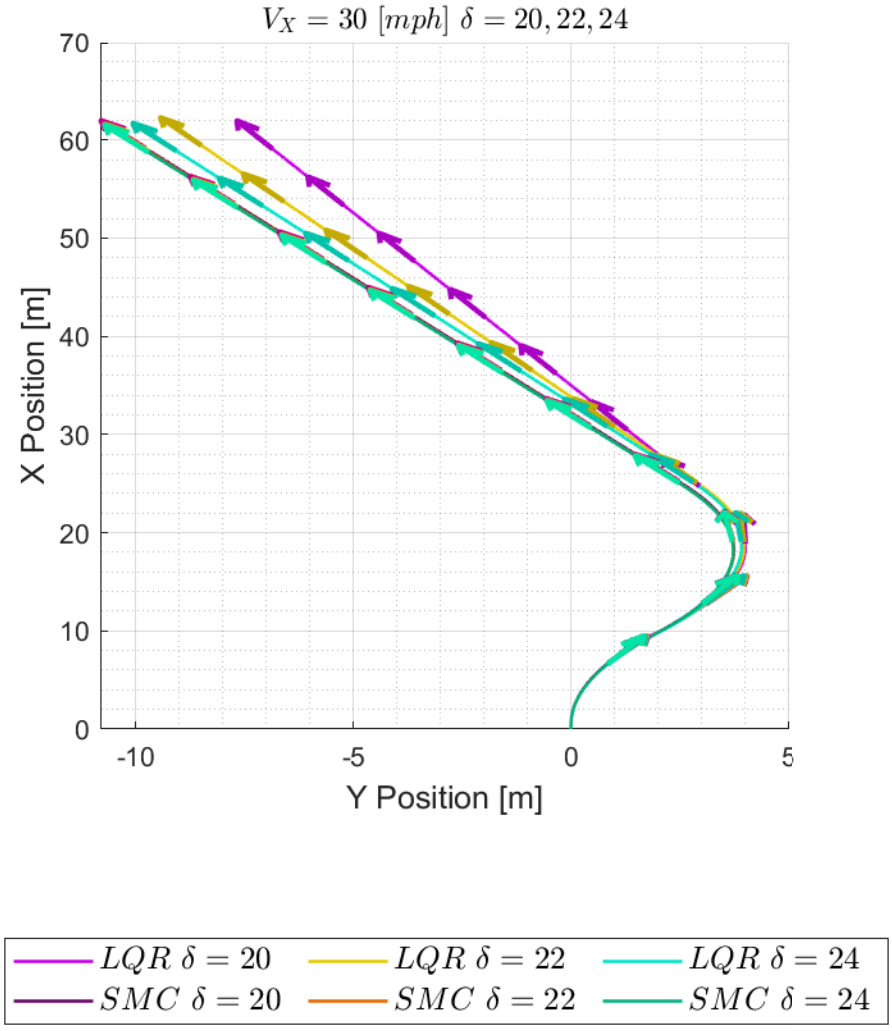

Figure A.27: *SD Test Comparison for LQR-STA and SMC Vehicle Trajectories at* $V_X = 30$ *and* $\delta = 20, 22, 24$

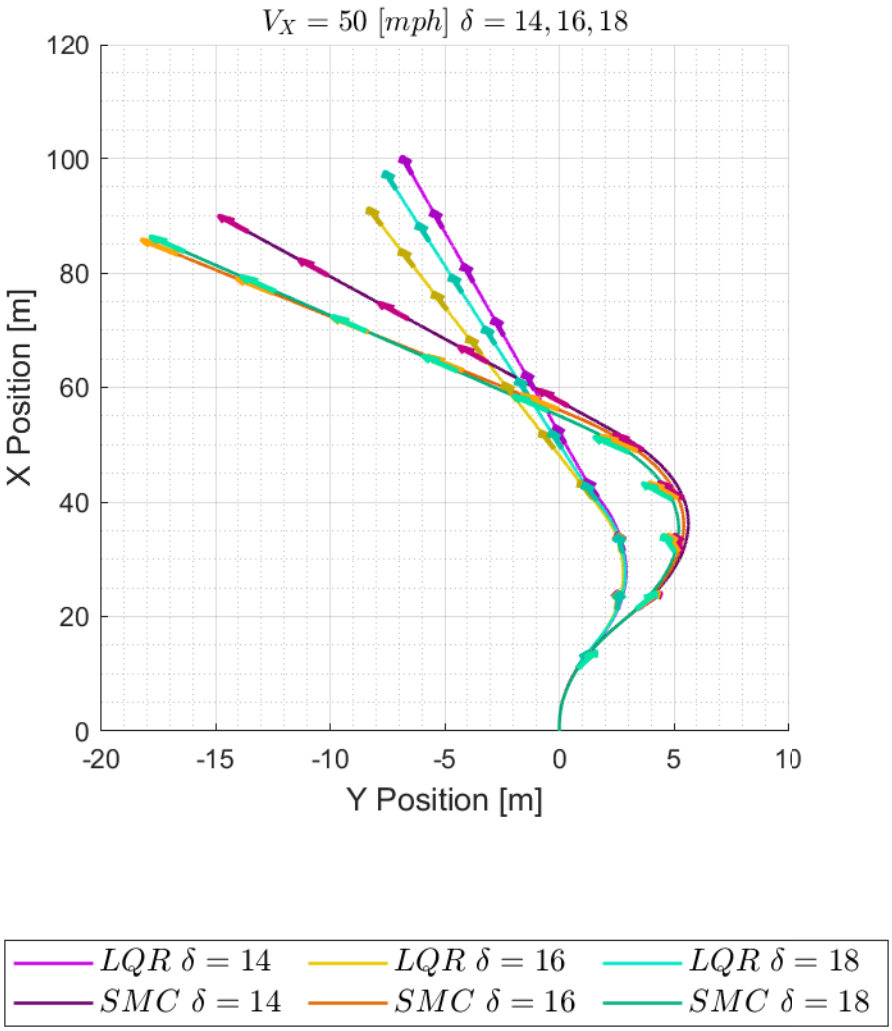

Figure A.28: *SD Test Comparison for LQR-STA and SMC Vehicle Trajectories at* $V_X = 50$ *and* $\delta = 14, 16, 18$

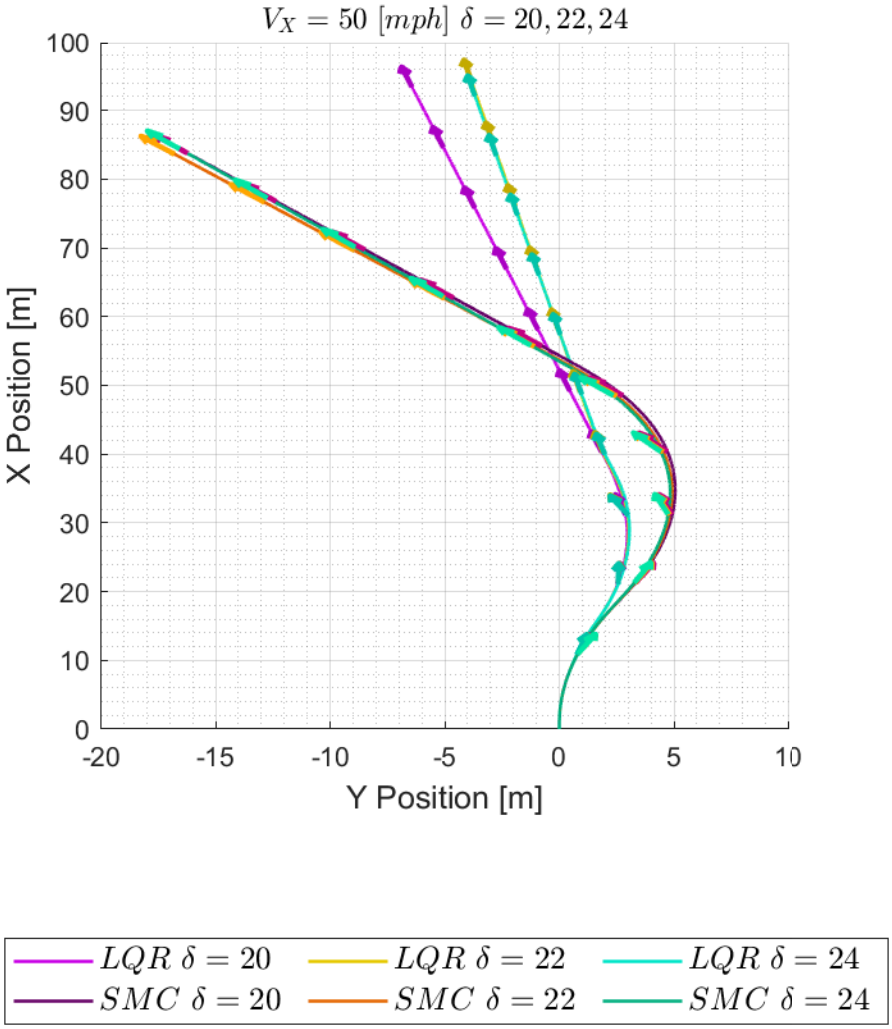

Figure A.29: *SD Test Comparison for LQR-STA and SMC Vehicle Trajectories at* $V_X = 50$ *and* $\delta = 20, 22, 24$

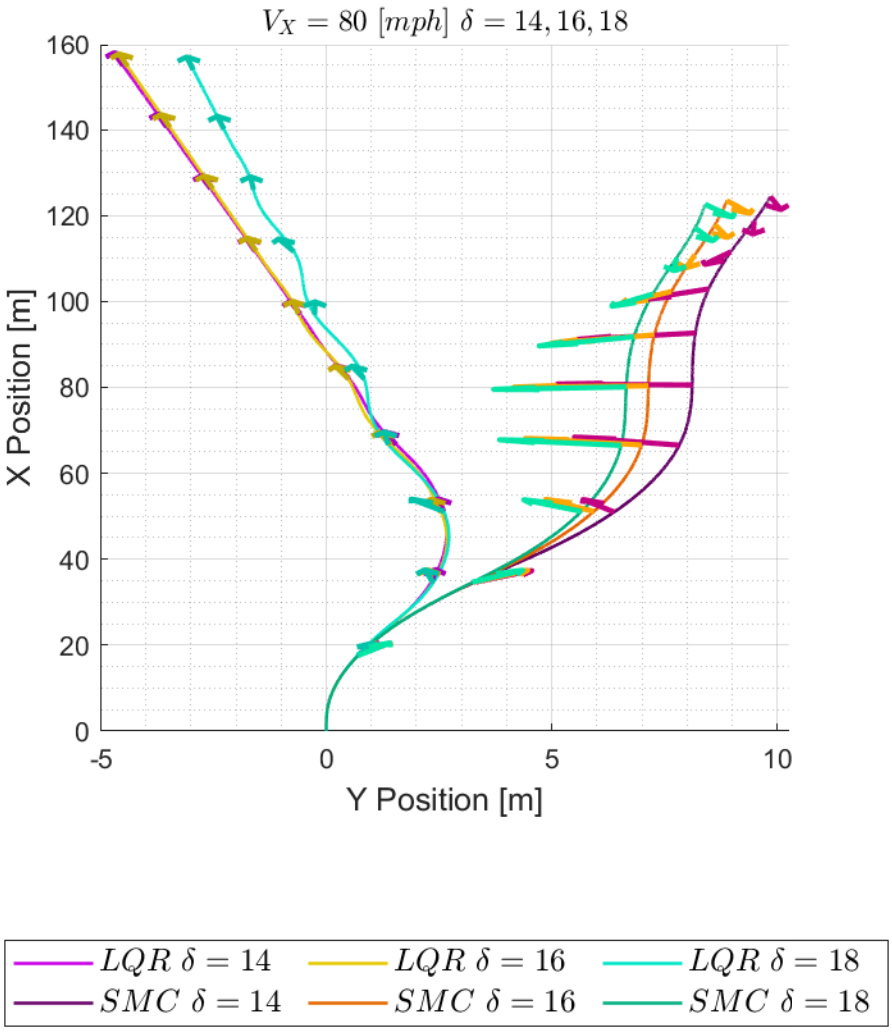

Figure A.30: *SD Test Comparison for LQR-STA and SMC Vehicle Trajectories at* $V_X = 80$ *and* $\delta = 14, 16, 18$

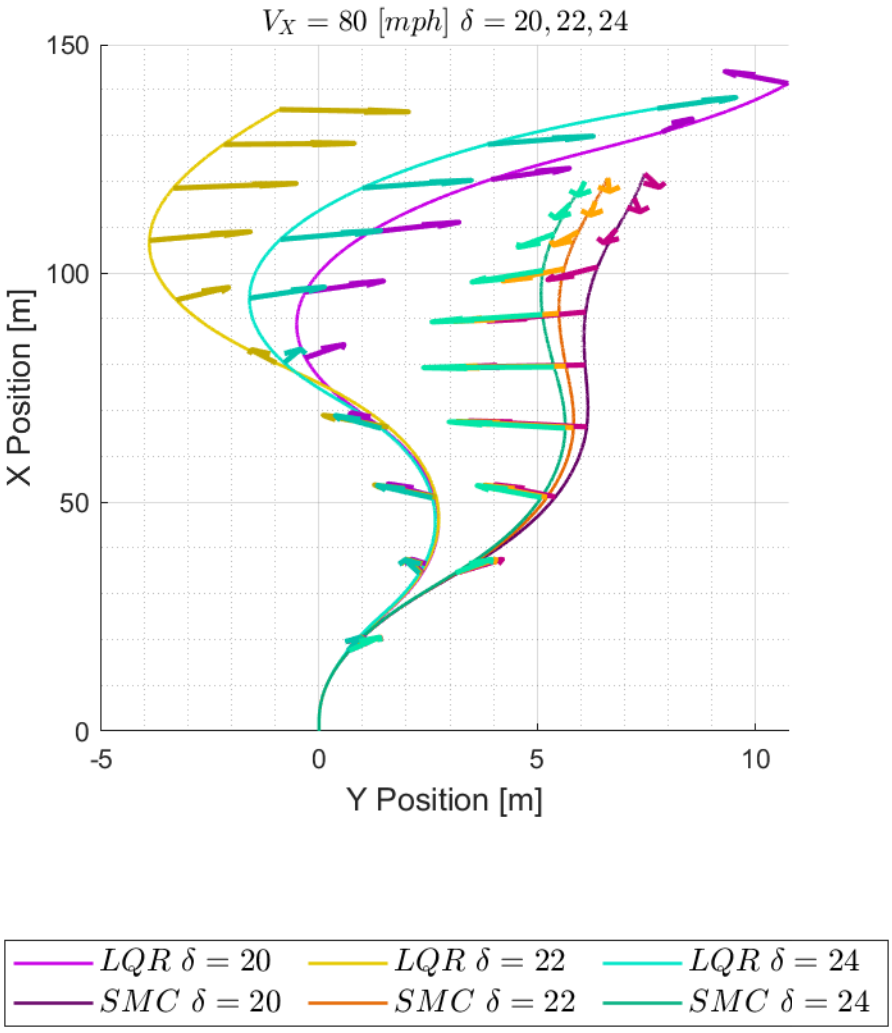

Figure A.31: *SD Test Comparison for LQR-STA and SMC Vehicle Trajectories at* $V_X = 80$ *and* $\delta = 20, 22, 24$

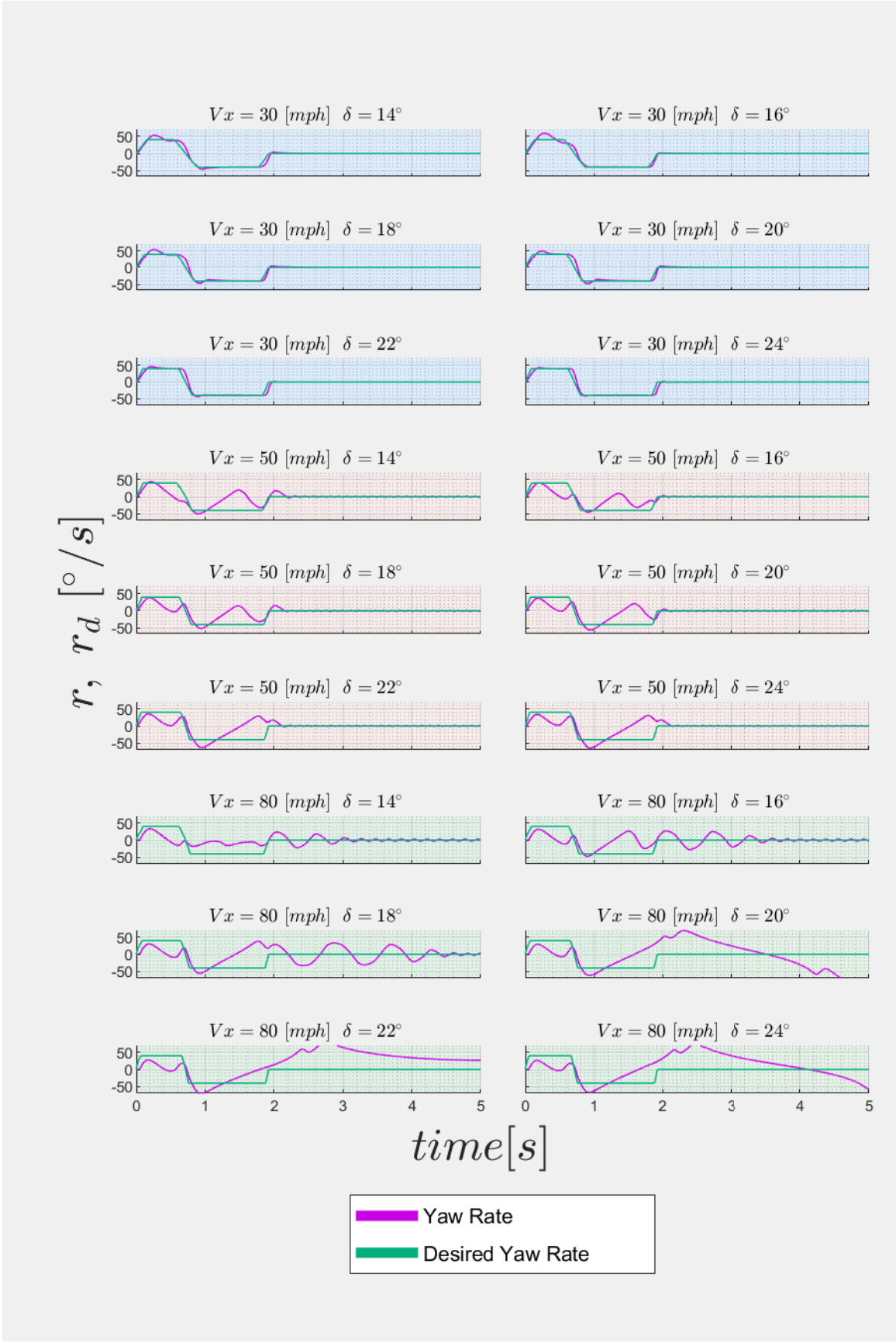

Figure A.32: *SD Test Yaw Errors for LQR-STA* ($\delta = 14 - 24$)

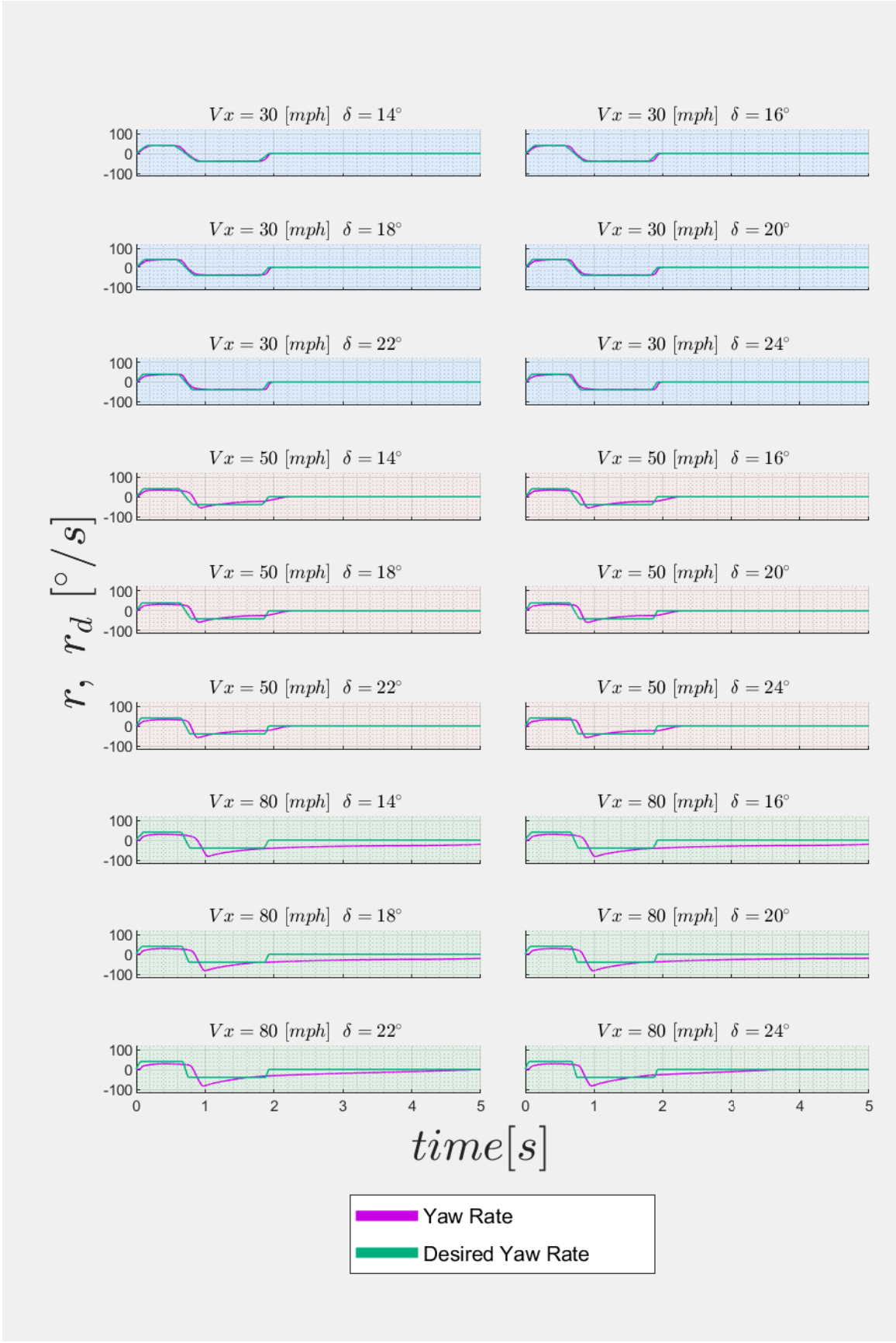

Figure A.33: *SD Test Yaw Errors for SMC ($\delta = 14 - 24$)*

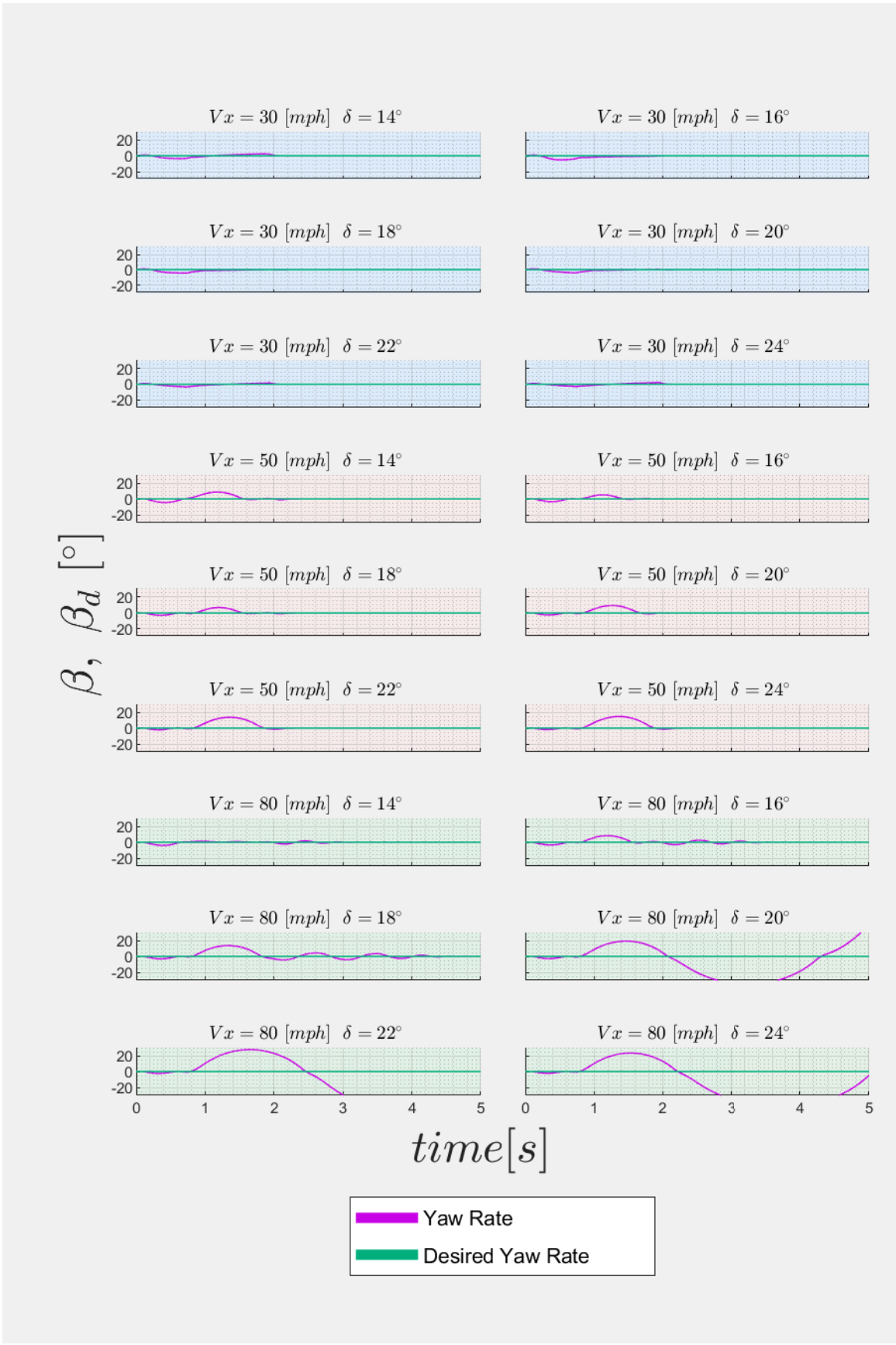

Figure A.34: *SD Test Side Slip Errors for LQR-STA* ($\delta = 14 - 24$)

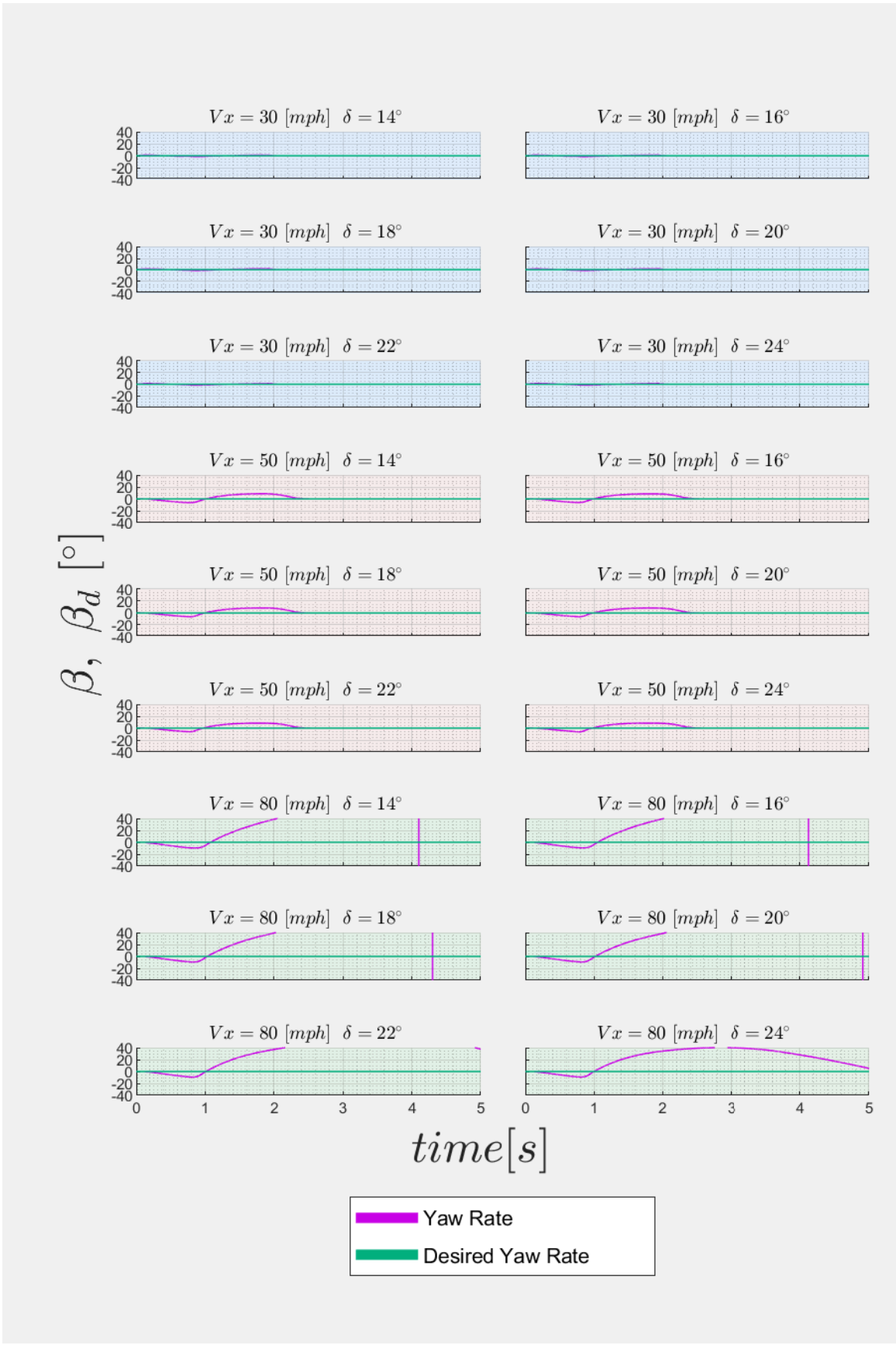

Figure A.35: *SD Test Side Slip Errors for SMC ($\delta = 14 - 24$)*

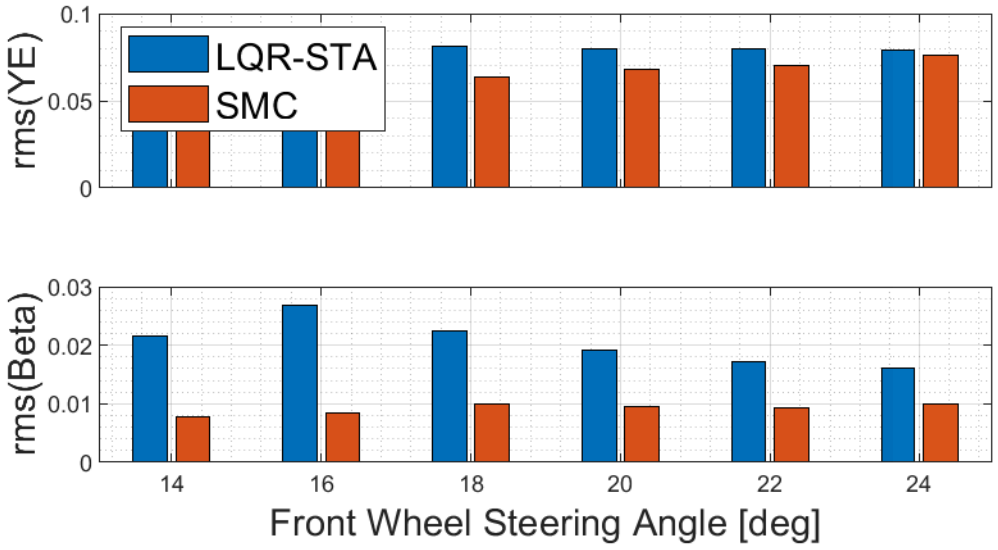

Figure A.36: *SD Test RMS Yaw and Side Slip Errors Comparison Between LQR-STA and SMC at* $V_X = 30$ *and* $\delta = 14 - 24$

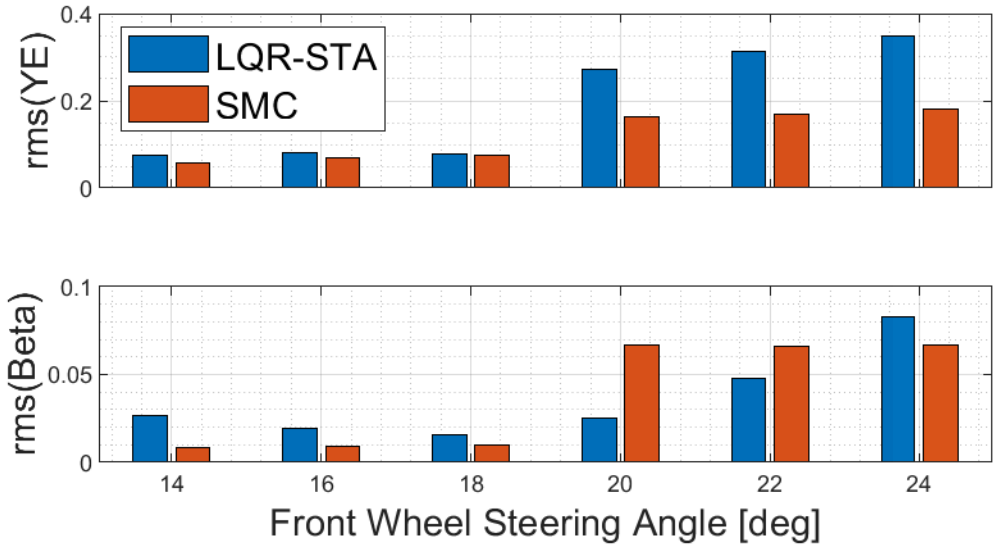

Figure A.37: *SD Test RMS Yaw and Side Slip Errors Comparison Between LQR-STA and SMC at* $V_X = 50$ *and* $\delta = 14 - 24$

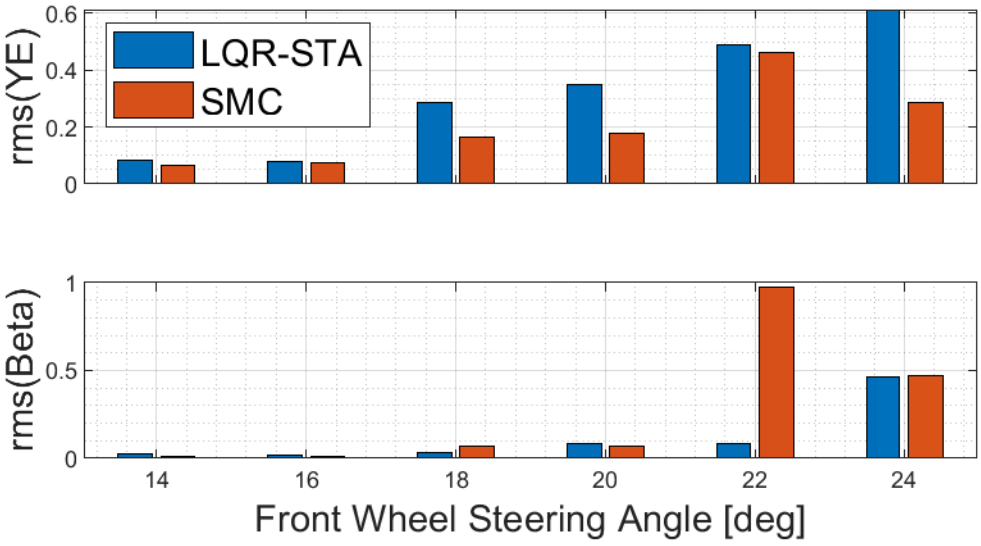

Figure A.38: *SD Test RMS Yaw and Side Slip Errors Comparison Between LQR-STA and SMC at* $V_X = 80$ *and* $\delta = 14 - 24$

A.3 CSA Test Figures for Steering Angles 2-12 Degrees

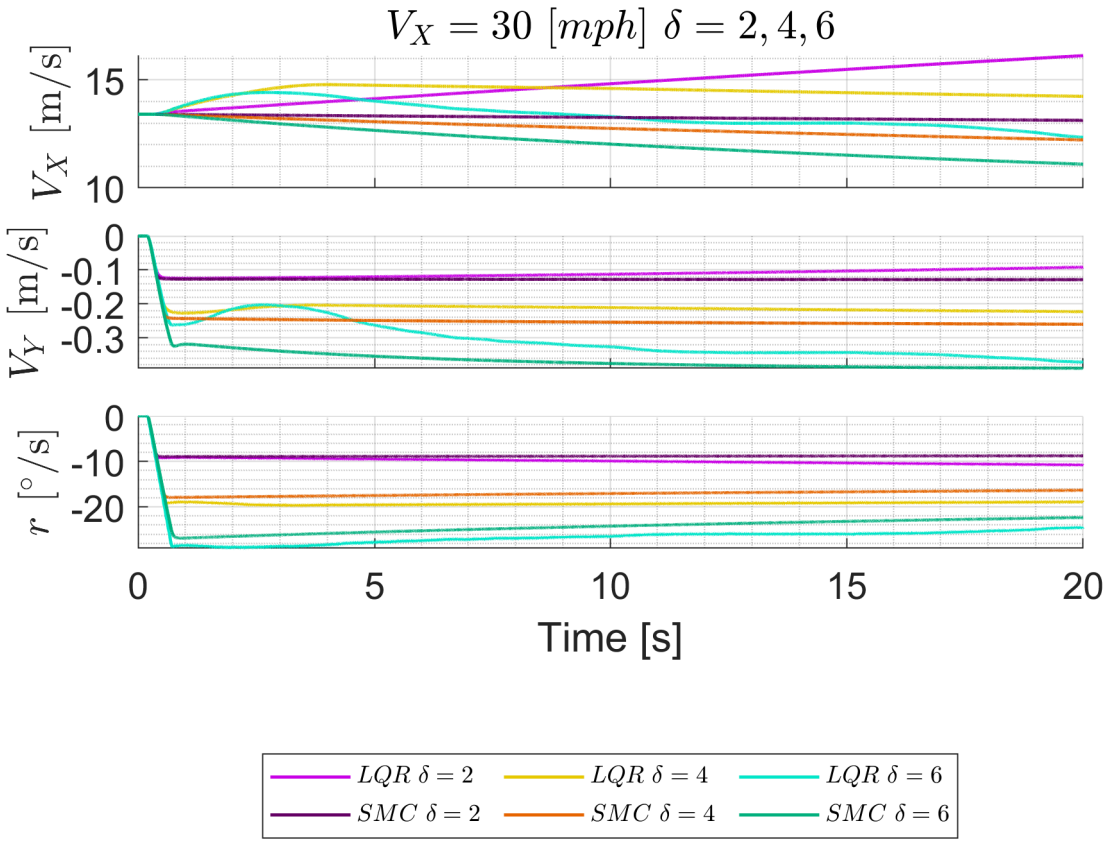

Figure A.39: *CSA Test Comparison for LQR-STA and SMC Telemetry at* $V_X = 30$ *and* $\delta = 2, 4, 6$

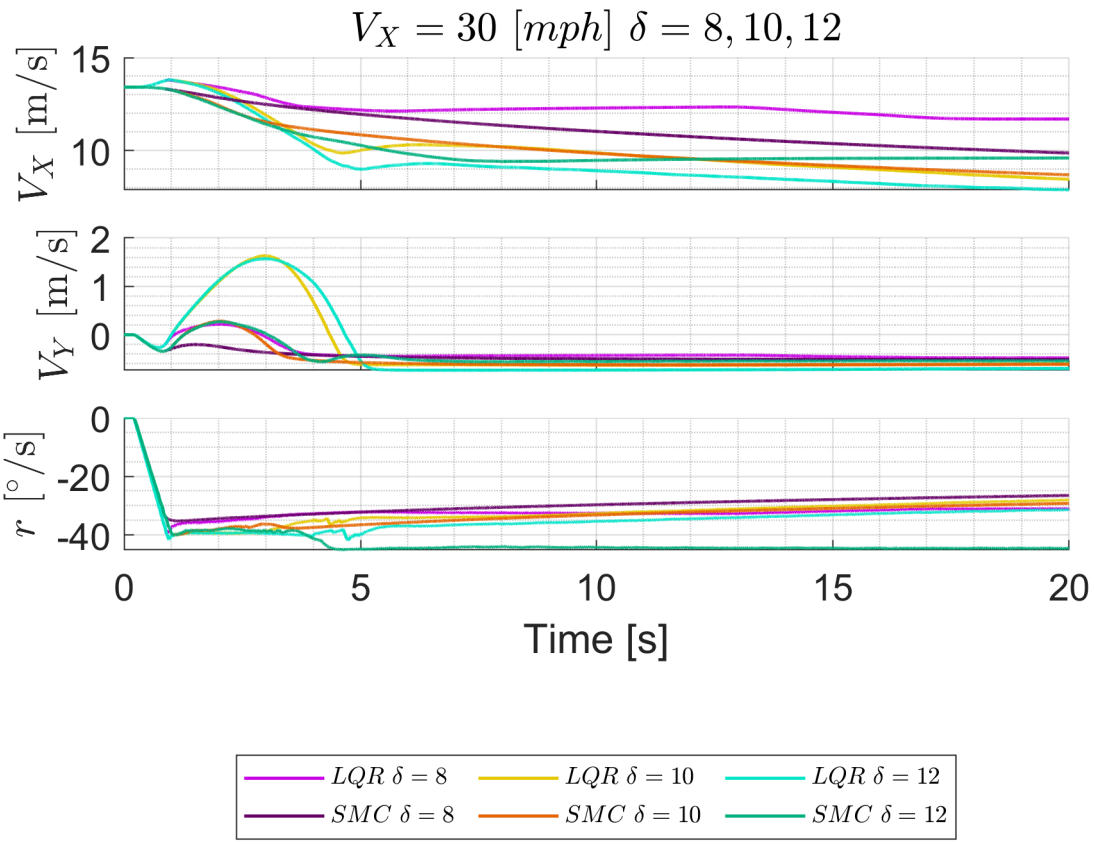

Figure A.40: *CSA Test Comparison for LQR-STA and SMC Telemetry at* $V_X = 30$ *and* $\delta = 8, 10, 12$

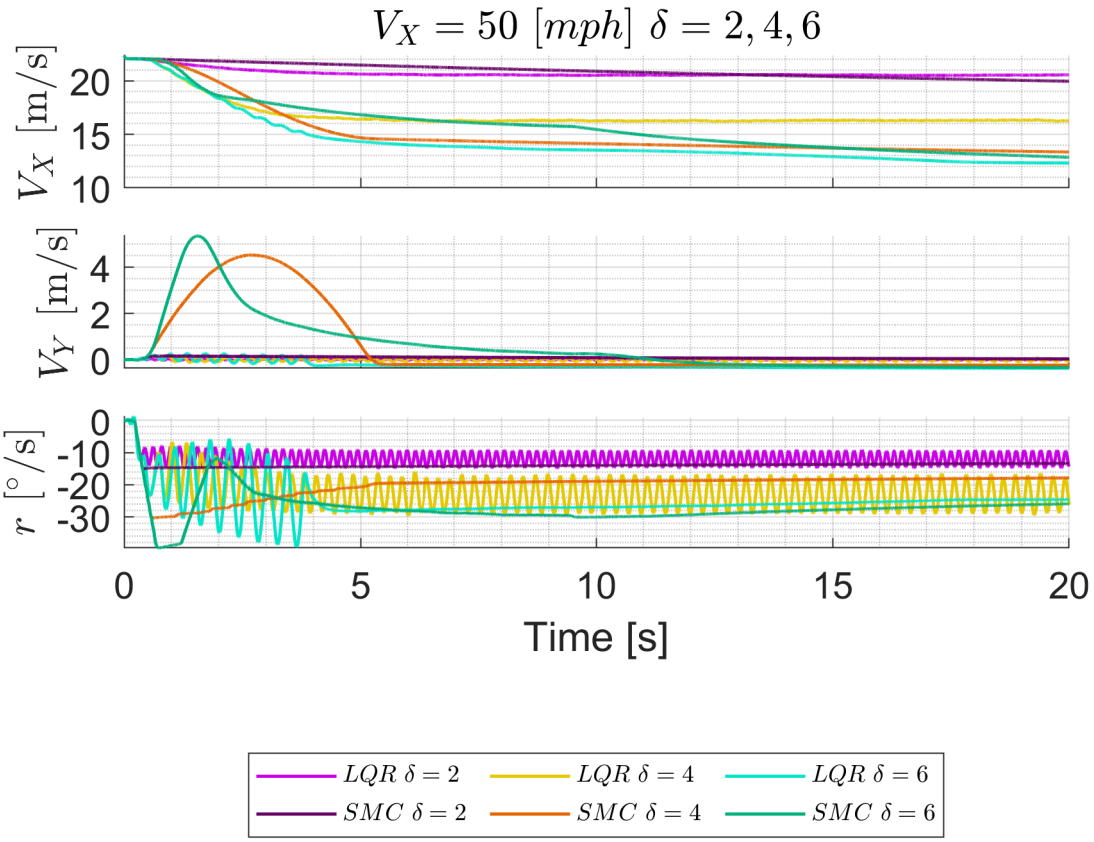

Figure A.41: *CSA Test Comparison for LQR-STA and SMC Telemetry at* $V_X = 50$ *and* $\delta = 2, 4, 6$

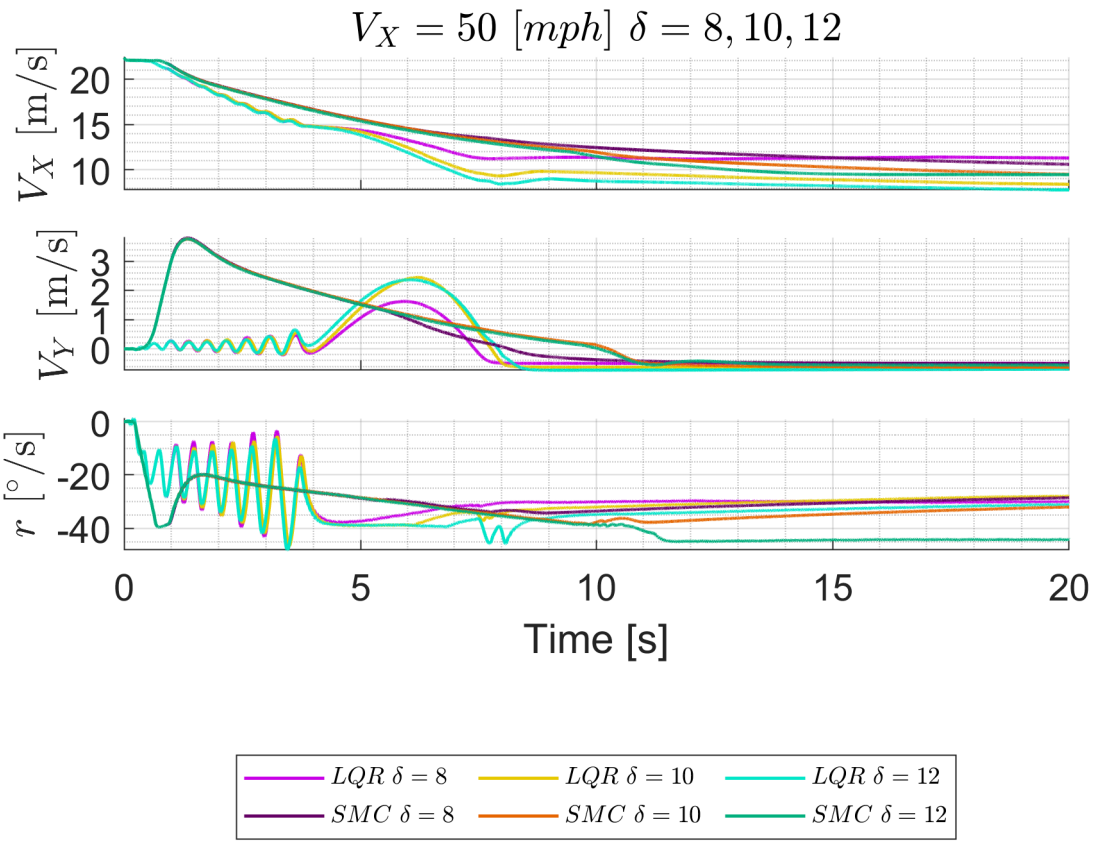

Figure A.42: *CSA Test Comparison for LQR-STA and SMC Telemetry at* $V_X = 50$ *and* $\delta = 8, 10, 12$

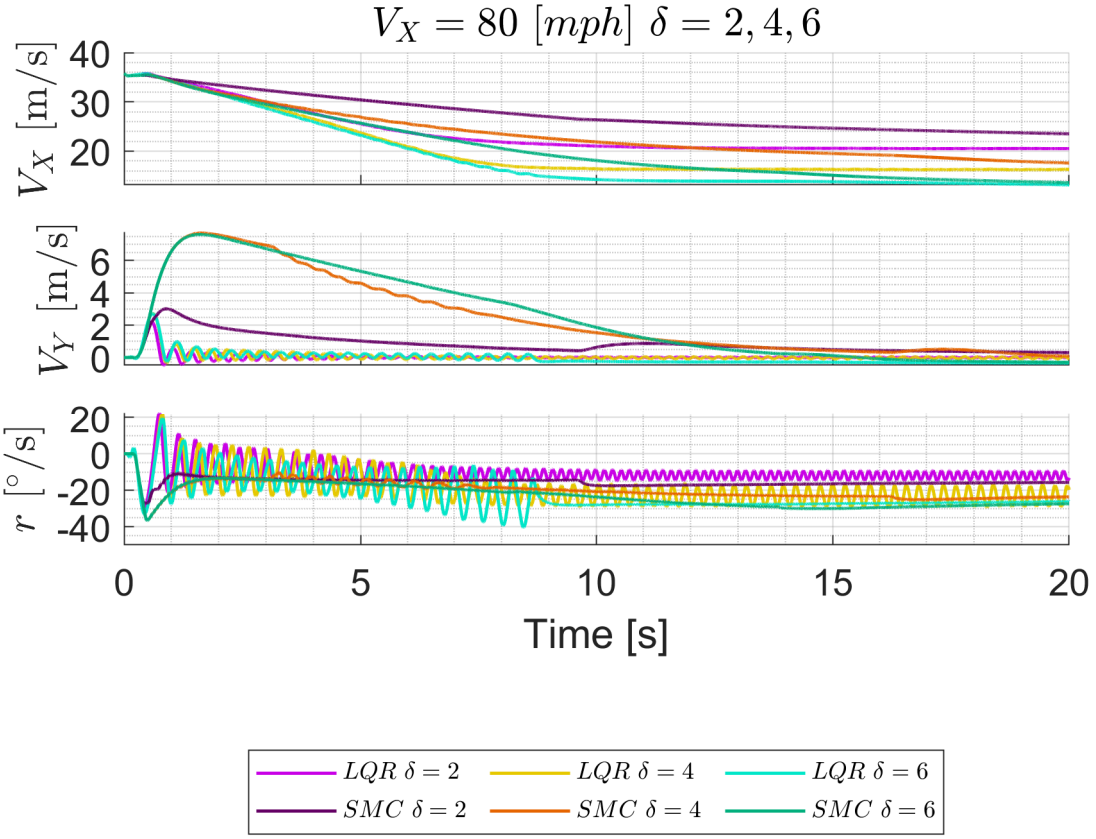

Figure A.43: *CSA Test Comparison for LQR-STA and SMC Telemetry at* $V_X = 80$ *and* $\delta = 2, 4, 6$

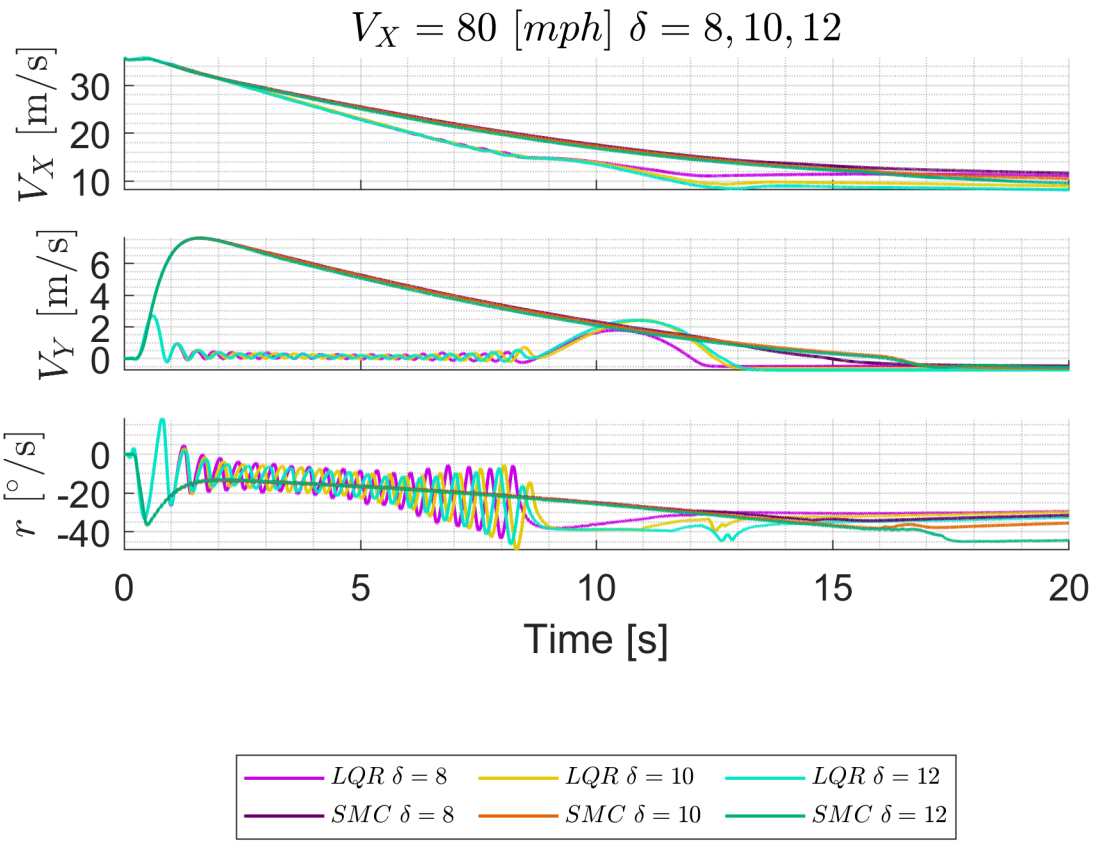

Figure A.44: *CSA Test Comparison for LQR-STA and SMC Telemetry at* $V_X = 80$ *and* $\delta = 8, 10, 12$

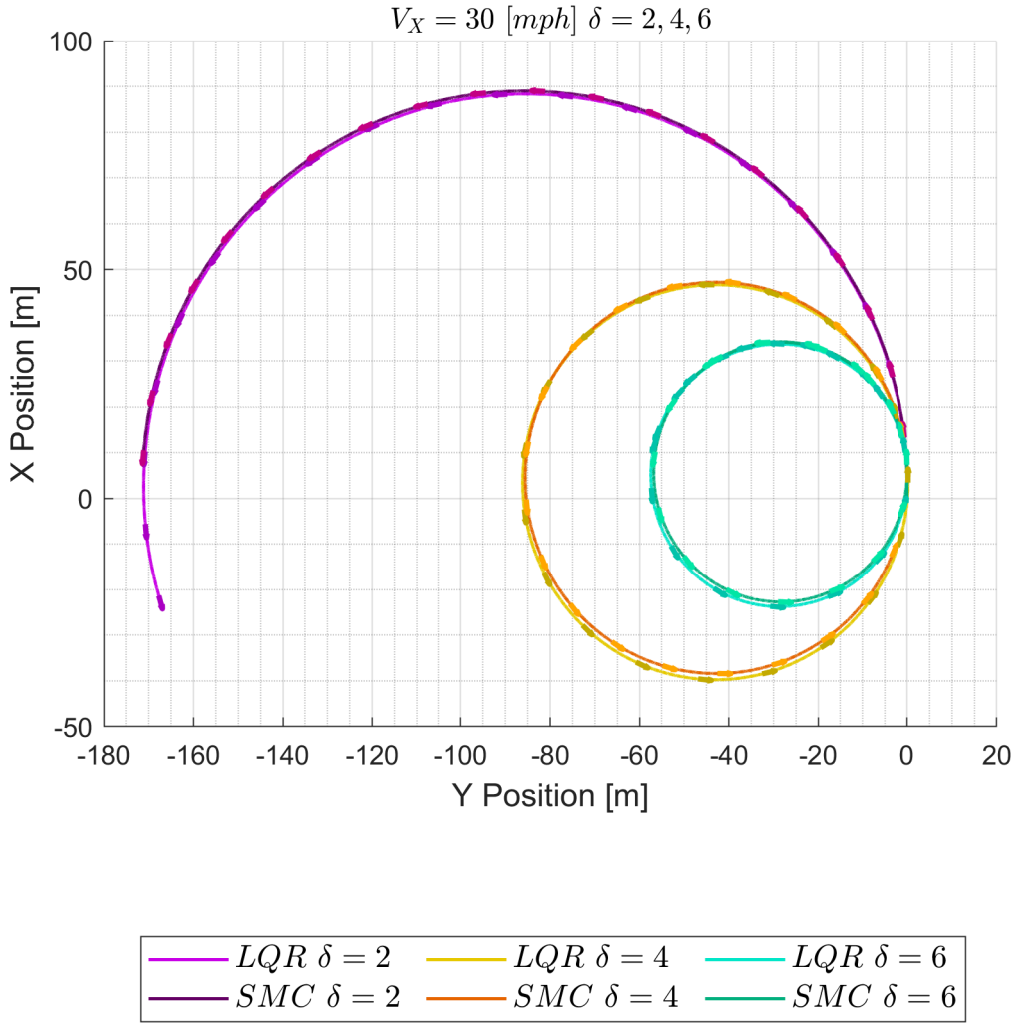

Figure A.45: *CSA Test Comparison for LQR-STA and SMC Vehicle Trajectories at* $V_X = 30$ *and* $\delta = 2, 4, 6$

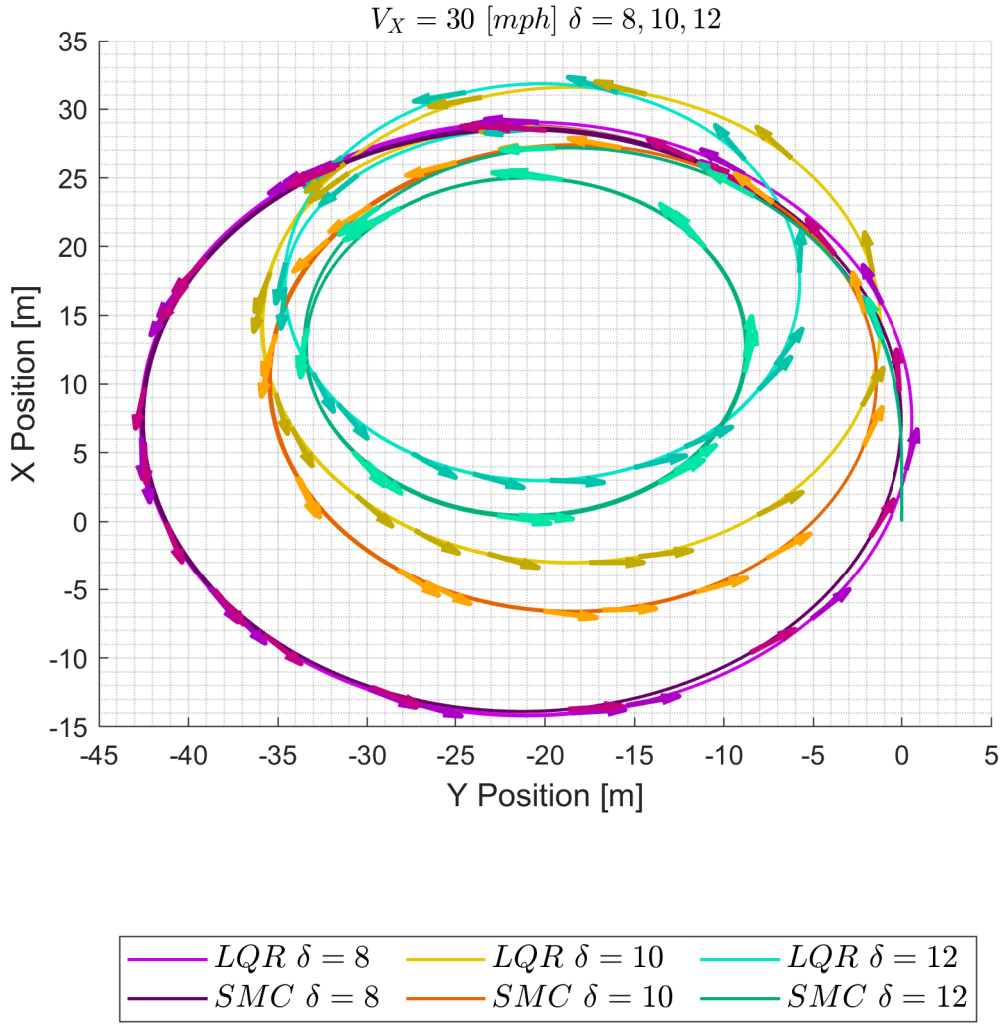

Figure A.46: *CSA Test Comparison for LQR-STA and SMC Vehicle Trajectories at* $V_X = 30$ *and* $\delta = 8, 10, 12$

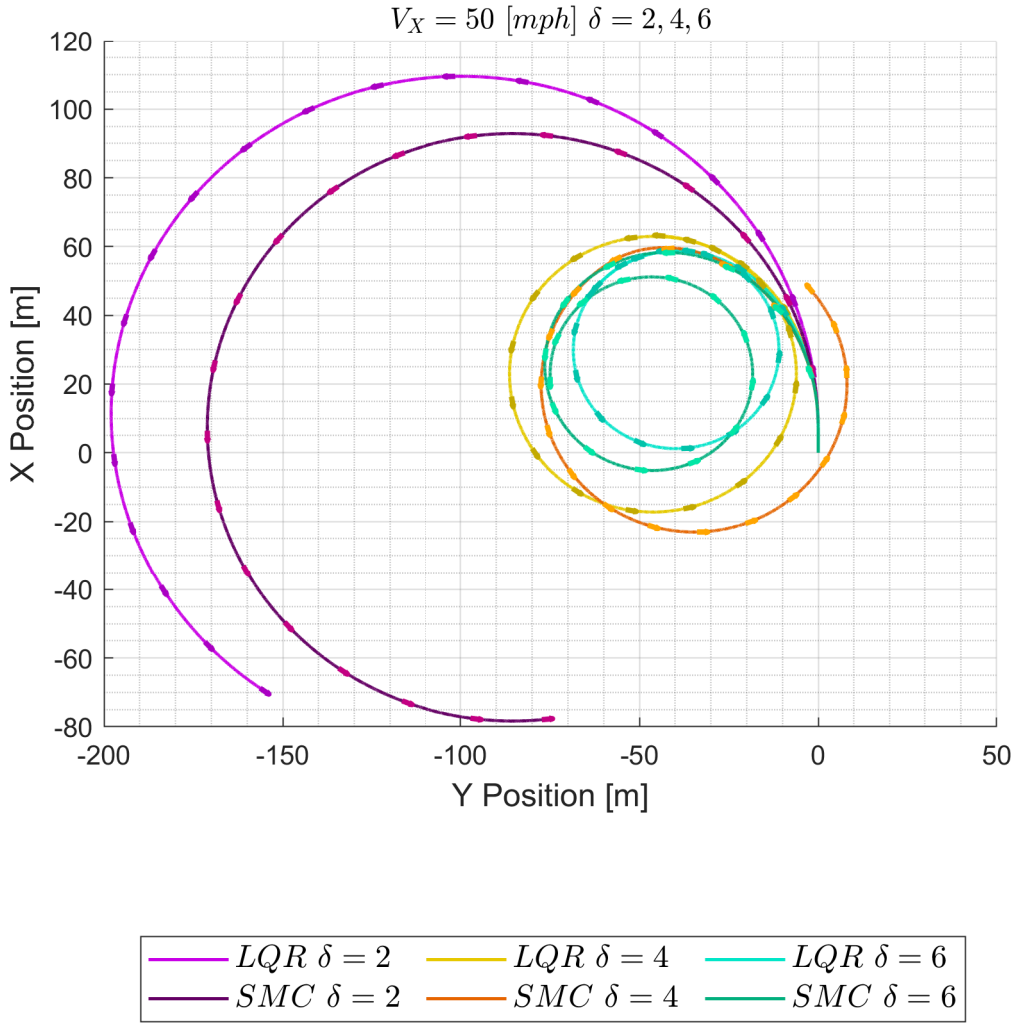

Figure A.47: *CSA Test Comparison for LQR-STA and SMC Vehicle Trajectories at* $V_X = 50$ *and* $\delta = 2, 4, 6$

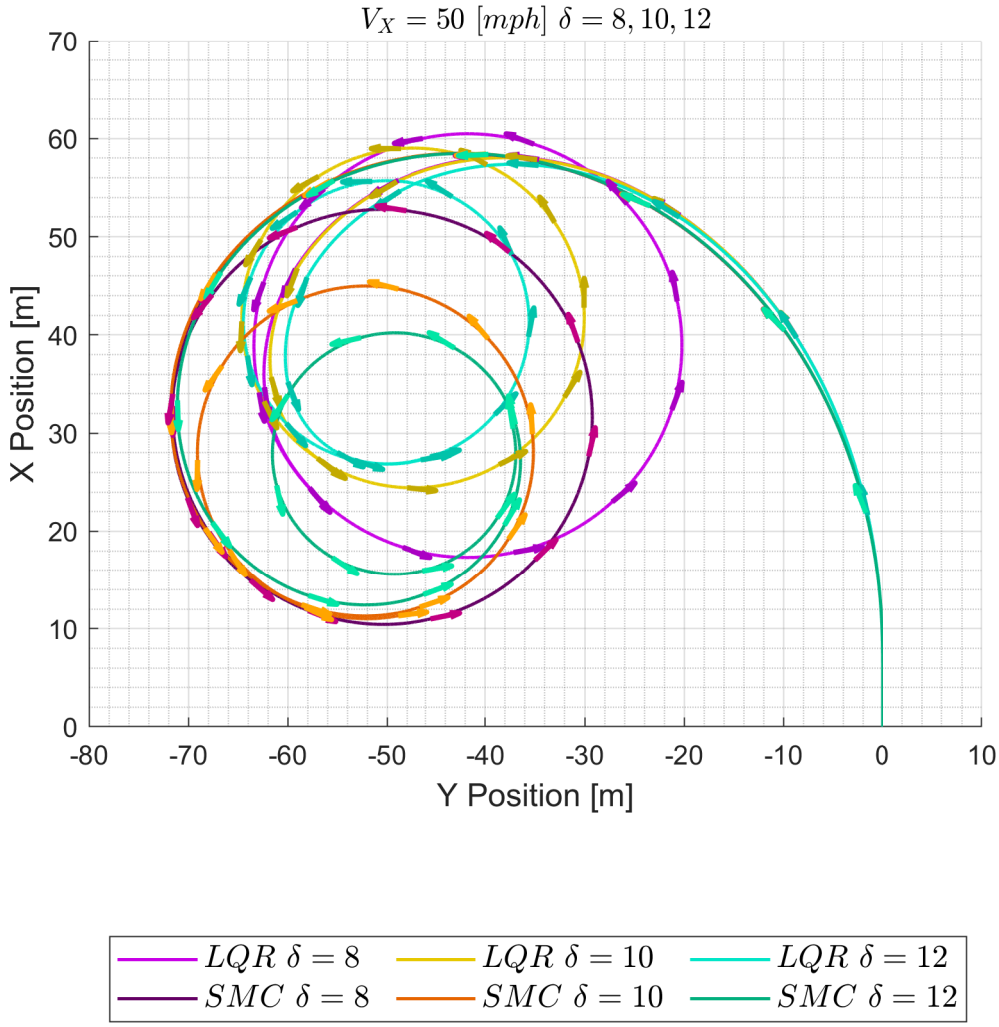

Figure A.48: *CSA Test Comparison for LQR-STA and SMC Vehicle Trajectories at* $V_X = 50$ *and* $\delta = 8, 10, 12$

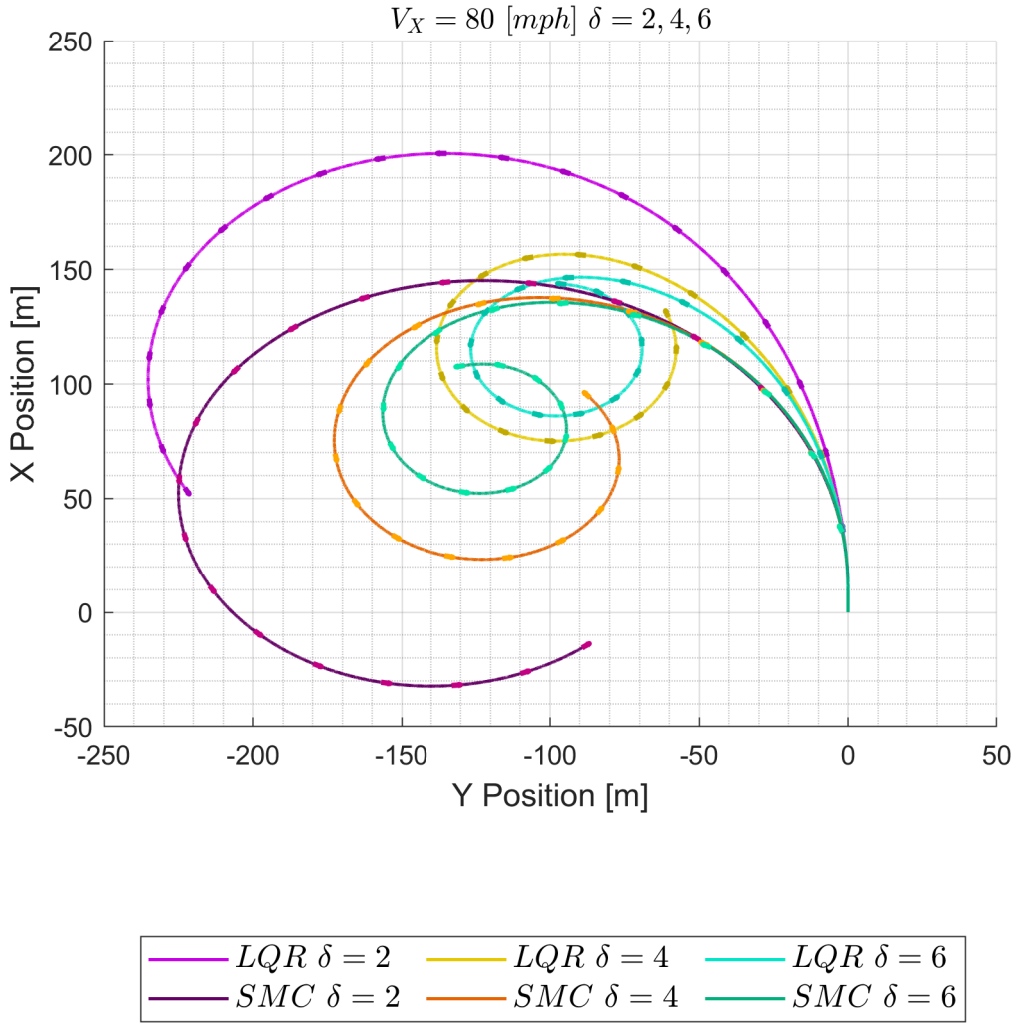

Figure A.49: *CSA Test Comparison for LQR-STA and SMC Vehicle Trajectories at* $V_X = 80$ *and* $\delta = 2, 4, 6$

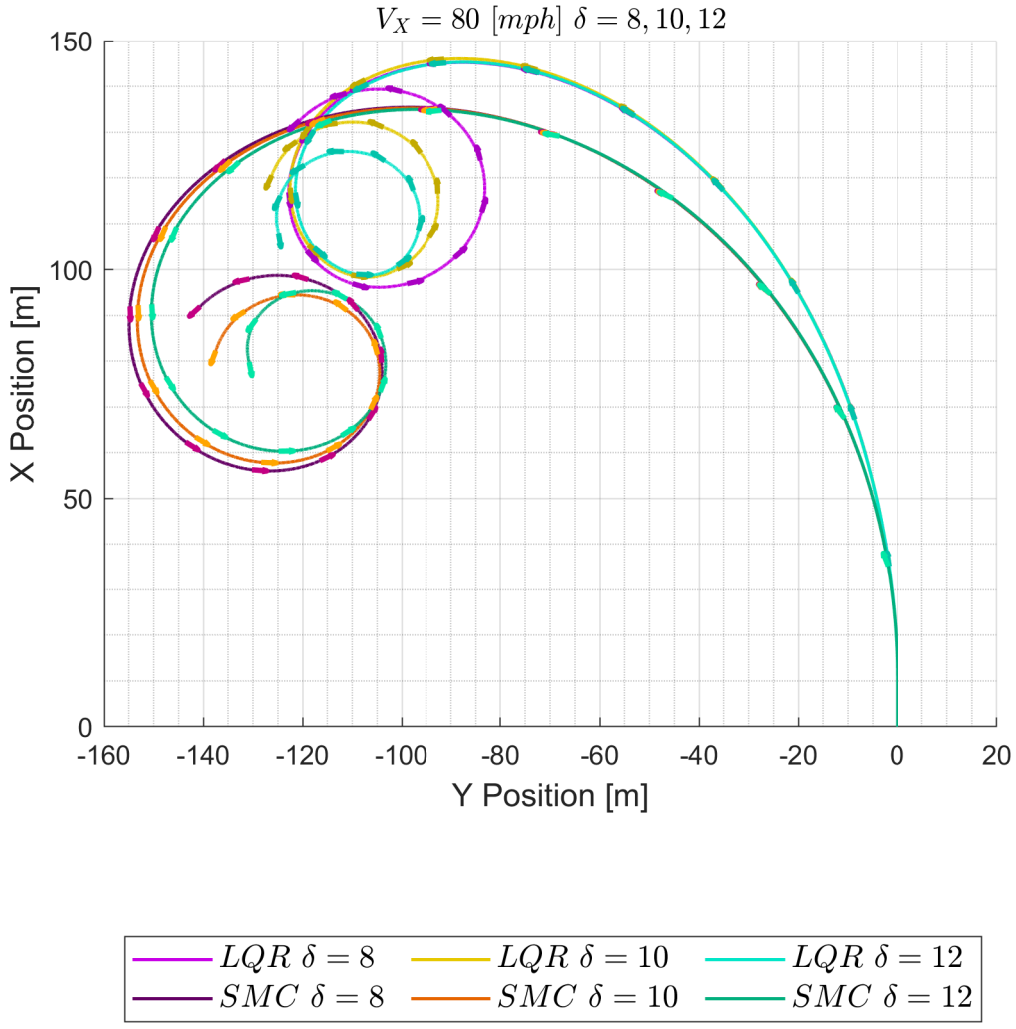

Figure A.50: *CSA Test Comparison for LQR-STA and SMC Vehicle Trajectories at* $V_X = 80$ *and* $\delta = 8, 10, 12$

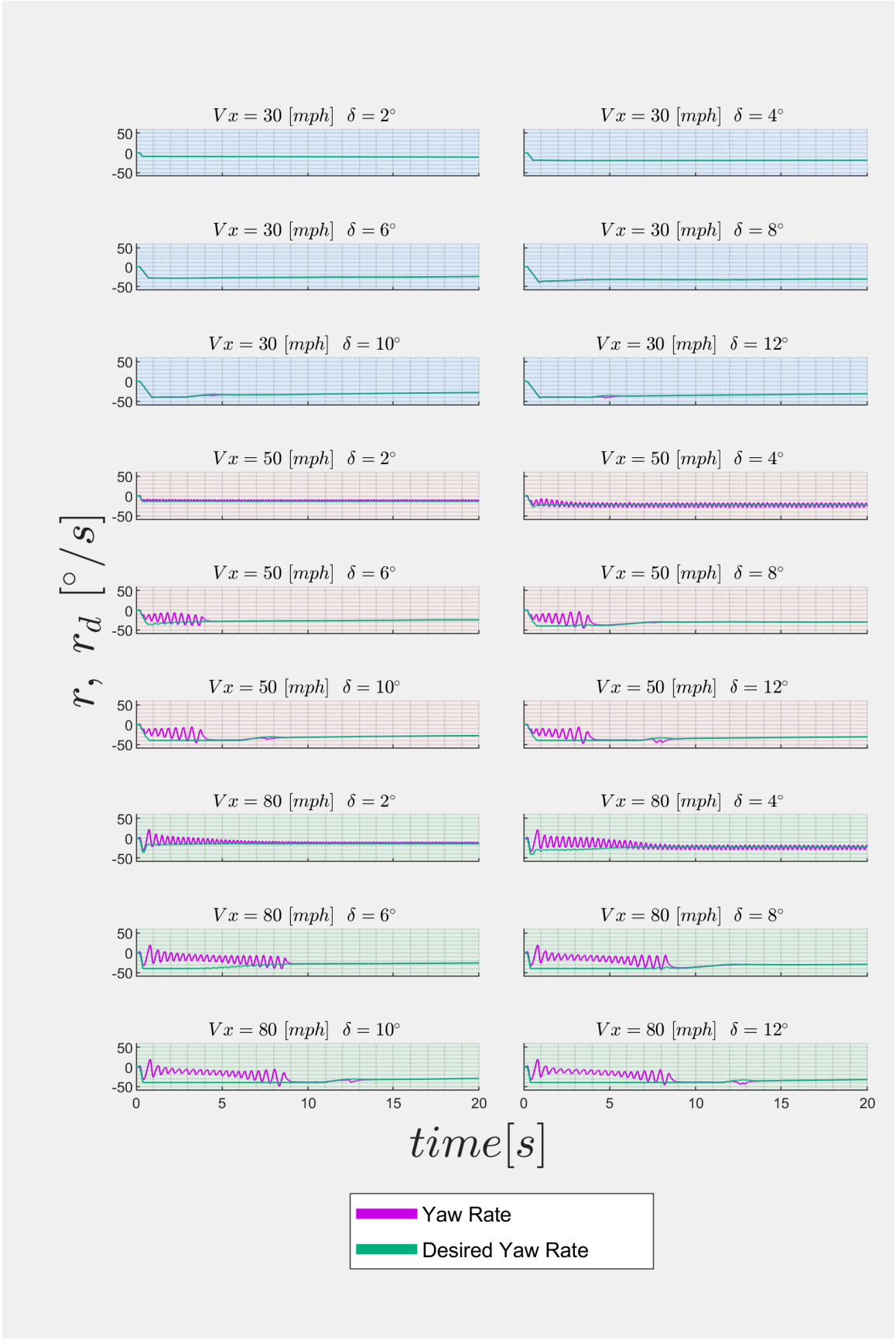

Figure A.51: *CSA Test Yaw Errors for LQR-STA* ($\delta = 2 - 12$)

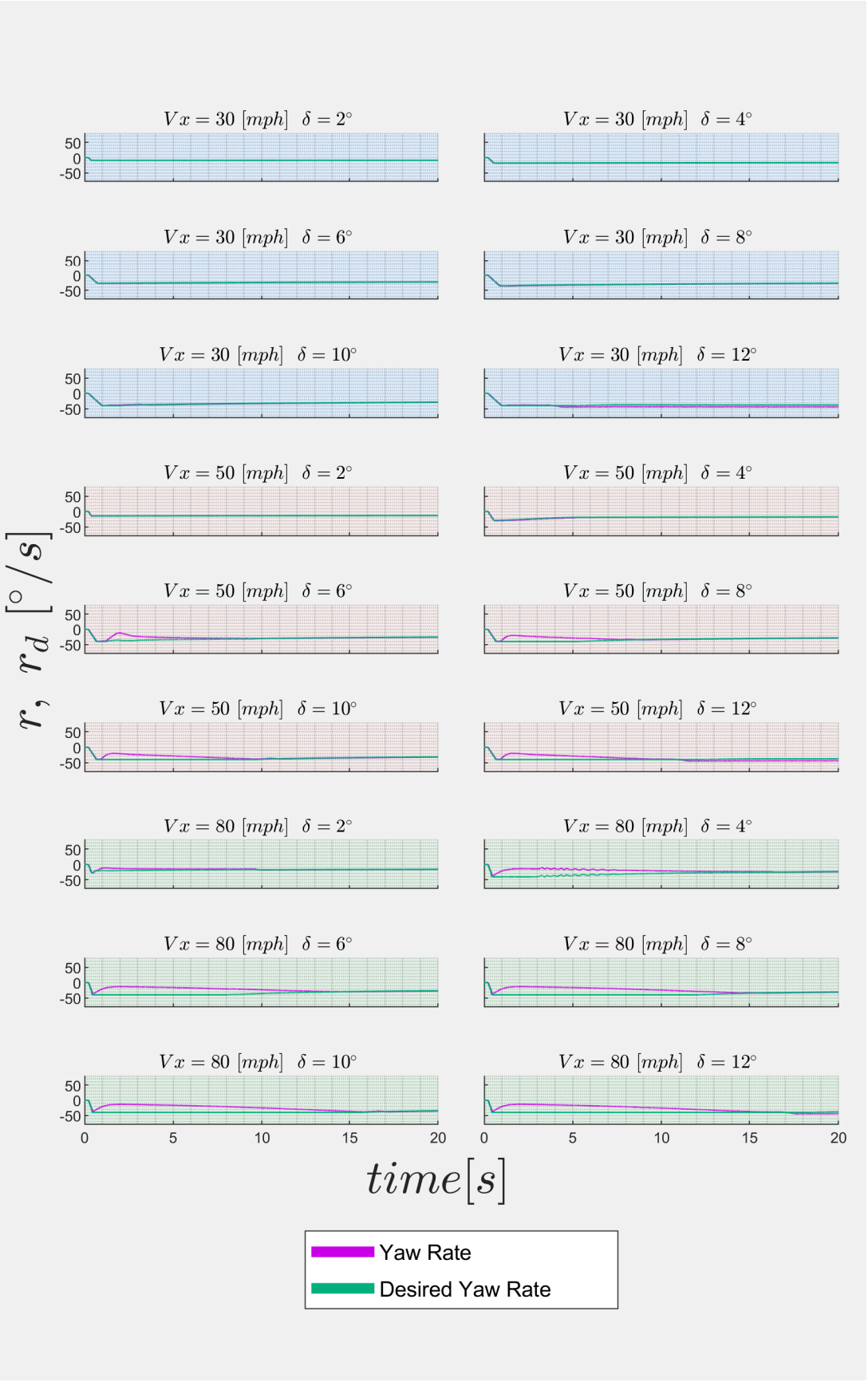

Figure A.52: *CSA Test Yaw Errors for SMC ($\delta = 2 - 12$)*

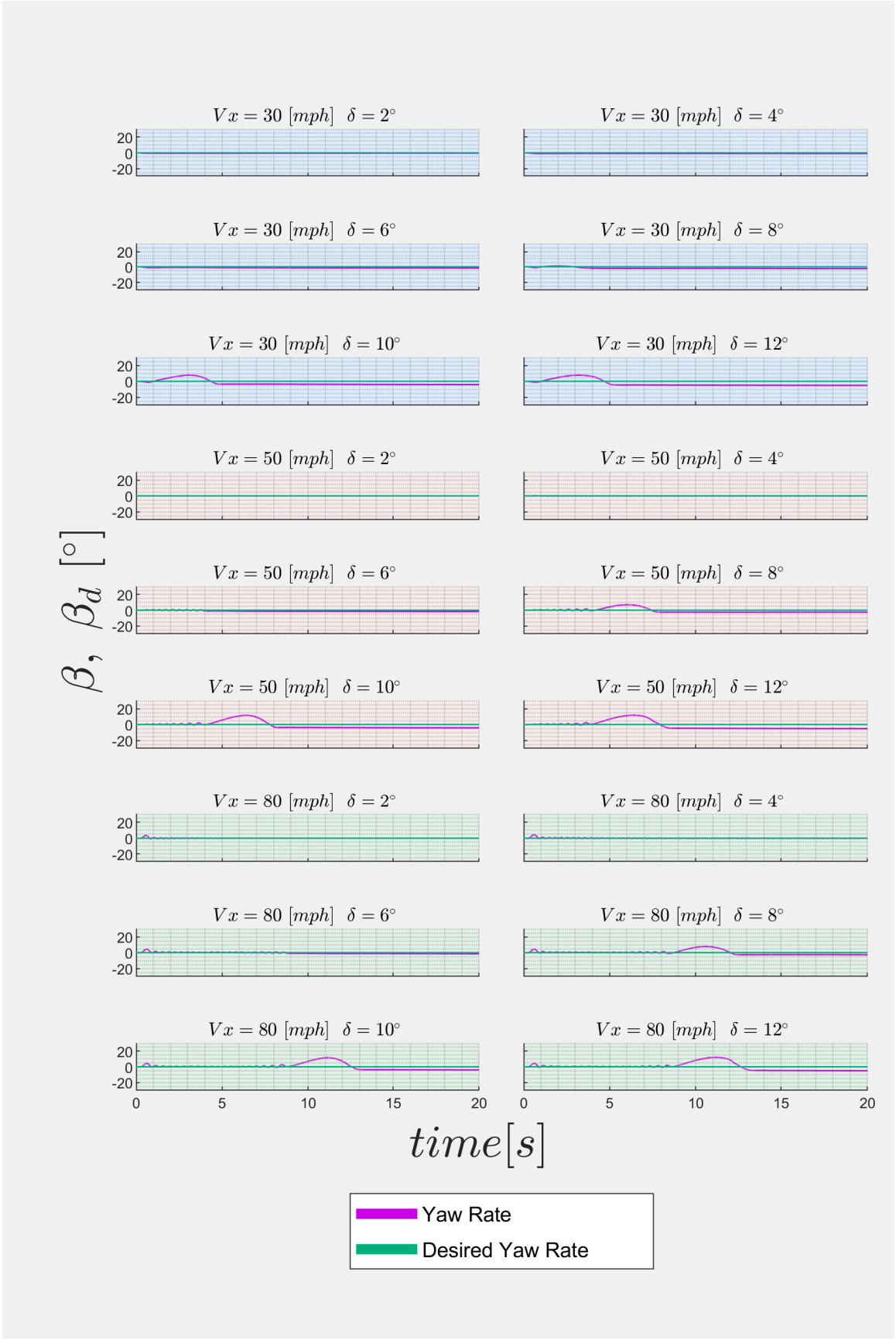

Figure A.53: *CSA Test Side Slip Errors for LQR-STA* ($\delta = 2 - 12$)

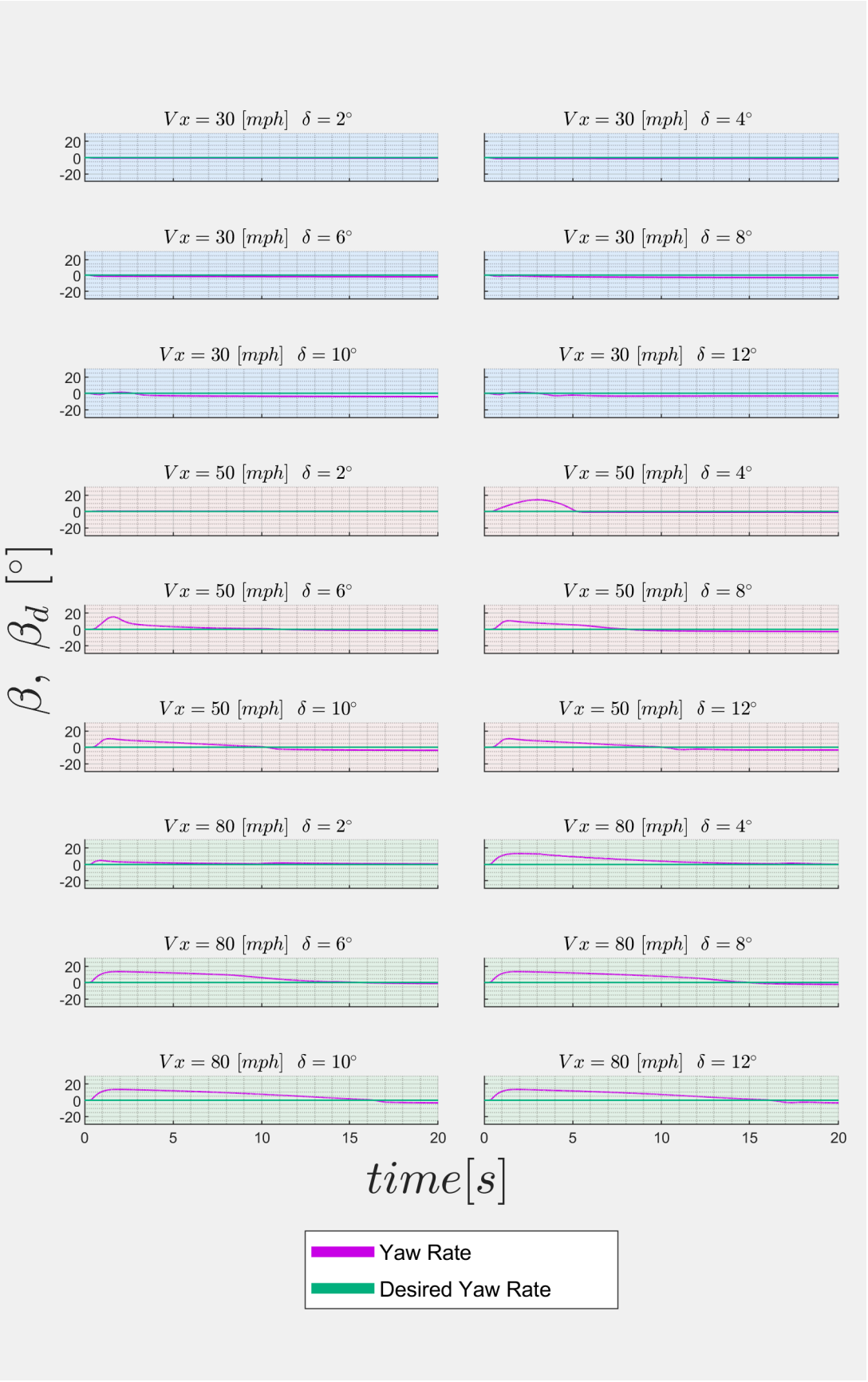

Figure A.54: *CSA Test Side Slip Errors for SMC ($\delta = 2 - 12$)*

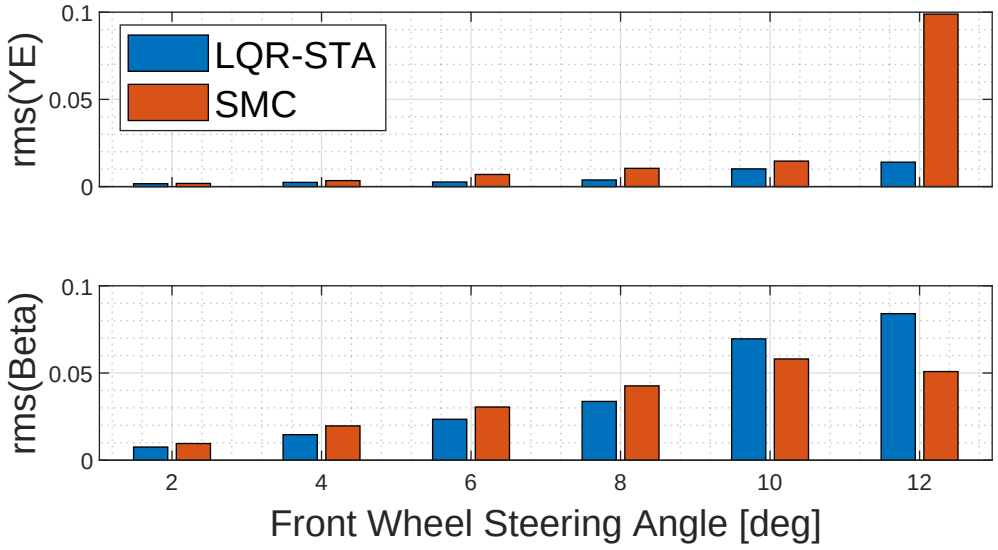

Figure A.55: *CSA Test RMS Yaw and Side Slip Errors Comparison Between LQR-STA and SMC at* $V_X = 30$ *and* $\delta = 2 - 12$

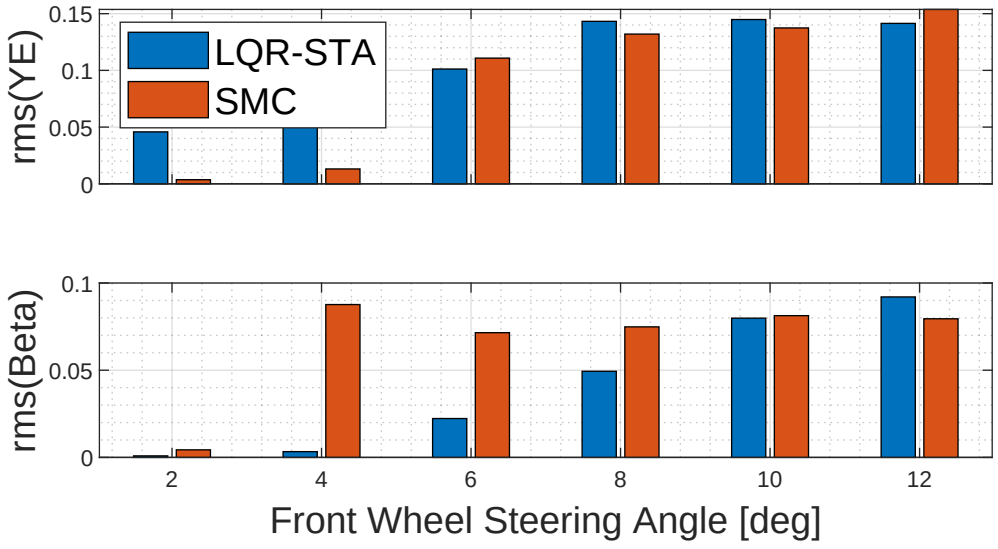

Figure A.56: *CSA Test RMS Yaw and Side Slip Errors Comparison Between LQR-STA and SMC at* $V_X = 50$ *and* $\delta = 2 - 12$

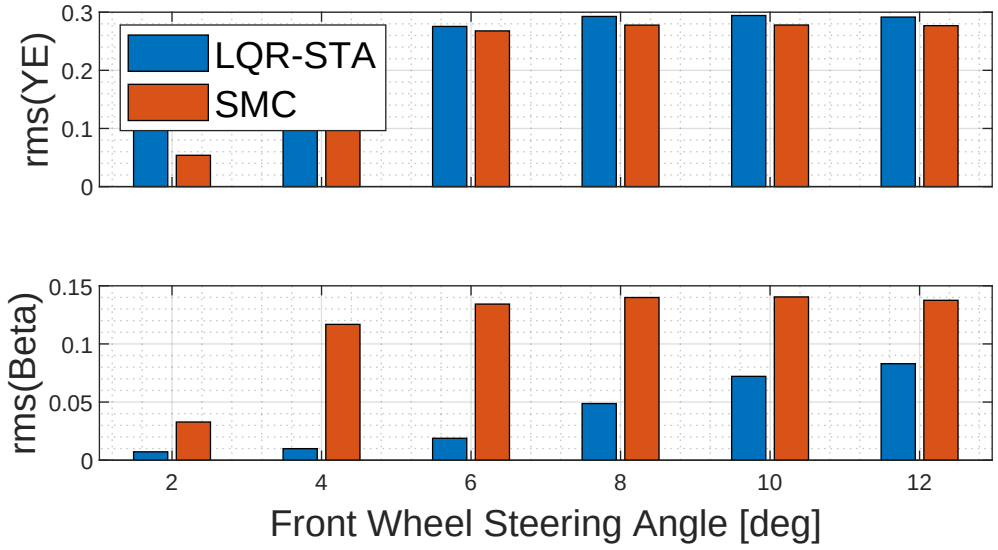

Figure A.57: *CSA Test RMS Yaw and Side Slip Errors Comparison Between LQR-STA and SMC at* $V_X = 80$ *and* $\delta = 2 - 12$

A.4 CSA Test Figures for Steering Angles 14-24 Degrees

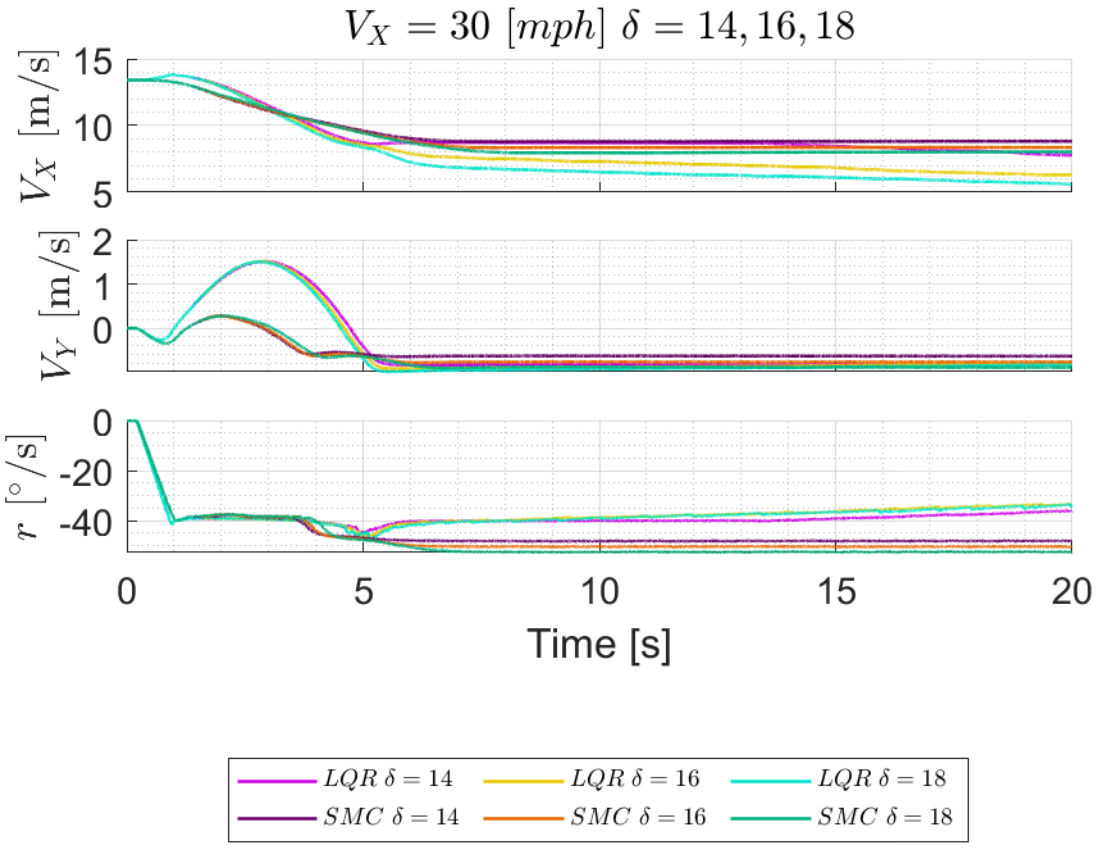

Figure A.58: *CSA Test Comparison for LQR-STA and SMC Telemetry at* $V_X = 30$ *and* $\delta = 14, 16, 18$

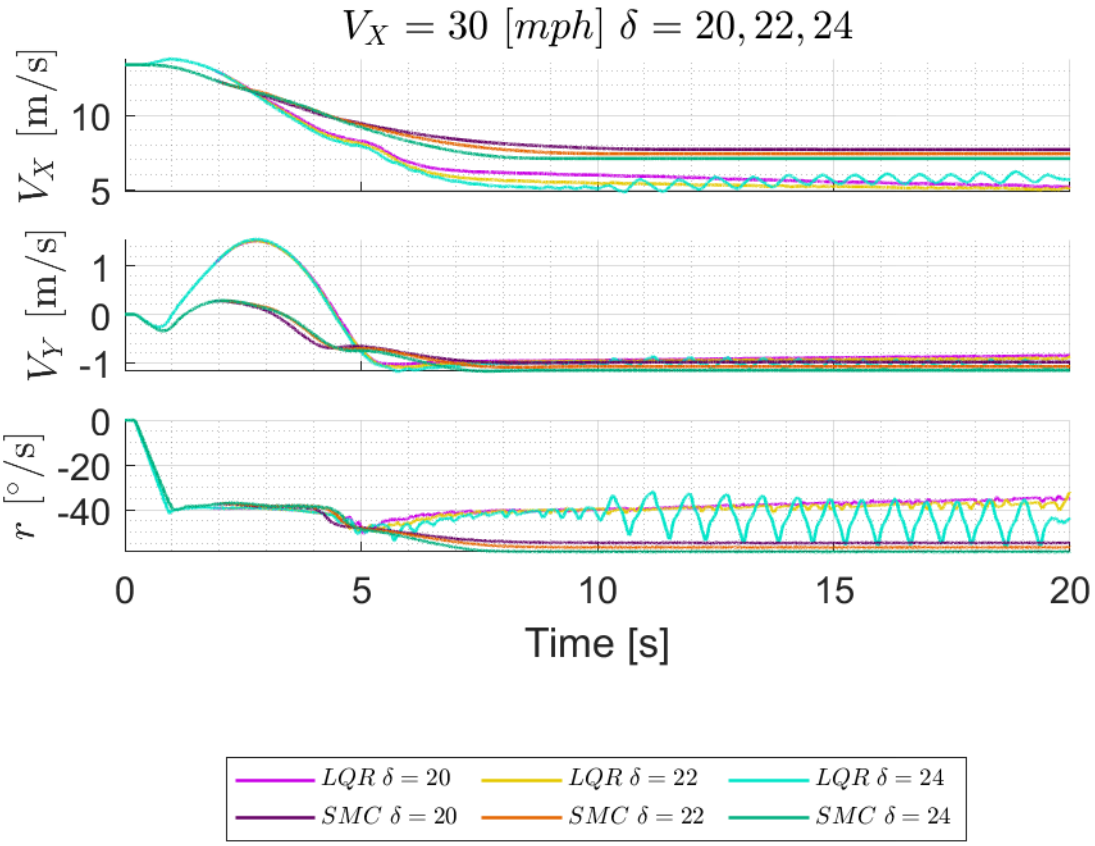

Figure A.59: *CSA Test Comparison for LQR-STA and SMC Telemetry at* $V_X = 30$ *and* $\delta = 20, 22, 24$

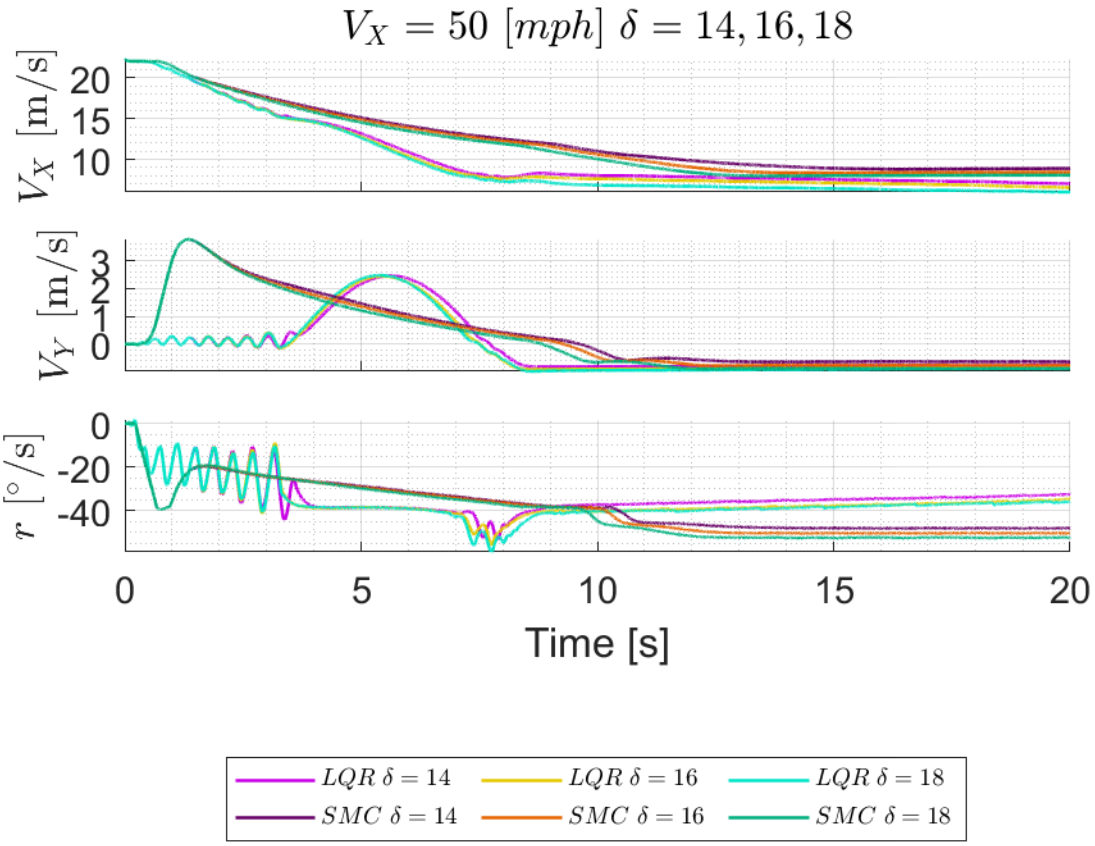

Figure A.60: *CSA Test Comparison for LQR-STA and SMC Telemetry at* $V_X = 50$ *and* $\delta = 14, 16, 18$

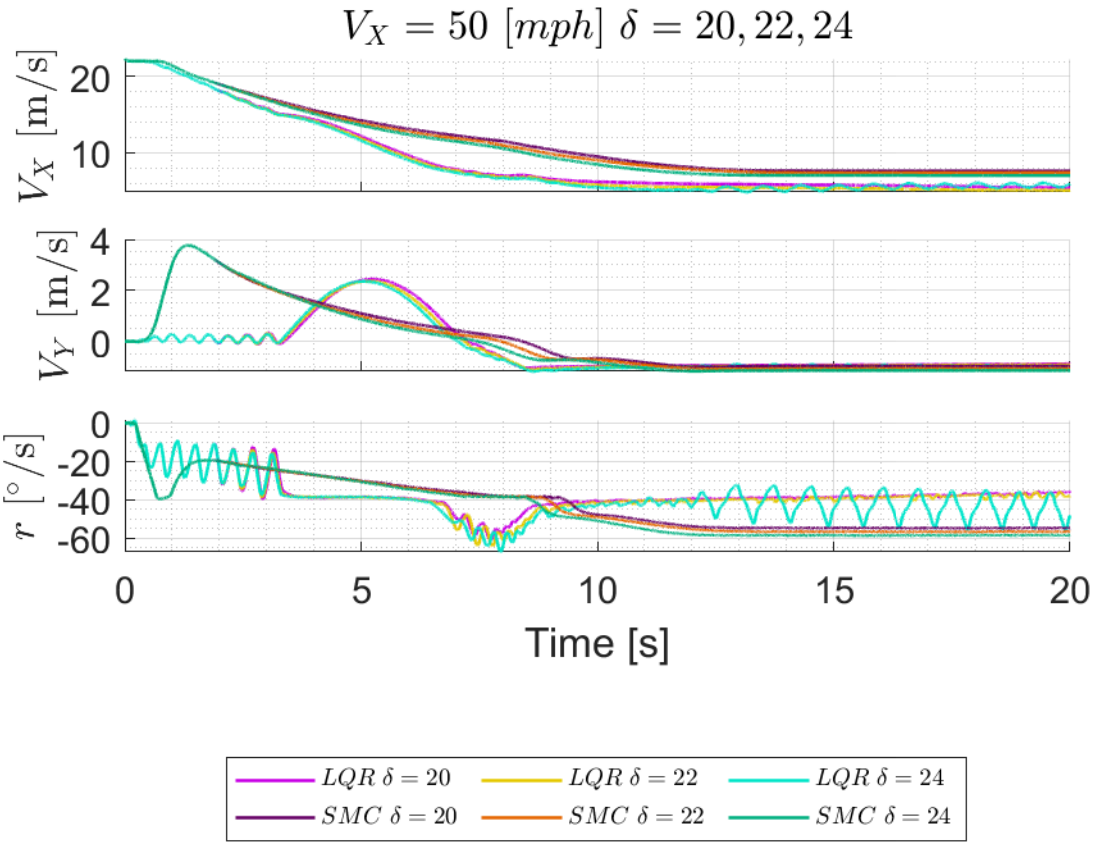

Figure A.61: *CSA Test Comparison for LQR-STA and SMC Telemetry at* $V_X = 50$ *and* $\delta = 20, 22, 24$

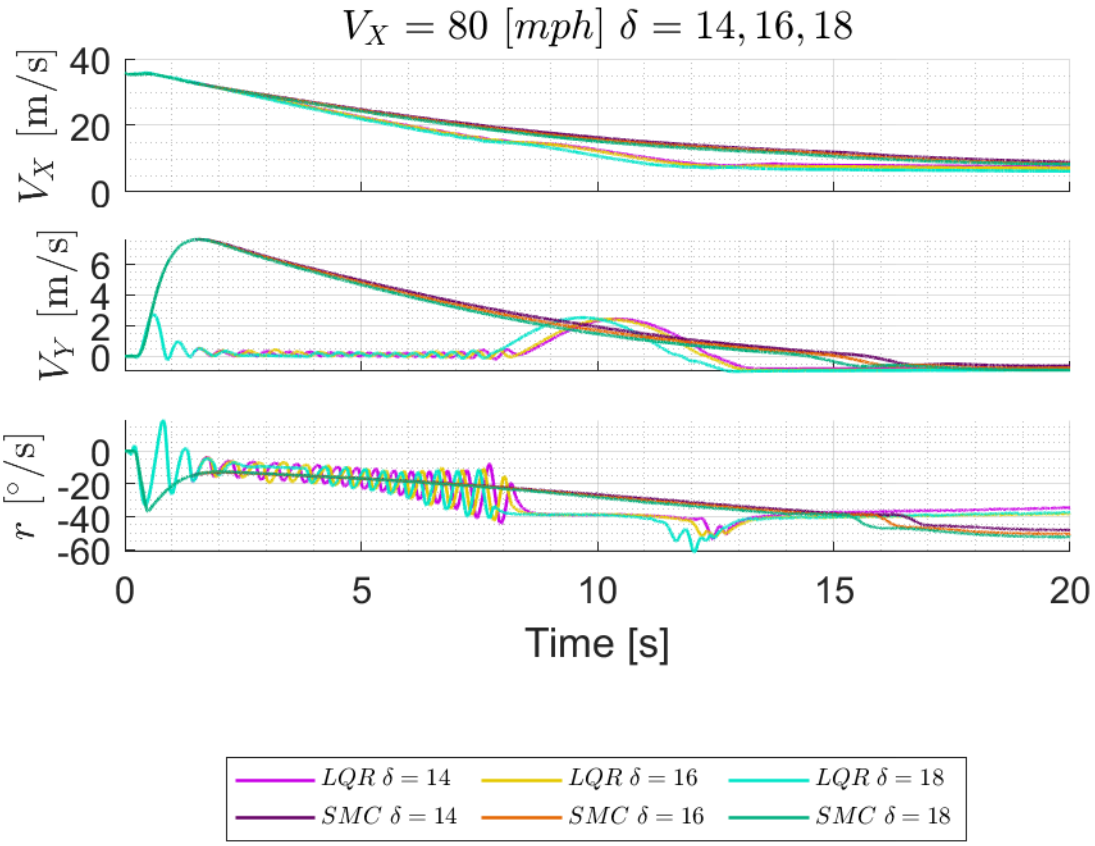

Figure A.62: *CSA Test Comparison for LQR-STA and SMC Telemetry at* $V_X = 80$ *and* $\delta = 14, 16, 18$

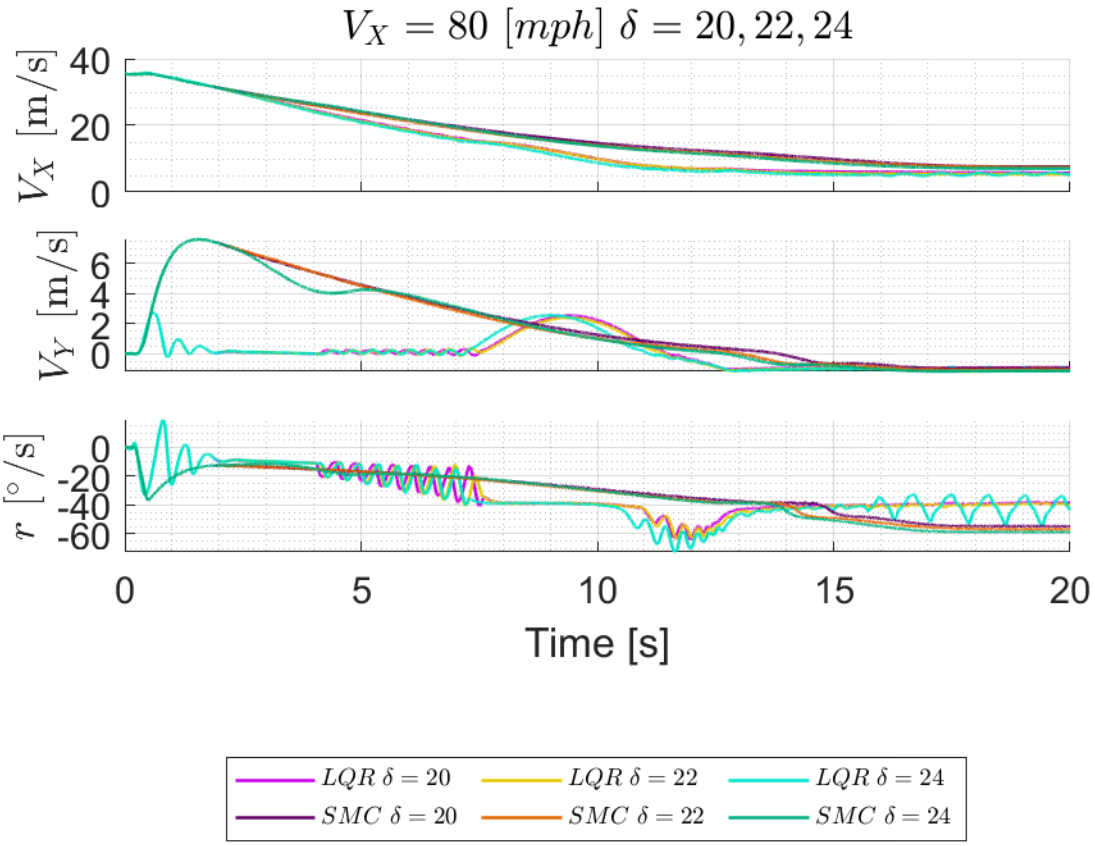

Figure A.63: *CSA Test Comparison for LQR-STA and SMC Telemetry at* $V_X = 80$ *and* $\delta = 20, 22, 24$

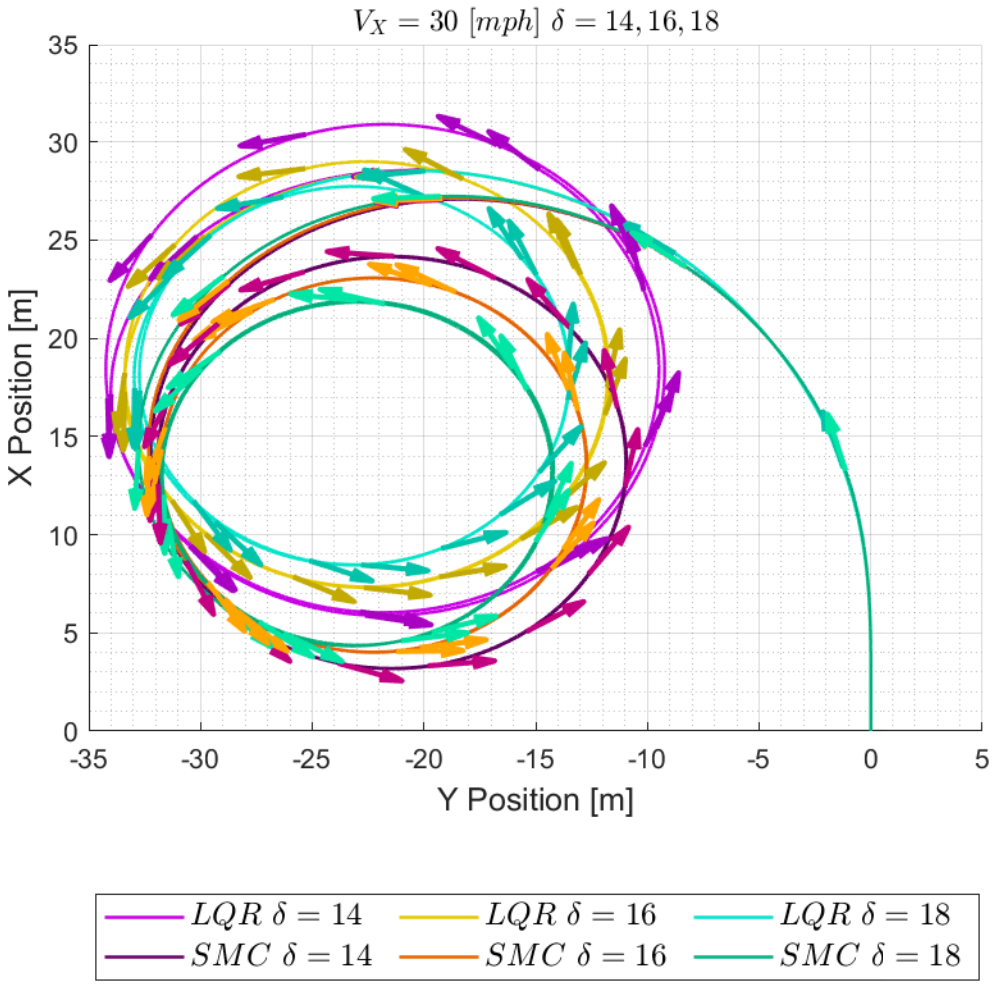

Figure A.64: *CSA Test Comparison for LQR-STA and SMC Vehicle Trajectories at* $V_X = 30$ *and* $\delta = 14, 16, 18$

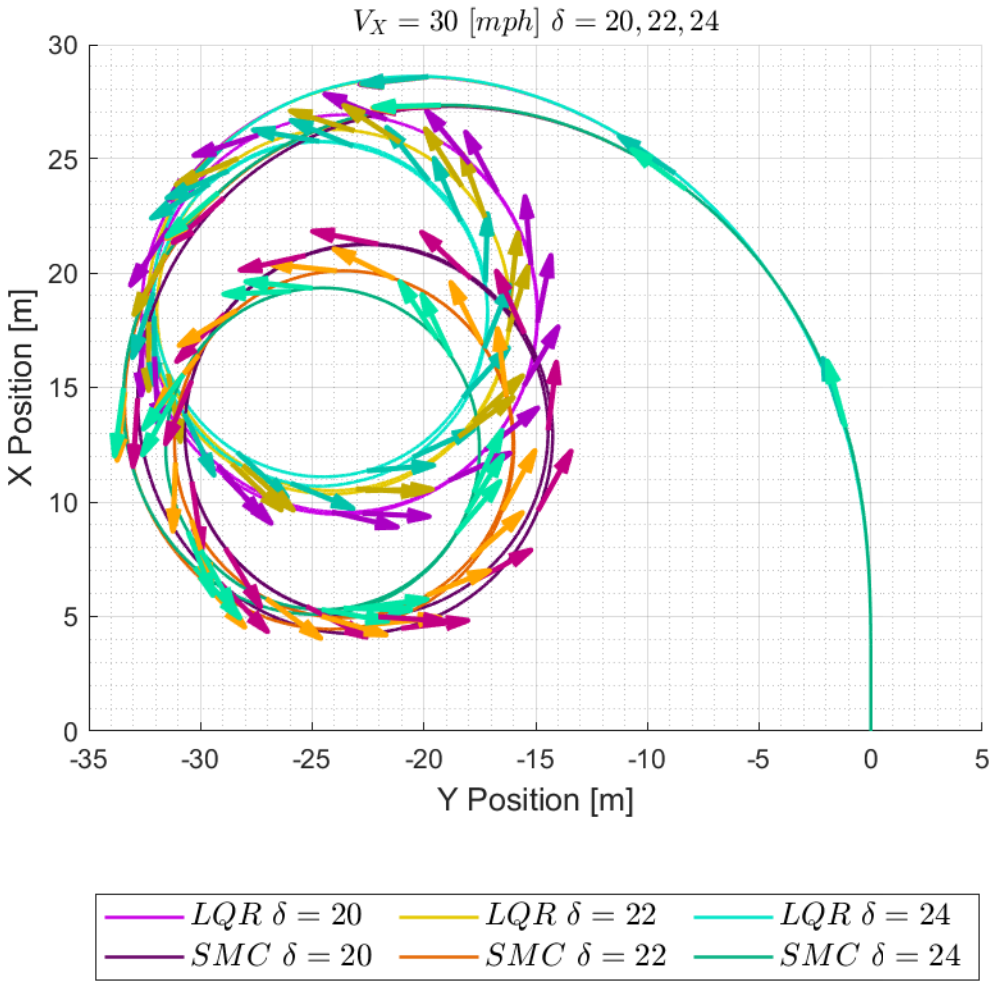

Figure A.65: *CSA Test Comparison for LQR-STA and SMC Vehicle Trajectories at* $V_X = 30$ *and* $\delta = 20, 22, 24$

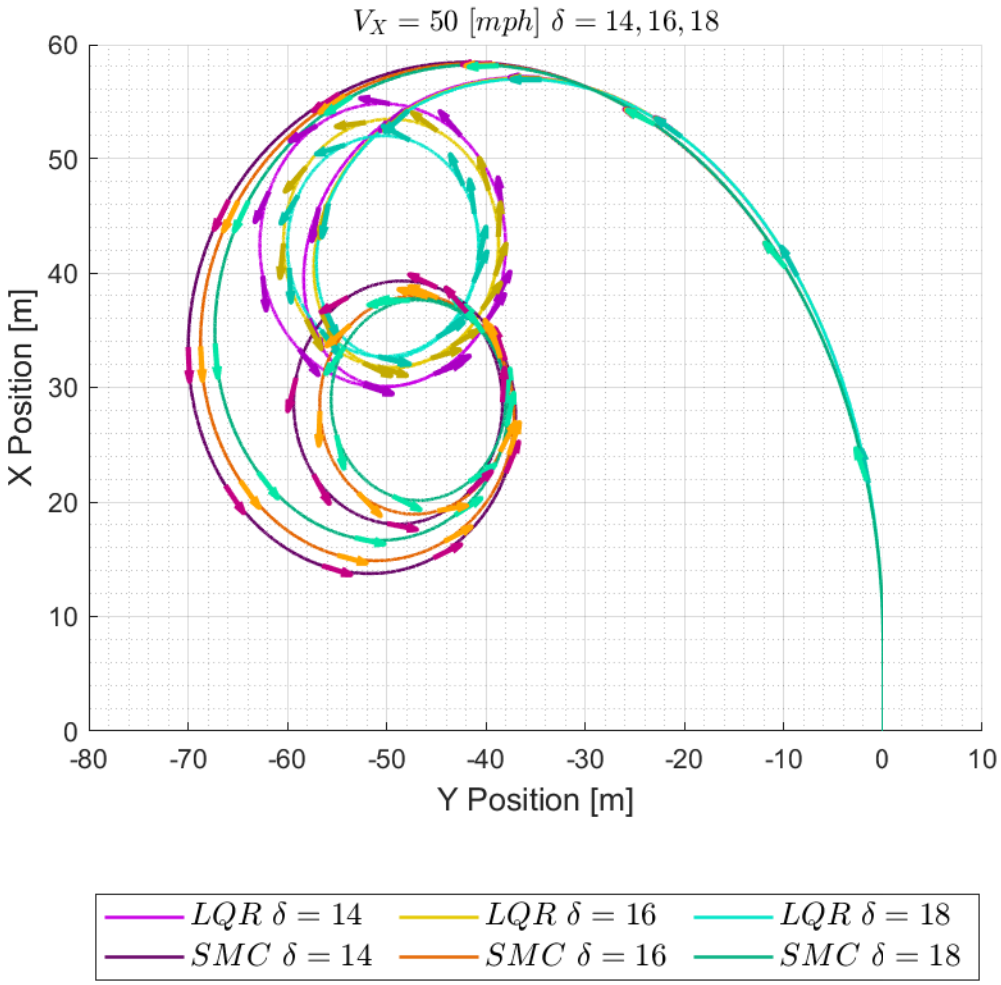

Figure A.66: *CSA Test Comparison for LQR-STA and SMC Vehicle Trajectories at* $V_X = 50$ *and* $\delta = 14, 16, 18$

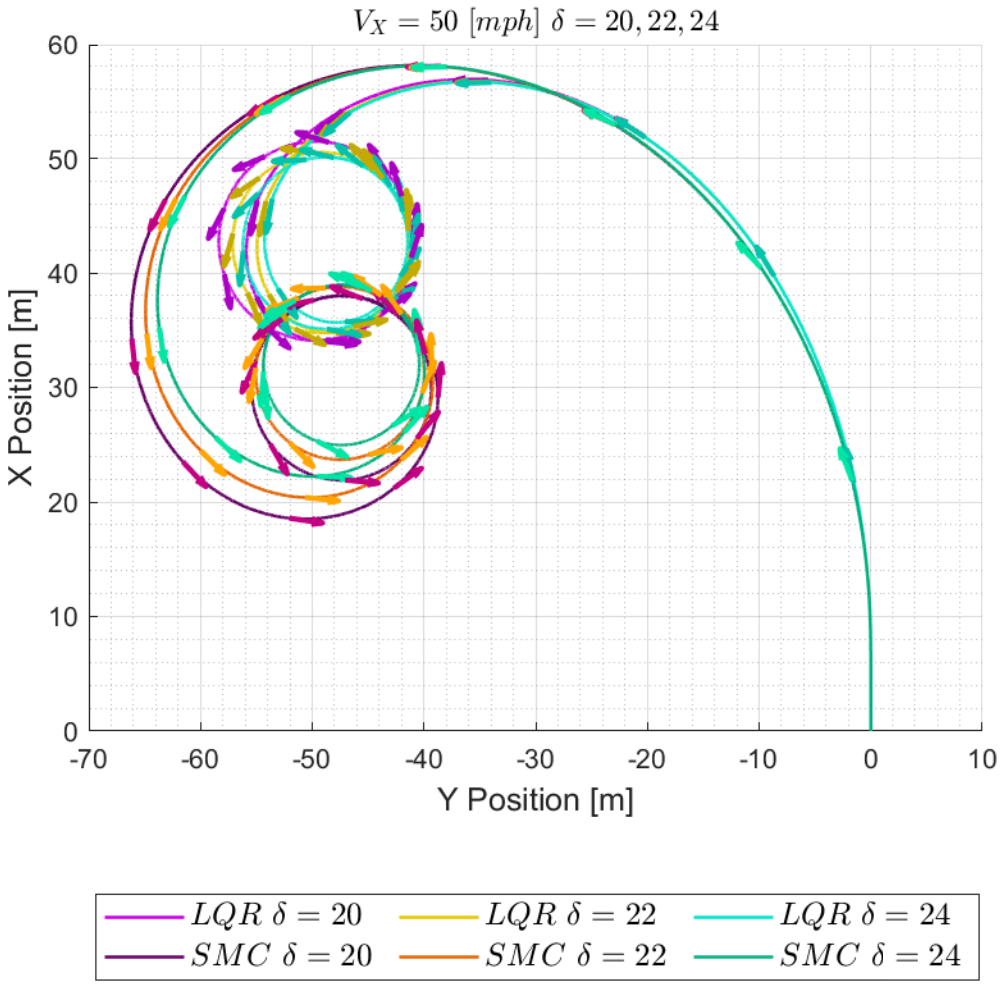

Figure A.67: *CSA Test Comparison for LQR-STA and SMC Vehicle Trajectories at* $V_X = 50$ *and* $\delta = 20, 22, 24$

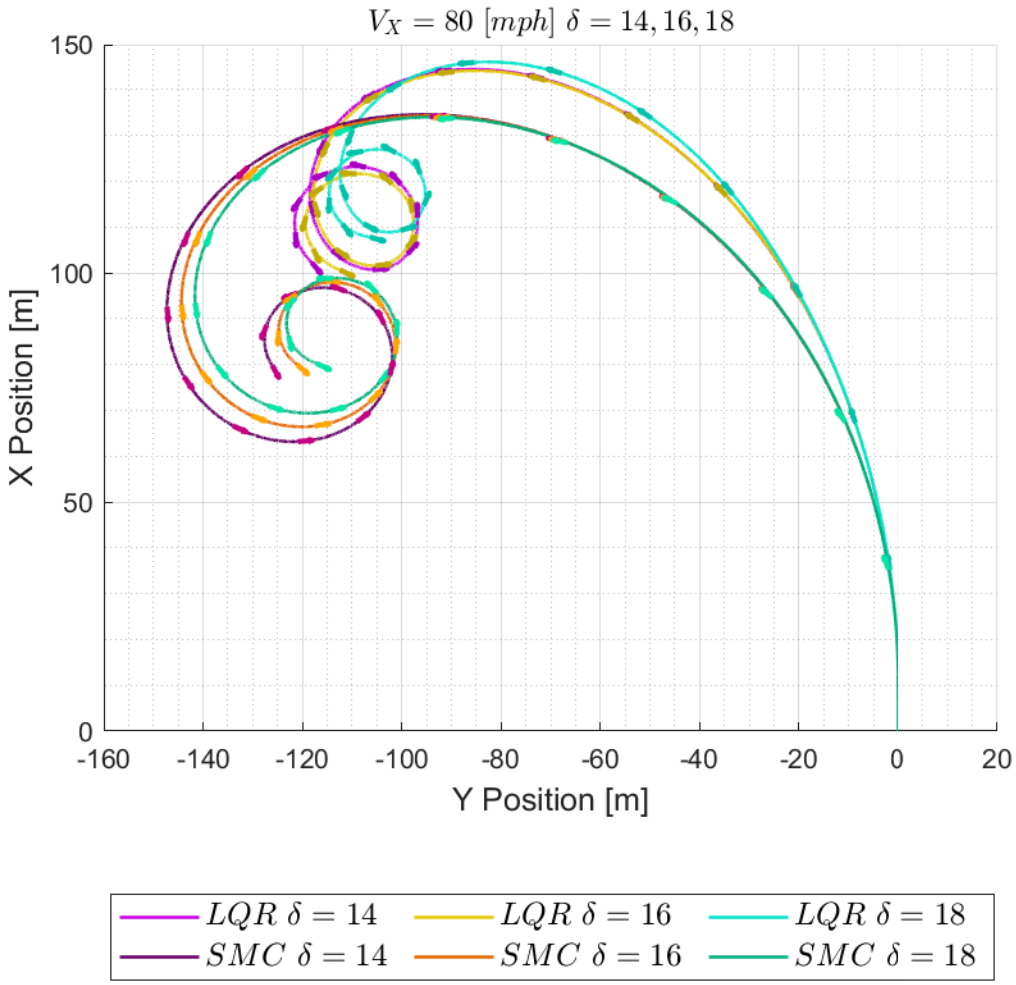

Figure A.68: *CSA Test Comparison for LQR-STA and SMC Vehicle Trajectories at* $V_X = 80$ *and* $\delta = 14, 16, 18$

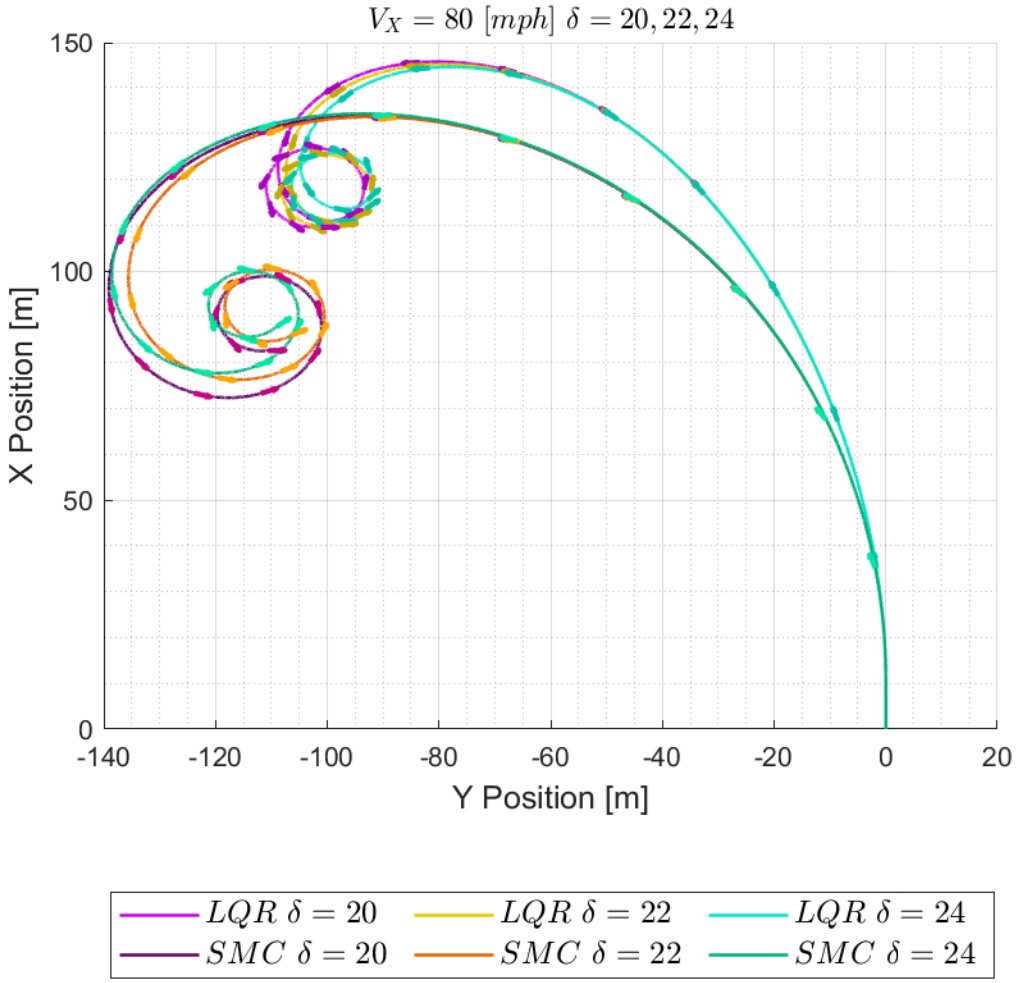

Figure A.69: *CSA Test Comparison for LQR-STA and SMC Vehicle Trajectories at* $V_X = 80$ *and* $\delta = 20, 22, 24$

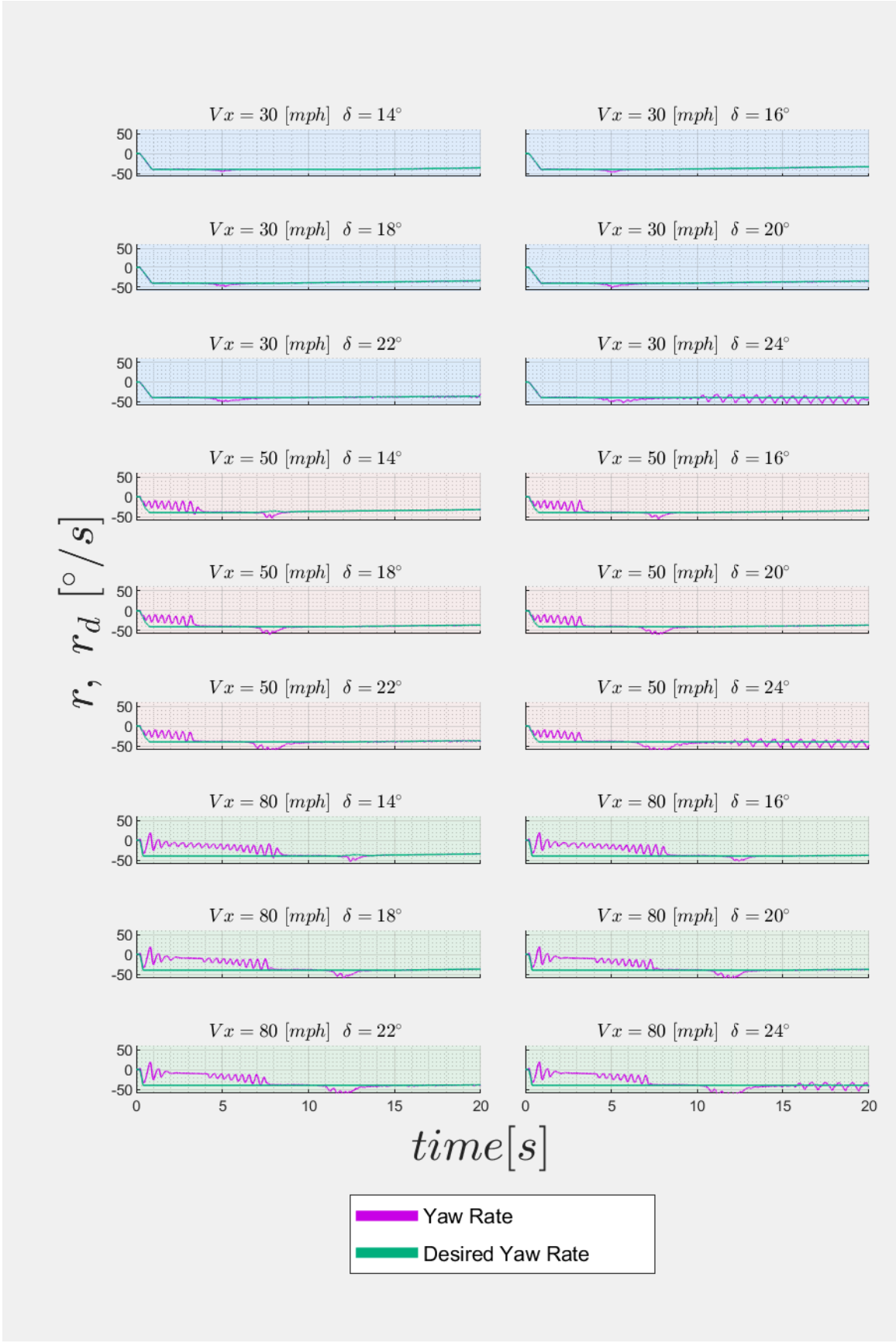

Figure A.70: *CSA Test Yaw Errors for LQR-STA ($\delta = 14 - 24$)*

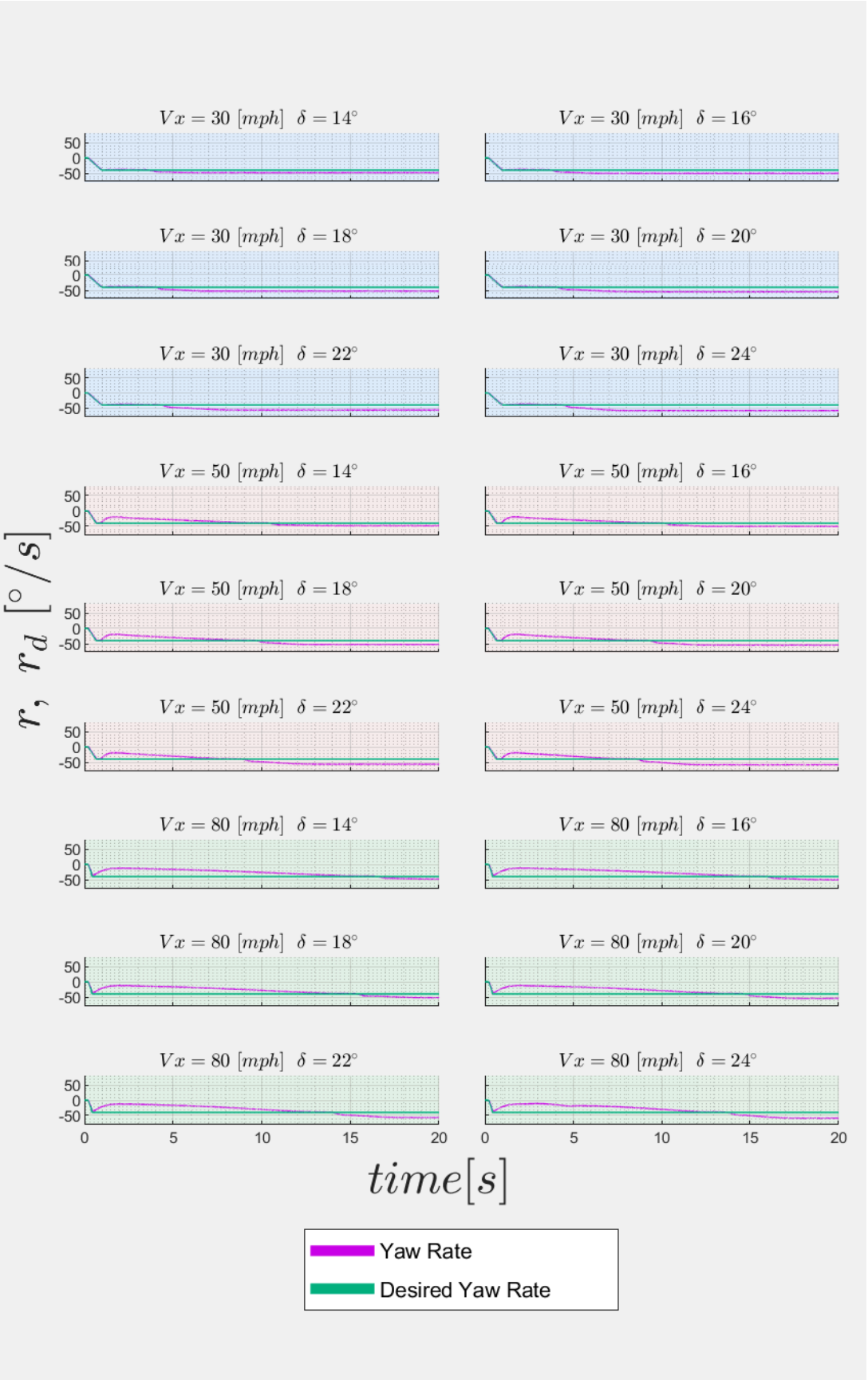

Figure A.71: *CSA Test Yaw Errors for SMC ($\delta = 14 - 24$)*

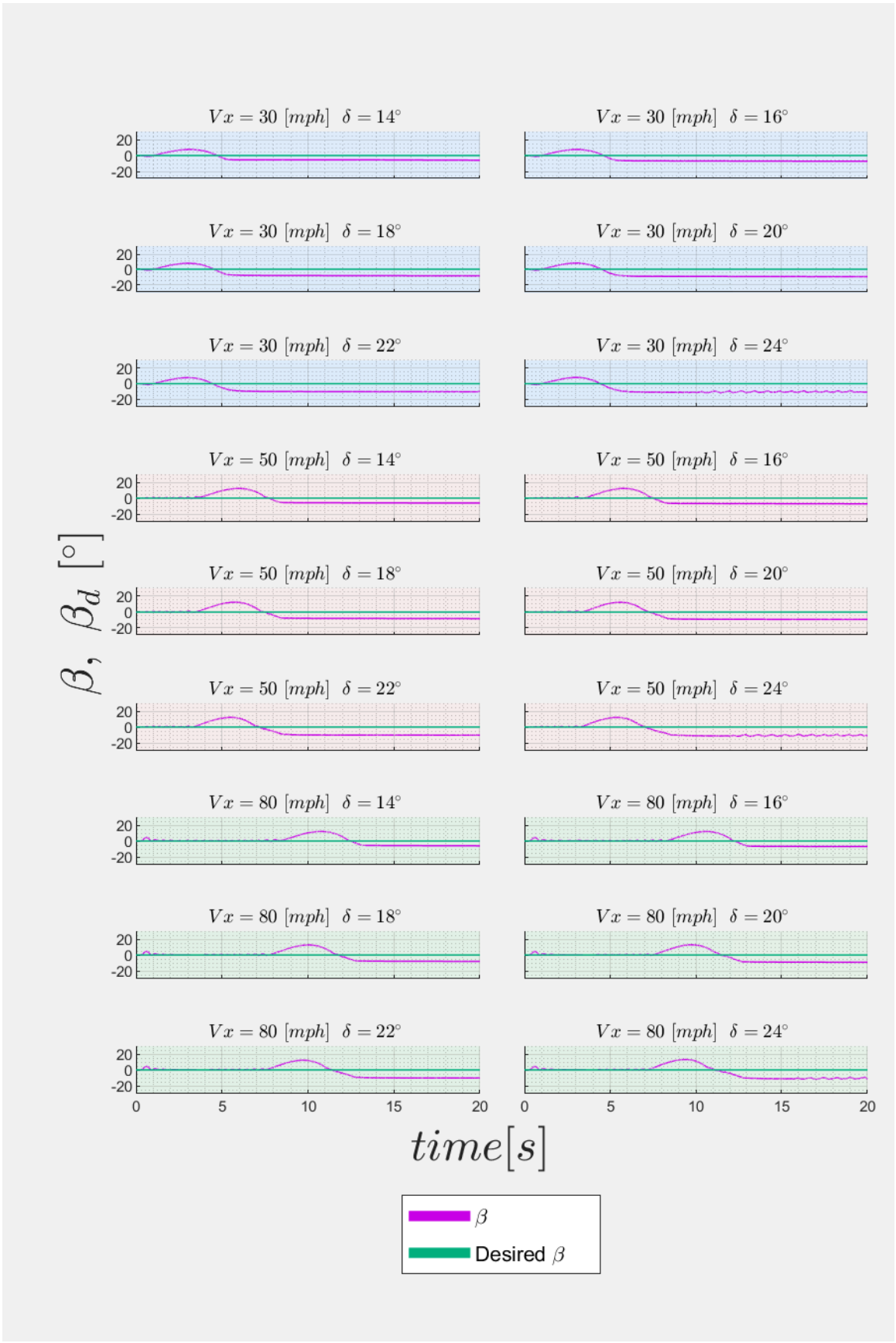

Figure A.72: *CSA Test Side Slip Errors for LQR-STA* ($\delta = 14 - 24$)

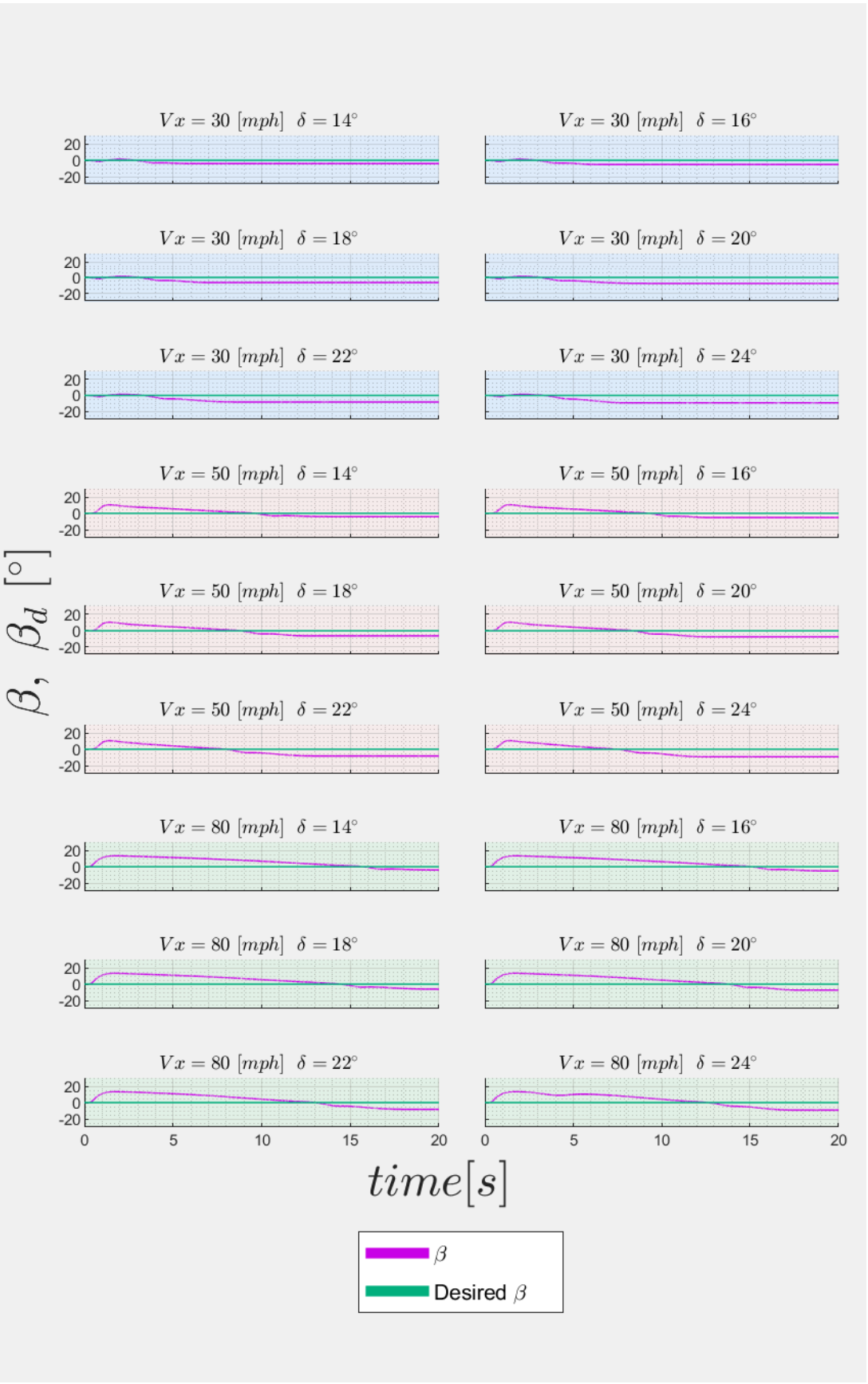

Figure A.73: *CSA Test Side Slip Errors for SMC ($\delta = 14 - 24$)*

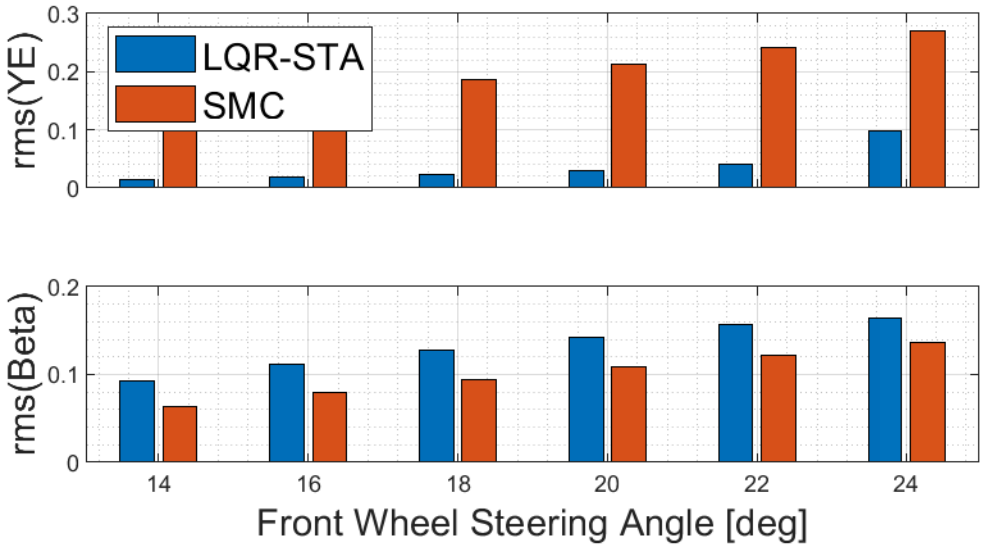

Figure A.74: *CSA Test RMS Yaw and Side Slip Errors Comparison Between LQR-STA and SMC at* $V_X = 30$ *and* $\delta = 14 - 24$

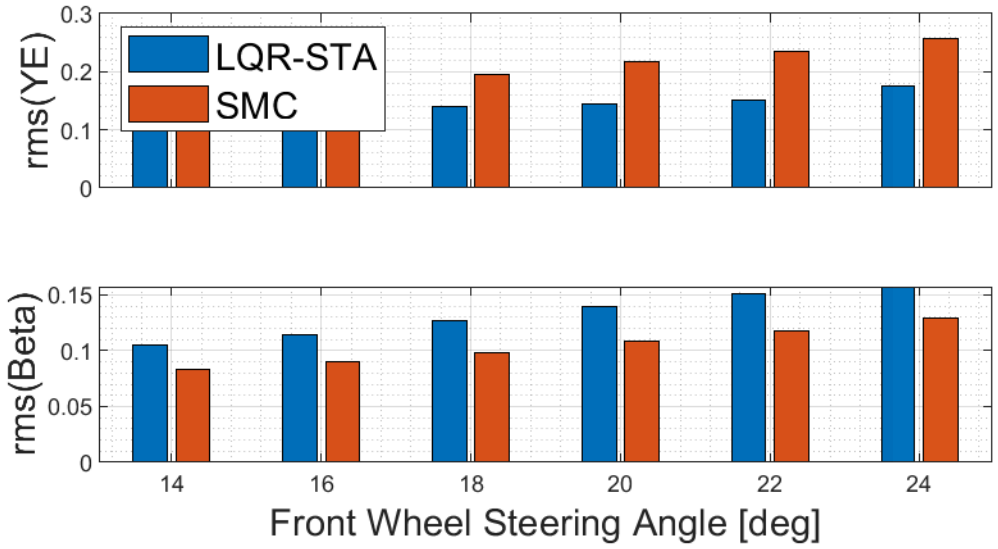

Figure A.75: *CSA Test RMS Yaw and Side Slip Errors Comparison Between LQR-STA and SMC at* $V_X = 50$ *and* $\delta = 14 - 24$

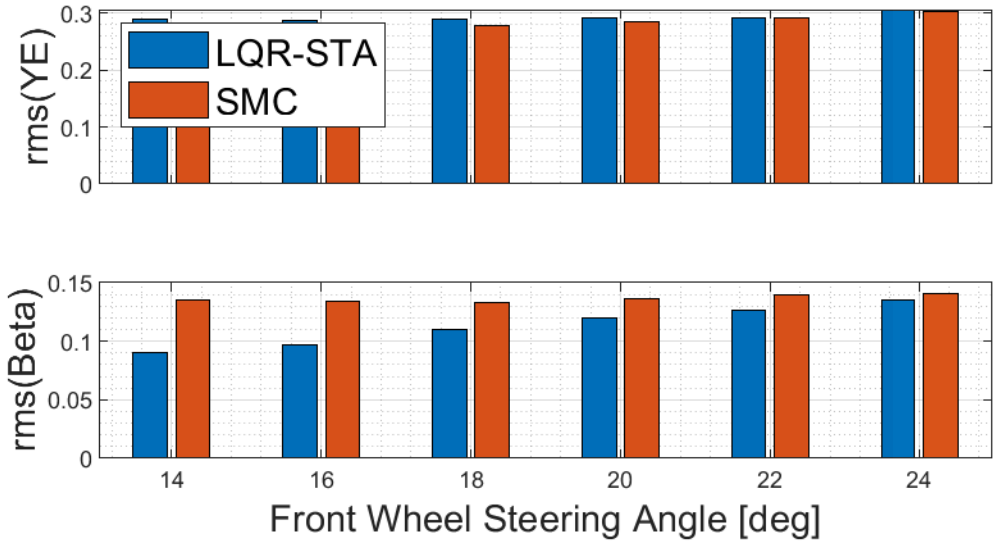

Figure A.76: *CSA Test RMS Yaw and Side Slip Errors Comparison Between LQR-STA and SMC at* $V_X = 80$ *and* $\delta = 14 - 24$

A.5 SD Telemetry Data for Steering Angles 2-12 Degrees

	δ											
	2		4		6		8		10		12	
Vxo	LS	SMC	LC	SMC	LC	SMC	LC	SMC	LC	SMC	LC	SMC
30	13.81	13.39	14.56	13.31	14.97	13.21	11.97	12.95	11.98	11.91	11.99	12.04
50	21.41	21.88	16.81	20.15	15.46	18.61	16.97	18.85	14.48	18.61	18.06	18.50
80	30.53	33.46	30.50	32.37	30.70	26.67	29.69	27.97	28.48	13.19	29.01	2.01

Table A.1: *Final Longitudinal Speed for All SD Test Cases for Steering Angles 2,4,6,8,10,12*

	δ											
	2		4		6		8		10		12	
Vxo	LS	SMC	LC	SMC	LC	SMC	LC	SMC	LC	SMC	LC	SMC
30	0.12	0.12	0.22	0.24	0.27	0.32	0.23	0.30	0.45	0.25	0.90	0.24
50	0.04	0.16	0.13	1.51	0.29	1.19	0.25	2.85	6.14	3.15	4.65	2.87
80	0.34	4.10	5.45	3.86	4.14	12.41	0.87	11.25	1.35	18.53	0.67	20.73

Table A.2: *Max Lateral Speed for All SD Test Cases for Steering Angles 2,4,6,8,10,12*

	δ											
	2		4		6		8		10		12	
Vxo	LS	SMC	LC	SMC	LC	SMC	LC	SMC	LC	SMC	LC	SMC
30	-0.12	-0.13	-0.22	-0.24	-0.20	-0.32	-0.21	-0.31	-0.25	-0.33	-0.51	-0.34
50	-0.04	-0.14	-0.12	-0.77	-0.42	-2.87	-1.42	-2.57	-2.78	-2.57	-2.19	-2.42
80	-0.47	-3.04	-4.05	-5.53	-3.19	-5.90	-2.57	-5.96	-2.30	-5.83	-2.28	-5.74

Table A.3: *Min Lateral Speed for All SD Test Cases for Steering Angles 2,4,6,8,10,12*

	δ											
	2		4		6		8		10		12	
Vxo	LS	SMC	LC	SMC	LC	SMC	LC	SMC	LC	SMC	LC	SMC
30	9.24	8.88	19.04	17.73	28.45	26.44	38.61	34.61	42.64	43.46	45.10	42.11
50	13.37	14.39	23.02	27.70	27.66	39.57	40.93	37.73	50.17	35.48	46.94	34.05
80	13.54	27.77	40.66	33.99	37.17	31.23	34.47	30.14	33.01	29.89	32.83	29.68

Table A.4: *Max Yaw rate for All SD Test Cases for Steering Angles 2,4,6,8,10,12*

	δ											
	2		4		6		8		10		12	
Vxo	LS	SMC	LC	SMC	LC	SMC	LC	SMC	LC	SMC	LC	SMC
30	-9.39	-8.96	-19.75	-17.89	-30.28	-26.82	-38.97	-34.95	-42.48	-41.95	-48.12	-42.76
50	-14.48	-14.71	-27.11	-27.48	-33.06	-34.30	-30.29	-43.96	-68.10	-50.56	-59.06	-53.99
80	-15.56	-22.16	-47.96	-30.97	-36.05	-49.33	-19.80	-62.05	-28.52	-71.54	-20.78	-77.33

Table A.5: *Min Yaw rate for All SD Test Cases for Steering Angles 2,4,6,8,10,12*

	δ											
	2		4		6		8		10		12	
Vxo	LS	SMC	LC	SMC	LC	SMC	LC	SMC	LC	SMC	LC	SMC
30	0.52	0.53	0.93	1.02	1.12	1.37	0.99	1.27	2.01	1.08	4.02	1.08
50	0.11	0.41	0.38	4.17	0.88	3.55	0.73	8.31	18.38	9.27	13.36	8.49
80	0.57	6.92	9.34	6.71	7.01	24.01	1.46	21.24	2.51	47.10	1.24	79.20

Table A.6: *Max Vehicle Side slip for All SD Test Cases for Steering Angles 2,4,6,8,10,12*

	δ											
	2		4		6		8		10		12	
Vxo	LS	SMC	LC	SMC	LC	SMC	LC	SMC	LC	SMC	LC	SMC
30	-0.52	-0.54	-0.89	-1.05	-0.84	-1.40	-0.87	-1.34	-1.07	-1.49	-2.17	-1.49
50	-0.10	-0.35	-0.36	-2.04	-1.09	-7.72	-3.70	-6.79	-7.34	-6.77	-5.79	-6.39
80	-0.77	-4.95	-6.57	-9.09	-5.19	-9.71	-4.19	-9.83	-3.75	-9.61	-3.72	-9.49

Table A.7: *Min Vehicle Side slip for All SD Test Cases for Steering Angles 2,4,6,8,10,12*

	δ											
	2		4		6		8		10		12	
Vxo	LS	SMC	LC	SMC	LC	SMC	LC	SMC	LC	SMC	LC	SMC
30	0.01	-0.00	0.19	0.01	0.18	0.01	-0.08	-0.00	-0.08	-0.00	0.12	0.00
50	-0.62	0.01	-0.07	-0.00	-1.04	-0.01	0.78	-0.00	-1.10	-0.01	-1.32	0.00
80	3.20	-0.00	1.75	-0.01	-1.24	-6.24	-4.34	-0.73	-1.44	-21.84	3.54	-27.25

Table A.8: *Yaw Rate at t = 1 Second After Steering Input Completion for All SD Test Cases for Steering Angles 2,4,6,8,10,12*

	δ											
	2		4		6		8		10		12	
Vxo	LS	SMC	LC	SMC	LC	SMC	LC	SMC	LC	SMC	LC	SMC
30	0.16	0.01	0.18	0.00	0.10	0.00	-0.06	0.01	-0.06	-0.00	-0.09	0.00
50	0.90	0.01	0.26	-0.01	0.81	0.00	0.19	-0.02	-0.94	-0.01	-0.41	-0.01
80	-2.98	0.01	2.54	-0.01	-3.30	-0.80	0.46	-0.88	4.66	-13.36	1.63	-22.09

Table A.9: *Yaw Rate at t = 1.75 Second After Steering Input Completion for All SD Test Cases for Steering Angles 2,4,6,8,10,12*

	δ											
	2		4		6		8		10		12	
Vxo	LS	SMC	LC	SMC	LC	SMC	LC	SMC	LC	SMC	LC	SMC
30	0.66	0.64	1.36	1.26	2.04	1.88	2.58	2.44	2.90	3.01	3.19	3.12
50	1.29	1.53	2.02	2.75	2.47	3.70	2.48	3.77	3.07	3.80	2.87	3.75
80	1.48	3.08	2.60	3.63	2.39	3.79	2.33	3.85	2.35	3.84	2.45	3.78

Table A.10: *Y-Position at t = 1.07 Seconds for All SD Test Cases for Steering Angles 2,4,6,8,10,12*

A.6 SD Telemetry Data for Steering Angles 14-24 Degrees

	δ											
	14		16		18		20		22		24	
Vxo	LS	SMC	LC	SMC	LC	SMC	LC	SMC	LC	SMC	LC	SMC
30	12.09	12.16	11.95	12.15	11.88	12.36	11.89	12.28	12.07	12.15	11.85	12.28
50	19.02	18.31	14.55	18.18	18.30	17.98	17.74	17.99	18.44	17.93	17.45	17.95
80	28.45	-3.76	28.21	-3.45	27.41	-2.57	16.66	-0.28	0.13	9.27	16.48	17.29

Table A.11: *Final Longitudinal Speed for All SD Test Cases for Steering Angles 14,16,18,20,22,24*

	δ											
	14		16		18		20		22		24	
Vxo	LS	SMC	LC	SMC	LC	SMC	LC	SMC	LC	SMC	LC	SMC
30	0.51	0.25	0.21	0.26	0.21	0.33	0.22	0.29	0.39	0.28	0.49	0.32
50	3.05	2.85	1.80	2.80	2.42	2.77	3.27	2.74	4.66	2.75	4.92	2.78
80	0.89	21.98	4.77	21.77	7.71	21.33	13.66	20.72	14.49	19.15	12.50	17.16

Table A.12: *Max Lateral Speed for All SD Test Cases for Steering Angles 14,16,18,20,22,24*

	δ											
	14		16		18		20		22		24	
Vxo	LS	SMC	LC	SMC	LC	SMC	LC	SMC	LC	SMC	LC	SMC
30	-0.84	-0.31	-1.21	-0.33	-0.98	-0.33	-0.89	-0.34	-0.77	-0.35	-0.66	-0.36
50	-1.75	-2.39	-1.33	-2.30	-1.11	-2.28	-0.95	-2.29	-0.82	-2.22	-0.71	-2.30
80	-2.41	-5.84	-2.12	-5.74	-2.38	-5.65	-15.24	-5.63	-19.41	-5.62	-16.85	-5.55

Table A.13: *Min Lateral Speed for All SD Test Cases for Steering Angles 14,16,18,20,22,24*

	δ											
	14		16		18		20		22		24	
Vxo	LS	SMC	LC	SMC	LC	SMC	LC	SMC	LC	SMC	LC	SMC
30	53.09	39.26	59.02	39.24	54.41	38.93	50.20	38.83	46.23	38.90	43.17	38.94
50	44.19	33.21	40.76	32.95	38.71	32.78	37.08	32.49	35.65	32.21	34.33	32.12
80	33.47	29.55	31.83	29.32	38.63	29.17	69.74	29.00	80.05	28.89	73.50	28.75

Table A.14: *Max Yaw rate for All SD Test Cases for Steering Angles 14,16,18,20,22,24*

	δ											
	14		16		18		20		22		24	
Vxo	LS	SMC	LC	SMC	LC	SMC	LC	SMC	LC	SMC	LC	SMC
30	-45.94	-39.32	-40.08	-38.90	-46.67	-38.78	-47.65	-38.83	-43.81	-38.71	-42.06	-38.94
50	-50.44	-56.09	-45.39	-56.46	-51.75	-57.18	-56.38	-57.55	-63.21	-58.08	-64.83	-58.25
80	-22.56	-81.61	-47.53	-82.52	-55.76	-82.84	-102.33	-83.14	-70.31	-83.41	-67.62	-82.83

Table A.15: *Min Yaw rate for All SD Test Cases for Steering Angles 14,16,18,20,22,24*

	δ											
	14		16		18		20		22		24	
Vxo	LS	SMC	LC	SMC	LC	SMC	LC	SMC	LC	SMC	LC	SMC
30	2.32	1.05	0.88	1.08	0.92	1.51	0.95	1.37	1.84	1.24	2.29	1.48
50	8.54	8.51	5.02	8.39	6.91	8.38	9.39	8.30	13.65	8.34	14.58	8.37
80	1.68	90.03	8.28	90.04	13.59	90.03	39.42	90.05	27.62	53.40	23.29	40.08

Table A.16: *Max Vehicle Side slip for All SD Test Cases for Steering Angles 14,16,18,20,22,24*

	δ											
	14		16		18		20		22		24	
Vxo	LS	SMC	LC	SMC	LC	SMC	LC	SMC	LC	SMC	LC	SMC
30	-3.61	-1.35	-5.24	-1.45	-4.30	-1.41	-3.92	-1.47	-3.37	-1.53	-2.90	-1.58
50	-4.62	-6.36	-3.51	-6.14	-2.92	-6.17	-2.49	-6.20	-2.15	-6.01	-1.87	-6.21
80	-3.94	-90.03	-3.46	-90.03	-4.42	-90.04	-34.92	-90.03	-89.51	-9.39	-44.72	-9.30

Table A.17: *Min Vehicle Side slip for All SD Test Cases for Steering Angles 14,16,18,20,22,24*

	δ											
	14		16		18		20		22		24	
Vxo	LS	SMC	LC	SMC	LC	SMC	LC	SMC	LC	SMC	LC	SMC
30	0.08	0.00	0.15	0.01	0.10	0.00	0.05	0.01	0.08	0.00	-0.17	0.01
50	0.65	0.00	-0.96	-0.01	-0.98	0.00	0.75	-0.00	-0.52	-0.01	1.10	-0.00
80	-4.87	-31.32	-1.12	-30.74	31.88	-29.64	28.83	-27.33	69.89	-20.45	44.38	-12.47

Table A.18: *Yaw Rate at t = 1 Second After Steering Input Completion for All SD Test Cases for Steering Angles 14,16,18,20,22,24*

	δ											
	14		16		18		20		22		24	
Vxo	LS	SMC	LC	SMC	LC	SMC	LC	SMC	LC	SMC	LC	SMC
30	-0.09	-0.00	0.16	0.01	-0.04	0.01	-0.12	0.01	-0.01	0.00	-0.10	0.00
50	1.24	-0.00	-0.99	0.00	-0.80	-0.00	-1.24	0.00	1.28	-0.01	-1.01	-0.00
80	2.97	-28.24	-0.42	-27.64	26.92	-26.21	-7.74	-23.09	40.64	-13.68	15.23	-1.37

Table A.19: *Yaw Rate at t = 1.75 Second After Steering Input Completion for All SD Test Cases for Steering Angles 14,16,18,20,22,24*

	δ											
	14		16		18		20		22		24	
Vxo	LS	SMC	LC	SMC	LC	SMC	LC	SMC	LC	SMC	LC	SMC
30	3.30	3.16	3.21	3.21	3.33	3.23	3.36	3.22	3.35	3.20	3.32	3.19
50	2.70	3.71	2.61	3.65	2.66	3.57	2.70	3.54	2.73	3.48	2.74	3.46
80	2.45	3.72	2.49	3.64	2.51	3.57	2.51	3.50	2.49	3.44	2.43	3.39

Table A.20: *Y-Position at t = 1.07 Seconds for All SD Test Cases for Steering Angles 14,16,18,20,22,24*

A.7 CSA Telemetry Data for Steering Angles 2-12 Degrees

	δ											
	2		4		6		8		10		12	
Vxo	LS	SMC	LC	SMC	LC	SMC	LC	SMC	LC	SMC	LC	SMC
30	16.12	13.13	14.24	12.22	12.34	11.10	11.69	9.86	8.44	8.68	7.87	9.59
50	20.55	19.96	16.26	13.35	12.32	12.85	11.30	10.60	8.41	9.50	7.80	9.47
80	20.51	23.50	16.28	17.58	13.15	13.60	11.10	11.67	8.98	10.52	8.19	9.60

Table A.21: *Final Longitudinal Speed for All CSA Test Cases for Steering Angles 2,4,6,8,10,12*

	δ											
	2		4		6		8		10		12	
Vxo	LS	SMC	LC	SMC	LC	SMC	LC	SMC	LC	SMC	LC	SMC
30	0.00	0.00	0.00	0.00	0.00	0.00	0.22	0.00	1.63	0.28	1.57	0.27
50	0.06	0.16	0.19	4.53	0.27	5.36	1.62	3.80	2.45	3.76	2.37	3.77
80	2.25	3.01	2.71	7.70	2.71	7.61	2.71	7.61	2.71	7.61	2.71	7.61

Table A.22: *Max Lateral Speed for All CSA Test Cases for Steering Angles 2,4,6,8,10,12*

	δ											
	2		4		6		8		10		12	
Vxo	LS	SMC	LC	SMC	LC	SMC	LC	SMC	LC	SMC	LC	SMC
30	-0.13	-0.13	-0.23	-0.26	-0.37	-0.39	-0.48	-0.51	-0.63	-0.62	-0.73	-0.56
50	-0.03	-0.02	-0.13	-0.24	-0.37	-0.35	-0.50	-0.51	-0.63	-0.62	-0.73	-0.56
80	-0.47	-0.01	-0.34	-0.01	-0.34	-0.29	-0.50	-0.47	-0.63	-0.60	-0.73	-0.55

Table A.23: *Min Lateral Speed for All CSA Test Cases for Steering Angles 2,4,6,8,10,12*

	δ											
	2		4		6		8		10		12	
Vxo	LS	SMC	LC	SMC	LC	SMC	LC	SMC	LC	SMC	LC	SMC
30	0.10	0.01	0.10	0.01	0.10	0.01	0.10	0.01	0.10	0.01	0.10	0.01
50	1.57	0.01	1.57	0.01	1.57	0.01	1.57	0.01	1.57	0.01	1.57	0.01
80	22.69	0.01	21.90	0.01	19.57	0.01	18.95	0.01	18.95	0.01	18.95	0.01

Table A.24: *Max Yaw rate for All CSA Test Cases for Steering Angles 2,4,6,8,10,12*

	δ											
	2		4		6		8		10		12	
Vxo	LS	SMC	LC	SMC	LC	SMC	LC	SMC	LC	SMC	LC	SMC
30	-10.92	-8.97	-19.82	-17.93	-29.08	-26.87	-39.53	-35.22	-41.53	-39.99	-41.71	-45.09
50	-14.95	-15.07	-29.58	-30.28	-39.31	-39.61	-46.21	-39.58	-46.67	-39.58	-48.08	-45.09
80	-31.20	-27.15	-33.17	-36.71	-40.34	-36.71	-43.33	-36.71	-49.27	-38.22	-46.36	-45.07

Table A.25: *Min Yaw rate for All CSA Test Cases for Steering Angles 2,4,6,8,10,12*

	δ											
	2		4		6		8		10		12	
Vxo	LS	SMC	LC	SMC	LC	SMC	LC	SMC	LC	SMC	LC	SMC
30	0.00	0.00	0.00	0.00	0.00	0.00	0.93	0.00	7.84	1.29	7.78	1.25
50	0.16	0.41	0.50	14.22	0.82	15.36	6.97	10.55	11.71	10.47	11.74	10.49
80	3.61	4.96	4.38	13.41	4.39	13.33	7.71	13.34	11.63	13.33	12.03	13.35

Table A.26: *Max Vehicle Side slip for All CSA Test Cases for Steering Angles 2,4,6,8,10,12*

	δ											
	2		4		6		8		10		12	
Vxo	LS	SMC	LC	SMC	LC	SMC	LC	SMC	LC	SMC	LC	SMC
30	-0.53	-0.56	-0.95	-1.22	-1.73	-2.01	-2.34	-2.96	-4.10	-4.02	-5.06	-3.40
50	-0.08	-0.05	-0.37	-1.05	-1.73	-1.54	-2.57	-2.74	-4.10	-3.75	-5.09	-3.36
80	-0.78	-0.01	-0.56	-0.01	-1.47	-1.24	-2.60	-2.30	-3.95	-3.26	-4.96	-3.26

Table A.27: *Min Vehicle Side slip for All CSA Test Cases for Steering Angles 2,4,6,8,10,12*

A.8 CSA Telemetry Data for Steering Angles 14-24 Degrees

	δ											
	14		16		18		20		22		24	
Vxo	LS	SMC	LC	SMC	LC	SMC	LC	SMC	LC	SMC	LC	SMC
30	7.77	8.82	6.29	8.37	5.59	8.03	5.18	7.70	5.07	7.41	5.65	7.09
50	7.00	8.88	6.52	8.43	5.99	8.06	5.40	7.62	5.08	7.40	5.92	7.03
80	7.38	8.95	7.16	8.47	6.24	8.30	5.69	7.59	5.31	7.36	5.20	7.07

Table A.28: *Final Longitudinal Speed for All CSA Test Cases for Steering Angles 14,16,18,20,22,24*

	δ											
	14		16		18		20		22		24	
Vxo	LS	SMC	LC	SMC	LC	SMC	LC	SMC	LC	SMC	LC	SMC
30	1.51	0.28	1.51	0.28	1.50	0.28	1.52	0.28	1.53	0.28	1.56	0.28
50	2.45	3.76	2.44	3.76	2.47	3.76	2.44	3.76	2.36	3.76	2.35	3.76
80	2.71	7.60	2.71	7.60	2.71	7.60	2.71	7.60	2.71	7.60	2.71	7.60

Table A.29: *Max Lateral Speed for All CSA Test Cases for Steering Angles 14,16,18,20,22,24*

	δ											
	14		16		18		20		22		24	
Vxo	LS	SMC	LC	SMC	LC	SMC	LC	SMC	LC	SMC	LC	SMC
30	-0.83	-0.64	-0.91	-0.78	-0.98	-0.90	-1.04	-1.01	-1.10	-1.10	-1.18	-1.18
50	-0.82	-0.64	-0.91	-0.78	-0.98	-0.89	-1.04	-1.00	-1.11	-1.09	-1.18	-1.17
80	-0.82	-0.64	-0.91	-0.78	-0.98	-0.90	-1.04	-1.00	-1.11	-1.10	-1.16	-1.18

Table A.30: *Min Lateral Speed for All CSA Test Cases for Steering Angles 14,16,18,20,22,24*

	δ											
	14		16		18		20		22		24	
Vxo	LS	SMC	LC	SMC	LC	SMC	LC	SMC	LC	SMC	LC	SMC
30	0.10	0.01	0.10	0.01	0.10	0.01	0.10	0.01	0.10	0.01	0.10	0.01
50	1.57	0.01	1.57	0.01	1.57	0.01	1.57	0.01	1.57	0.01	1.57	0.01
80	18.95	0.01	18.95	0.01	18.95	0.01	18.95	0.01	18.95	0.01	18.95	0.01

Table A.31: *Max Yaw rate for All CSA Test Cases for Steering Angles 14,16,18,20,22,24*

	δ											
	14		16		18		20		22		24	
Vxo	LS	SMC	LC	SMC	LC	SMC	LC	SMC	LC	SMC	LC	SMC
30	-45.12	-48.44	-46.58	-50.66	-48.42	-52.85	-50.35	-54.87	-49.50	-56.80	-56.53	-58.75
50	-53.61	-48.40	-55.79	-50.65	-59.09	-52.79	-60.92	-54.92	-64.11	-56.84	-67.21	-58.71
80	-53.57	-48.22	-51.86	-50.54	-61.46	-52.49	-63.66	-54.85	-63.33	-56.84	-72.44	-58.76

Table A.32: *Min Yaw rate for All CSA Test Cases for Steering Angles 14,16,18,20,22,24*

	δ											
	14		16		18		20		22		24	
Vxo	LS	SMC	LC	SMC	LC	SMC	LC	SMC	LC	SMC	LC	SMC
30	7.51	1.33	7.54	1.29	7.52	1.30	7.68	1.31	7.76	1.33	7.97	1.33
50	12.20	10.49	12.19	10.49	12.48	10.49	12.38	10.49	12.14	10.49	12.09	10.49
80	12.04	13.31	12.01	13.29	12.66	13.29	12.84	13.29	12.15	13.29	13.17	13.29

Table A.33: *Max Vehicle Side slip for All CSA Test Cases for Steering Angles 14,16,18,20,22,24*

	δ											
	14		16		18		20		22		24	
Vxo	LS	SMC	LC	SMC	LC	SMC	LC	SMC	LC	SMC	LC	SMC
30	-5.90	-4.10	-7.25	-5.22	-8.37	-6.32	-9.44	-7.35	-10.51	-8.33	-11.69	-9.32
50	-6.16	-4.11	-7.18	-5.22	-8.23	-6.29	-9.32	-7.33	-10.42	-8.30	-11.71	-9.28
80	-6.04	-4.04	-6.94	-5.20	-8.13	-6.19	-9.23	-7.31	-10.29	-8.34	-11.72	-9.30

Table A.34: *Min Vehicle Side slip for All CSA Test Cases for Steering Angles 14,16,18,20,22,24*

Nomenclature

α	Slip angle of tire
α_{ij}	Slip angle of tire
β	Vehicle side slip angle
δ	Steering angle of front wheels
λ_{ij}	Wheel slip ratio
ω	Rotational velocity of wheel
$f1x$	Longitudinal force on front right wheel
$f2y$	Lateral force on front left wheel
$f3z$	Vertical force on rear right wheel
hg	Height of center of gravity of vehicle from the ground
i	Variable substituted for R or F (Rear or Front)
ijF_X	Longitudinal force of each separate tire
ijF_Y	Lateral force of each separate tire
j	Variable substituted for L or R (Left or Right)
L_f	Length of front of vehicle to center of gravity
L_r	Length of rear of vehicle to center of gravity

L_w Width of vehicle

r Yaw rate around the vehicle center of gravity

R_w Radius of vehicle wheel at slip point

u Planck constant

V_X Longitudinal Velocity of Vehicle center of gravity

V_Y Lateral Velocity of Vehicle center of gravity

V_{Xij} Longitudinal Velocity of Each Wheel